Exploration of Spectrally Featureless Asteroids:

Reflectance Measurements of Meteorites and

Characterization of a Commercial Camera System for the Psyche Mission

by

Steven Dibb

A Dissertation Presented in Partial Fulfillment
of the Requirements for the Degree
Doctor of Philosophy

Approved November 2021 by the
Graduate Supervisory Committee:

James Bell, Chair
Craig Hardgrove
Laurence Garvie
Linda Elkins-Tanton
Maitrayee Bose

ARIZONA STATE UNIVERSITY

December 2021

ABSTRACT

Characterizing the surface mineralogy of asteroids is critical to constraining their formation history and provides insight into the processes of planetary formation. One method of determining the surface mineralogy of asteroids is comparison of their visible to near-infrared reflectance (VNIR) spectra with laboratory spectra from meteorites and minerals. Subsequent in-situ investigation of these asteroids by spacecraft can supplement or supersede interpretations derived from Earth-based observations.

I investigated a suite of aubrites, sulfide minerals, and metal-rich chondrites in a variety of forms (hand samples, powders, and slabs) to identify similarities with ‘spectrally featureless’ asteroids. I collected VNIR spectra and powder X-ray diffraction patterns of these samples and compared their overall reflectance and spectral slope with X-complex and T-, L-, and D-type asteroid spectra.

The Psyche Mission will orbit asteroid (16) Psyche beginning in 2026. I provide a pre-flight assessment of the surface composition of Psyche by comparing spectra of Psyche to a large spectral library of possible surface analog materials (e.g., iron meteorites, mesosiderites, pallasites, sulfides, enstatite, ordinary, and metal-rich chondrites, endmember silicates, and mixtures of silicates, metal, and sulfides). Spectra of Psyche are generally consistent with iron meteorite powder, mixtures of iron meteorite powder and low-Fe, low-Ca pyroxene, sulfide minerals, and the CH/CBb chondrite Isheyevo. Next, I demonstrate some anticipated capabilities of the Psyche Multispectral Imager by comparing spectral parameters derived from Imager-convolved data to those

from high resolution laboratory spectra. I offer preliminary strategies for classifying surface composition based on Imager filter ratios and overall reflectance.

Last, I present an assessment of a benchtop, commercial-off-the-shelf (COTS) version of the Psyche Imager. The COTS Imager uses the same model CCD and a similar f-number commercial camera lens. I measured the gain, full well, linearity, read noise, quantum efficiency, and modulation transfer function to compare with eventual calibration data from the flight Imager. I validate the results of a radiometric model developed for the flight Imager with signal measurements from the COTS Imager. This work demonstrates that the COTS Imager is an effective testbed for validating Imager requirements and developing software and procedures for eventual calibration of the flight instrument.

ACKNOWLEDGMENTS

The work presented in this dissertation is a substantial part of nearly six years of concerted effort, personal growth, and both joyful and painful leaps in my knowledge and understanding. I owe much to my committee (Jim, Lindy, Craig, Laurence, and Maitrayee) for shaping me into the scientist I am now and changing how I view myself, others, and the world. I am extremely appreciative of the course they have set me on and the opportunities they deemed me worthy of. The work presented in this dissertation was largely supported by NASA Grant NNM16AA09C.

Besides my committee, there are many other mentors who have fostered my passion and curiosity. These include Joe O'Rourke, Dave Williams, Suzanne Nowicki, Tim McCoy, Cassie Bowman, Chris Haberle, Insoo Jun, Luz Maria Martinez Sierra, Scott Smas, Walter Kiefer, and Doug Hemingway, among others. Through these people and my committee, I am inspired to support the next generation of scientists and explorers.

Next, I would like to acknowledge the love, humor, and support from my family, which have been vital in seeing this thing through. Mom and Dad – your unending enthusiasm and love is the wellspring from which I draw motivation on hard days. Brittany, Kevin, and Tom – thank you for being such inspirational role models. I'll see you guys over a game of Catan. Finally, to my sweet dog Canyon, thank you for always pulling me through (seriously, ease up on that leash).

As with any human endeavor, there are a great deal of other people who contributed to this work behind the scenes. Without them, it would not have been possible. For this reason, I am very grateful to the following peer mentors, collaborators, friends, and groups who are responsible for sustaining my excitement about the natural world and understanding our place within it. They are presented in a pseudo-randomized list: Claire Richardson, Travis Gabriel, Hannah Bercovici, Kevin Hubbard, Andy Winhold, John Hayes, Alex Sabo, Mitchell Philips, Jessie Bersson, Lena Heffern, Jon Hoh, Grace Carlson, Bella Breen, Sean Czarnecki, Hannah Kerner, Vishaal Singh, Alex Pye, Joel Leonard, Nivedita Mahesh, Soumya Ray, Zack Torrano, Jack Lightholder, Allison Fox, Ellie Armstrong, Alyssa Pascuzzo, Dave Bernstein, Elinor Mullin, Harrison Seny, Yassi Khairolomour, Maya Midzik, the staff of SESE, the ASU Center for Meteorite Studies, the current and former Notorious Bell Research Group, and the entire Psyche Mission Team.

And last, but not least, in the words of Snoop Dogg: “I want to thank me for believing in me, I want to thank me for doing all this hard work, I want to thank me for having no days off, I want to thank me for never quitting, I want to thank me for always being a giver and trying to give more than I receive, I want to thank me for trying to do more right than wrong, and I want to thank me for just being me at all times.”

TABLE OF CONTENTS

CHAPTER Page

CHAPTER Page

LIST OF TABLES

LIST OF FIGURES

Figure Page

Figure Page

CHAPTER 1

INTRODUCTION

1.1 Prologue

Besides the terrestrial and giant planets, our Solar System is home to millions of compositionally diverse ‘small bodies’. These objects include asteroids, many of which lie between the orbits of Mars and Jupiter and may represent leftover components from planetary formation. Identifying compositional and dynamical relationships between types of asteroids and the planets remains an outstanding field of research in planetary science. Several fundamental questions remain unresolved: Are asteroids representative of primordial nebular material, or are they the product of violent collisions of differentiated bodies? Do the parent bodies of different meteorite classes still exist and, if so, where are they? How representative are asteroids of the surfaces and/or interiors of the terrestrial planets, including our own? Are asteroids potential economic resources? More worrisome: what kind of threat do asteroids present to Earth’s biosphere? The work presented in this dissertation represents a small but substantive advance in our attempts to understand the nature of some asteroids and contribute to a pool of knowledge that can answer the above questions.

Part of the answers to the above questions come from an understanding of what asteroids are made of. A primary method for studying the composition of asteroids is comparison to meteorites and minerals using reflectance spectroscopy at visible to near-infrared wavelengths from ~350-2500 nm. This wavelength band offers a practical window for studying asteroids because it avoids significant atmospheric absorption windows and is easily measured by commercially available scientific-grade devices (e.g., CCDs, radiometers) at observatories on Earth and by instrumentation on spacecraft. Furthermore, radiation measured from asteroids across this wavelength band is dominated by reflected sunlight rather than thermal emission (which dominates at wavelengths longer than ~4000 nm).

1.2 Why Do Minerals Have Absorption Features?

Visible to near-infrared (VNIR, ~350-2500 nm) reflectance spectroscopy is an effective method for assessing the surface composition of planetary surfaces. This is because many thousands of minerals exhibit diagnostic spectral parameters indicative of their chemistry (and to a lesser extent, the material's grain size and the measurement's phase angle) within this wavelength range (Burns 1993, Rossman and Ehlmann 2020).

At VNIR wavelengths, absorption features in common rock-forming minerals are typically caused by electronic and vibrational processes of the atoms in the mineral's crystal lattice (Burns 1993, Clark 1999, Rossman and Ehlmann 2020). Different elements in minerals cause shifts in the electronic or vibrational processes, and thus by measuring the relationship between mineral chemistry and spectroscopic signatures, we can remotely infer the mineralogy of a planetary surface. For planetary remote sensing, the elements of most interest are those that are abundant and cause absorption features. In most rock-forming minerals, these elements are those in the first transition series on the periodic table. These elements (especially Fe, Ti, Co, and Cu) are the dominant causes of features attributed to crystal field effects (Burns 1993). In free space, an atom of these elements will typically have its valence electrons evenly distributed in sets of probabilistic locations around the nucleus called orbitals (Burns 1993, Rossman and Ehlmann 2020). In this setting, electrons in each of these orbitals will have equal energy.

When these transition metal elements are bound in the crystal structure of a mineral, the electrons about the nucleus are repulsed by the presence of the electrons surrounding the nucleus of anions (which is commonly oxygen in planetary-relevant minerals; Burns 1993, Rossman and Ehlmann 2020). This repulsion causes a distortion of the orbital energy levels such that electrons require a certain amount of energy to be excited into “higher” energy levels. It is this required energy that gives rise to much of the color we see in most minerals as visible light at certain wavelengths is preferentially absorbed by electrons. These types of transitions are broken into two groups: spin-allowed, in which the number of unpaired electrons does not change before and after the absorption of a photon, and spin-forbidden, in which the opposite is true. Spin-forbidden features are typically much weaker than spin-allowed transitions and are orders of magnitude less likely to occur; however, certain conditions can arise such that spin-forbidden transitions become very prominent in spectra of minerals. Furthermore, the distance between the transition metal ion and the anions plays a strong role in shaping the absorption feature in the spectrum of a mineral (Burns 1993, Rossman and Ehlmann 2020). These distances are often distorted by thermal motion of the atoms (the cause of broadening of the absorption features) and pressure, which can distort the shape and center of an absorption feature as the crystal structure of a mineral is compressed.

Finally, and perhaps most importantly, replacement of specific elements in the crystallographic sites can both be the cause of and change the center, shape, and depth of absorption features in a mineral’s spectrum. An example most relevant to the work in this dissertation is Ca and Fe replacing Mg in pyroxene. Fe-rich pyroxenes typically form in an orthorhombic structure and have absorption bands centered at ~900 and 1900 nm due to crystal field transitions of ferrous iron occupying the M2 crystallographic site (Cloutis and Gaffey 1991, Burns 1993, Horgan et al. 2014). Ca-rich pyroxenes, which typically form in a monoclinic crystal structure, exhibit two 'types' of reflectance spectra, Type A and Type B (Cloutis and Gaffey 1991, Horgan et al. 2014). Type B clinopyroxene spectra exhibit absorption features similar to orthorhombic pyroxene, except the two absorption features are at longer wavelengths (~1050 nm and 2300 nm). Type A clinopyroxene spectra exhibit more complex, multilobed absorption features at ~1000 nm. It's important to note that the absorption features in Ca-rich clinopyroxene still come from the presence of ferrous iron in the M2 site, but the features in Type A clinopyroxene spectra are caused by ferrous iron occupying both the M1 and M2 crystallographic site (Cloutis and Gaffey 1991, Horgan et al. 2014). The abundance of Fe in the crystal structure is a strong control on the shape and center of the absorption feature in pyroxene.

Other important causes of absorption features in the visible to near-infrared are oxygen-metal charge transfer (OMCT), intervalence charge transfer (IVCT), and vibrational processes (Clark 1999, Rossman and Ehlmann 2020). OMCTs and IVCTs are typically hundreds to thousands of times stronger than crystal field effect transitions. OMCTs typically require higher energy (because of the distance between the anion and cation) and thus cause absorption features in the ultraviolet and bluer end of the spectrum. These transitions are the cause of the steep spectral slope for some silicate minerals (e.g., Fe-O transitions in olivine and pyroxene) in the ultraviolet. IVCT describes the transfer of an electron between two physically close cations (e.g., Fe^{2+} -

Fe^{3+} and Fe^{2+} - Ti^{4+}). IVCTs typically cause absorption at visible wavelengths. An example is the red color of hematite and goethite, caused by strong UV and blue absorption from the Fe^{2+} - Fe^{3+} IVCT (Clark 1999).

Finally, vibrational processes can cause absorption features at visible to near-infrared wavelengths (Clark 1999). The atoms of molecules can move rhythmically like masses attached via springs. Energy input to this system can cause vibration along set orientations. Harmonic motion occurs at fundamental frequencies related to certain wavelengths of light, and both multiples (called 'overtones') and combinations of a molecule's fundamental frequencies can occur (Clark 1999). Some molecules (e.g., H_2O, CO_3) have overtones and/or combinations that cause absorption in the near-infrared. For example, an overtone of OH stretching occurs at ~1400 nm and a combination of H-O-H bending and OH stretching occurs at ~1900 nm. The presence or absence of the 1900 nm feature in a spectrum that has the 1400 nm feature indicates whether the mineral has water or just the hydroxl group (e.g., kaolinite). Carbonates typically exhibit multiple overtone and combination absorptions between 1800 and 2500 nm.

Sulfide minerals (e.g., troilite, FeS, and cinnabar, HgS) typically exhibit varying absorption "edges" at visible to near-infrared wavelengths characteristic of semiconductor materials (Hunt et al. 1971, Clark 1999). This wavelength position of this edge corresponds to the energy level of the band gap between the valence band, where electrons are attached to single atoms, and the conduction band, in which electrons can move freely about the crystal lattice. Photons with high enough energies to excite electrons into the conduction band are absorbed by the material, and thus there is low reflection at these or shorter wavelengths (Hunt et al. 1971, Cloutis and Gaffey 1994).

For spectra of pure sulfur and large single crystals of sulfides, the absorption edge is very sharp (e.g., Cloutis and Gaffey 1994, Clark 1999). For most natural sulfides (i.e., those found in meteorites), the degree of crystallinity, the presence of grain boundaries, and the presence of impurities act to “round off” the absorption edge (Hunt et al. 1971, Cloutis and Gaffey 1994, Burbine et al. 2002). Thus, the reflectance spectrum of a natural sample of a mineral like troilite is typically not characterized by a strong absorption edge.

The reflectance properties of metals are described by the Drude model (Britt and Pieters 1988, Dresselhaus 2001). In this model, metals (i.e., iron meteorites) are treated as electrically conductive materials, and thus incident light induces an electric field in the lattice of metal atoms. Incident photons are subject to the induced field and are absorbed or reflected dependent on their wavelength. The spectral reflectivity of metals is characteristic of the strength of the induced field, the plasma frequency of the metal (the resonance frequency of the electrons in the conduction band of the metal), and the wavelength of light. Each metal has a specific plasma frequency. The Drude model predicts that iron will exhibit increasing reflectance with increasing wavelength at visible to near-infrared wavelengths. This theoretical model has been verified by spectral measurements of iron meteorites (e.g., Britt and Pieters 1988, Cloutis et al. 2010) and measurements of the optical constants of iron-nickel alloys (e.g., Cahill et al. 2019). A notable feature in these measurements in a change in slope between 400-600 nm in spectra of iron meteorites, which, as shown in Chapter 3, will be useful for discriminating iron meteorites from other ‘spectrally featureless’ materials on the surface of (16) Psyche.

In summary, reflectance spectra of geologic materials are characterized primarily by their constituent minerals, which can exhibit diagnostic absorption features (also called absorption bands) characteristic of their crystal structure and composition. Because the reflectance spectra and mineralogy of meteorites can be precisely characterized in laboratories on Earth, matching the shape, band center, and band depth of absorption features in reflectance spectra of both meteorites and asteroids can be used to infer the presence or absence of certain minerals on the surfaces of asteroids and therefore place constraints on their bulk composition and formation history.

1.3 An Overview of Asteroid Classification

One of the more common methods for classifying asteroids is by their spectral properties. Currently there are two major taxonomies for asteroids based on spectral classification schemes: the scheme developed by Tholen in his 1984 PhD dissertation using data from the Eight Color Asteroid Survey, and the scheme developed by Bus and Binzel in the former's 2002 PhD dissertation using data from the Small Main-Belt Asteroid Spectroscopic Survey (Tholen 1984, Bus and Binzel 2002). Tholen's scheme strengthened the previously developed major asteroid classes (e.g., C-type, S-types) based on similarities to spectra of meteorites and minerals. The X-type class discussed by Tholen was a catch-all for asteroids with spectra that did not exhibit strong absorption features and were red-sloped (increasing wavelength with increasing reflectance) (Tholen 1984). Tholen broke the X-types down further based on visible wavelength albedos (p_v) into the E-types ($p_v > 0.3$), M-types ($0.1 < p_v < 0.3$), and P-types ($p_v < 0.1$) (Tholen 1984). These letter assignments are no accident: the E-types were assigned to asteroids with enstatite-like spectra, M-types were thought to be metal-rich, and P-types were thought to be primitive, undifferentiated objects. In the Bus-Binzel taxonomy, many of the original classes of Tholen's taxonomy were adjusted or removed, and several more were added. The most recent major update to the Bus-Binzel taxonomy was by DeMeo et al. (2009). This update utilized data from new telescopic instruments sensitive to wavelengths further into the infrared (out to 2450 nm), and thus enabled further classification. In the new DeMeo/SMASS taxonomy, many of the asteroids that are Tholen X-types are folded into the larger 'X-complex', which includes classes similar to the Tholen E- and P-types. (Fig. 1.1). The asteroids in the X-complex, as well as the T-, L-, and D-type asteroids, exhibit spectra that are red-sloped (increasing reflectance with increasing wavelength) and are 'featureless', meaning they exhibit minimal absorption features or none that can

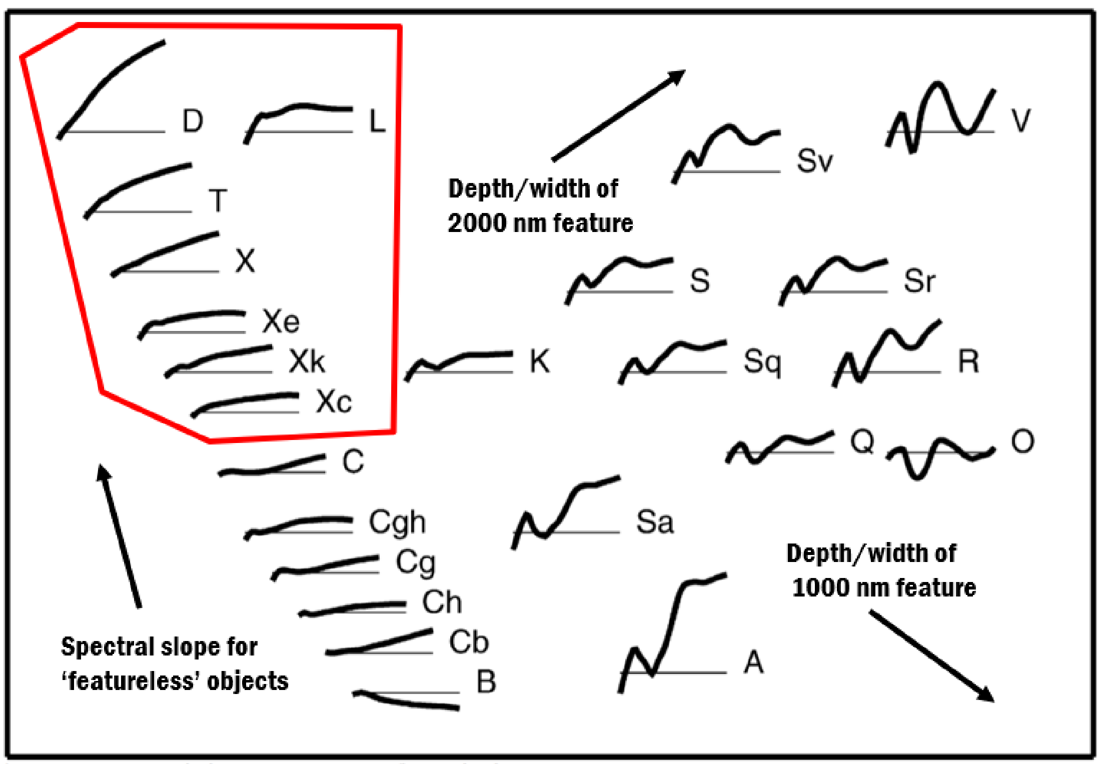

Fig. 1.1 A key for interpreting the asteroid taxonomy developed by DeMeo et al. (2009). The mean 450-2450 nm spectrum of asteroids from each taxonomic group is plotted in their approximate location in principal components space. Approximate trends for absorption features and spectral slopes are indicated. The asteroids referred to as 'spectrally featureless' in this dissertation are inside the red polygon.

be measured with current observing methods and detector technology. These asteroids are grouped in a red polygon in Fig. 1.1. To characterize the surfaces of spectrally ‘featureless’ asteroids, more simple spectral parameters, such as visible wavelength (typically 550 or 560 nm) reflectance and changes in spectral slope, are used to constrain the relationship between certain classes of asteroids and meteorites.

1.4 Asteroid (16) Psyche and the Psyche Mission

Asteroid (16) Psyche is a large asteroid in the main asteroid belt (Elkins-Tanton et al. 2020). Observations of the density, radar reflectivity, emissivity, and VNIR reflectance are consistent with Psyche being metal-rich (30-55 vol.% metal; Elkins-Tanton et al. 2020). Psyche is classified in the Tholen taxonomy as an M-type and in the DeMeo/SMASS taxonomy as an X-type or Xk-type. Thus, it is common to see Psyche described as an M-/X-type asteroid. In short, these labels mean that the visible to near-infrared spectrum of Psyche is relatively featureless, red-sloped, and exhibits a weak feature at ~900 nm, interpreted as the presence of low-Fe, low-Ca silicates (DeMeo et al. 2009). More discussion of the spectral properties of (16) Psyche can be found in Chapters 2 and 3 of this dissertation.

The density of Psyche is one of the most compelling lines of evidence that suggest a metal-rich composition. Estimates for the density of Psyche come from dividing estimates of its mass by estimates of its volume. The mass of an asteroid can be determined by mutual deflections of the orbits of the asteroid in question and another body (usually another asteroid) (e.g., Baer and Chesley 2017, Siltala and Granvik 2021). Psyche was determined to have a mass of ~1.15 x 10^{-11} solar masses by Baer and Chesley

(2017). The volume of an asteroid is typically measured in three ways: time-resolved high-resolution images (e.g., Viikinkoski et al. 2018, Ferrais et al. 2020), measurements of radar echoes (e.g., Shepard et al. 2017, Shepard et al. 2021), or imaging during stellar occultation (e.g., Viikinkoski et al. 2018, Shepard et al. 2021). From these methods, Psyche has been determined to be a triaxial ellipsoid with dimensions ~278 (−4/+8) × 238 (−4/+6) × 171 km (−1/+5), with an effective spherical diameter D_{eff} = 222 (-1/+4) km (Shepard et al. 2021). These masses and volumes give a preferred density of 3.78 ± 0.34 g/cm^3 (Elkins-Tanton et al. 2020). More recent estimates are consistent with this value (4.20 ± 0.60 g/cm3 from Ferrais et al. 2020 and 3.88 ± 0.25 g/cm3 from Siltala and Granvik 2021). These estimates for the density of Psyche are at the upper end of densities for main belt asteroids (Carry 2012, Hanuš et al. 2017) and at the upper end of most silicate minerals, suggesting that Psyche is a mixture of silicate minerals and some higher density phase. The most likely higher density phases are iron nickel metal (e.g., kamacite and/or taenite) and sulfide minerals (the simplest of which is troilite – FeS), both of which are common in iron meteorites.

The next line of evidence that suggests Psyche has a high metal abundance is its radar reflectivity (also called radar albedo). This property is measured by sending radio waves from Earth-based facilities at specified frequencies (either at 2380 MHz [λ = 12.6 cm] from Arecibo Observatory or 8560 MHz [λ = 3.5 cm] from Goldstone Deep Space Communications Complex) and measuring the returned spectral power distribution over time (Ostro 1993, Ostro et al. 2002; Shepard et al. 2008). An asteroid's apparent diameter at a particular rotation angle is related to the instantaneous bandwidth of the returned radar echo at that rotation angle (note that the frequency of the returned echo is 'smeared' about the original transmitted frequency due to the rotation of the asteroid during the measurement window), the rotation period of the asteroid, the cosine of the sub-Earth latitude, and a constant particular to the wavelength being used (Shepard et al. 2017).

Furthermore, these radio waves are typically emitted with circular polarization and the echo is measured in both the same sense polarization and opposite sense polarization. Upon reflection from a smooth, mirror-like surface, the polarization of the wave is perfectly inverted, resulting in opposite sense polarization (Ostro et al. 1993). The ratio of the same sense versus opposite sense polarization at the receiver is called the circular polarization ratio and gives an indication of the surface roughness. Values near zero indicate a smooth surface while values near or over 1.0 indicate a very rough surface. Intermediate values indicate a roughness on the order of the wavelength of the transmitted radio waves. Psyche's circular polarization ratio is 0.1 ± 0.1, which indicates a relatively smooth surface on the scale of the radar wavelengths (Shepard et al. 2008, Shepard et al. 2017, Shepard et al. 2021).

Next, radar cross sections (in km^2) can be estimated by integrating spectra of the Doppler shift of the reflected radio waves (Shepard et al. 2008). Finally, the radar albedo of an asteroid is computed by dividing the radar cross section by the square of the apparent diameter and multiplying by π/4. Radar albedos measured for main-belt asteroids range from 0.039 for CP-class asteroid (247) Eukrate up to 0.6 for M-type asteroid (216) Kleopatra. Psyche's mean radar albedo is 0.34 ± 0.08, which is more than double the radar albedo of main-belt S- and C-type asteroids (Shepard et al. 2021). The most reasonable interpretation of this is an enhancement in metal abundance in the near-surface (~1 m depth) regolith of the asteroid (Shepard et al. 2021).

The final measurement that suggests Psyche has a metal-rich composition is its emissivity at various wavelengths. In general, observations of asteroids at thermal infrared wavelengths (>~8000 nm) are collected at Earth or space-based observatories and used to refine thermophysical models of an asteroids surface properties, including surface roughness, particle size distribution, and composition. Matter et al. (2013) reported the emission of Psyche from 8000-13000 nm and determined the thermal inertia (computed as the square root of an object's thermal conductivity, density, and heat capacity) to be one of the highest ever measured for a main belt asteroid (114-133 ± 40 J $m^{-2}\ s^{-0.5}\ K^{-1}$). Because metallic materials have high thermal conductivities, this high value for thermal inertia was interpreted to be further evidence of a metal-rich surface composition (Matter et al. 2013).

In contrast, Landsman et al. (2018) used measurements of Psyche's 8000-15000 nm emission from the Spitzer Space Telescope and reported a thermal inertia of 5-25 J $m^{-2}\ s^{-0.5}\ K^{-1}$, more consistent with S- and C-type asteroids in the main belt. Furthermore, Landsman et al. (2018) demonstrated similarities between the relative spectral emissivity of Psyche and those of fine-grained silicates, particularly low-Fe pyroxene with a grain size of <75 microns. The general interpretation from the study is that Psyche likely has a smooth surface composed of metallic bedrock coated in fine-grained silicates.

Finally, de Kleer et al. (2021) reported measurements of Psyche's 1.3 mm emissivity from the Atacama Large (sub)Millimeter Array telescope. The authors then used a modified version of the thermophysical model used by Matter et al. (2013) to estimate Psyche's thermal inertia as 280 ± 100 J $m^{-2}\ s^{-0.5}\ K^{-1}$, which is significantly higher than the results of Landsman et al. (2018) and within 1σ of the values from Matter et al. (2013). The average of the three measurements is ~ (123 + 15 + 280 / 3) = ~139 J m^{-2} $s^{-0.5}$ K^{-1}, which is substantially higher than dusty surfaces and most other asteroids, but significantly lower than solid rock (~2500 J m^{-2} $s^{-0.5}$ K^{-1}) or solid metals (~16700 J m^{-2} $s^{-0.5}$ K^{-1} for solid iron) (Matter et al. 2013, Crane et al. 2013). It is important to note that powdered surfaces of both silicate and metal composition have thermal conductivities ~0.1% of their solid counterparts, and thus a surface with a thermal inertia of ~200 J m^{-2} $s^{-0.5}$ K^{-1} is still consistent with a metal-rich surface albeit in powdered form.

To resolve these Earth-based measurements and test hypotheses of Psyche's formation, the Psyche Mission will study the asteroid from a series of increasingly close orbits starting in approximately January 2026. The five objectives of the Psyche Mission are to: (1) determine whether Psyche is a planetesimal core, (2) determine the relative ages of the regions of Psyche's surface, (3) determine whether small bodies incorporate the same light elements as are expected in the Earth's high-pressure core, (4) determine whether Psyche was formed under conditions more oxidizing or reducing than Earth's core, and (5) characterize Psyche's topography. To address the objectives, the Psyche spacecraft will carry a set of science instruments designed to make key measurements of Psyche, including a magnetometer, a gamma-ray and neutron spectrometer, and a pair of multispectral cameras. In addition, tracking of the Psyche spacecraft and Doppler shift of the returned radio signals will enable the interior structure of Psyche to be resolved. Together, these investigations will provide a wealth of data on a type of object that has never been explored by spacecraft: a metal-rich body. The measurements made by the Psyche Mission may provide strong control on models of solar system formation and greatly advance our understanding of the formation of our own planet.

1.5 Overview of Chapters

To provide insight into the surface compositions of spectrally ‘featureless’ asteroids, the work presented in Chapter 2 of this dissertation reports spectral similarities between some aubrites, metal-rich chondrites, and sulfide minerals compared to X-complex (defined as the X-, Xc-, Xk-, and Xe-type) and T-, L-, and D-type asteroids. I compare their visible reflectance (at 550 nm) and visible and near-infrared spectral slopes (measured from 450-700 nm and 760-1200 nm). The spectral properties of aubrite samples are somewhat consistent with Xe-type asteroids while the spectral properties of the metal-rich chondrites are somewhat consistent with X-, Xc-, and Xk-type asteroids. Finally, sulfide minerals exhibit spectral properties intermediate to the T- and L-type asteroids. I show that D-type asteroids are not well-matched by the samples in the study. Finally, I show that spectra of the CH/CBb chondrite Isheyevo and spectra from troilite (FeS) from the Nantan meteorite are consistent with spectra of the second largest X-type asteroid, (16) Psyche.

In Chapter 3, I provide an updated assessment of the surface composition of (16) Psyche using reflectance spectroscopy. I gathered a library of 359 reflectance spectra of materials that may be present on the surface of Psyche based on spectral measurements and other physical/chemical properties. These materials include iron meteorites, metal-rich silicate-bearing achondrite meteorites (e.g., mesosiderites, pallasites), metal-rich chondrites (CB/CH chondrites and some ungrouped), sulfide minerals, and endmember silicates with well-characterized compositions. I used a chi-square goodness-of-fit test (essentially curve matching) to compare wavelength-by-wavelength all published spectra of Psyche to those in the library. My results indicate that the surface of Psyche is consistent with powder from iron meteorites, sulfide minerals, and the CH/CBb chondrite Isheyevo.

The Psyche spacecraft will be equipped with a suite of instruments designed to make observations to test hypotheses of the asteroid's formation. One of these instruments, the Psyche Multispectral Imager, will provide high spatial resolution images of the surface at key visible to near-infrared wavelengths. This multispectral capacity will be used to map absorption features diagnostic of silicate and sulfide minerals on the surface of Psyche. In Chapter 3, I provide a preliminary assessment of how data returned from the Imager can be used to reconstruct spectral parameters similar to those determined from high resolution laboratory spectra and discriminate between different surface compositions using band ratios and overall brightness.

The development of instrumentation for space missions typically culminates in a period of extensive testing to fully characterize an instrument's response to different possible inputs. This process is vital for credibly translating the measurements made by the instrument to values with scientific meaning. Depending on the instrument, this calibration can take days or weeks, a team of people, and sophisticated calibration equipment. In Chapter 4, I present a comprehensive characterization of a commercial-off-the-shelf (COTS) version of the Psyche Imager (called the COTS Imager). I report performance metrics of the COTS Imager, including gain, full well, read noise, linearity, modulation transfer function (MTF), and quantum efficiency. I also present data from the COTS Imager that was used to validate a radiometric model of the flight Imager's performance. The COTS Imager has served as an effective testbed for developing procedures and code for the eventual calibration of the flight Imagers.

References

Baer, J., & Chesley, S. R. (2017). Simultaneous mass determination for gravitationally coupled asteroids. The Astronomical Journal, 154(2), 76.

Britt, D. T., & Pieters, C. M. (1988). Bidirectional reflectance properties of iron-nickel meteorites. In Lunar and Planetary Science Conference Proceedings (Vol. 18, pp. 503-512).

Burbine T.H., McCoy T.J., Nittler L.R., Benedix G.K., Cloutis E.A., and Dickinson T.L. (2002). Spectra of extremely reduced assemblages: Implications for Mercury. Meteoritics & Planetary Science 37(9):1233-1244.

Burns, R. G. (1993). Mineralogical applications of crystal field theory (No. 5). Cambridge University Press.

Bus S.J. and Binzel R.P. (2002). Phase II of the small main-belt asteroid spectroscopic survey: A feature-based taxonomy. Icarus 158(1):146-177.

Cahill, J. T., Blewett, D. T., Nguyen, N. V., Boosalis, A., Lawrence, S. J., & Denevi, B. W. (2019). Optical constants of iron and nickel metal and an assessment of their relative influences on silicate mixture spectra from the FUV to the NIR. Icarus, 317, 229-241.

Carry B. (2012). Density of asteroids. Planetary and Space Science 73(1):98-118.

Clark R.N. (1999). Spectroscopy of rocks and minerals, and principles of spectroscopy. In Manual of Remote Sensing, 3rd ed., edited by Rencz A. N. John Wiley & Sons. pp.3-58.

Cloutis E.A. and Gaffey M.J. (1994). An X-ray diffraction and reflectance spectroscopy study of iron sulphides (abstract #273). 25th Lunar and Planetary Science Conference.

Cloutis, E. A., Hardersen, P. S., Bish, D. L., Bailey, D. T., Gaffey, M. J., & Craig, M. A. (2010). Reflectance spectra of iron meteorites: Implications for spectral identification of their parent bodies. Meteoritics & Planetary Science, 45(2), 304-332.

Crane, K. T., Minton, D. A., & Emery, J. P. (2013). Thermal Inertia of a Metallic Regolith: A Simulant Sample Experiment. In Lunar and Planetary Science Conference (No. 1719, p. 1018).

de Kleer, K., Cambioni, S., & Shepard, M. (2021). The Surface of (16) Psyche from Thermal Emission and Polarization Mapping. arXiv preprint arXiv:2105.11372.

DeMeo F.E., Binzel R.P., Slivan S.M., and Bus S.J. (2009). An extension of the Bus asteroid taxonomy into the near-infrared. Icarus 202(1):160-180.

Dresselhaus, M. S. (2001). Solid state physics part ii optical properties of solids. Lecture Notes (Massachusetts Institute of Technology, Cambridge, MA), 17, 15-16.

Elkins-Tanton L.T., Asphaug E., Bell III J.F., Bercovici H., Bills B., Binzel R., et al. (2020). Observations, meteorites, and models: a preflight assessment of the composition and formation of (16) Psyche. Journal of Geophysical Research: Planets 125(3):e2019JE006296.

Ferrais, M., Vernazza, P., Jorda, L., Rambaux, N., Hanuš, J., Carry, B., et al. (2020). Asteroid (16) Psyche's primordial shape: A possible Jacobi ellipsoid. Astronomy & Astrophysics, 638, L15.

Hanuš, J., Viikinkoski, M., Marchis, F., Ďurech, J., Kaasalainen, M., Delbo, M., et al. (2017). Volumes and bulk densities of forty asteroids from ADAM shape modeling. Astronomy & Astrophysics, 601, A114.

Horgan, B. H., Cloutis, E. A., Mann, P., & Bell III, J. F. (2014). Near-infrared spectra of ferrous mineral mixtures and methods for their identification in planetary surface spectra. Icarus, 234, 132-154.

Hunt, G. R., Salisbury, J. W., Lenhoff, C. J. (1971). Visible and near-infrared spectra of minerals and rocks: IV sulphides and sulphates. Modern Geology, 3, 1-14.

Landsman, Z. A., Emery, J. P., Campins, H., Hanuš, J., Lim, L. F., & Cruikshank, D. P. (2018). Asteroid (16) Psyche: Evidence for a silicate regolith from spitzer space telescope spectroscopy. Icarus, 304, 58-73.

Matter, A., Delbo, M., Carry, B., & Ligori, S. (2013). Evidence of a metal-rich surface for the Asteroid (16) Psyche from interferometric observations in the thermal infrared. Icarus, 226(1), 419-427.

Ostro, S. J. (1993). Planetary radar astronomy. Reviews of Modern Physics, 65(4), 1235.

Ostro, S. J., Hudson, R. S., Benner, L. A., Giorgini, J. D., Magri, C., Margot, J. L., & Nolan, M. C. (2002). Asteroid radar astronomy. Asteroids III, 151-168.

Rossman, G. R., & Ehlmann, B. L. (2019). Electronic Spectra of Minerals in the Visible and Near-Infrared Regions. Remote Compositional Analysis: Techniques for Understanding Spectroscopy, 3-20.

Shepard, M. K., Clark, B. E., Nolan, M. C., Howell, E. S., Magri, C., Giorgini, J. D., et al. (2008). A radar survey of M-and X-class asteroids. Icarus, 195(1), 184-205.

Shepard, M. K., Richardson, J., Taylor, P. A., Rodriguez-Ford, L. A., Conrad, A., de Pater, I., et al. (2017). Radar observations and shape model of asteroid 16 Psyche. Icarus, 281, 388-403.

Shepard, M. K., de Kleer, K., Cambioni, S., Taylor, P. A., Virkki, A. K., Rívera-Valentin, E. G., et al. (2021). Asteroid 16 Psyche: Shape, Features, and Global Map. The Planetary Science Journal, 2(4), 125.

Siltala, L., & Granvik, M. (2021). Mass and Density of Asteroid (16) Psyche. The Astrophysical Journal Letters, 909(1), L14.

Tholen D. J. (1984). Asteroid taxonomy from cluster analysis of photometry. Ph.D. thesis, University of Arizona, Tucson, Arizona, United States.

Viikinkoski, M., Vernazza, P., Hanuš, J., Le Coroller, H., Tazhenova, K., Carry, B., et al. (2018). (16) Psyche: A mesosiderite-like asteroid?. Astronomy & Astrophysics, 619, L3.

CHAPTER 2

SPECTRAL REFLECTANCE VARIATIONS OF AUBRITES, METAL-RICH METEORITES, AND SULFIDES: IMPLICATIONS FOR EXPLORATION OF (16) PSYCHE AND OTHER 'SPECTRALLY FEATURELESS' ASTEROIDS

Steven D. Dibb[1]*, James F. Bell III[1], and Laurence A.J. Garvie[1,2]

[1]School of Earth and Space Exploration, Arizona State University, Tempe, AZ

[2]Center for Meteorite Studies, Arizona State University, Tempe, AZ

*Corresponding author. E-mail: sd.dibb@gmail.com

Citation: Dibb, S. D., Bell, III, J. F., Garvie, L. A. J. Spectral Reflectance Variations of Aubrites, Metal-rich Meteorites, and Sulfides: Implications for Exploration of (16) Psyche and other 'Spectrally Featureless' Asteroids. In review by *Meteoritics and Planetary Science.*

Abstract

The 350-2500 nm reflectance spectra of five enstatite achondrites (aubrites), five metal-rich chondrites (CBa, CBb, CH/CBb, and ungrouped), and seven sulfide mineral samples (three troilites, pyrrhotite, pentlandite, a mixture of pentlandite and chalcopyrite, and oldhamite) have been measured to search for spectral parameters that may offer insight into the surface composition of so-called 'spectrally featureless' asteroids. We measured the samples as powders, slabs, and hand samples. Aubrites exhibit high reflectance, generally positive slopes at visible wavelengths, and low-to-negative infrared slopes, consistent with E-/Xe-type asteroids. The metal-rich chondrites exhibit low

reflectance, moderate visible slopes, and low near-infrared slopes, somewhat consistent with M-/X-complex asteroids. The metal-rich chondrites exhibit absorption features at ~900 nm due to Fe^{2+}-bearing silicates. Sulfides exhibit low to moderate reflectance and high visible and near-infrared slope, intermediate to the T- and L-type asteroids. The D-type asteroids, which have very high visible and near-infrared slopes, are not well-matched by sulfides. Spectral data of the largest M-/X-type asteroid, (16) Psyche, are consistent with both powder from the Isheyevo CH/CBb chondrite and powder of meteoritic troilite. The data presented here will enable interpretation of data returned from future spacecraft missions to 'spectrally featureless' asteroids, like the Psyche, Lucy, and DART/Hera missions.

2.1 Introduction

Many asteroids exhibit relatively featureless reflectance spectra at visible to near-infrared wavelengths and have been variously categorized in different taxonomies in the past several decades (e.g., Tholen 1984; Bus and Binzel 2002; Clark et al. 2004a; Clark et al. 2004b; DeMeo et al. 2009). In Tholen's taxonomy, the featureless, red-sloped (increasing reflectance with increasing wavelength) X-types were further separated into the E-, M-, and P-type asteroids on the basis of their visible wavelength albedos: E-types have visible albedos >0.3, M-types have visible albedos between 0.1 and 0.3, and P-types <0.1 (Tholen 1984). These asteroids represented ~26% of the objects studied in the Eight-Color Asteroid Survey from which Tholen created the taxonomy (Tholen 1984; Zellner et al. 1985). In the Small Main-Belt Asteroid Spectroscopic Survey (SMASS), ~15% of asteroids studied were categorized into the 'X-complex' and separated by principal component analysis of their 435-900 nm reflectance spectra into the Xe-, Xc-, Xk-, and X-types (Bus and Binzel. 2002). DeMeo et al. (2009) further developed the Bus taxonomy using spectral measurements out to ~2500 nm. While not fitting into the Bus-DeMeo X-complex, the T-, L-, and D- type asteroids are also relatively spectrally featureless and generally have steeper spectral slopes than the X-complex asteroids (DeMeo et al. 2009). We adopt the term 'featureless' from Clark et al. (2004b) to refer to any asteroid who's visible to near-infrared reflectance spectrum is red-sloped and exhibits either no significant absorption features or subtle, weak features (<~5% band depth) at most. This includes the Tholen E-, M-, and P-types and the Bus-DeMeo X-, Xc-, Xe-, and Xk-type asteroids. We also include the Bus-DeMeo T-, L-, and D-types.

Because visible to near-infrared spectra are among the few kinds of overlapping datasets between large numbers of asteroids and meteorites, many authors have sought to establish connections between these two sets of objects (e.g., Cloutis et al. 1990; Binzel and Xu 1993; Gaffey and Kelley 2004; Sunshine et al. 2008). However, because of their relatively featureless spectra, mineralogical interpretation of the surfaces of 'featureless' asteroids is often inconclusive. Here we present new visible to near-infrared reflectance spectra of materials that may be analogs for the surfaces of these objects. Our sample set contains five aubrites, seven sulfide minerals, and five metal-rich chondrites. These materials exhibit relatively featureless, red-sloped reflectance spectra and are plausible analogs for the surfaces of 'spectrally featureless' asteroids due to physical and mineralogical properties (e.g., relatively high density, low FeO silicates). In addition to supporting telescopic observations of asteroids from Earth, robust libraries of visible to near-infrared spectra are critical for interpretation of data returned from future missions to ‘spectrally featureless’ asteroids, such as the Psyche, Lucy, and Hera missions, which will carry visible to near-infrared imaging systems (Bell et al. 2016; Levison et al. 2016; Ferrari et al. 2021). Because the nature of any regolith on these asteroids is poorly constrained, we report reflectance spectra of some of these materials in different physical forms (e.g., hand samples, slabs, different grain sizes) and over a range of phase angles to supplement future investigations of ‘featureless’ asteroids. To support mineralogical interpretations of the spectra of these samples, we also present powder X-ray diffraction data where possible. The combination of these two datasets will support interpretation of data from future space missions to members of these enigmatic asteroid taxa.

2.1.1 Tholen X-type Asteroids

Many of the Tholen X-type asteroids are also categorized in the Bus-DeMeo taxonomy as X-complex asteroids. The Tholen E-types are roughly equivalent to the Bus-DeMeo Xe-types, while the Tholen M-types were categorized under each of the Bus-DeMeo X-complex subtypes (X-, Xe-, Xk-, and Xc-types). Finally, the Tholen P-types fall mostly within the Bus-DeMeo X- and Xk-types (DeMeo et al. 2009). Here, we discuss mineralogical interpretations of each of these asteroid types from the perspective of the Tholen E-, M-, and P-types.

The E-types have been linked to the enstatite achondrite meteorites (also known as aubrites) because of similar visible albedo and reflectance properties at near-infrared wavelengths (Zellner et al. 1977; Clark et al. 2004a). Because these meteorites required a significant degree of igneous processing, exploration of E-type asteroids could offer unique constraints on models of planetary formation (Watters and Prinz 1979). E-type asteroids have been further distinguished into EI, EII, and EIII subtypes (Gaffey and Kelley 2004; Fornasier et al. 2008). The EI asteroids are characterized by featureless, red-sloped spectra consistent with nearly Fe-free enstatite as seen in aubrites (Clark et al. 2004a). In contrast, the EII and EIII asteroids exhibit red-sloped spectra with some absorption features diagnostic of certain minerals. Absorptions at ~500 nm and ~960 nm in the spectra of EII asteroids are interpreted as originating from the calcium sulfide mineral oldhamite, which, if present, indicates a highly reducing formation environment (Watters and Prinz 1979; Clark et al. 2004a; Gaffey and Kelley 2004; Fornasier et al. 2008). Spectra of the EIII asteroids exhibit absorption features at ~900 nm consistent with Fe-bearing pyroxene, which would indicate a more oxidizing environment than that suggested by the EIIs. This discrepancy indicates that our understanding of the linkage between E-types and aubrites is not complete (Clark et al. 2004a).

M-type asteroids are thought to have a significant metal component based on observations of density, emissivity, radar reflectivity, and spectral reflectance (e.g., Cloutis et al. 1990; Clark et al. 2004b; Hardersen et al. 2011; Carry 2012; Shepard et al. 2015; Elkins-Tanton et al. 2020). Density estimates for the M-types are typically greater than 3.2 g/cm3, while radar albedos of many members of this class exceed 0.3, a threshold consistent with a surface dominated by metal (Carry et al. 2012; Shepard et al., 2015). The inferred presence of a large fraction of metal in most M-type asteroids indicates that they likely formed in a reduced environment and could be remnant core material from disrupted differentiated planetesimals or are perhaps stripped cores themselves.

Spectra of the largest M-type asteroid, (16) Psyche, exhibit subtle absorption features at ~900 nm consistent with low-Fe pyroxenes, which would be further consistent with a reduced formation environment (Fornasier et al. 2010; Hardersen et al. 2011). However, recent spectral observations of (16) Psyche by Sanchez et al. (2017) are consistent with much more Fe-rich pyroxene, suggesting that our understanding of the formation and nature of M-types could be incomplete. Furthermore, some M-type asteroids exhibit a weak absorption feature at 3-µm consistent with the presence of hydrated silicates, and thus inconsistent with the interpretation that M-types are primarily metal, which might be expected for a remnant core (Rivkin et al. 1995; Rivkin et al. 2000).

Finally, while no meteoritic analog for P-type asteroids yet exists, they have been interpreted as possibly containing carbonaceous chondritic material, anhydrous silicates, phyllosilicates, ice, and/or unidentified opaque materials (Rivkin et al. 2002; Clark et al. 2004b; Hiroi et al. 2004). These components are primarily inferred from the relatively low bulk density of these asteroids (~0.8-1.5 g/cm3), their orbital locations, and the near-total lack of absorption features in their visible to near-infrared spectra (Hiroi et al. 2004; Carry 2012; Vernazza et al. 2015; Hanuš et al. 2017). A review of 22 P-type asteroid spectra by Fornasier et al. (2014) found that only one exhibited absorption features at visible wavelengths consistent with hydrated silicates, and observations of these asteroids at 3-µm have had mixed results, with most studies not observing any 3-µm absorptions for P-type asteroids (Jones et al. 1990; Lebofsky et al. 1990; Emery and Brown 2003; Takir and Emery 2012). One fascinating hypothesis for P-type (and the related D-type asteroids) is that they may be the sources for a significant amount of the interplanetary dust particles (IDPs) in terrestrial collections (Bradley et al. 2003; Vernazza et al. 2015). Roughly half of IDPs are classified as "chondritic porous" (CP) IDPs, which are composed predominately of Fe-poor pyroxene and olivine, sulfides, FeNi metal, glasses, and carbonaceous material (Bradley et al. 2003). The morphology of the component grains and the presence of solar flare tracks in IDPs suggests that these particles were formed during vapor-phase condensation of the solar nebula; some inclusions are likely presolar and could have even formed in the atmospheres of other stars. Using microspectrophotometry, Bradley at al. (1996) established a connection between CP IDPs and the P- and D-type asteroids. If true, these asteroids would represent an unparalleled source for unprocessed, presolar material. Because of the uncertainty surrounding their origin and nature, P-type asteroids remain a subject of important study.

2.1.2 Bus-DeMeo D-, T-, and L-type Asteroids and the Jupiter Trojans

The T-type asteroids are characterized by featureless, concave down spectra with moderate slope (DeMeo et al. 2009). Similar to T-types, L-type asteroids are characterized by reflectance spectra with steep visible slopes that shallow in the near-infrared, producing an overall concave spectrum (DeMeo et al. 2009). Some L-types exhibit a subtle absorption feature in the near-infrared at ~900 nm while others may exhibit a feature at 2-µm (DeMeo et al. 2009). Spectra of D-type asteroids are characterized by a very steep red slope, with some exhibiting a change to lower slope at near-infrared wavelengths (DeMeo et al. 2009).

The surface compositions of these three types of asteroids are poorly constrained. Britt et al. (1992) compared the T-types to laboratory reflectance spectra of troilite, while others have compared spectra of T- and D-type asteroids to the ungrouped carbonaceous chondrite Tagish Lake (e.g., Hiroi et al. 2001; Izawa et al. 2010). Finally, observations of L-type asteroids suggest a surface rich in spinel (as seen in calcium-aluminum inclusions), albeit at abundances greater than known meteorites (Burbine et al. 1992; Sunshine et al. 2008; Devogèle et al. 2018).

Analysis of the visible to near-infrared spectra of the Jupiter Trojan asteroids suggests that they are split into two spectral groups: a 'red' group with spectra consistent with D-type asteroids, and a 'less-red' group consistent with P-types (Emery and Brown 2003, Emery et al. 2011, Emery et al. 2015). Due to a lack of any significant absorption features, mineralogical interpretations of the surface of these asteroids remains elusive. The densities of these asteroids are consistent with ice and organics, but the lack of definitive absorption features limits the abundance and nature of these possible components. Furthermore, it is still debated if the two Trojan spectral populations share a common origin (e.g., Emery et al. 2015, Brown 2016).

2.1.3 Spacecraft exploration of 'featureless' asteroids

One method to resolve the outstanding questions surrounding 'featureless' asteroids is to send spacecraft to explore them. To date, only two 'featureless' asteroids have been visited by a spacecraft: the European Space Agency's Rosetta spacecraft encountered the E-/Xe-type asteroid (2867) Šteins and the M-/Xk-type asteroid (21) Lutetia in 2008 and 2010, respectively (Keller et al. 2010; Coradini et al. 2011). While (253) Mathilde has a relatively featureless spectrum consistent with C-type asteroids, its blue slope (decreasing reflectance with increasing wavelength) at visible to near-infrared wavelengths observed by the NEAR spacecraft (e.g., Clark et al. 1999) precludes it from the definition of red-sloped, 'spectrally featureless' asteroids used in this paper.

Fly-by observations of (2867) Šteins indicated the surface was largely enstatite-rich with a significant component of sulfide minerals (e.g., oldhamite - CaS) based on observations of a strong absorption feature centered at ~490 nm. Asteroid (21) Lutetia's high density (~3.4 g/cm3) and featureless, red-sloped spectrum indicate that it has a high metal abundance. The surface colors of both asteroids were observed to be spectrally homogeneous, which was interpreted as a lack of space weathering-induced spectral contrasts (Keller et al. 2010; Coradini et al. 2011).

Because of their potential as snapshots into the process of solar system formation and planetary differentiation, 'featureless' asteroids are targets of multiple future space missions. These include the Psyche mission to the largest M-type asteroid, (16) Psyche, the Lucy mission, which will visit six Jupiter Trojan asteroids, including P- and D-types, and the DART and Hera missions to the Xk-type near-Earth asteroid (65803) Didymos. The Psyche and Lucy spacecraft will be equipped with multispectral imagers, while the Milani cubesat of the Hera mission will be equipped with a hyperspectral imager (Bell et al. 2016, Levison et al. 2016, Ferrari et al. 2021). Data returned by these instruments will be compared with laboratory reflectance spectra to make interpretations about the surface composition of the target asteroids. Our goal in this paper is to compare spectral properties of 'spectrally featureless' asteroids with new spectra of possible analogs and to supplement existing spectral libraries to support future investigation of these 'featureless' asteroids.

2.2 Samples and Methods

2.2.1 Samples and Preparation

Samples were loaned from the Center for Meteorite Studies (CMS) at Arizona State University (ASU). We acquired a set of aubrites, sulfide minerals, and metal-rich chondrites. The aubrites in our study are Aubres, Norton County, Mayo Belwa, Shallowater, and Khor Temiki. The sulfide mineral samples we studied are troilite (FeS), oldhamite (CaS), pyrrhotite ($Fe_{1-x}S$), pentlandite ($(Fe,Ni)_9S_8$), and a mixture of pentlandite and chalcopyrite ($CuFeS_2$). Finally, we measured spectra from five metal-rich chondrites: the CB chondrites Isheyevo, Quebrada Chimborazo 001, Hammadah al Hamra 237, and a pair of ungrouped chondrites, Northwest Africa 5492 and Northwest Africa 12273. Characteristics of each sample studied, including name, physical form, the phase angle of the reflectance measurements, and spectral properties are listed in Table 2.1. Detailed mineralogical information of the samples is in Supplemental Table 2.1.

It is a well-documented phenomenon that the surface roughness and grain size of materials influence their visible to near-infrared reflectance spectra (e.g., Clark 1999). Therefore, we collected spectra from multiple physical forms of the samples in our study. For the aubrite samples, we measured pre-existing hand samples, slabs, and unsorted powders (~<1 mm) that were readily available in the CMS collection. We measured sulfide samples from the CMS collection in both slab, gravel, and powder form. Powders were produced from larger samples of meteoritic and terrestrial troilite as well as for the pyrrhotite and the pentlandite/chalcopyrite samples. For the metal-rich chondrites, we measured most in slab form only except for the CH/CB chondrite Isheyevo, of which a small piece was crushed into powder.

Table 2.1. Physical and spectral properties of samples used in this study.

Sample name	Form	Grain size (μm) or *Roughness*[1]	Phase angle (i/e)	550 nm ref[2] (%)	Vis. slope (% ref./100 nm)[3]	NIR slope (% ref./100 nm)[3]	Band center (nm)[4]	Band depth (%)[5]
Aubrites								
Mayo Belwa	hand sample	***1, no rust***	30/0	20.9	1.62	-2.29	906	0.42
	powder	unsorted, <1000	30/0	20.3	2.86	-0.84	875	0.85
Aubres	slab	***4***	30/0	47.8	-0.34	-4.00	--	--
Khor Temiki	powder	unsorted, <1000	30/0	45.7	6.09	0.39	920	0.42
Norton County	hand sample	***1, no rust***	30/0	34.8	5.36	-0.29	887	0.53
	powder	unsorted, <1000	30/0	50.3	4.59	1.74	865	1.76
Shallowater	slab	***6***	30/0	12.9	10.40	-2.59	966	7.62
Chondrites								
NWA 5492	slab	***3***	38/8	10.2	11.93	-0.65	934	5.03
	slab	***6***	38/8	6.5	17.31	0.07	925	5.42
Hammadah al Hamra 237	slab	***3***	38/8	8.9	3.50	2.29	896	6.91
	slab	***4***	38/8	2.8	8.16	-0.50	932	10.80
Quebrada Chimborazo 001	slab	***4***	38/8	6.1	10.64	-1.86	930	10.80
	slab	***6***	38/8	3.7	19.92	-1.46	921	18.89
Isheyevo	slab	***6***	38/8	2.8	4.90	2.73	935	1.45
	powder	unsorted, <1000	38/8	6.8	6.24	2.53	872	1.89
	powder	<75	38/8	13.7	6.68	1.96	944	0.51
	powder	>75	38/8	8.1	7.17	1.56	927	1.51
	powder	<75	23/8	9.5	6.47	2.08	902	0.90
	powder	>75	23/8	6.9	6.86	2.03	937	1.28
	powder	<75	53/8	6.6	6.33	3.43	857	3.51
	powder	>75	53/8	5.3	6.71	3.18	881	3.45
NWA 12273	slab	***6***	38/8	2.1	7.47	0.38	929	16.88
	slab	***4***	38/8	5.7	5.00	-0.07	919	9.56
Sulfides								
Bushveld Pentlandite	hand sample	***1, no rust***	38/8	14.7	13.02	4.50	--	--
	powder	unsorted, <1000	38/8	12.5	11.44	2.72	--	--
Norton Co. CaS	powder	unsorted, <1000	38/8	10.7	23.09	6.32	951	22.25
Nantan FeS	slab	***5***	38/8	9.2	12.69	5.46	--	--

	slab	***3***	38/8	15.3	9.60	3.04	--	--
	powder	<500	38/8	6.9	9.77	2.95	--	--
	powder	<75	38/8	7.8	10.02	2.70	--	--
	powder	>75	38/8	11.5	10.22	2.39	--	--
	powder	<75	23/8	6.9	10.04	3.32	--	--
	powder	>75	23/8	9.2	10.33	3.10	--	--
	powder	<75	53/8	8.1	10.22	3.19	--	--
	powder	>75	53/8	12.5	10.30	2.48	--	--
Auburn FeS	slab	***5***	38/8	1.6	15.08	6.68	--	--
	powder	unsorted, <1000	38/8	6.8	12.46	3.32	--	--
	powder	<75	38/8	10.1	11.93	3.27	--	--
	powder	>75	38/8	9.2	11.74	2.98	--	--
Del Norte County FeS	slab	***2***	38/8	13.0	12.03	4.73	--	--
	powder	unsorted, <1000	38/8	6.6	9.64	2.39	--	--
	powder	<75	38/8	5.3	9.52	2.67	--	--
	powder	>75	38/8	7.4	9.87	2.25	--	--
Minas Gerais Pyrrhotite	powder	unsorted, <1 cm	38/8	11.2	12.03	6.00	--	--
	powder	<75	38/8	11.4	9.69	5.00	--	--
	powder	>75	38/8	12.0	10.67	5.30	--	--
	powder	<75	23/8	9.5	9.68	5.21	--	--
	powder	>75	23/8	9.3	10.79	6.41	--	--
	powder	<75	53/8	10.5	9.76	5.73	--	--
	powder	>75	53/8	12.4	10.39	4.23	--	--
Norilsk Pentlandite/ Chalcopyrite	powder	***1, no rust***	38/8	4.8	21.62	6.97	861	3.70
	powder	unsorted, <1000	38/8	11.3	16.14	1.19	898	6.10
	powder	<75	38/8	11.0	16.76	0.84	906	5.49
	powder	>75	38/8	12.1	16.24	2.05	890	5.67
	powder	<75	23/8	12.9	18.03	1.76	904	5.08
	powder	>75	23/8	14.6	17.60	1.86	906	5.97
	powder	<75	53/8	13.5	18.04	1.10	909	5.02
	powder	>75	53/8	12.7	17.73	2.60	887	5.35

1 - Surfaces roughness values assigned as follows: (***1***) unprepared hand sample, (***2***) - rough surface with saw marks, ***(3)*** - 180 grit finish, (***4***) - 600 grit finish, (***5***) - 1200 grit finish, (***6***) - 1-µm diamond paste finish

2 - Uncertainty on reflectance is less than 0.001%

3 - Uncertainty on slope measurement is less than 0.02 % ref/100 nm.

4 - Uncertainty on 1-µm band center is ~1 nm.

5 - Uncertainty on 1-µm band depth is <0.1 %.

Powders were made using a Chemplex stainless steel impact mortar and pestle (Chemplex catalog #850). The impact mortar and pestle were cleaned with ethanol after each sample was comminuted. In addition to an unsorted fraction, we dry sieved powdered samples into fractions with grain sizes greater than and less than 75 μm to explore any spectral effects that variation in grain size might cause. This grain size range was chosen as it is consistent with reported grain sizes ranges for the largest M-/X-type asteroid, (16) Psyche (Dollfus et al. 1979; Landsman et al. 2018). Sieves were also cleaned with ethanol and allowed to dry between each sample.

2.2.2 Visible to Near-Infrared Spectroscopy

Spectra were acquired using an ASD FieldSpec 4 Standard-Res spectroradiometer over the visible to shortwave infrared (350-2500 nm) wavelength range in air at a phase angle of 30° and calibrated relative to a Spectralon white reference target. This instrument has a spectral resolution of 3 nm from 350-1000 nm and 10 nm resolution from 1000-2500 nm. For the metal-rich chondrites and sulfide samples, we found that a viewing geometry of i = 38°, e = 8° eliminated stray light artifacts from strong specular reflections with negligible impact on the reflectance or spectral slope. For some samples, we collected additional spectra at phase angles of 15° and 45° to explore changes in spectral properties with changing viewing geometry. We collected spectra from visibly fresh (i.e., non-weathered) surfaces of the hand samples and slabs. For hand samples, slabs, and gravels, we collected spectra from at least four different orientations and then averaged them together to create a “bulk” spectrum more representative of the whole sample. For powder samples, we poured the powder into an aluminum sample cup and rotated the cup at 90° increments through a full rotation. We then emptied the powder onto clean weighing paper and refilled it before repeating spectral measurements, then averaged all spectra for that sample to create a representative bulk powder spectrum. All spectra of powders were measured within 15 minutes of comminution to minimize interaction with the ambient lab atmosphere.

From the spectral data, we measured reflectance at 550 nm, the visible and near-infrared spectral slopes, and the center and depth of an absorption features present near ~1000 nm. The visible spectral slope was computed between 450-700 nm and the near-infrared slope was computed between 760-1200 nm. Both slopes were calculated after the spectra were normalized to 1.0 at 550 nm. To calculate band center and depth, we follow the method of Clark and Roush (1984) and Cloutis et al. (2015). First, visually-estimated shoulders of any absorption feature were used to fit a straight line continuum across the absorption feature. The continuum was removed by dividing the sample's absolute reflectance by this continuum line. The band centers were then found by fitting a cubic polynomial to the 20 values on either side of the minimum value of the continuum-removed features. The minimum value of the cubic polynomial was taken to be the continuum-removed band center. Band depth was determined using Equation 32 of Clark and Roush (1984):

$$D_b = \frac{(R_c - R_b)}{R_c}$$

where D_b is band depth, R_c is reflectance of the continuum at the band center, and R_b is the continuum-removed reflectance at the band center. This process is repeated 50 times for each absorption feature in each spectrum using a normally distributed set of shoulder wavelengths centered on the original input shoulder wavelengths with a variance of 10 nm. Band centers and depths in Table 2.1 are the mean of the 50 calculated values for each absorption feature in each spectrum. Uncertainties on these values are listed in the footnotes of Table 2.1.

2.2.3 X-ray Diffraction (XRD) Analysis

For samples specifically powdered for this study (i.e., most of the sulfides as well as a piece of the Isheyevo CH/CB chondrite), we acquired powder X-ray diffraction (XRD) data of separated fractions smaller than 75 μm using a Rigaku MiniFlex 600. Our MiniFlex is equipped with a Cu Kα X-ray source that emits 1.5406 Å wavelength radiation. This diffractometer is operated with Cu Kα radiation and is equipped with a post-diffraction graphite monochromator and automatic divergence slit system. Powders were deposited on a glass slide and wet with methanol to reduce orientation effects in the diffraction data. The methanol was then allowed to evaporate (which typically takes <30 seconds) before the slide was inserted into the MiniFlex. We ran the samples for a minimum of 1 hour at 2-theta angles from 2° to 75° at 0.02° increments. The resulting diffractograms were analyzed using the CrystalMaker and CrystralDiffract software. We used simulated patterns of expected endmember minerals in our samples to constrain the bulk mineralogy and interpret spectral trends.

2.3 Results

2.3.1 X-ray diffraction of powdered samples

Supplemental Figs. S2.1, S2.2, and S3.3 show the XRD patterns of the Isheyevo powder and sulfides in our study. The Isheyevo powder diffractogram is dominated by reflections from kamacite, pyroxene, and forsterite, as expected from its mineralogical analysis (Garvie et al. 2017). Reflections in the diffractograms of the troilites confirm that our samples are indeed dominated by troilite with minor pyrrhotite, pentlandite, daubréelite, and graphite. Finally, the diffractograms of the Bushveld pentlandite and Minas Gerais pyrrhotite confirm these samples are dominated by pentlandite and pyrrhotite, respectively, while the Norilsk sample is a subequal mixture of chalcopyrite and pentlandite.

2.3.2 Visible to near-infrared spectroscopy

The spectra of aubrites are featureless and red-sloped at visible (450-700 nm) wavelengths (Fig. 2.1). They exhibit variation in near-infrared (760-1200 nm) spectral slope with most spectra exhibiting a blue-slope, which is consistent with published spectra of aubrites (e.g., Gaffey 1976; Burbine et al. 2002; Cloutis et al. 2016). Despite the low Fe content of the aubrites, the strong decrease in reflectance towards UV wavelengths is characteristic of a metal-oxygen charge transfer, which are typically thousands of times stronger than absorptions caused by crystal field transitions (Gaffey 1976; Clark 1999). The lack of significant absorption features at ~1000 nm (except in the case of Shallowater) is a strong indication that pyroxene in these samples is mostly Fe-free enstatite, consistent with the reported mineralogy of these samples by Watters and Prinz (1979). Shallowater, which has a much higher abundance of troilite (7.1 vol.%) than the other aubrites, is considerably darker (Watters and Prinz 1979). Our aubrite spectra also exhibit subtle absorption features at ~1900 nm, indicative of the presence of some H_2O in the samples. Visual inspection and the absence of additional hydroxyl features at 1400 nm indicates that our sample is not heavily rusted and likely just contains

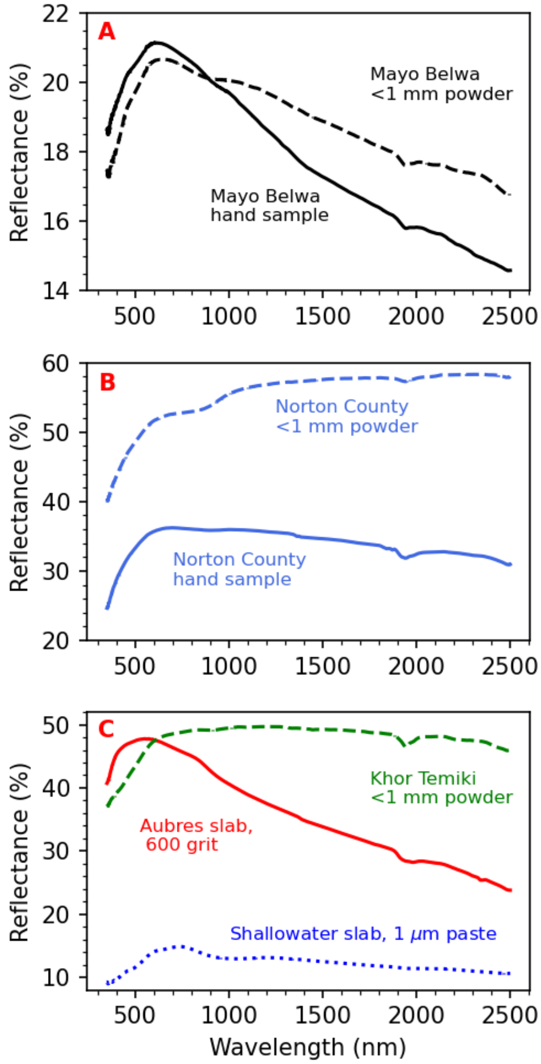

Fig. 2.1. Reflectance spectra of aubrite slabs and powders. A – spectra from a hand sample (solid) and <1 mm powder (dashed) of Mayo Belwa, B – spectra from a hand sample (solid) and <1 mm powder (dashed) of Norton County, C – Aubres, Khor Temiki, and Shallowater, D – spectra from a <1 mm powder of Khor Temiki (green dashed line), a slab of Aubres (solid red line), and a slab of Shallowater (dotted blue line).

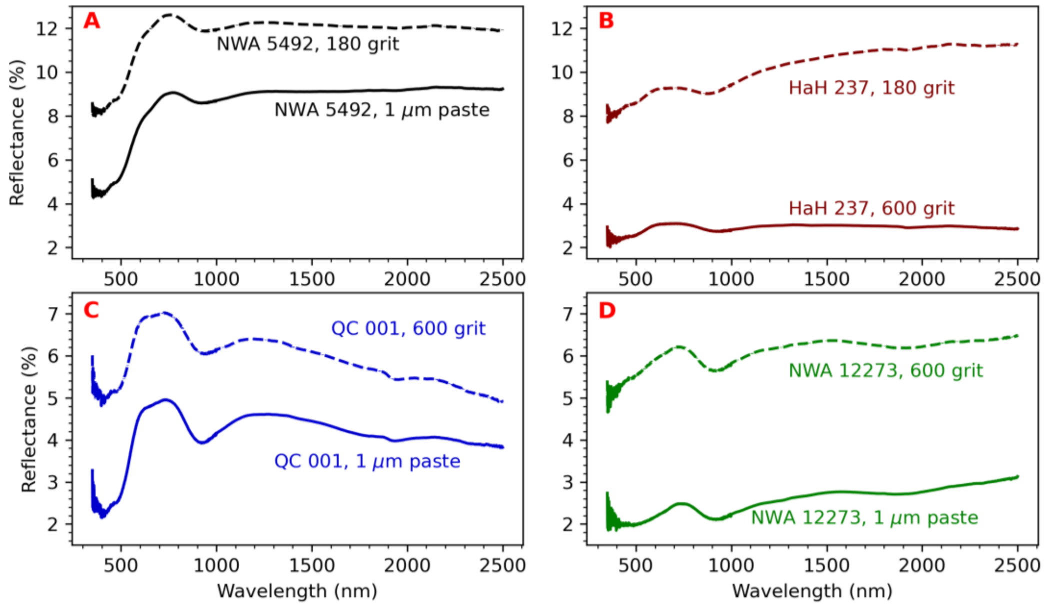

Fig. 2.2. Reflectance spectra of metal-rich chondrite slabs. The spectra are dark (less than 15% reflectance) and exhibit positive visible slopes and variable near-infrared slopes. The metal-rich chondrites in our study also generally have a subtle absorption feature at ~900 nm. For clarity, the finish applied to each slab is listed after the chondrite name next to each spectrum. A – spectra from slabs of NWA 5492, B – spectra from slabs of HaH 237, C – spectra from slabs of QC 001, D – spectra from NWA 12273.

some adsorbed water (Clark 1999). Consistent with Cloutis et al. (2016), we find that decreasing grain size (i.e., powders versus slabs) results in more red-sloped spectra for aubrites.

Reflectance spectra of the metal-rich chondrites are generally dark (<15% reflectance) and exhibit minor absorption features at ~900 nm due Fe-bearing pyroxene (Fig. 2.2, 2.3)(Adams 1975; Gaffey 1976). NWA 12273 exhibits a relatively significant ~1900 nm feature, consistent with its much higher Fe-pyroxene content. For all of the metal-rich chondrite slabs, rougher slabs exhibit higher overall reflection. HaH 237 and QC 001 exhibit a narrow absorption feature at ~1900 nm that, like the aubrites, is likely due to adsorbed water. NWA 5492 and QC 001 have the strongest visible slopes but lowest near-infrared slopes, while HaH 237 and NWA 12273 have more moderate visible

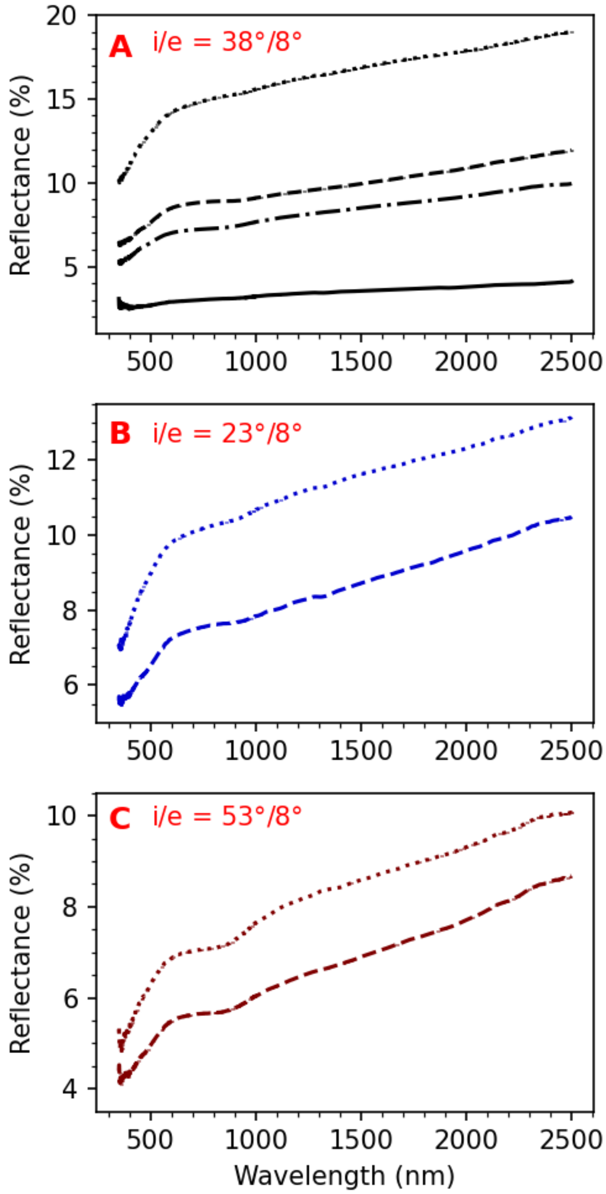

Fig. 2.3. Reflectance spectra of Isheyevo at different phase angles and grain size. A) Reflectance spectra of Isheyevo at a phase angle of 30°, B) at 15°, and C) at 45°. Grain size fractions are represented as: dotted = <75 µm, dashed = >75 µm, dashdot = unsorted, <1 mm, solid = slab.

slopes and nearly flat near-infrared slopes. Because NWA5492 has a much lower metal content than the other metal-rich chondrites (~20 vol.% compared to >60 vol.%), spectra

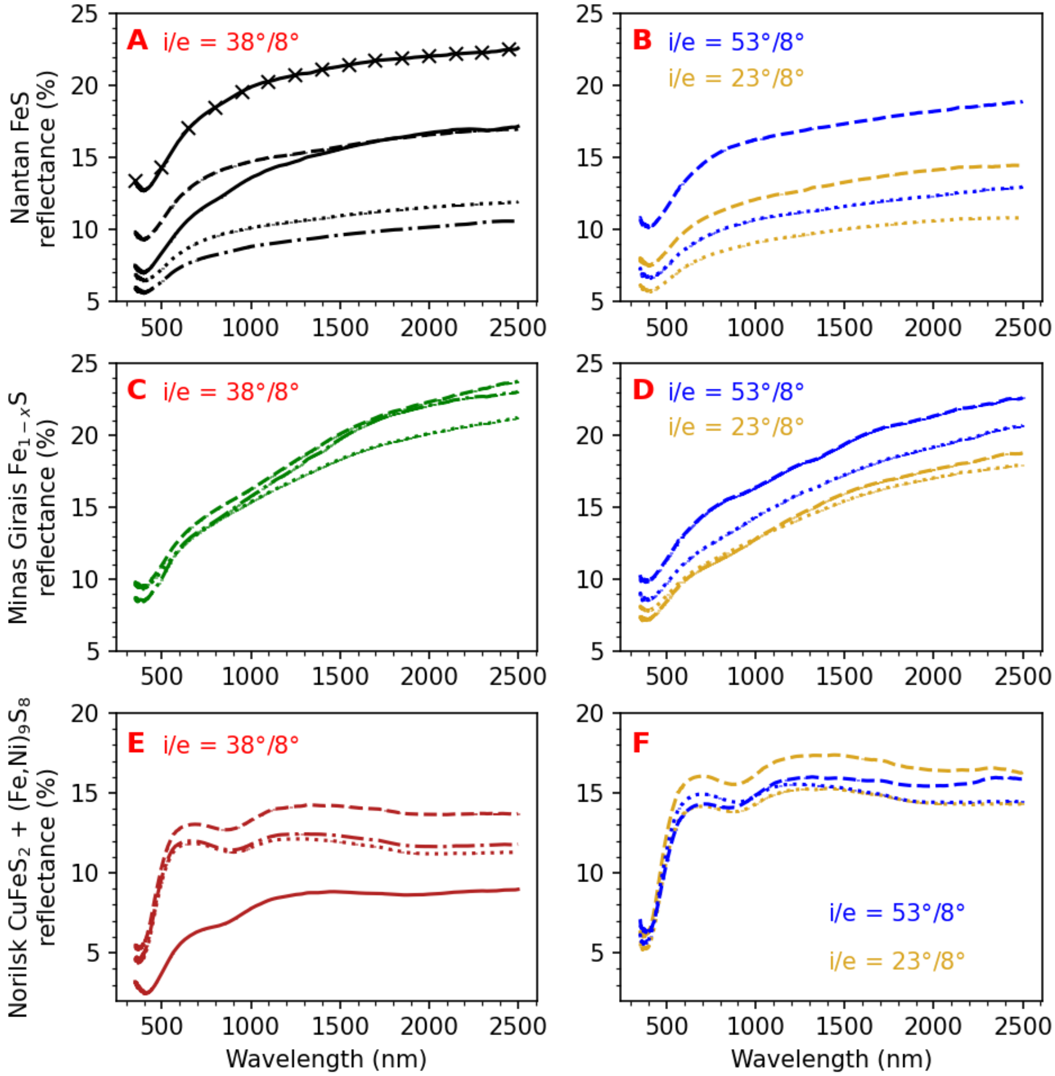

Fig. 2.4. Troilite (A and B) from the Nantan meteorite and pyrrhotite (C and D) from Minas Gerais are red-sloped and relatively featureless, while the mixture of chalcopyrite and pentlandite (E and F) from Norilsk have a feature at ~900 nm. Grain size fractions are represented as: dotted = <75 µm, dashed = >75 µm, dashdot = unsorted, <1 mm, solid = slab. The spectrum of Nantan that is solid and cross-hatched is from the 180 grit slab, while the other solid line is from a slab polished with 1200 grit paper.

of this sample likely contain a much stronger metal-oxygen charge transfer absorption in the ultraviolet from silicates, which may result in a much steeper visible slope (Clark 1999). A similar effect may be happening in the spectra of QC 001, which contains far larger chondrules than the other samples (~1 cm compared to ~mm), and so our method

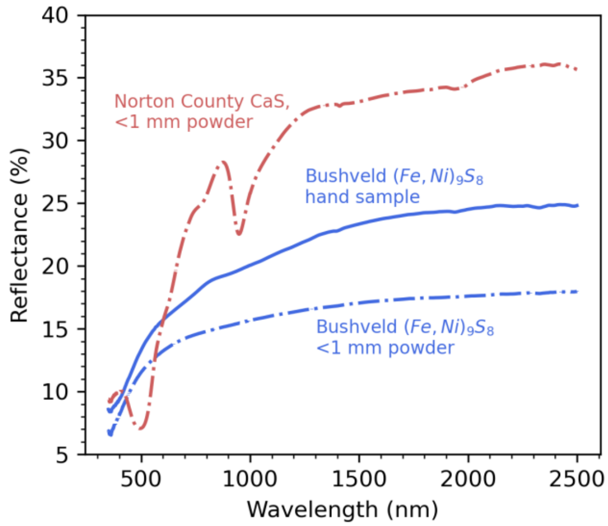

Fig. 2.5. Reflectance spectra of Bushveld pentlandite and Norton County oldhamite are red-sloped at both visible and near-infrared wavelengths. The oldhamite exhibits two strong absorption features at ~500 and 950 nm.

of collecting a raster of spectra across the slab surface may result in a more linear spectral mixture of silicates and metal. This areal rather than intimate mixing effect may result in an apparently stronger metal-oxygen charge transfer absorption despite the comparable bulk metal content in the sample to HaH 237 and NWA 12273. Our spectrum of NWA 12273 is darker and less red-sloped than that of Reddy et al. (2019), perhaps due to a difference in where on the surface of the sample spectra were collected from.

The spectra of Isheyevo (Fig. 2.3) are broadly consistent with a composition dominated by metal, as evidenced by red spectral slopes and a lack of strong absorption features. Subtle absorption features exist at ~900 nm in each of the spectra of Isheyevo, with the spectra at the highest phase angle exhibiting the largest continuum-removed band depths. Secondly, smaller grain sizes exhibit higher overall reflectance, consistent with a higher likelihood of multiple scattering in smaller grains (Clark 1999). For a given

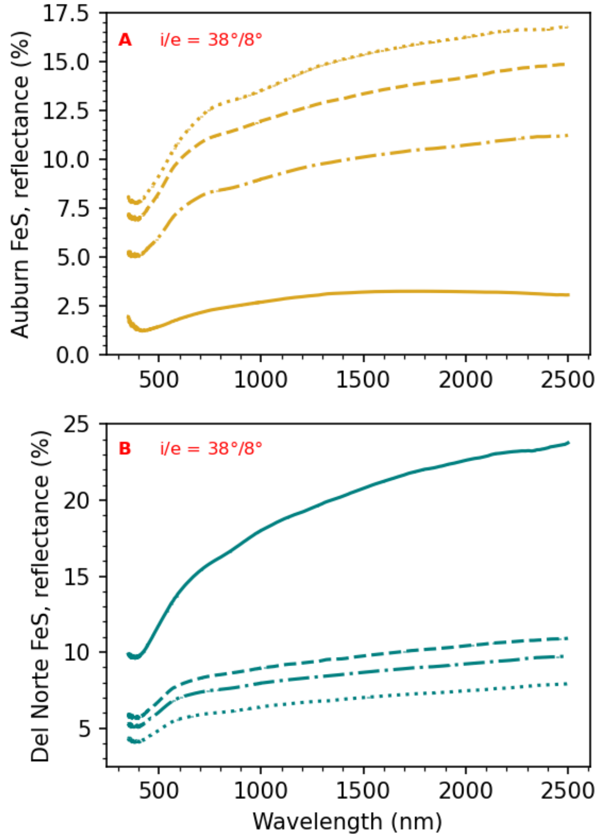

Fig. 2.6. Reflectance spectra of troilite from the Auburn meteorite (A) and Del Norte County, California (B). Grain size fractions are represented as: dotted = <75 µm, dashed = >75 µm, dashdot = unsorted, <1 mm, solid = slab.

grain size, we find that spectra collected with a phase angle of 30° have the highest reflectance and visible slopes, while spectra collected at a phase angle of 45° have the highest near-infrared slopes and band depths. There do not appear to be any consistent trends of the variation in band centers seen in these spectra with either grain size or phase angle.

For the Nantan troilite (Fig. 2.4a, b), the slab roughened with 180 grit paper (solid line with cross-hatching) exhibits the highest reflectance (15.3% at 550 nm), while the mixed grain size powder exhibits the lowest reflectance. Converse to the Isheyevo powder, we find that larger grain size fractions exhibit higher reflection at all phase angles. Values for visible and near-infrared slope are relatively uniform across all of the Nantan spectra, except for the smoothly polished slab, which has the highest visible slope. Spectra of the Minas Gerais pyrrhotite exhibit consistent reflectance (varying by ~2.5% at 550 nm) and spectral slopes across grain sizes when viewed at a 30° phase angle (Fig. 2.4c). The Nantan and Minas Gerais samples exhibit measurable differences in reflectance at 550 nm with increasing phase angle (Fig. 2.4b, d), contrary to the results of Varatharajan et al. (2019), who found no spectral variation at visible wavelengths in sulfides with varying viewing geometry. Finally, spectra of the chalcopyrite-pentlandite mixture from Norilsk are shown in Fig. 2.4e and 2.4f. The hand sample of this mixture (solid line in Fig. 2.4e) exhibits the lowest reflectance (4.8% at 550 nm) and the highest values for both visible and near-infrared slope. Trends in spectral slope between grain size are independent of phase angle, with the larger grain size fraction always less steeply sloped at visible wavelengths and more steeply sloped at near-infrared wavelengths. Furthermore, the difference in slope at near-infrared wavelengths between grain sizes is larger with increasing phase angle. The feature at ~900 nm is consistent with previous measurements of chalcopyrite but may be shifted to shorter wavelengths due to the abundance of pentlandite in this sample (Vaughan and Craig 1978). Vaughan and Craig (1978) attribute this feature to metal-metal charge transfer.

Fig. 2.5 shows spectra of terrestrial pentlandite and oldhamite from the Norton County aubrite. The pentlandite lacks the absorption feature at ~400 nm found in all of our troilite spectra and the spectra of the Norilsk chalcopyrite-pentlandite mixture, indicating that this feature may be related to variations in the crystal structure caused by changes in the Fe:S ratio or the presence of Ni (Vaughan and Craig 1978). This sample is also relatively bright compared to the other iron sulfides in our study. The visible spectral slope of oldhamite is the highest of any of the sulfides measured in our study (23.1 %/100 nm). The oldhamite powder exhibits two absorption features at ~495 nm and 951 nm, consistent with previous measurements of oldhamite from the Norton County meteorite (Burbine et al. 2002). Studies of synthetic oldhamite typically report a single absorption feature around 400 nm (Izawa et al. 2013; Helbert et al. 2013). Wheelock et al. (1994) measured ferromagnesian alabandite ((Fe,Mg,Mn)S; 9.7 vol. %) in typical clasts of oldhamite from this meteorite with an average of 15.4 wt. % Fe. While no Fe was measured in the oldhamite of Norton County by Wheelock et al. (1994), other aubrites contain oldhamite with up to several wt. % Fe (Watters and Prinz 1979). Thus, it is possible that crystal-field transitions of Fe^{2+} octahedrally coordinated with S^{2-} in either alabandite or oldhamite are the source of these two absorption features. Finally, Fig. 2.6 illustrates spectral differences between a meteoritic and terrestrial troilite sample. These samples are from the Auburn meteorite and a mine in Del Norte County, California, respectively. Cloutis and Burbine (1999) noted strong variability in spectral trends between natural and synthetic troilites due to both structural and compositional variation at microscales. Our data suggest that there may be similarly significant differences between terrestrial and meteoritic troilite. For the Auburn troilite spectra, we find that smaller grain sizes result in higher overall reflectance. Conversely, the smallest grain size fraction is the darkest for the Del Norte troilite. This may be due to an unidentified, opaque mineral in the Del Norte troilite that dominates the reflectance spectrum at lower grain sizes. There is significant difference in the overall reflectance of the slab spectra between the two troilite samples. The Auburn troilite slab (polished with 1200 grit paper) is much darker than the Del Norte slab (rough cut hand sample), likely due to greater specular reflection reducing the light scattering into the fiber optic of our spectrophotometer.

2.4 Discussion

2.4.1 Comparison to asteroid data

Because of their abundance and various compositional possibilities, constraining the surface compositions of 'spectrally featureless' asteroids offers strong controls on our understanding of planetary formation and the current composition of the main asteroid belt. Reflectance and spectral slopes of our samples are broadly consistent with spectral properties of asteroids from 'featureless' classes described in Section 1 (Fig. 2.7). The range of asteroid reflectance values are from the mean and standard deviations of the visible albedos for all asteroids of a particular type in the JPL Small Body Database (https://ssd.jpl.nasa.gov/). Asteroid spectral slopes were calculated from the mean spectrum of each asteroid type in the Bus-DeMeo taxonomy (DeMeo et al. 2009).

Generally, aubrites in our study have high reflectance (>20%), low-to-moderate visible slopes, and low-to-negative infrared slopes, most consistent with Xe-type asteroids. The connection between aubrites and the Tholen E-/Bus-DeMeo Xe-type asteroids is consistent with previous studies (Zellner 1975; Zellner et al. 1977; Clark et al. 2004a; Gaffey and Kelley 2004; Fornasier et al. 2008). The near-infrared slopes of our aubrites are less consistent with the range of near-infrared slopes for Xe-types, suggesting that the surfaces of these asteroids are not entirely composed of aubrite material and/or

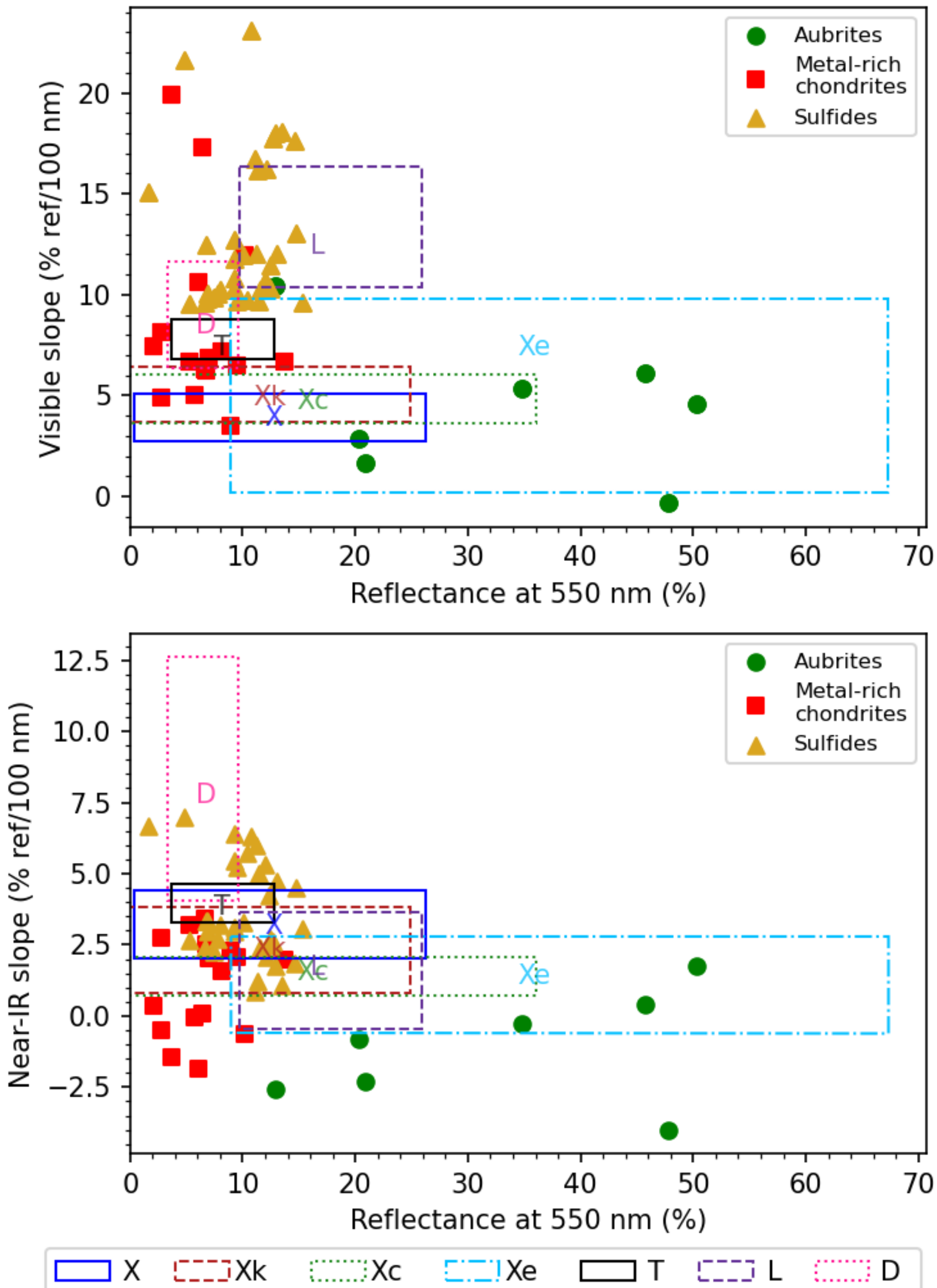

Fig. 2.7. Reflectance and spectral slopes of our samples are broadly consistent with albedos and spectral slopes of the 'featureless' asteroid classes from the Bus-DeMeo taxonomy. Albedos for asteroids are from the JPL Small Body Database (https://ssd.jpl.nasa.gov/). Spectral slopes for asteroids are computed from the mean spectra in the Bus-DeMeo taxonomy (available at http://smass.mit.edu/busdemeoclass.html).

that their surfaces are being modified, possibly by space weathering. While most aubrite densities (~2.8-3.0 g/cm^3) are within the range of mean densities of the Xe-type asteroids (3.4±0.8 g/cm^3), the addition of a higher density metal (e.g., sulfides and/or metal) to the aubrites would bring both their densities and spectral properties more in line with Xe-type asteroids (Macke et al. 2011; Carry 2012). This interpretation that the surfaces of Xe-type asteroids may be a mixture of aubrite-like components mixed with higher density phases is consistent with measurements of the only Xe-type visited by spacecraft, (2867) Šteins (Keller et al. 2010; Gulkis et al. 2010; Leyrat et al. 2011).

Our spectra of metal-rich chondrites are consistent with published spectra of other CH and CB chondrites (e.g., Cloutis et al. 2012; Trigo-Rodriguez et al. 2013; Kiddell et al. 2018; Reddy et al. 2019) and are somewhat consistent with the X-, Xk-, and Xc-type asteroids (Fig. 2.7). We note that the spectra of the slabs of metal-rich chondrites fall outside of the 1σ range of the near-infrared slopes of X-, Xk-, and Xc-types, which suggests that the surfaces of these asteroids are (not surprisingly) likely not smoothly polished slabs.

A connection between metal-rich chondrites and X-type asteroids has been explored in past studies (e.g., Hardersen et al. 2011; Moyano-Cambero et al. 2016). Spectral surveys of X-complex asteroids report absorption band centers ranging from ~870 nm to >1000 nm, consistent with the measured absorption features in our spectra of metal-rich chondrites (Clark et al. 2004b; Fornasier et al. 2010; Hardersen et al. 2011). However, the band depths of the spectra from slabs of the metal-rich chondrites are significantly deeper than what has been reported for X-complex asteroids, which typically range from 1-3% (Clark et al. 2004b; Fornasier et al. 2010; Hardersen et al. 2011). Because the absorption bands for the Isheyevo powders are much shallower, if a metal-rich chondrite lithology is present on the surfaces of X-type asteroids, it is likely in a powder form. Because of the high metal contents of these meteorites, it is likely that their densities (which are currently not measured) are consistent with the range of densities of X-, Xc-, or Xk-type asteroids (3.3±2.5, 4.0±1.5, and 4.6±1.7 g/cm^3, respectively)(Carry 2012).

Finally, the sulfides in our study have low to moderate reflectance (<20% at 550 nm), high visible spectral slope (>9% ref./100 nm), and always have a positive near-infrared spectral slope. Most of the sulfides in our study lie between ranges of reflectance and spectral slopes for the T- and L-type asteroids. There is some overlap of the reflectance and visible spectral slope of sulfides and the D-types asteroids; however, the lack of consistency between the near-infrared spectral slope of the sulfides and the D-types precludes a strong connection. Similar to our study, Britt et al. (1992), Cloutis and Gaffey (1994), and Cloutis and Burbine (1999) reported reflectance spectra of troilite consistent with spectra of T-type asteroids. Britt et al., (1992) hypothesized that these asteroids may be nearly pure FeS. Despite spectral similarities, Carry (2012) only reports a single T-type asteroid density for (96) Aegle of 2.6±2.5 g/cc. Given the high uncertainty on this density and the associated macroporosity (34±97%), we do not consider this strongly supportive of an interpretation that these objects are dominated by solid troilite (ρ=4.6 g/cc). As described in Section 2.1.2, L-type asteroids are categorized in the Bus-DeMeo taxonomy as occasionally having a ~2000 nm absorption feature. This feature has been hypothesized to arise from high abundance of Fe-bearing spinel as seen in calcium-aluminum inclusions (Burbine et al. 1992; Sunshine et al. 2008). The only sulfides in our study that exhibit such a feature are the mixture of chalcopyrite and pentlandite from Norilsk. While spectrally similar, the interpretation that L-type asteroids contain significant chalcopyrite (~50 vol.%) would require abundances of copper far beyond that seen in meteorites (Rubin 1997; Mittlefehldt et al. 1998).

2.4.2 Asteroid (16) Psyche

Asteroid (16) Psyche is the largest M-/X-type asteroid and is the target of the NASA Psyche Mission (Elkins-Tanton et al. 2020). Visible to near-infrared spectroscopy, radar reflectivity, thermal emissivity, and density estimates of (16) Psyche suggest it has a significant metal component (Hardersen et al. 2011; Shepard et al. 2017; Matter et al.

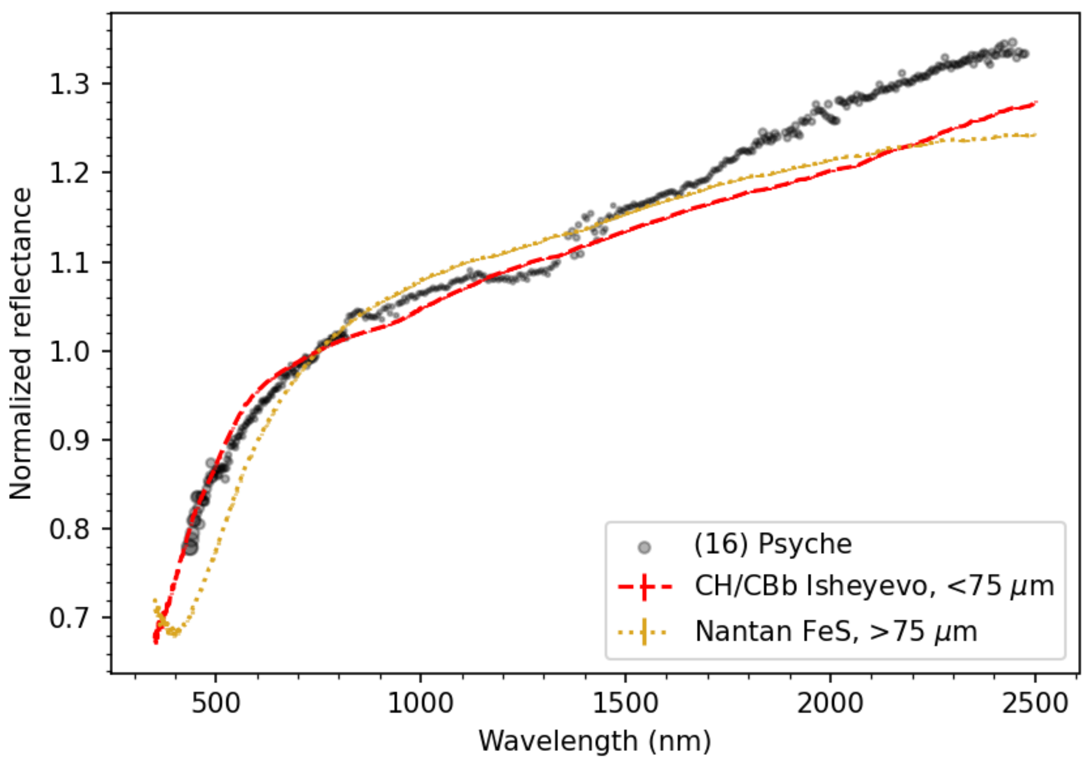

Fig. 2.8. The reflectance spectrum of (16) Psyche exhibits similar spectral slopes to spectra of <75 µm powder of CH/CBb chondrite Isheyevo and >75 µm powder of troilite (FeS) from Nantan. Both laboratory spectra are at a phase angle of 30°. Data for (16) Psyche are from the SMASS (DeMeo et al. 2009). All spectra are normalized to 1.0 at 750 nm.

2013; Landsman et al. 2018; Elkins-Tanton et al. 2020). Elkins-Tanton et al. (2020) highlighted uncertainties in the bulk porosity and the nature of the non-metal component of (16) Psyche required to resolve density estimates with compositional information from spectroscopy. Fig. 2.8 shows the 435-2475 nm reflectance spectrum of (16) Psyche from the SMASS scaled to its IRAS albedo (0.1203) at 550 nm (Tedesco et al. 2002; DeMeo et al. 2009). The spectrum of (16) Psyche is red-sloped and exhibits a subtle absorption feature centered at ~900 nm interpreted to indicate the presence of a low-abundance of Fe-bearing pyroxene on the surface. Reported band centers for (16) Psyche range from 913-950 nm while reported band depths range from ~0-2.9% (Ockert-Bell et al. 2010; Fornasier et al. 2010; Hardersen et al. 2011; Sanchez et al. 2017). This range of band centers is consistent with a wide range of possible pyroxene chemistries (Adams 1975; Cloutis and Gaffey 1991; Klima et al. 2007; Horgan et al. 2014).

Fig. 2.8 also shows reflectance spectra of <75 µm powder of the CH/CBb chondrite Isheyevo and >75 µm powder of troilite from the Nantan IAB iron. Their reflectance spectra exhibit similar spectral slopes to (16) Psyche, and their reflectance at 550 nm are comparable to the asteroid's IRAS albedo (13.7% and 11.5%, respectively). However, only the spectrum of the Isheyevo powder exhibits a ~900 nm absorption feature consistent with (16) Psyche (Table 2.1, Figs. 2.3 and 2.8). A connection between (16) Psyche and Isheyevo is further supported by observations of both objects at 3-µm. Absorption features in this wavelength range can arise due to the presence of hydrated silicates (~2.75 µm) or H_2O (~3.1 µm)(Rivkin et al. 1995). Takir et al. (2019) measured a 3-µm absorption feature in the spectrum of Isheyevo with a ~21% band depth. While initial measurements of (16) Psyche at 3-µm did not reveal a significant absorption (e.g., Rivkin et al. 1995), a more recent study by Takir et al. (2017) reported an absorption feature at 3-μm that was ~3.0% deep. Isheyevo contains sedimentary laminations consistent with gently swept-up ejecta from a glancing blow between two planetesimals, as well as chondritic material suggestive of multiple chondrule-forming events and both aqueous and thermal alteration (Krot et al. 2007; Bonal et al. 2010; Morris et al. 2015; Garvie et al. 2017). The spectral connection between Isheyevo and (16) Psyche suggests that the asteroid may be a mechanical (areal) mixture of disparate components, some of which are pristine, undifferentiated materials. Conversely, the similarity between the spectrum of (16) Psyche and troilite supports the interpretation that at least some degree of differentiation has occurred (Elkins-Tanton et al. 2020). One intriguing possibility is that a sulfur-rich immiscible liquid might have erupted onto the surface of a mantle-stripped planetesimal following catastrophic impacts (Elkins-Tanton et al. 2020). Testing such hypotheses for the origin and evolution of the asteroid is the objective of the Psyche Mission.

2.5 Conclusions

The data presented here allow us to explore trends in reflectance, spectral slope, and absorption band center and depth correlated with sample composition, surface roughness/grain size, and viewing geometry. We have sampled a range of compositions present in aubrites and sulfides relevant to spectrally featureless asteroids and are presenting new reflectance spectra of relatively unstudied metal-rich chondrites.

- Aubrites typically exhibit high reflectance and are red-sloped at visible wavelengths, exhibit a reflectance maximum at ~600 nm, and are blue-sloped in the near-infrared. Consistent with the low-Fe content of nearly pure enstatite, aubrites typically do not exhibit a ~900 nm absorption feature.

- In all forms, the metal-rich chondrites in our study exhibit low reflectance (<15% at 550 nm). Slabs exhibit variable visible slopes depending on the metal content and chondrule size and composition. Slabs generally exhibit low-to-negative near-infrared slopes. The ~900 nm absorption features in spectra of slabs are likely a complex function of silicate mineralogy, chondrule size, and metal content.
- Sulfides generally exhibit low to moderate reflectance (<20 % at 550 nm), high visible spectral slope, and always positive near-infrared spectral slope. Absorption features in some sulfides could prove diagnostic of certain minerals in the spectra of some asteroids. Consistent with previous studies, we have shown variability in the spectral properties of troilite.
- Aubrites are generally consistent with spectra of Tholen E- / Bus-DeMeo Xe-type asteroids, although the difference in near-infrared slopes of these two classes suggests that the composition of E-/Xe-type asteroids is not completely described by aubrites.
- Spectra of slabs of metal-rich chondrites are only consistent with the albedo and visible slope of X-, Xc-, and Xk-type asteroids. Powder of the Isheyevo CH/CBb chondrite is a better match for these asteroid types, suggesting their surfaces are covered in regolith.
- Spectra of sulfide minerals are generally not consistent with a specific asteroid type but instead lie between T- and L-type asteroids when reflectance is plotted against slope.

- The reflectance of asteroid (16) Psyche more closely matches a spectrum of the powdered Isheyevo CH/CBb chondrite and a spectrum of one of our powdered troilites. The presence of these materials on the surface of the asteroid would offer insight its formation. Identifying such materials on the surface of the asteroid is a primary science goal of the NASA Psyche Mission.

Acknowledgements

This study was supported by funding from NASA Psyche Mission Grant NNM16AA09C. Meteoritic samples were generously provided for study from the Arizona State University Center for Meteorite Studies. Thanks to Dr. Timothy McCoy and the Smithsonian Institution for providing the oldhamite sample used in this study. We are extremely grateful for the reviewers who helped improve this manuscript.

References

Adams J.B. 1975. Interpretation of visible and near-infrared diffuse reflectance spectra of pyroxenes and other rock-forming minerals. In Infrared and Raman spectroscopy of lunar and terrestrial minerals, 1st ed., edited by Karr C. Elsevier. pp.91-116.

Agee C.B., Vaci Z., Ziegler K., and Spilde M.N. 2019. Northwest Africa 12273: unique ungrouped metal-rich chondrite (abstract #1176). 50th Lunar and Planetary Science Conference.

Bell J., Elkins-Tanton L.T., Polanskey C.A., Ravine M.A., Caplinger M.A., Asphaug E., Bercovici D., Bills B.G., Binzel R.P., Bottke W.F., and Jaumann R. 2016. The Psyche multispectral imager investigation: Characterizing the geology, topography, and compositional properties of a metallic world (abstract #1366). 47th Lunar and Planetary Science Conference.

Binzel R.P. and Xu S. 1993. Chips off of asteroid 4 Vesta: Evidence for the parent body of basaltic achondrite meteorites. Science 260(5105):186-191.

Bonal L., Huss G.R., Krot A.N., Nagashima K., Ishii H.A., and Bradley J.P. 2010. Highly 15N-enriched chondritic clasts in the CB/CH-like meteorite Isheyevo. Geochimica et Cosmochimica Acta 74(22):6590-6609.

Bradley J.P., Keller L.P., Brownlee D.E., and Thomas K.L. 1996. Reflectance spectroscopy of interplanetary dust particles. Meteoritics & Planetary Science 31(3):394-402.

Bradley J.P. 2003. Interplanetary dust particles. In Treatise on Geochemistry, 1st ed., edited by Holland H.D. and Turekian K.K. Elsevier Science. pp.711-735.

Britt D.T., Bell J.F., Haack H., and Scott E.R.D. 1992. The reflectance spectrum of troilite (abstract #1083). 23rd Lunar and Planetary Science Conference.

Burbine T.H., Gaffey M.J., and Bell J.F. 1992. S-asteroids 387 Aquitania and 980 Anacostia: Possible fragments of the breakup of a spinel-bearing parent body with C03/CV3 affinities. Meteoritics 27(4):424-434.

Burbine T.H., McCoy T.J., Nittler L.R., Benedix G.K., Cloutis E.A., and Dickinson T.L. 2002. Spectra of extremely reduced assemblages: Implications for Mercury. Meteoritics & Planetary Science 37(9):1233-1244.

Bus S.J. and Binzel R.P. 2002. Phase II of the small main-belt asteroid spectroscopic survey: A feature-based taxonomy. Icarus 158(1):146-177.

Carry B. 2012. Density of asteroids. Planetary and Space Science 73(1):98-118.

Clark R.N. 1999. Spectroscopy of rocks and minerals, and principles of spectroscopy. In Manual of Remote Sensing, 3rd ed., edited by Rencz A. N. John Wiley & Sons. pp.3-58.

Clark R.N. and Roush T.L. 1984. Reflectance spectroscopy: Quantitative analysis techniques for remote sensing applications. Journal of Geophysical Research: Solid Earth 89(B7):6329-6340.

Clark B. E., Veverka J., Helfenstein P., Thomas P.C., Bell III J.F., Harch A., Robinson M.S., Murchie S.L., McFadden L.A. and Chapman C.R. 1999. NEAR photometry of Asteroid 253 Mathilde. Icarus 140(1):53-65.

Clark B.E., Bus S.J., Rivkin A.S., McConnochie T., Sanders J., Shah S., Hiroi T., and Shepard M. 2004a. E-type asteroid spectroscopy and compositional modeling. Journal of Geophysical Research: Planets 109(E2).

Clark B.E., Bus S.J., Rivkin A.S., Shepard M.K., and Shah S. 2004b. Spectroscopy of X-type asteroids. The Astronomical Journal 128(6):3070-3081.

Cloutis E.A. and Burbine T.H. 1999. The spectral properties of troilite/pyrrhotite and implications for the E-asteroids (abstract #1875). 30th Lunar and Planetary Science Conference.

Cloutis E.A. and Gaffey M.J. 1991. Pyroxene spectroscopy revisited: Spectral-compositional correlations and relationship to geothermometry. Journal of Geophysical Research: Planets 96(E5):22809-22826.

Cloutis E.A. and Gaffey M.J. 1994. An X-ray diffraction and reflectance spectroscopy study of iron sulphides (abstract #273). 25th Lunar and Planetary Science Conference.

Cloutis E.A., Gaffey M.J., Smith D.G., and Lambert R.S.J. 1990. Reflectance spectra of “featureless” materials and the surface mineralogies of M-and E-class asteroids. Journal of Geophysical Research: Solid Earth 95(B1):281-293.

Cloutis, E.A., Hudon P., Hiroi T., Gaffey M.J., and Mann P. 2012. Spectral reflectance properties of carbonaceous chondrites: 8.“Other” carbonaceous chondrites: CH, ungrouped, polymict, xenolithic inclusions, and R chondrites. Icarus 221(2):984-1001.

Cloutis E.A., Sanchez J.A., Reddy V., Gaffey M.J., Binzel R.P., Burbine T.H., Hardersen P.S., Hiroi T., Lucey P.G., Sunshine J.M., and Tait K.T. 2015. Olivine–metal mixtures: Spectral reflectance properties and application to asteroid reflectance spectra. Icarus 252:39-82.

Cloutis E.A., Gaffey M.J., and Applin D.M. 2016. Spectral reflectance properties of aubrites (abstract #1709). 47th Lunar and Planetary Science Conference.

Coradini A., Capaccioni F., Erard S., Arnold G., De Sanctis M.C., Filacchione G., Tosi F., Barucci M.A., Capria M.T., Ammannito E., and Grassi D. 2011. The surface composition and temperature of asteroid 21 Lutetia as observed by Rosetta/VIRTIS. Science 334(6055):492-494.

DeMeo F.E., Binzel R.P., Slivan S.M., and Bus S.J. 2009. An extension of the Bus asteroid taxonomy into the near-infrared. Icarus 202(1):160-180.

Devogèle M., Tanga P., Cellino A., Bendjoya P., Rivet J.P., Surdej J., Vernet D., Sunshine J.M., Bus S.J., Abe L., and Bagnulo S. 2018. New polarimetric and spectroscopic evidence of anomalous enrichment in spinel-bearing calcium-aluminium-rich inclusions among L-type asteroids. Icarus 304:31-57.

Dollfus A., Mandeville J.C., and Duseaux M. 1979. The nature of the M-type asteroids from optical polarimetry. Icarus 37(1):124-132.

Elkins-Tanton L.T., Asphaug E., Bell III J.F., Bercovici H., Bills B., Binzel R., Bottke W.F., Dibb S., Lawrence D.J., Marchi S., and McCoy T.J. 2020. Observations, meteorites, and models: a preflight assessment of the composition and formation of (16) Psyche. Journal of Geophysical Research: Planets 125(3):e2019JE006296.

Emery J.P. and Brown R.H. 2003. Constraints on the surface composition of Trojan asteroids from near-infrared (0.8–4.0 μm) spectroscopy. Icarus 164(1):104-121.

Emery J.P., Burr D.M. and Cruikshank D.P. 2010. Near-infrared spectroscopy of Trojan asteroids: Evidence for two compositional groups. The Astronomical Journal 141(1):25.

Emery J.P., Marzari F., Morbidelli A., French L.M. and Grav T. 2015. The complex history of Trojan asteroids. Asteroids IV 203.

Ferrari F., Franzese V., Pugliatti M., Giordano C. and Topputo F. 2021. Preliminary mission profile of Hera's Milani CubeSat. Advances in Space Research 67(6):2010-2029.

Fornasier S., Migliorini A., Dotto E., and Barucci M.A. 2008. Visible and near infrared spectroscopic investigation of E-type asteroids, including 2867 Steins, a target of the Rosetta mission. Icarus 196(1):119-134.

Fornasier S., Clark B.E., Dotto E., Migliorini A., Ockert-Bell M., and Barucci M.A. 2010. Spectroscopic survey of M-type asteroids. Icarus 210(2):655-673.

Fornasier S., Lantz C., Barucci M.A., and Lazzarin M. 2014. Aqueous alteration on main belt primitive asteroids: Results from visible spectroscopy. Icarus 233:163-178.

Friend P., Zipfel J., Gellissen M., Kleinschrodt R., Muenker C., Pack A., Schulz T., Stracke A., and Palme H. 2011. Northwest Africa 5492: An extremely reduced chondritic meteorite with low volatile element contents (abstract #1095). 42nd Lunar and Planetary Science Conference.

Füri E. and Marty B. 2015. Nitrogen isotope variations in the Solar System. Nature Geoscience 8(7):515-522.

Gaffey M.J. 1976. Spectral reflectance characteristics of the meteorite classes. Journal of Geophysical Research 81(5):905-920.

Gaffey M.J. and Kelley M.S. 2004. Mineralogical variations among high albedo E-type asteroids: Implications for asteroid igneous processes (abstract #1812). 35th Lunar and Planetary Science Conference.

Garvie L.A., Knauth L.P., and Morris M.A. 2017. Sedimentary laminations in the Isheyevo (CH/CBb) carbonaceous chondrite formed by gentle impact-plume sweep-up. Icarus 292:36-47.

Gulkis S., Keihm S., Kamp L., Backus C., Janssen M., Lee S., Davidsson B., Beaudin G., Biver N., Bockelée-Morvan D., and Crovisier J. 2010. Millimeter and submillimeter measurements of asteroid (2867) Steins during the Rosetta fly-by. Planetary and Space Science 58(9):1077-1087.

Hanuš J., Viikinkoski M., Marchis F., Ďurech J., Kaasalainen M., Delbo M., Herald D., Frappa E., Hayamizu T., Kerr S., and Preston S. 2017. Volumes and bulk densities of forty asteroids from ADAM shape modeling. Astronomy & Astrophysics 601:A114-155.

Hardersen P.S., Cloutis E.A., Reddy V., Mothé-Diniz T., and Emery J.P. 2011. The M-/X-asteroid menagerie: Results of an NIR spectral survey of 45 main-belt asteroids. Meteoritics & Planetary Science 46(12):1910-1938.

Helbert J., Maturilli A., and D'Amore M. 2013. Visible and near-infrared reflectance spectra of thermally processed synthetic sulfides as a potential analog for the hollow forming materials on Mercury. Earth and Planetary Science Letters 369:233-238.

Hiroi T., Zolensky M.E., and Pieters C.M. 2001. The Tagish Lake meteorite: A possible sample from a D-type asteroid. Science 293(5538):2234-2236.

Hiroi T., Pieters C.M., Rutherford M.J., Zolensky M.E., Sasaki S., Ueda Y., and Miyamoto M. 2004. What are the P-type asteroids made of? (abstract #1616). 35th Lunar and Planetary Science Conference.

Horgan B.H., Cloutis E.A., Mann P., and Bell III J.F. 2014. Near-infrared spectra of ferrous mineral mixtures and methods for their identification in planetary surface spectra. Icarus 234:132-154.

International tables for crystallography. Vol. C. Mathematical, physical, and chemical tables. 1993. Edited by A. J. C. Wilson. Dordrecht:Kluwer Academic Publishers.

Ivanova M.A., Kononkova N.N., Franchi I.A., Verchovsky A.B., Korochantseva E.V., Trieloff M., Krot A.N., and Brandstätter F. 2006. Isheyevo Meteorite: Genetic link between CH and CB chondrites? (abstract #1100). 37th Lunar and Planetary Science Conference.

Ivanova M.A., Kononkova N.N., Krot A.N., Greenwood R.C., Franchi I.A., Verchovsky A.B., Trieloff M., Korochantseva E.V., and Brandstätter F. 2008. The Isheyevo meteorite: Mineralogy, petrology, bulk chemistry, oxygen, nitrogen, carbon isotopic compositions, and 40Ar-39Ar ages. Meteoritics & Planetary Science 43(5):915-940.

Izawa M.R., Flemming R.L., King P.L., Peterson R.C., and McCausland P.J. 2010. Mineralogical and spectroscopic investigation of the Tagish Lake carbonaceous chondrite by X-ray diffraction and infrared reflectance spectroscopy. Meteoritics & Planetary Science 45(4):675-698.

Izawa M.R.M., Applin D.M., Mann P., Craig M.A., Cloutis E.A., Helbert J., and Maturilli A. 2013. Reflectance spectroscopy (200–2500 nm) of highly-reduced phases under oxygen-and water-free conditions. Icarus 226(2):1612-1617.

Jones T.D., Lebofsky L.A., Lewis J.S., and Marley M.S. 1990. The composition and origin of the C, P, and D asteroids: Water as a tracer of thermal evolution in the outer belt. Icarus 88(1):172-192.

Keil K. 2010. Enstatite achondrite meteorites (aubrites) and the histories of their asteroidal parent bodies. Geochemistry 70(4):295-317.

Keller H.U., Barbieri C., Koschny D., Lamy P., Rickman H., Rodrigo R., Sierks H., A'Hearn M.F., Angrilli F., Barucci M.A., and Bertaux J.L. 2010. E-type asteroid (2867) Steins as imaged by OSIRIS on board Rosetta. Science 327(5962):190-193.

Kiddell C.B., Cloutis E.A., Dagdick B.R., Stromberg J.M., Applin D.M., and Mann J.P. 2018. Spectral reflectance of powder coatings on carbonaceous chondrite slabs: Implications for asteroid regolith observations. Journal of Geophysical Research: Planets 123(10):2803-2840.

Klima R.L., Pieters C.M., and Dyar M.D. 2007. Spectroscopy of synthetic Mg-Fe pyroxenes I: Spin-allowed and spin-forbidden crystal field bands in the visible and near-infrared. Meteoritics & Planetary Science 42(2):235-253.

Koch T.E., Brenker F.E., Krot A.N., and Bizzarro M. 2016. Petrography of Quebrada Chimborazo 001—A New CBa Chondrite (abstract #1968). 47th Lunar and Planetary Science Conference.

Krot A.N., Ivanova M.A., and Ulyanov A.A. 2007. Chondrules in the CB/CH-like carbonaceous chondrite Isheyevo: Evidence for various chondrule-forming mechanisms and multiple chondrule generations. Geochemistry 67(4):283-300.

Krot A.N., Ulyanov A.A., and Ivanova M.A. 2008. Refractory inclusions in the CH/CB-like carbonaceous chondrite Isheyevo: I. Mineralogy and petrography. Meteoritics & Planetary Science 43(9):1531-1550.

Landsman Z.A., Emery J.P., Campins H., Hanuš J., Lim L.F., and Cruikshank D.P. 2018. Asteroid (16) Psyche: Evidence for a silicate regolith from spitzer space telescope spectroscopy. Icarus 304:58-73.

Lebofsky L.A., Jones T.D., Owensby P.D., Feierberg M.A., and Consolmagno G.J. 1990. The nature of low-albedo asteroids from 3-μm multi-color photometry. Icarus 83(1):16-26.

Levison H.F. and the Lucy Science Team. 2016. Lucy: surveying the diversity of the Trojan asteroids, the fossils of planet formation (abstract #2061). 47th Lunar and Planetary Science Conference.

Leyrat C., Coradini A., Erard S., Capaccioni F., Capria M.T., Drossart P., De Sanctis M.C., Tosi F., and VIRTIS Team. 2011. Thermal properties of the asteroid (2867) Steins as observed by VIRTIS/Rosetta. Astronomy & Astrophysics 531:A168.

Macke R.J., Britt D.T., and Consolmagno G.J. 2011. Density, porosity, and magnetic susceptibility of achondritic meteorites. Meteoritics & Planetary Science 46(2):311-326.

Matter A., Delbo M., Carry B., and Ligori S., 2013. Evidence of a metal-rich surface for the Asteroid (16) Psyche from interferometric observations in the thermal infrared. Icarus 226(1):419-427.

Meibom A., Righter K., Chabot N., Dehn G., Antignano A., McCoy T.J., Krot A.N., Zolensky M.E., Petaev M.I., and Keil K. 2005. Shock melts in QUE 94411, Hammadah al Hamra 237, and Bencubbin: Remains of the missing matrix?. Meteoritics & Planetary Science 40(9-10):1377-1391.

Mittlefehldt D.W., McCoy T.J., Goodrich C.A., and Kracher A. 1998. Non-chondritic meteorites from asteroidal bodies. In Planetary Materials, edited by Papike J.J. Albuquerque:De Gruyter. pp.523-718.

Morris M.A., Garvie L.A., and Knauth L.P. 2015. New insight into the solar system's transition disk phase provided by the metal-rich carbonaceous chondrite Isheyevo. The Astrophysical Journal Letters 801(2):L22.

Moyano-Cambero C.E., Trigo-Rodríguez J.M., Llorca J., Fornasier S., Barucci M.A., and Rimola A. 2016. A plausible link between the asteroid 21 Lutetia and CH carbonaceous chondrites. Meteoritics & Planetary Science 51(10):1795-1812.

Ockert-Bell M.E., Clark B.E., Shepard M.K., Isaacs R.A., Cloutis E.A., Fornasier S., and Bus S.J. 2010. The composition of M-type asteroids: Synthesis of spectroscopic and radar observations. Icarus 210(2):674-692.

Reddy V., Pearson N., Agee C.B., Cantillo D.C., Le Corre L., Campbell T., and Chabra O. 2019. Spectral Investigation of Anomalous Metal-Rich Chondrite Northwest Africa (NWA) 12273: Implications for Asteroid (16) Psyche (abstract #2212). 50th Lunar and Planetary Science Conference.

Rivkin A.S., Howell E.S., Britt D.T., Lebofsky L.A., Nolan M.C., and Branston D.D. 1995. 3-μm spectrophotometric survey of M-and E-class asteroids. Icarus 117(1):90-100.

Rivkin A.S., Howell E.S., Lebofsky L.A., Clark B.E., and Britt D.T. 2000. The nature of M-class asteroids from 3-μm observations. Icarus 145(2):351-368.

Rivkin A.S., Howell E.S., Vilas F., and Lebofsky L.A. 2002. Hydrated minerals on asteroids: The astronomical record. In Asteroids III, edited by Bottke W.F., Cellino A., Paolicchi P., Binzel R.P. Tucson:University of Arizona Press. pp.235-253.

Rubin A.E. 1997. Mineralogy of meteorite groups. Meteoritics & Planetary Science 32(2):231-247.

Sanchez J.A., Reddy V., Shepard M.K., Thomas C., Cloutis E.A., Takir D., Conrad A., Kiddell C., and Applin D. 2017. Detection of rotational spectral variation on the M-type asteroid (16) Psyche. The Astronomical Journal 153(1):29-37.

Shepard M.K., Taylor P.A., Nolan M.C., Howell E.S., Springmann A., Giorgini J.D., Warner B.D., Harris A.W., Stephens R., Merline W.J., and Rivkin A. 2015. A radar survey of M-and X-class asteroids. III. Insights into their composition, hydration state, & structure. Icarus 245:38-55.

Shepard M.K., Richardson J., Taylor P.A., Rodriguez-Ford L.A., Conrad A., de Pater I., Adamkovics M., de Kleer K., Males J.R., Morzinski K.M., and Close L.M. 2017. Radar observations and shape model of asteroid 16 Psyche. Icarus 281:388-403.

Sunshine J.M., Connolly H.C., McCoy T.J., Bus S.J., and La Croix L.M. 2008. Ancient asteroids enriched in refractory inclusions. Science 320(5875):514-517.

Takir D., Reddy V., Sanchez J.A., Shepard M.K., and Emery J.P. 2017. Detection of water and/or hydroxyl on asteroid (16) Psyche. The Astronomical Journal 153(1):31.

Takir D. and Emery J.P. 2012. Outer main belt asteroids: Identification and distribution of four 3-μm spectral groups. Icarus 219(2):641-654.

Takir D., Stockstill-Cahill K.R., Hibbitts C.A., and Nakauchi Y. 2019. 3-μm reflectance spectroscopy of carbonaceous chondrites under asteroid-like conditions. Icarus 333:243-251.

Tedesco E.F., Noah P.V., Noah M., and Price S.D. 2002. The supplemental IRAS minor planet survey. The Astronomical Journal, 123(2):1056-1085.

Tholen D. J. 1984. Asteroid taxonomy from cluster analysis of photometry. Ph.D. thesis, University of Arizona, Tucson, Arizona, United States.

Trigo-Rodriguez J.M., Moyano-Cambero C.E., Llorca J., Fornasier S., Barucci M.A., Belskaya I., Martins Z., Rivkin A.S., Dotto E., Madiedo J.M., and Jacinto A.A. 2013. UV to far-IR reflectance spectra of carbonaceous chondrites–I. Implications for remote characterization of dark primitive asteroids targeted by sample-return missions. Monthly Notices of the Royal Astronomical Society 437(1):227-240.

Varatharajan I., Maturilli A., Helbert J., Alemanno G., and Hiesinger H. 2019. Spectral behavior of sulfides in simulated daytime surface conditions of Mercury: Supporting past (MESSENGER) and future missions (BepiColombo). Earth and Planetary Science Letters 520:127-140.

Vaughan D.J. and Craig J. R. 1978. Mineral chemistry of metal sulfides, 1st ed., Cambridge: Cambridge University Press.

Vernazza P., Marsset M., Beck P., Binzel R.P., Birlan M., Brunetto R., DeMeo F.E., Djouadi Z., Dumas C., Merouane S., and Mousis O. 2015. Interplanetary dust particles as samples of icy asteroids. The Astrophysical Journal 806(2):204-214.

Watters T.R. and Prinz M. 1979. Aubrites-Their origin and relationship to enstatite chondrites. Proceedings, 10th Lunar and Planetary Science Conference. pp. 1073-1093.

Weisberg M.K., Prinz M., Clayton R.N., Mayeda T.K., Sugiura N., and Zashu S. 1998. The Bencubbinite (B) group of the CR clan. Meteoritics and Planetary Science Supplement 33:A166.

Weisberg M.K., Bunch T.E., Wittke J.H., Rumble III D., and Ebel D.S. 2012. Petrology and oxygen isotopes of NWA 5492, a new metal-rich chondrite. Meteoritics & Planetary Science 47(3):363-373.

Wheelock M.M., Keil K., Floss C., Taylor G.J., and Crozaz G. 1994. REE geochemistry of oldhamite-dominated clasts from the Norton County aubrite: Igneous origin of oldhamite. Geochimica et Cosmochimica Acta 58(1):449-458.

Zellner B. 1975. 44 NYSA-an iron-depleted asteroid. The Astrophysical Journal 198:L45-L47.

Zellner B., Leake M., Morrison D., and Williams J.G. 1977. The E asteroids and the origin of the enstatite achondrites. Geochimica et Cosmochimica Acta 41(12):1759-1767.

Zellner B., Tholen D.J., and Tedesco E.F. 1985. The eight-color asteroid survey: Results for 589 minor planets. Icarus 61(3):355-416.

Zipfel J., Wlotzka F., and Spettel B. 1998. Bulk chemistry and mineralogy of a new" unique" metal-rich chondritic breccia, Hammadah al Hamra 237 (abstract #1417). 29th Lunar and Planetary Science Conference.

CHAPTER 3

VISIBLE TO NEAR-INFRARED REFLECTANCE SPECTROSCOPY (VNIR) OF ASTEROID (16) PSYCHE: IMPLICATIONS FOR THE PSYCHE MISSION'S SCIENCE INVESTIGATIONS

Steven. D. Dibb[1], James. F. Bell, III[1], Linda. T. Elkins-Tanton[1], David. A. Williams[1], and the Psyche Mission Team[1]

School of Earth and Space Exploration, Arizona State University, Tempe, AZ 85287.

Corresponding author: Steven Dibb (sdibb@asu.edu)

Citation: Dibb, S. D., Bell, III, J. F., Elkins-Tanton, L. T., Williams, D. A., and the Psyche Mission Team. Visible to Near-Infrared Reflectance Spectroscopy (VNIR) of Asteroid (16) Psyche: Implications for the Psyche Mission's Science Investigations. In preparation for *Earth and Space Science*.

Abstract

The NASA Psyche Discovery-class mission, set to launch in 2022, will explore the shape, structure, composition, and other properties of asteroid (16) Psyche to test hypotheses about its formation and evolution. Variations in radar reflectivity, density, thermal inertia, and visible to near-infrared reflectance (VNIR) spectra of Psyche suggest a highly metallic composition with mafic silicate minerals (e.g., pyroxene) heterogeneously distributed on the surface in low abundance (<10 vol.%). The Psyche spacecraft's Multispectral Imager is designed to map ≥ 80% of the surface at high spatial resolution (≤ 20 m/pixel) through a single panchromatic filter, and to provide compositional information about ≥ 80% of the surface using 7 narrowband filters at VNIR (~400 to 1100 nm) wavelengths and at spatial scales of ≤ 500 m/pixel. We analyzed 359 reflectance spectra from samples and mixtures with compositions consistent with current uncertainties in Psyche's composition and compared them to published telescopic reflectance spectra of the asteroid using a modified chi-square test for goodness of fit. The three best matches for reflectance spectra of Psyche include iron meteorite powder, powders from the sulfide minerals troilite and pentlandite, and powder from the CH/CBb chondrite Isheyevo. Comparison of absorption band centers and depths support the interpretation that Psyche's surface is a mixture of metal and silicates, although the exact abundance and chemistry of the silicate component remains poorly constrained. We convolve spectra of meteorites and minerals to the Imager's spectral throughput to demonstrate preliminary strategies for mapping the surface composition of the asteroid using filter ratios and reconstructed band parameters. Our results provide interesting pre-flight predictions of the kinds of surface compositional information that the Psyche mission could reveal on the solar system's largest M-type asteroid.

3.1 Introduction

Asteroid (16) Psyche is the largest of the M-type asteroids and is the target of the NASA Psyche mission (Elkins-Tanton et al., 2020). Within the last few decades, multiple studies have observed the surface of Psyche at ultraviolet to infrared wavelengths and have generally interpreted the surface to be dominated by FeNi metal with a minor (<10 vol.%) component of low-Fe, low-Ca pyroxene (e.g., Hardersen et al., 2005; DeMeo et al., 2009; Fornasier et al., 2010; Ockert-Bell et al., 2010). Since NASA's selection of the Psyche Mission in early 2017, there has been renewed interest in visible to near-infrared (VNIR) spectroscopic study and interpretation of the asteroid's surface mineralogy (e.g., Sanchez et al., 2017; Takir et al., 2017; Becker et al., 2020; Cantillo et al., 2021). In addition to spectroscopic observations, density estimates and measurements of radar reflectivity and the thermal inertia of Psyche are consistent with the presence of core-like materials, such as iron meteorites and sulfide minerals like troilite (FeS) (Matter et al., 2013; Landsman et al., 2018; Elkins-Tanton et al., 2020; Shepard et al., 2021; de Kleer et al., 2021; Siltala and Granvik 2021).

A synthesis of observations of Psyche indicates that plausible bulk compositions could be far less metallic (~30-55 vol.% metal) than previously thought, with significant pore space and a still unknown non-metal component (Elkins-Tanton et al., 2020). New studies since selection do not alter the mission's primary hypothesis, which is that the asteroid is a remnant core of a differentiated planetesimal that had its silicate mantle mostly stripped in a series of hit-and-run style collisions (e.g., Asphaug 2010; Sarid et al., 2015). Other hypotheses for the formation of Psyche include the reaccretion of mostly core materials from a catastrophically disrupted planetesimal, or preservation of a primitive, undifferentiated body with high metal content. If Psyche indeed contains materials from a planetesimal core, it offers an unparalleled opportunity to explore the nature and evolution of planetary interiors. Data returned from the mission will offer strong constraints on models of solar system evolution and greatly inform our understanding of terrestrial planet formation.

To test these hypotheses, the Psyche spacecraft will be equipped with a set of science instruments that includes the Psyche Multispectral Imager system (henceforth called the “Imager”; Bell et al., 2016). The Imager is equipped with one broadband and seven narrowband science filters at visible to near-infrared wavelengths (~400-1100 nm) chosen to study the asteroid’s surface geology, composition, and topography (Table 3.1; Bell et al., 2016; Dibb et al., 2018). The spacecraft’s Gamma Ray and Neutron Spectrometer (GRNS) will measure the elemental composition of Psyche’s surface at high energy resolution but relatively low spatial resolution, while the Imager will acquire high spatial resolution (~20 m/pixel) information about the asteroid’s surface mineralogy. Integration of data from the two instruments will be critical for understanding the surface composition of Psyche.

Table 3.1. Psyche Imager Bandpasses.

#	ECAS name[1]	Center wvl. (nm)	Effective Center[2] (nm)	FWHM (nm)	Justification
0	--	--	--	--	ND5 'Sun safe' blocking filter
1	CLR	540	516	280	Unfiltered CCD for OpNav, topography, and geology
2	b	437	442	50	Sulfide detection and blue component of true color
3	o	495	498	25	Sulfide detection
4	v	550	553	25	Sulfide detection and green component of true color
5	w	725	727	40	Typical peak reflectance continuum and red component of true color
6	x	850	850	50	Search for Fe-bearing silicates and other 1000 nm features
7	p	948	946	50	Search for Fe-bearing silicates and other 1000 nm features
8	z	1041	1015	90	Search for Fe-bearing silicates and other 1000 nm features

1 - Filter names that are comparable to those from the Eight Color Asteroid Survey (Zellner et al., 1985)
2 - Effective centers are computed after convolution of each bandpass with Imager quantum efficiency, solar emission, and representative spectra of Psyche.

3.2 Materials and Methods

3.2.1 Natural and Synthetic Laboratory Samples and Mixtures

To support future interpretation of Imager data, we compiled a library of 359 reflectance spectra from possible analog materials that fall within the range of expected Psyche surface minerals, given the hypotheses and uncertainties surrounding the asteroid's origin (Elkins-Tanton et al., 2020). These materials include a variety of meteorites (irons, pallasites, mesosiderites, CB chondrites, ordinary and enstatite chondrites, aubrites, a diogenite and lodranite, and anomalous, ungrouped metal-rich chondrites). We also measured spectra from isolated sulfide minerals (troilite (FeS), pyrrhotite (Fe1-xS), pentlandite ((Fe,Ni)9S8), oldhamite (CaS), and a mixture of chalcopyrite (CuFeS2) and pentlandite) and mixtures of iron meteorite metal and troilite (Dibb et al., 2021). We also gathered spectra of iron meteorites, enstatite chondrites, mixtures of silicate minerals, and mixtures of silicates and iron meteorite powder from the University of Winnipeg Planetary Spectroscopy Facility (Cloutis et al., 2009; Cloutis et al., 2010; Izawa et al., 2010; Horgan et al., 2014). We included reflectance spectra from the Brown University RELAB database of synthetic olivine and pyroxene of a variety of compositions to prepare for areas of differing silicate chemistry or abundance (Klima et al., 2007; Dyar et al., 2009). Finally, we included additional spectra of synthetic and natural sulfide minerals from the RELAB database to account for differences in spectra of natural and synthetic sulfides (e.g., Helbert et al., 2013; Varatharajan et al., 2019).

3.2.2 Sample Preparation and Measurements

The source, name, physical form (e.g., hand sample, powder, slab), mineralogy, and measurement phase angle of the spectra in our library are shown in Appendix B Table S3.1. For measurements at ASU, we collected visible to near-infrared (350-2500 nm) reflectance spectra from samples loaned from the ASU Center for Meteorite Studies. Spectra were measured using an ASD FieldSpec 4 Standard-Res spectroradiometer. The spectral sampling of this instrument is 1 nm, while the spectral resolution is 3 nm in the visible to near-infrared (350-1000 nm) and 10 nm in the shortwave infrared (1000-2500 nm). Spectra were measured relative to a Spectralon white reference target in air at a phase angle of 30°. We measured spectra of strongly specularly reflecting samples at an incidence angle of 38° and emission angle of 8° to avoid stray light artifacts from the order-sorting filter in the FieldSpec 4 instrument. This has negligible impact on reflectance, spectral slope, or band parameters. For some samples, spectra were collected at additional phase angles of 15° and 45° to explore trends in spectral parameters with phase angles. For hand samples, slabs, and gravels, we created average spectra representative of the bulk sample by rastering across the available surface of each sample, given that the surface was visibly free of weathering, oxidation, or other contamination. Powder samples were measured in an aluminum sample cup. We rotated the sample cup at 90° increments, collecting spectra through a full rotation. We then emptied the powder onto clean weighing paper before repeating the process, then averaged all spectra to create a representative bulk spectrum.

3.2.3 Visible to Near-Infrared Telescopic Spectral Data of (16) Psyche

Table 3.2 lists studies within the past several decades that have collected spectral data of Psyche at visible to near-infrared wavelengths (e.g., Hardersen et al., 2005; Ockert-Bell et al., 2008; DeMeo et al., 2009; Fornasier et al., 2010; Sanchez et al., 2017). These data show that the spectrum of Psyche is red-sloped and relatively featureless, with a subtle absorption feature at ~1000 nm. This feature is interpreted as being caused by a relatively low abundance of low-Fe, low-Ca orthopyroxene (i.e., enstatite). Uncertainties on reported band centers allow possible band centers between ~913 and ~960 nm and band depths ranging from ~0% to 2.9%.

Table 3.2. Spectral measurements and properties of (16) Psyche.

Study	Observation date (UTC time)	Solar phase angle (°)	Wvl. range (nm)	Visual albedo	Band 1 center (nm)	Band 1 depth (%)
SMASS/DeMeo et al., 2009	2000 Oct 09	13.35[1]	435-2500[2]	n.r.	n.r.	n.r.
Ockert-Bell et al., 2010	2005 Nov 15	9.9, 10.2	435-3000[2]	0.19	950 +/- 10	0.015 +/- 0.003
Fornasier et al., 2010	2004 Nov 15 (19:31)	22.13[1]	400-2400	0.12	949 +/- 8	2.9
Hardersen et al., 2005/2011	2002 Mar 22	7.12	750-2500	0.1203	932 +/- 8	~1
Sanchez et al., 2017	2015 Dec 08 (10:30)	1.8	690-2500	n.r.	940 +/- 10	1.3 +/- 0.1
	2015 Dec 08 (11:43)	1.8	690-2500	n.r.	940 +/- 5	1.4 +/- 0.1
	2015 Dec 08 (12:47)	1.8	690-2500	n.r.	935 +/- 10	1.0 +/- 0.1
	2015 Dec 09 (14:01)	1.7	690-2500	n.r.	940 +/- 3	1.2 +/- 0.1
	2016 Feb 10 (5:10)	19.5	690-2500	n.r.	935 +/- 4	1.3 +/- 0.1
	2016 Feb 10 (5:30)	19.5	690-2500	n.r.	919 +/- 6	1.0 +/- 0.1
	2016 Feb 10 (6:34)	19.5	690-2500	n.r.	919 +/- 3	1.3 +/- 0.1
	2016 Feb 10 (8:05)	19.5	690-2500	n.r.	928 +/- 6	1.5 +/- 0.1

1 - Not reported (n.r.), but determined based on reported observation date using the JPL HORIZONS tool

2 - Used data from the SMASS II data set (Bus and Binzel 2002)

Studies of the variation in pyroxene band center with changes in pyroxene chemistry suggest that the chemistry of the purported pyroxene on Psyche could vary significantly more than previously reported. Cloutis and Gaffey (1991) report that pyroxenes with Ca contents between 0 and 30 mol.% and Fe contents <65 mol.% have band centers between ~910 and 950 nm. Similarly, spectra of synthetic pure Fe-pyroxene from Klima et al. (2007) have band centers at wavelengths lower than 950 nm. To account for such uncertainty, we include in our spectral library samples with pyroxenes with a wider range of chemistries than what has been reported for Psyche.

3.2.4 Analysis of Spectral Data

Once the library was assembled, we compared laboratory spectra with telescopic observations of Psyche using a chi-square curve-matching method and by comparing measured depths and centers of any absorption features. We then interpolated all asteroid spectra and lab spectra to 1 nm spacing, convolved the library and telescopic spectra to Imager filter bandpasses, and developed analysis strategies to support future Imager operations and mapping. All data processing was performed in Python 3.6.

Our first investigation was to compare the full wavelength range of each spectrum of Psyche to the laboratory spectra. We normalized both asteroid and sample spectra to 1.0 at 750 nm before computing a chi-square goodness-of-fit statistic using the following formula:

$$\chi^2 = \frac{1}{N_w} \sum_{i=1}^{N_w} \frac{(R_i - w_i)^2}{w_i}$$

where R_i and w_i are the reflectance at wavelength i of the meteorite and asteroid reflectance spectra, respectively, and N_w is the total number of wavelengths used. This kind of goodness-of-fit analysis is well-established in asteroid spectral studies (e.g., Nedelcu et al., 2007; Fornasier et al., 2010; Ockert-Bell et al., 2010) and offers a simple way to filter a spectral library for best matches. In this context, the chi-square metric is not used to evaluate a null hypothesis using a p-value, but instead quantifies the difference between the spectra of Psyche and those in our library. It is essentially the same as the sum of squared residuals. Thus, a meteorite spectrum with the minimum chi-square value for a certain spectrum of Psyche represents the best fit spectrum in our library. It is important to note that this metric weights every wavelength of the two spectra equally, and thus is not sensitive to specific absorption features. To match albedo values for Psyche, we filtered our library for spectra with >6% and <20% reflectance at 550 nm. The 'reflectance-filtered' library used in our chi-square analysis contains 160 spectra. The chi-square goodness-of-fit metric for all spectra in the full library is available is Appendix B Table S3.2.

Further mineralogical interpretation of an asteroid's surface requires a comparison of the center and depth of any absorption features present in the spectrum to those in laboratory spectra (Gaffey et al., 2002). We report the depth and center of any ~1000 nm

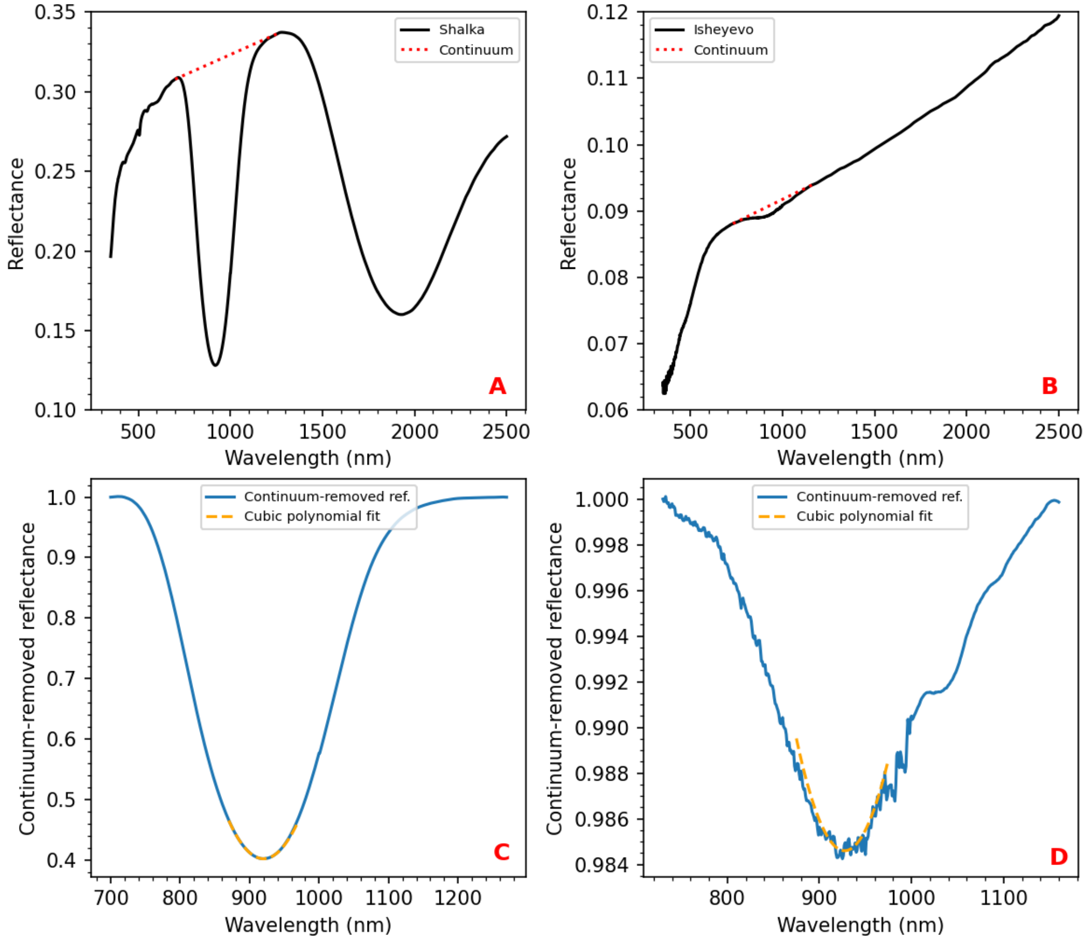

Fig. 3.1 Many of the spectra in our library contain absorption features at ~1000 nm that we compared to similar features in spectra of (16) Psyche. A spectrum of the diogenite Shalka (black line in A) exhibits strong absorption features, while spectra from the CH/CBb chondrite Isheyevo (black line in B) exhibit a weak feature comparable to Psyche. We divide the spectra by a linear continuum fit across the absorption feature (dotted red lines in A, B) and fit a 3rd order polynomial to the minimum 40 values (dashed orange line in C, D) to determine band parameters (see text for details). For clarity, in panels C and D the 3rd order polynomial is extended out to the minimum 100 values of the continuum-removed absorption feature.

absorption features in the spectra in our library in Appendix B Table S3.1. These parameters were calculated using the methods of Clark and Roush (1984) and Cloutis et al. (2015), which are depicted graphically in Fig. 3.1. First, visually-estimated shoulders of any absorption feature were used to fit a straight line continuum across the absorption feature (dashed red lines in Fig. 3.1A and 3.1B). The continuum was removed by dividing the sample's absolute reflectance by this continuum line (blue lines in Fig. 3.1C and 3.1D). The band centers were then found by fitting a 3rd order polynomial to the 20 wavelengths on either side of the minimum value of the continuum-removed features (orange dashed lines in Fig. 3.1C and 3.1D). The minimum value of the 3rd order polynomial was taken to be the continuum-removed band center. Band depth was determined using Equation 32 of Clark and Roush (1984):

$$D_b = \frac{(R_c - R_b)}{R_c}$$

where D_b is band depth, R_c is reflectance of the continuum at the band center, and R_b is the continuum-removed reflectance at the band center. This process is repeated 50 times for each absorption feature in each spectrum, using a normally-distributed set of shoulder wavelengths centered on the original input shoulder wavelengths with a variance of 10 nm. We report the mean and standard deviation of the 50 calculated values for each absorption feature in each spectrum (Appendix B Table S3.1).

3.2.5 Diagnostic Spectral Parameters

To support Imager science goals, we developed a set of parameters that can be used to identify major compositions that could potentially be found on the surface of Psyche based on potential meteorite analogs and previous telescopic observations. First, we convolve the high-resolution laboratory spectral data to the Imager's spectral throughput using the following equation:

$$I_{\lambda_1,\lambda_2} = \frac{\int_{\lambda_1}^{\lambda_2} R(\lambda) * QE(\lambda) * T(\lambda) * L_{sun}(\lambda)}{\int_{\lambda_1}^{\lambda_2} QE(\lambda) * T(\lambda) * L_{sun}(\lambda)}$$

where $R(\lambda)$, $QE(\lambda)$, $T(\lambda)$, and $L_{sun}(\lambda)$ are the sample reflectance, detector quantum efficiency, filter and telescope transmission, and solar radiance at wavelength λ, respectively. This process effectively downsamples the laboratory spectral data into an estimate of what the Imager would 'see' if each library spectrum occurred on the surface of Psyche. To emulate probable measurement uncertainty of the Imager, we uniformly vary the reflectance at each wavelength of each input laboratory spectrum by 2%, perform the convolution 1000 times, and then use the mean and standard deviation of the convolved values. An uncertainty of 2% is consistent with other flight instruments with similar designs and electronics to the Psyche Imager (e.g., Bell et al., 2021).

Because of variable band depths and centers of the spectra in our library, we developed three methods for measuring silicate absorption features in the Imager-convolved spectra. These are graphically depicted in Figure 3.2. The first method (Fig. 3.2A) is effective for spectra with strong absorption features centered near ~948 nm (e.g., Fe-rich pyroxene). In this case, we fit a cubic spline to the convolved data from the four longest wavelength filters (725, 850, 948, and 1041 nm). We then generated a flat 'continuum' connecting the convolved point at 725 nm to a point on the cubic spline longward of 1041 nm that had the same reflectance as the 725 nm convolved point. Then,

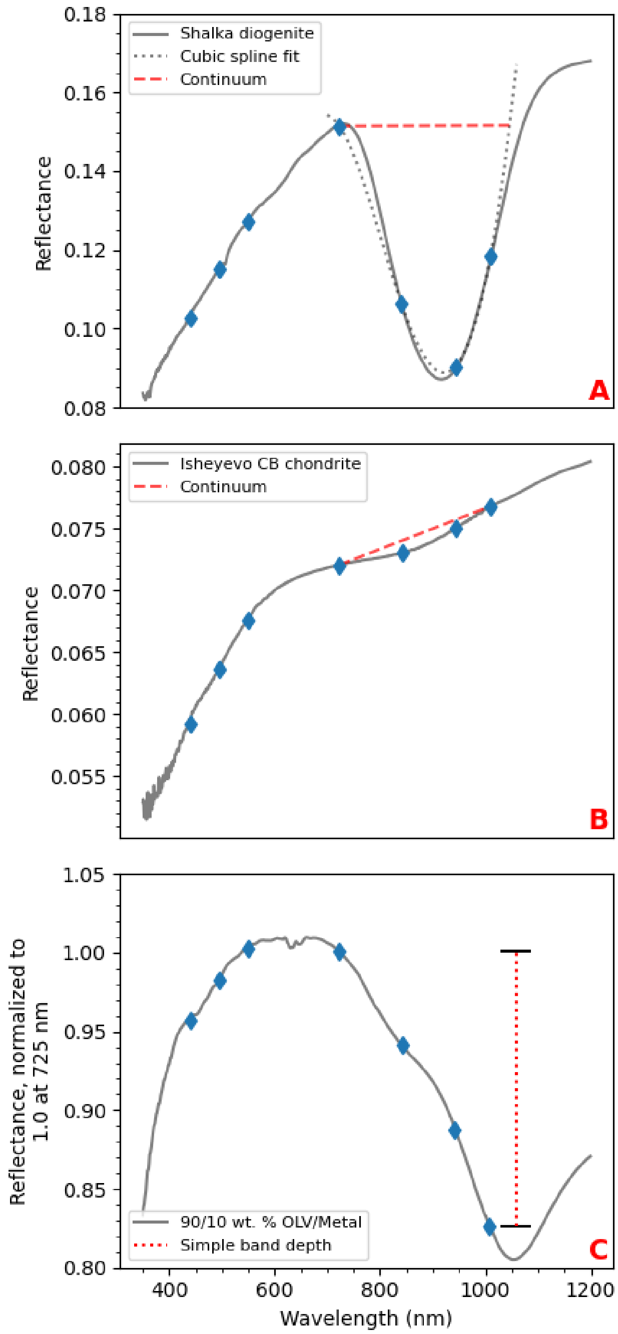

Figure 3.2. Three methods for measuring band depths and centers in spectra convolved to Imager bandpasses. High resolution laboratory spectra (gray lines) are downsampled to multispectral resolution data (blue diamonds) during the convolution process. See text for discussion.

we divided the values of the cubic spline by the flat continuum. We used the wavelength of the minimum value of the quotient as the band center and computed the band depth as the difference between the minimum continuum-removed reflectance value and 1.0.

The second method (Fig. 3.2B) is similar to the first but is useful for spectra with strong near-infrared slopes (e.g., mixtures dominated by metal). In this case, we fit a linear continuum between the convolved values for the 725 and 1041 nm filters. We then divided a cubic spline fit to the four near-infrared filters by this continuum. Similar to the first method, we assume the wavelength of the minimum value of the quotient as the band center and computed the band depth as the difference between the minimum continuum-removed value and 1.0. The third method (Fig. 3.2C) is simpler and is useful for spectra with absorption features centered at wavelengths longer than ~1000 nm (e.g., Fe-bearing olivine). First, the convolved data are normalized to unity at the 725 nm filter value. The band depth is then computed as the difference in the convolved values for the 725 and 1041 nm filters after.

3.3 Comparison of Spectra of (16) Psyche to Laboratory Spectra

3.3.1 $\chi 2$ Goodness-of-fit comparison

The five laboratory spectra with the lowest chi-square goodness-of-fit value for each spectrum of Psyche are listed in Table 3.3. This number of best-fitting spectra was chosen to be shown in Table 3 to be consistent with past analyses using the chi-square method (e.g., Nedelcu et al., 2007) and to show the spread of different compositions with spectra similar to Psyche (see Appendix B Table 3.2 for all chi-square values for each sample compared to each spectrum of Psyche). Brief descriptions of the samples, their

Table 3.3. Best chi-square matches for (16) Psyche for spectra in our library after filtering for reflectance >6% and <20% at 550 nm.

(16) Psyche spectrum reference	ID/Spectrum name	Sample Name	Grain size / Surface Roughness	Phase Angle (i/e)	$\chi 2$ ($x10^6$)
SMASS/DeMeo et al., 2009	30_06	Isheyevo powder	>75	23/8	290 ± 2
	mar0207.060	MET01A	<45	60/-30	390 ± 29
	mar0207.036	MET01A	<45	60/60	400 ± 31
	30_02	Isheyevo powder	<1000	38/8	420 ± 3
	MPMIX 1011	MET101A	<45	35/0	450 ± 31
Hardersen et al., 2005	mar0707a.004	MET01A	<45	30/60	180 ± 23
	30_07	Isheyevo powder	<75	53/8	190 ± 7
	feb1607.006	MET02A	<45	30/0	390 ± 37
	feb1607.009	MET03A	<45	30/0	400 ± 34
	mar0107.004	MET01A	<45	0/30	400 ± 37
Fornasier et al., 2010	25_07	Gibeon powder	>75	23/8	840 ± 23
	25_05	Gibeon powder	>75	38/8	1250 ± 29
	39_05	Sikhote-Alin powder	>75	23/8	1400 ± 27
	39_07	Sikhote-Alin powder	>75	53/8	1430 ± 29
	feb1607.007	MET02B	45-90	30/0	1790 ± 77
Sanchez et al., 2017 - 2015 Dec 08 10:30	35_02	Auburn FeS powder	<1000	38/8	140 ± 4
	35_03	Auburn FeS powder	<75	38/8	200 ± 6
	mar0207.012	MET01A	<45	30/30	310 ± 29
	41_02	MTMIX2	<75	38/8	340 ± 6
	35_04	Auburn FeS powder	>75	38/8	340 ± 7
Sanchez et al., 2017 - 2015 Dec 08 11:43	30_07	Isheyevo powder	<75	53/8	410 ± 33
	mar0107.004	MET01A	<45	0/30	410 ± 8
	mar0707a.004	MET01A	<45	30/60	430 ± 36
	35_02	Auburn FeS powder	<1000	38/8	510 ± 10
	35_03	Auburn FeS powder	<75	38/8	600 ± 11
Sanchez et al., 2017 - 2015 Dec 08 12:47	mar0707a.004	MET01A	<45	30/60	340 ± 30
	feb1607.009	MET03A	<45	30/0	390 ± 35
	feb1607.006	MET02A	<45	30/0	400 ± 35
	30_07	Isheyevo powder	<75	53/8	450 ± 6
	mar0107.004	MET01A	<45	0/30	650 ± 42
Sanchez et al., 2017 - 2015 Dec 08 14:01	feb1607.010	MET03B	45-90	30/0	160 ± 21
	41_01	MTMIX1	<75	38/8	180 ± 3
	feb1607.008	MET02C	90-250	30/0	240 ± 25

	feb1607.004	MET01B	45-90	30/0	240 ± 26
	25_08	Gibeon powder	<75	53/8	280 ± 3
Sanchez et al., 2017 - 2016 Feb 10 05:10	36_01	Del Norte County FeS slab	1200 grit	38/8	130 ± 1
	feb1607.010	MET03B	45-90	30/0	340 ± 30
	38_07	Minas Gerais Pyrrhotite powder	>75	53/8	340 ± 2
	41_01	MTMIX1	<75	38/8	420 ± 2
	25_04	Gibeon powder	<75	38/8	430 ± 2
Sanchez et al., 2017 - 2016 Feb 10 05:30	C1AG03	AG-BXR-003 Pentlandite powder	212-600	30/0	180 ± 72
	feb1607.005	MET01C	90-250	30/0	420 ± 33
	32_01	Nickel sulfide, hand sample	hand sample	30/0	530 ± 2
	feb1607.009	MET03A	<45	30/0	710 ± 42
	feb1607.006	MET02A	<45	30/0	730 ± 43
Sanchez et al., 2017 - 2016 Feb 10 06:34	C1AG03	AG-BXR-003 Pentlandite powder	212-600	30/0	140 ± 55
	feb1607.005	MET01C	90-250	30/0	150 ± 21
	feb1607.009	MET03A	<45	30/0	270 ± 26
	feb1607.006	MET02A	<45	30/0	290 ± 27
	39_02	Sikhote-Alin powder	<75	38/8	700 ± 2
Sanchez et al., 2017 - 2016 Feb 10 08:05	32_01	Nickel sulfide, hand sample	hand sample	30/0	510 ± 2
	C1AG03	AG-BXR-003 Pentlandite powder	212-600	30/0	740 ± 129
	feb1607.005	MET01C	90-250	30/0	1060 ± 55
	feb1607.009	MET03A	<45	30/0	1060 ± 52
	feb1607.006	MET02A	<45	30/0	1080 ± 53

physical form (grain size/surface roughness), and the phase angle of the measurement are also listed in Table 3.3. In general, spectral data of Psyche are consistent with iron meteorite powders and slabs, sulfide powders and slabs, and powder from the CH/CBb chondrite Isheyevo (Table 3.3).

The spectrum with the lowest chi-square value (i.e., the best match) is plotted over the corresponding spectrum of Psyche in Figure 3.3. Similar to Psyche, these materials exhibit relatively featureless, red-sloped spectra at visible to near-infrared

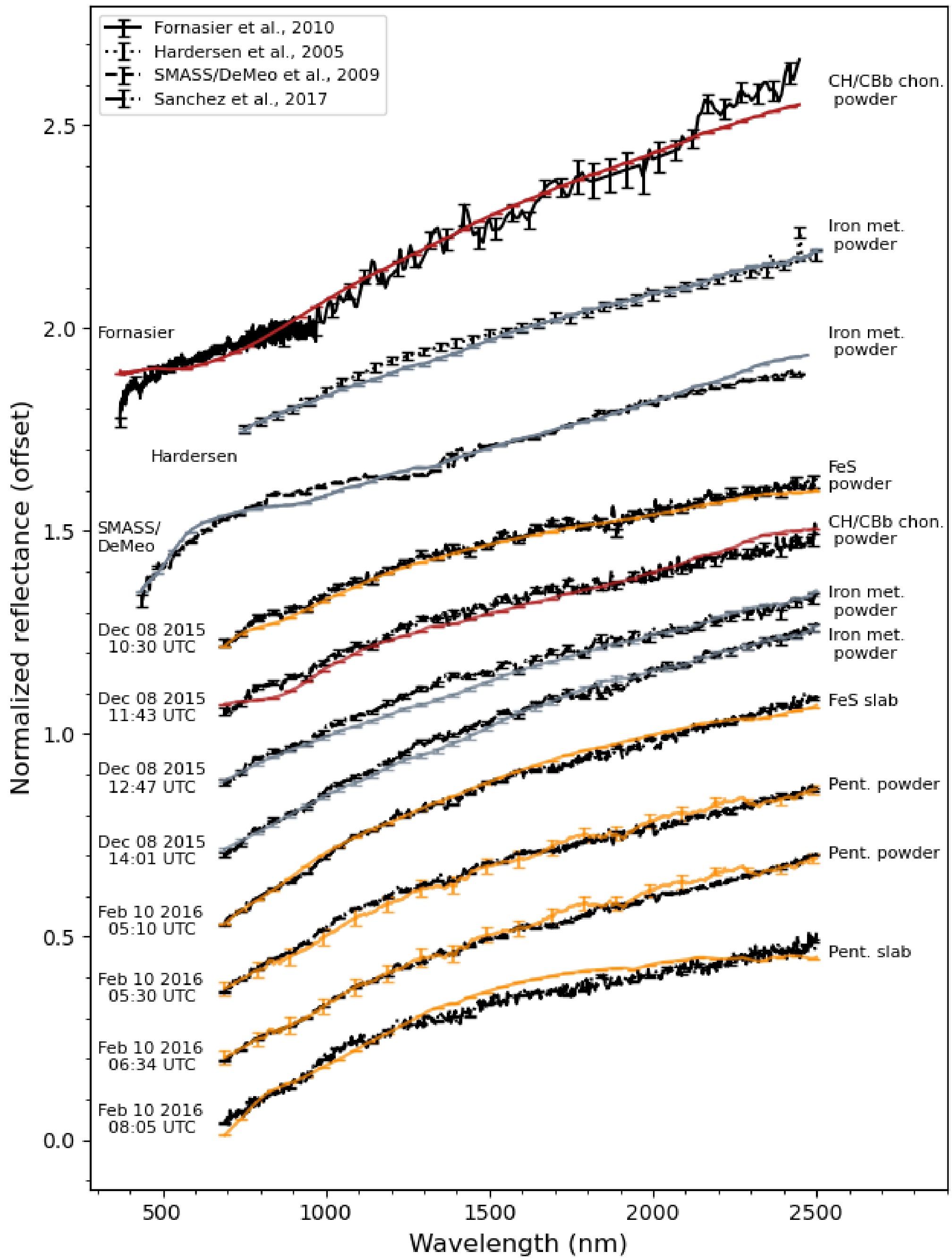

Figure 3.3. Reflectance spectra of (16) Psyche (black) plotted with their best fit spectrum in our library (red – CH/CBb chondrite, gray – iron meteorites, yellow – sulfide). The 'Best fit' is the spectrum with the minimum chi-square value. Data of Psyche are from Fornasier et al. (2010) (solid black), Hardersen et al. (2005) (dotted black), the SMASS (Bus and Binzel, 2002 and DeMeo et al., 2009, dashed black), and Sanchez et al. (2017) (dash-dot black). The multiple observations from Sanchez et al. (2017) are labeled by observation time (lower 8 spectra).

wavelengths (Figure 3.3). As mentioned previously, it is important to note that the chi-square test used here weights the entire spectrum equally and is therefore not particularly sensitive to subtle absorption features. Therefore, the samples listed in Table 3.3 can only be interpreted as the most probable surface mineralogy for Psyche within the range of composition and mineralogies sampled in our spectral library. The consistency with which certain materials have low chi-square values when compared to multiple observations of Psyche provides increased support for a comparable mineralogy between that material and the surface of the asteroid.

Consistent with previous studies, our results demonstrate similarity between reflectance spectra of Psyche and those of iron meteorite powder and/or low-Fe silicates (e.g., enstatite). For example, Cloutis et al. (1990) demonstrated that the spectrum of Psyche was intermediate in spectral properties to powder from the Odessa IAB iron meteorite and powder from the acid-insoluble fraction of the Happy Canyon enstatite chondrite. Happy Canyon is an impact melt breccia that consists of ~85 vol.% enstatite ($Fs_{0.4}$), 5-10 vol.% An_{26} plagioclase, 5 vol.% $Fs_{0.9}$ diopside, and minor Fe,Ni metal and troilite (Olsen et al., 1977; McCoy et al., 1995).

We note, however, that enstatite chondrites are absent from the top five best spectral matches for all spectra of Psyche (Table 3.3). The enstatite chondrite with the lowest chi-square value for a particular spectrum of Psyche is LEW 88180. The value for this sample ranks 27th out of the 160 spectra in our reflectance-filtered library when compared to the SMASS/DeMeo et al. (2009) spectrum. The spectra of enstatite chondrites in this study have near-infrared (~1000-2500 nm) spectral slopes that are lower than spectra of Psyche, which causes a high chi-square value relative to iron meteorites, sulfides, and the powder from Isheyevo. The spectral differences between enstatite chondrites and spectra of Psyche observed here are consistent with past comparisons of spectra of Psyche with meteorites (e.g., Cloutis et al., 1990; Hardersen et al., 2005; Fornasier et al., 2010). While they are a worse spectral match for Psyche than other materials in our study, the presence of an enstatite chondrite-like mineralogy on the surface of the asteroid cannot be completely ruled out. Both radar and emissivity data of Psyche are consistent with an enstatite chondrite-like surface mineralogy with areas of enhanced metal abundance (e.g., Matter et al., 2013; Landsman et al., 2018; Shepard et al., 2021; de Kleer et al., 2021). Additionally, enstatite chondrites are a likely analog composition for the only other M-type asteroid visited by spacecraft, (21) Lutetia (Vernazza et al., 2011).

Fornasier et al. (2010) found the spectrum of Psyche to be best matched by iron meteorite powder and attributed a subtle absorption feature at ~900 nm to low-Fe, low-Ca orthopyroxene. A connection between Psyche and the metal-rich CB/CH chondrites (e.g., Isheyevo) was discouraged by Hardersen et al. (2011) because the long wavelength band center measured for Psyche (>940 nm) was thought to be inconsistent with the low-Fe silicates seen in CB/CH chondrites. However, our results, in combination with studies showing the variation in band center with Fe in pyroxenes (e.g., Cloutis and Gaffey 1991; Klima et al., 2007), suggests that a link could still exist. Furthermore, Shepard et al. (2021) and de Kleer et al. (2021) measured radar and millimeter emissivity and polarization that is consistent with a CB chondrite-like composition with a near-surface porosity of 75%. Compositionally, sections of Isheyevo range between two lithologies (metal-rich/CBb-like and metal-poor/CH-like) and the meteorite exhibits laminar features interpreted as evidence of gentle reaccretion of material in the impact plume of a glancing collision between planetesimals (Krot et al., 2007; Ivanova et al., 2008; Morris et al., 2015; Garvie et al., 2017). Isheyevo is ~60 vol.% metal and its ferromagnesian chondrules are typically Fe-poor (Ivanova et al., 2008). If Psyche is indeed a stripped planetary core, an Isheyevo-like lithology could be present on the surface.

We note that it is unlikely that other types of carbonaceous chondritic material dominate the surface composition of Psyche. Generally, spectra from carbonaceous chondrites are too dark, too blue-sloped (decreasing reflectance with increasing wavelength), and/or exhibit relatively strong absorption features not found in spectra of Psyche (Cloutis et al., 2011a,b; 2012a-f). However, the variations in Psyche's spectral reflectance, radar reflectivity, and emissivity suggest that residual material from infalling carbonaceous chondritic impactors could be present on the surface. This would be consistent with observations of carbonaceous material on the surface of (4) Vesta (e.g., Reddy et al., 2012) and the results of Cantillo et al. (2021) demonstrating that a spectrum of Psyche is consistent with a mixture of metal, low-Fe pyroxene, and powder from the Murchison CM2 chondrite.

Other meteorite types that have been associated with Psyche include mesosiderites (e.g., Sanchez et al., 2017; Viikinkoski et al., 2018) and ureilites (e.g., Hardersen et al., 2005; Goodrich et al., 2018). Mesosiderites are mixtures of metal, basaltic, gabbroic, and/or pyroxenitic silicates, and troilite. These meteorites are typically >40 wt.% silicates, the majority of which is pyroxene with >20 mol.% Fe (Mittlefehldt 1998). Because of the high abundance of Fe-bearing pyroxene, spectra of mesosiderites exhibit 1000 nm absorption features with band depths that exceed those measured in spectra of Psyche as well as ~1900 nm features absent in spectra of Psyche (this study and Burbine et al., 2007a). Thus, it is unlikely that Psyche's surface is dominated by a mesosiderite-like lithology. Ureilites, which are carbon-bearing ultramafic meteorites dominated by olivine and pyroxene, have been invoked as a possible precursor material for M-type asteroids like Psyche that underwent a high-temperature (>850 °C) smelting reaction (Mittlefehldt 1998; Hardersen et al., 2005). The olivine and pyroxene in these meteorites typically contain >10-15 mol.% Fe (Mittlefehldt 1998). The smelting reaction would have reduced this Fe-bearing olivine (fayalite) in the precursor material to Fe-free pyroxene, metal, carbon dioxide, and silica, proceeding at a rate dependent on the limiting reactant (either carbon or fayalite; Hardersen et al., 2005). However, the presence of some Fe-bearing pyroxene on Psyche (inferred from observed band centers) implies incomplete reduction of the fayalite component, which would theoretically remain on the surface. Spectra of ureilites and low-Fe fayalite have band centers >1000 nm, and thus its presence on the surface of Psyche is not supported by current observations of the asteroid. Thus, it is unlikely that ureilite-like material currently exists on Psyche's surface (Hardersen et al., 2005).

The interpretation that the surface of Psyche could be enriched in (and possibly dominated by) sulfide minerals is relatively new. Fornasier et al. (2010) attributed some reflectance features at ~490 nm in the spectra of M-type asteroids to sulfide minerals like troilite and/or oldhamite, although Psyche lacked such a feature. The densities of troilite (~4.8 g/cm3) and pentlandite (~4.9 g/cm3) are within the range of values reported for Psyche (Elkins-Tanton et al., 2020; Siltala and Granvik 2021). Furthermore, de Kleer at al. (2021) measured thermal inertia and millimeter emissivity values of Psyche that are consistent with sulfides dominating the 'metallic' portion of the asteroid, with a surface porosity of 40%. Sulfide minerals are common in both chondritic and achondritic meteorites (e.g., Mittlefehldt 1998; Scott and Krot 2003) and can form both directly from the solar nebula (Lauretta et al., 1997) and through both high and low-temperature processes expected during planetary formation (Schrader et al., 2016 and references therein). While few meteorites with high abundances (tens of vol.%) of sulfide minerals exist in terrestrial collections, models of trace element behavior in iron meteorites suggest that sulfur may have been present in high enough abundance during early planetesimal core formation to form an immiscible sulfide liquid (Ulff-Møller 1998; Chabot 2004; Goldstein et al., 2009; Bercovici 2020). If Psyche is indeed composed of remnant core materials, a significant amount of sulfide material could remain detectable on the surface. However, constraining the exact nature of any sulfide components on the surface of Psyche from reflectance spectroscopy remains challenging due to spectral differences between natural and synthetic sulfides and the limited number of spectra of natural oldhamite (e.g., Burbine et al., 2002; Helbert et al., 2013; Varatharajan et al., 2019). Further reanalysis of Psyche's properties in the context of sulfide minerals could help to constrain this hypothesis.

Finally, while Binzel et al. (1995) initially observed no rotational spectral variations for Psyche, a more recent study by Sanchez et al. (2017) reported rotational variations in the band center of the ~1000 nm feature. This variation in band center was interpreted by the authors as evidence for variation in the abundance and chemistry of a purported pyroxene component. We note that the two studies of rotational variation are not mutually exclusive: Binzel et al. (1995) observed Psyche at a nearly equatorial latitude while Sanchez et al. (2017) were observing at ~-46° and ~-52° latitude. Similar to

Sanchez et al. (2017), our chi-square results suggest that there could be significant compositional variation on the surface of the asteroid. This is further supported by variations in radar reflectivity from Shepard et al. (2021) that are correlated with changes in optical albedo, consistent with potential variation in the metal-silicate ratio across the surface of the asteroid.

3.3.2 Comparison of Band Parameters

Surface mineralogy can also be constrained by comparing the depths and centers of absorption features at ~1000 nm in the spectra in our library to telescopic spectra of Psyche (Fig. 3.4). Similar to previous studies, our band parameter measurements suggest that the surface of Psyche is consistent with a metal-rich composition mixed with a silicate component. An example of this is the 90/10 wt.% mixture of powder from the Odessa iron meteorite and Fs45.6 orthopyroxene from Cloutis et al. (2009), labeled MPMIX1010 in Fig. 4. We note that the pyroxene in this mixture is more Fe-rich (En50.8 Fs45.6) than what is typically inferred from telescopic spectra of Psyche.

Of the three types of materials with minimized chi-square values (iron meteorites, sulfides, and powder from Isheyevo), only spectra from Isheyevo exhibit an absorption feature at ~1000 nm consistent with absorption features seen in spectra of Psyche. In Figure 3.4, points labeled with a '30_' prefix are samples from Isheyevo. The scatter in points from this sample is consistent with previous measurements of variation in band depth and center as grain size and phase angle vary. Samples 30_03 and 30_04 are from <75 micron and >75 micron fractions of powder from Isheyevo, respectively. Both

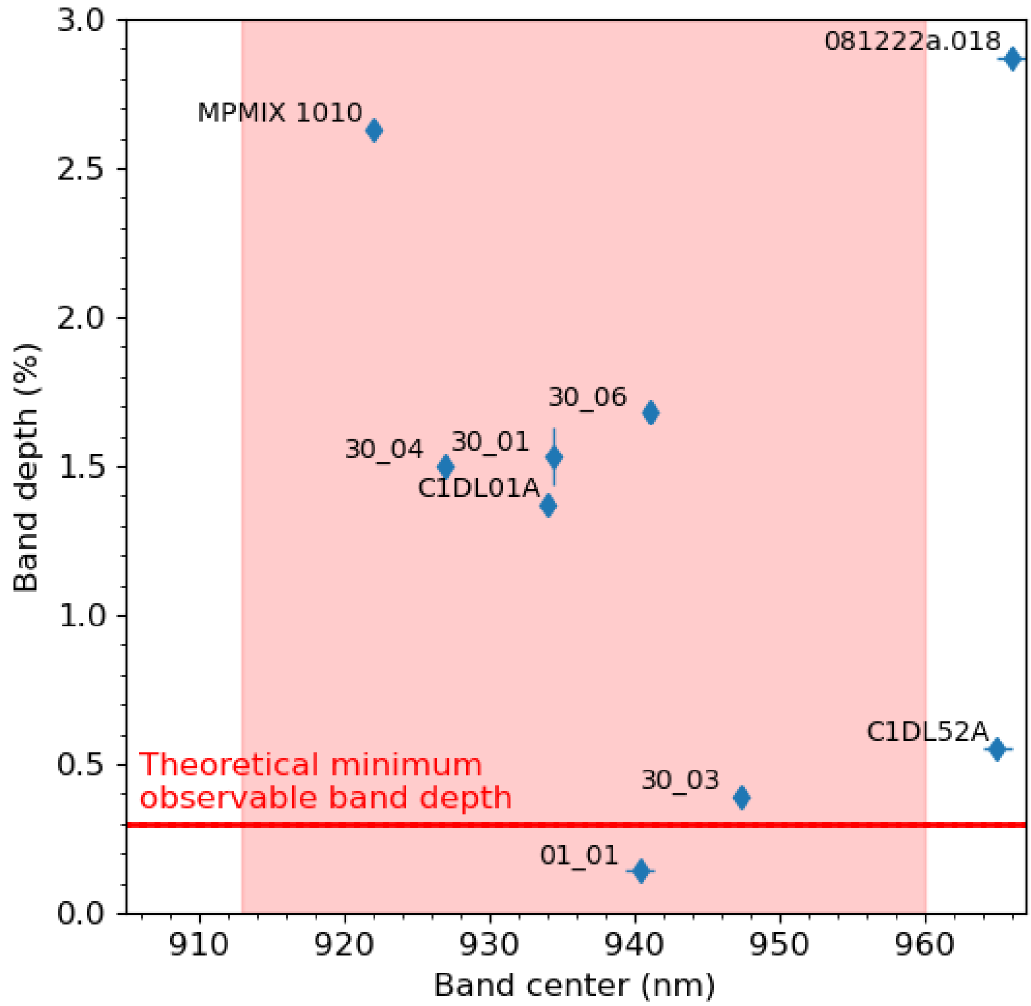

Figure 3.4. The range of reported ~1000 nm band centers and depths of spectra of (16) Psyche (pink region) are consistent with band parameters from samples containing metal and/or low-Fe, low-Ca pyroxene (e.g., enstatite). Samples with the '30_...' prefix are samples of the CH/CBb chondrite Isheyevo. Sample 01_01 is a hand sample of the aubrite Mayo Belwa. MPMIX1010 is a powder mixture of 90 wt.% iron meteorite metal and 10 wt.% $En_{50.8}$ $Fs_{45.6}$ orthopyroxene (Cloutis et al., 2009). Samples C1DL01A and C1DL52A are synthetic pyroxenes with En_{100} and $En_{90}Wo_{10}$ compositions, respectively (Klima et al., 2007). Sample 081222a.018 is powder from the EH4 chondrite MET 00783. The red line represents the theoretical minimum observable band depth measurable by the Imager.

spectra were measured at a phase angle of (i/e) 38°/8°. The finer fraction (sample 30_03) exhibits a shallower absorption feature (consistent with trends for finer grained pyroxene) and a longer wavelength band center (consistent with a shift caused by blue-sloped spectra of finer grained metal; Cloutis et al., 1990; Cloutis et al. 2010). Additionally, it is possible that sample 30_03 has a higher proportion of iron-bearing silicates (e.g., pyroxene and olivine) than the coarser fraction due to the ease with which silicates are comminuted compared to metal. The higher relative abundance of olivine compared to metal could shift the band center to longer wavelengths (e.g., Cloutis et al., 1990). Furthermore, spectra from the powders of Isheyevo at the same grain size but different phase angle (i.e., 30_04 at i/e 38°/8° and 30_06 at i/e 23°/8°) are consistent with published trends for metal-rich compositions. For example, Cloutis et al. (2010) measured decreasing spectral slope with decreasing phase angle for iron meteorite powders. With a lower (or even negative) spectral slope, the band center of metal-silicate mixtures could shift to longer wavelengths relative to a spectrum of the metal-silicate mixture measured at a larger phase angle.

Absorption band parameters from a hand sample of the aubrite Mayo Belwa (sample 01_01 in Fig. 3.4) are also consistent with those of Psyche. Like other aubrites, this meteorite is composed mostly of almost Fe-free enstatite (97.5 vol.% En99; Watterz and Prinz, 1979). Another enstatite-rich sample, the enstatite chondrite MET 00783 (sample 081222a.018), exhibits a band center slightly longward of the upper range of reported band parameters for Psyche. MET 00783 is mostly enstatite (67 wt.%) with troilite (12 wt.%), albite (6 wt.%), kamacite (6 wt.%), and gypsum (5 wt.%) (Izawa et al., 2010). The presence of albite and gypsum (a terrestrial weathering product), which exhibit broad absorption features centered at ~ 1200 nm and 1400 nm, respectively, may be the cause of the longer wavelength center of MET 00783. Finally, absorption features of En100 and En90Wo10 synthetic pyroxenes from Klima et al. (2007) (samples

C1DL01A and C1DL52A, respectively) are also consistent with reported band depths and band centers for Psyche.

Also shown in Figure 3.4 is a theoretical minimum observable band depth that the Imager can measure (~0.3%). This limit is based on radiometric modeling of the Imager's performance during nominal Orbit B operations using equations from Table 9-15 from Larson and Wertz (1999). We use this radiometric model to estimate the signal-to-noise ratio (SNR) for pixels in images taken through each filter. During Orbit B operations, we estimate the SNR in the two longest wavelength filters (centered at 948 and 1041 nm) to be ~118 and ~98, respectively, assuming pixel summing (2x2 and 3x3, respectively) and the longest possible exposure times before the spacecraft's velocity causes smearing of a half-pixel (167.4 ms and 251.1 ms, respectively). These SNR estimates translate to relative errors of 0.85% and 1.02%. Assuming Psyche's albedo at 1000 nm is ~0.14, these relative errors translate to absolute reflectance uncertainties of ~0.12% and 0.14%. The sum of these two absolute reflectance uncertainties represents the theoretical minimum observable band depth (~0.3%). This limit suggests that absorption features from very low-Fe natural pyroxenes, like those in spectra of Mayo Belwa, could be undetectable by the Imager. However, very low-Fe enstatite-rich compositions (e.g., aubrites) are typically much brighter than the measured visible wavelength reflectance of Psyche, and thus current observations suggest that these compositions are not likely to occur on the asteroid's surface.

3.4 Preliminary Strategies for Using Imager Data to Assess Surface Composition

Three of the five major science objectives of the Psyche Mission that require data from the Imager filters are: (1) to determine if Psyche is a remnant planetary core; (2) to determine if small bodies incorporate the same light elements as are expected in the Earth's core; and (3) to determine the redox conditions under which Psyche was formed (Elkins-Tanton et al., 2016; Elkins-Tanton et al., 2020). To address these objectives, the Imager must assess the homogeneity of metal-silicate mixing, identify any diagnostic sulfur-bearing phases present, and discriminate between silicate or sulfide compositions that could help to constrain redox conditions (Bell et al., 2016; Elkins-Tanton et al., 2020). Using the laboratory spectra in our library, we have developed a set of parameters using spectra convolved to the Imager's spectral throughput that could allow rapid processing of future Imager multispectral data to derive compositional information about the surface of Psyche at the resolution of single images, and thus to help address the mission's relevant science objectives.

While the generally featureless, red-sloped spectra from most disk-integrated telescopic measurements of the asteroid (Table 3.2) are typically interpreted as evidence of a surface dominated by metal but potentially with some low-Ca, low-Fe silicates, they do not rule out the possibility of small (unresolved) areas on the surface enriched in silicate minerals with higher Ca or Fe contents (e.g., MPMIX1010 in Fig. 3.4). This possibility is consistent with the rotational spectral variation reported by Sanchez et al. (2017), who measured areas of differing silicate abundance and chemistry heterogeneously distributed on the surface of Psyche. Thus, it is prudent to explore how

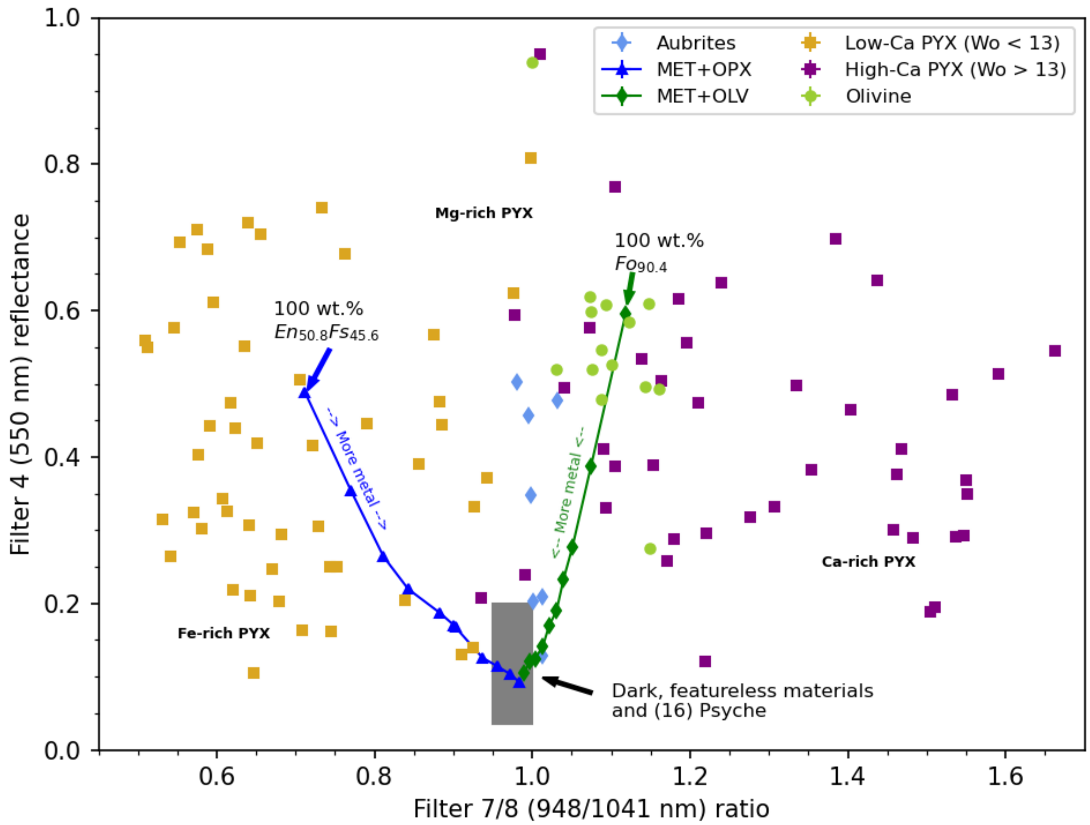

Figure 3.5. Low-Ca pyroxene (Wo < 13, yellow squares) can be discriminated from other silicates that could be present on the surface of Psyche, like high-Ca pyroxene (purple squares) or olivine (green circles) using the ratio between Imager Filters 7/8 (948/1041 nm). Furthermore, these iron-bearing silicates can be discriminated from lower reflectance, featureless materials using both the Filter 7/8 ratio and the Filter 4 (550 nm) reflectance. The range of values for Psyche, iron meteorites, sulfides, and metal-rich chondrites are represented by a gray rectangle. Mixtures of pyroxene and metal (MET+OPX, dark blue triangle and solid line) and mixtures of olivine and metal (MET+OLV, dark green diamonds and solid line) at 10 wt.% intervals indicate that mixtures with increasing metal content exhibit lower 550 nm reflectance and become 'featureless' (948/1041 nm ratio of ~1.0). Uncertainty is typically smaller than the size of the points.

the Imager could discriminate various compositions with higher abundances of silicates and/or variable silicate chemistries.

For example, the nature of iron-bearing silicates relevant to Psyche (e.g., pyroxene and olivine) can potentially be constrained via the ratio of the 948/1041 nm filter reflectance plotted versus the 550 nm filter reflectance (Fig. 3.5). Low-Ca, Fe-bearing pyroxenes (yellow squares in Fig. 3.5) typically exhibit an absorption feature between ~910 and ~960 nm due to Fe2+ in the M2 crystallographic site (Adams 1974; Cloutis and Gaffey 1991; Klima et al., 2007). This is expressed in Imager data as a ratio in the 948/1041 nm filters less than 1. Conversely, spectra of high-Ca pyroxene (purple squares in Fig. 3.5) and olivine (green circles in Fig. 3.5) exhibit absorption features at wavelengths longer than ~1000 nm, and thus the 948/1041 nm ratio is typically greater than 1. High-Mg silicates (e.g., some of the olivines and pyroxenes shown in Fig. 3.5 as well as the aubrites) have much shallower or no absorption features, and thus exhibit 948/1041 nm filter ratios close to 1. Most pure silicates in our library exhibit higher reflectance than the range of values reported for Psyche, represented in Figure 3.5 by a gray box. The more metal-rich compositions (e.g., iron meteorites, enstatite and CB chondrites) and sulfides also plot within the gray box in Figure 3.5. Finally, mixtures of iron meteorite metal and Fo90.4 olivine (green triangles in Fig. 3.5) and iron meteorite metal and En50.8 Fs45.6 orthopyroxene (blue triangles in Fig. 3.5) from Cloutis et al. (2009) are also shown in Fig. 3.5. Both of these sets of mixtures exhibit lower 550 nm filter reflectance and become featureless (i.e., migrate towards a 948/1041 nm filter ratio of 1) with increasing metal content.

Secondly, some relationships among absorption feature parameters that have been well-established from previous high spectral resolution laboratory studies can also be recovered from spectra in our library convolved to the Imager's spectral throughput. For example, Fig. 3.6 shows the band centers reconstructed from Imager-convolved spectra of natural and synthetic pyroxenes using the methods described in Fig. 3.2 plotted against the band center derived from the high-resolution laboratory spectra. The pyroxenes in

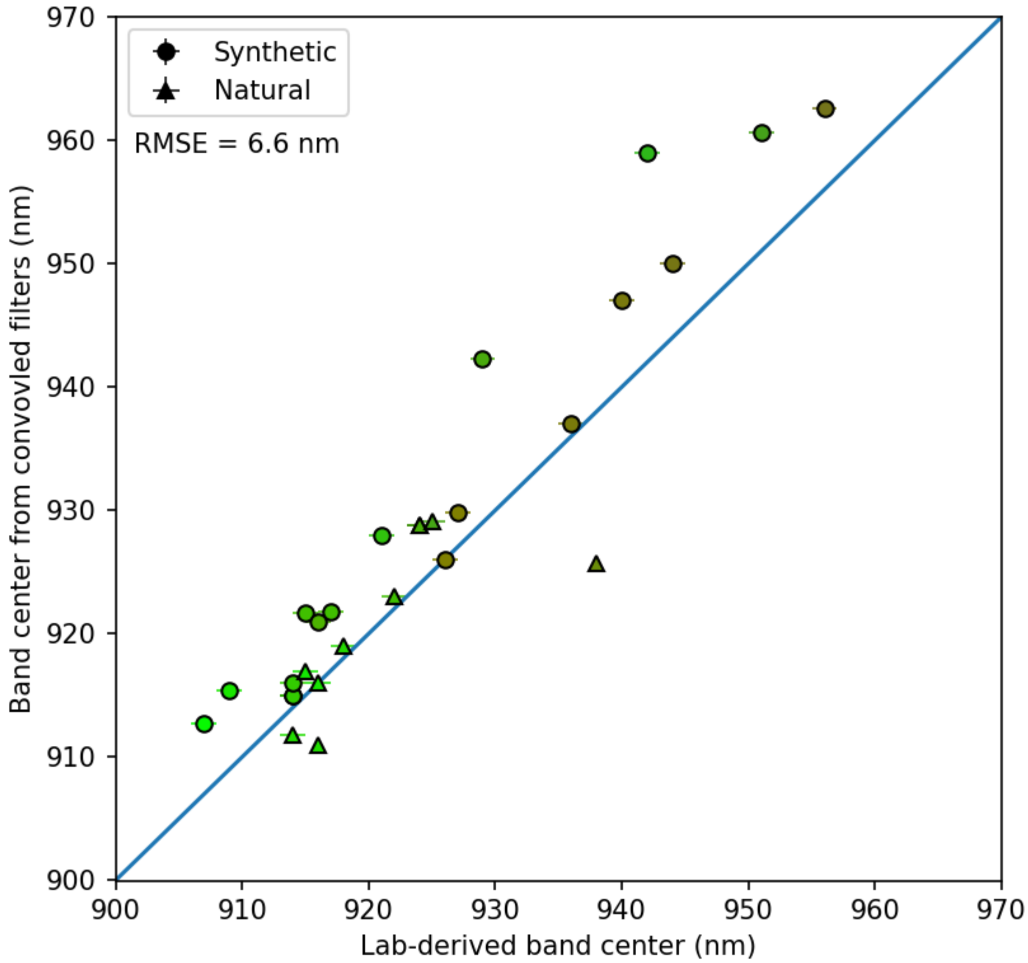

Figure 3.6. Band centers from synthetic (circles) and natural pyroxenes (triangles) can be measured in spectra convolved to the Imager's bandpasses (RMS error = 6.6 nm). The samples shown here have compositions covering the range of inferred pyroxene chemistries on the surface of Psyche by Sanchez et al. (2017). This includes all pyroxenes in our library with Fs ≤ 51.5 mol.% and Wo ≤ 12.9 mol.%. Points are colored according to their chemistry using an R/G/B = Fe/Mg/Ca scheme. Because the pyroxene on Psyche reported in Sanchez et al. (2017) is mostly Mg-rich, most points are green/brown. The blue line of slope = 1 indicates perfect recreation of the band center in the Imager-convolved spectra.

Fig. 3.6 are those that have chemistries within the range measured by Sanchez et al. (2017). The residual mean squared error (RMSE) from this comparison is 6.6 nm. Using the equations developed by Burbine et al. (2007b) for relating the ~1000 nm band center in spectra of HED meteorites to their chemistry, our RMSE translates to an uncertainty in

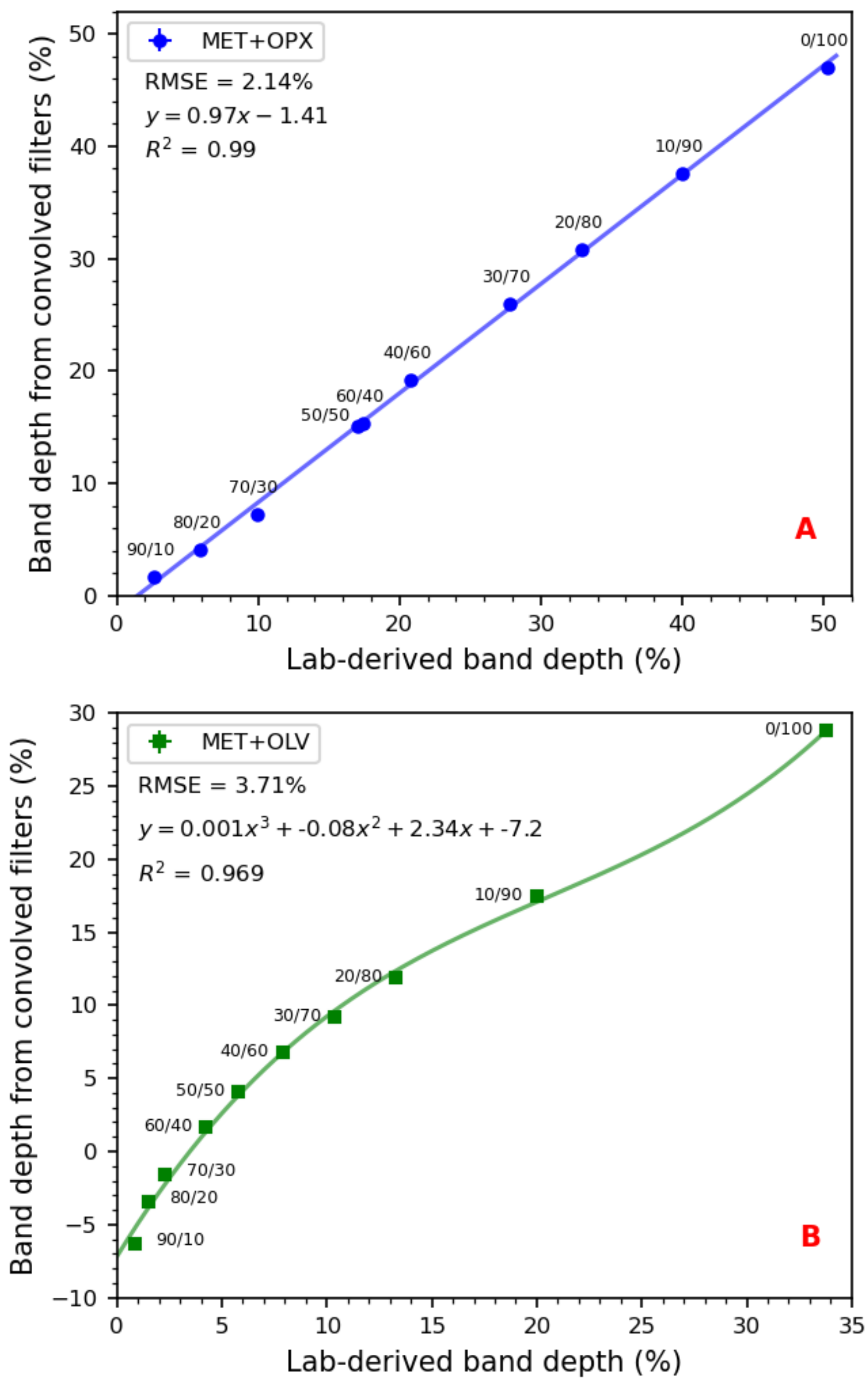

Figure 3.7. Band depths from high-resolution laboratory spectra and Imager-convolved spectra of metal-orthopyroxene mixtures (A) and metal-olivine mixtures (B) from Cloutis et al. (2009). The ratio of the components (in wt.% intervals of metal/silicates) is shown next to each point.

the inferred pyroxene chemistry of ± 8.5 mol.% En, ± 6.8 mol.% Fs, and ± 2.7 mol.%

Wo. Accurate measurement of absorption band centers may be used to constrain the Fe content in silicates as well as the pyroxene/olivine ratio on the surface, and thus provide insight into the redox state of the asteroid (e.g., McSween 1992; Hardersen et al., 2005).

Furthermore, the abundance of pyroxene in metal-pyroxene mixtures can be accurately measured from Imager-convolved spectra by comparing band depths of spectra convolved to the Imager's throughput to band depths from high-resolution laboratory spectra (Fig. 3.7A) (RMSE = 2.14%). Band depths of spectra from metal-olivine mixtures (Fig. 3.7B) can be measured from Imager-convolved data using Method 3 in Fig. 3.2. For mixtures with high abundance of metal, band depths become increasingly shallow and the overall spectra become more red-sloped. Band depths from mixtures with >40 wt.% olivine measured from Imager-convolved spectra can be accurately recreated, and a cubic polynomial can be used to infer band depth for mixtures with <40 wt.% olivine (Fig. 7B). The RMS error for metal-olivine band depths is 3.71%.

In Figure 3.8 we offer a preliminary strategy for discriminating the low reflectance, 'featureless' compositions that could be present on the surface of the asteroid as suggested by remote sensing and our chi-square analysis. These compositions include iron meteorites, sulfides, and CB and enstatite chondrites. Fig. 3.8 shows the Filter 4/8 (550/1041 nm) ratio versus the Filter 3/4 (495/550 nm) ratio for spectra from these compositions in our library that had ~1000 nm band depths < 3.0% measured from Imager-convolved spectra. This limit is the approximately highest reported band depth in spectra of Psyche (Table 3.2). The Filter 3/4 ratio effectively separates the iron meteorites and sulfides due to the typically higher visible wavelength slopes of sulfides. Britt and

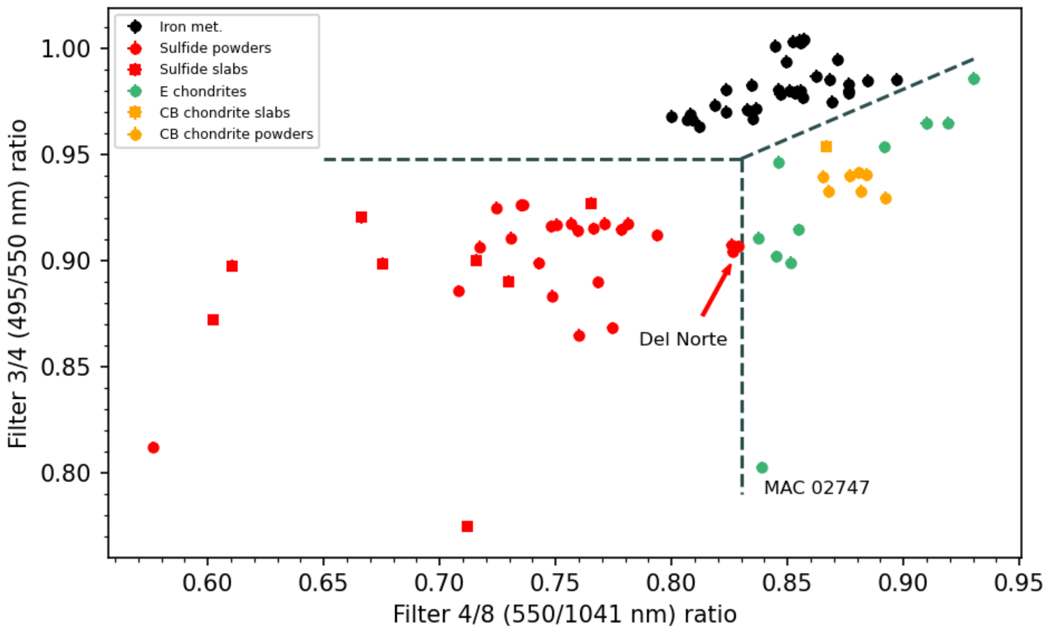

Figure 3.8. Compositions with 'featureless' spectra that are consistent with telescopic spectra of (16) Psyche can be discriminated based on ratios between Filters 4/8 (550/1041 nm) and Filters 3/4 (495/550). Spectra of powder from terrestrial sulfides from Del Norte County, California and an outlier enstatite chondrite, MAC 02747, are labeled. The Del Norte sulfide is dominated by troilite and pyrrhotite with minor cubanite ($CuFe_2S_3$). MAC 02747 has the lowest metal content of the enstatite chondrites in this study and is weathered. See text for discussion.

Pieters (1988) and Cloutis et al. (2010) demonstrated that spectra of iron meteorites at various grain sizes and compositions are relatively invariant to this ratio, and this is reflected by the clustering of iron meteorites in Fig. 3.8.

Conversely, sulfides exhibit a larger range of Filter 4/8 and Filter 3/4 ratios (Fig. 3.8), likely due to the textural and mineralogical variation in the sulfide samples in our library (Appendix B Table S3.1). Unlike the other sulfides, a cluster of points from spectra of a sulfide sample from Del Norte County, California exhibits Filter 4/8 ratios >0.8. This sample is dominated by troilite and pyrrhotite, but also contains a significant amount (<~20 vol.%) of cubanite ($CuFe_2S_3$). This mineral exhibits a shallower near-infrared spectral slope consistent with other Cu-bearing Fe-sulfides, which is likely the cause of Filter 4/8 (550/1041 nm) ratios closer to 1.0 (Wood and Strens 1979; Pirard et al., 2008). While cubanite has been found in CI chondrites (Berger et al., 2011), material returned from comet 81P/Wild 2 (Brownlee 2014), and in exogenous regolith grains in Itokawa (Burgess and Stroud 2021), cubanite is only found in metal-rich meteorites as a terrestrial alteration product (Rubin 1997, Rubin and Ma 2017). The presence of cubanite in extraterrestrial materials constrains the maximum temperature experienced to <~250°C (Berger et al., 2015), and thus identification of cubanite on the surface of Psyche could significantly constrain the asteroid's formation history.

Finally, 'featureless' spectra of the CB and enstatite chondrites in our library exhibit Filter 3/4 and Filter 4/8 ratios distinct from the iron meteorites. We include enstatite chondrites in this plot because their spectra at Imager-relevant wavelengths (~400-1100 nm) are comparable to spectra of Psyche (despite their near-infrared spectra deviating from those of Psyche) and because they have been previously invoked as possible Psyche analogs. Both the enstatite chondrites and CB chondrites are characterized by a high abundance of low-Fe, low-Ca pyroxene and/or olivine in chondrules (20-80 vol.%) mixed with metal, and sulfides. Some of the enstatite chondrites also contain several wt.% feldspar and terrestrial alteration products (e.g., gypsum). The enstatite chondrite MAC 02747 exhibits a Filter 2/4 (437/550 nm) ratio much lower than the other enstatite chondrites in our study. This sample has the lowest metal content of the enstatite chondrites in Fig. 3.8 (Izawa et al., 2010), and thus may have an enhanced metal-oxygen charge transfer absorption relative to the other enstatite chondrites. This enhancement may result in a stronger visible slope and thus lower Filter 3/4 (495/550 nm) ratio. While this sample is reported to be weathered (Izawa et al. 2010), it's visible to near-infrared spectrum exhibits no obvious absorption features from terrestrial weathering products and so we kept it in our study.

3.5 Conclusions

The Psyche Mission will explore the solar system's largest M-type asteroid, (16) Psyche, starting in early 2026. We have assembled a library of laboratory spectra that are consistent with current uncertainties in Psyche's surface composition based on spectral properties, density, radar reflectivity, and emissivity. We have performed a chi-square analysis that has shown that available telescopic spectra of Psyche, while consistent with iron meteorites, are also consistent with sulfide minerals (e.g., troilite and pentlandite) and powder from the CH/CBb chondrite Isheyevo. Secondly, we have compared band centers of ~1000 nm absorption features found in spectra of Psyche to similar features in the spectra in our library. Results from this investigation are consistent with previous interpretations of the asteroid's surface being metal-rich with a low-Fe, low-Ca pyroxene component, but are also consistent with a metal-rich composition mixed with a small abundance of Fe-rich pyroxene (e.g., 90 wt.% iron meteorite metal and 10 wt.% En50.8 Fs45.6 orthopyroxene). Our investigation provides new insight into the surface composition of the asteroid and is consistent with recent studies that suggest the surface composition of Psyche might not be as metallic as once thought.

To address the Psyche mission's science objectives and to resolve these various compositional possibilities, the Psyche spacecraft's Multispectral Imager will map the surface from orbit at visible to near-infrared wavelengths and at high spatial resolution.

We have demonstrated that spectra of silicates and metal-silicate mixtures convolved to the Psyche Imager’s filters can be discriminated based on their Filter 4 (550 nm) reflectance and Filter 7/8 (948/1041 nm) ratio. Band centers derived from Imager-convolved data are predicted to be accurate to within <10 nm, while band depths derived from spectra of metal-silicate mixtures are predicted to be accurate to within about 5%. Finally, the low reflectance, ‘featureless’ materials in our spectral library that are consistent with telescopic spectra of Psyche can be discriminated using the Imager Filter 3/4 (495/550 nm) and Filter 4/8 (550/1041 nm) ratios. Multispectral Images acquired by the Imager, in combination with data from the spacecraft’s GRNS and magnetometer investigations, will allow hypotheses of the asteroid’s formation history to be tested and help to constrain critical processes in terrestrial planet formation.

Acknowledgments, Samples, and Data

This study was funded by NASA Grant NNM16AA09C. We are extremely grateful to Dr. Laurence Garvie, the ASU Center for Meteorite Studies, Dr. Timothy McCoy, and the Smithsonian Institution for providing the samples used in this study. We thank Dr. Juan Sanchez and collaborators for sharing the spectral data of (16) Psyche from Sanchez et al. (2017). All spectral data collected at ASU are available in the Open Science Foundation repository #####. Spectral data from the Brown University RELAB are available at http://www.planetary.brown.edu/relab/ and spectral data from the University of Winnipeg Planetary Spectrophotometer Facility are available at https://psf.uwinnipeg.ca/.

References

Adams, J. B. (1974). Visible and near-infrared diffuse reflectance spectra of pyroxenes as applied to remote sensing of solid objects in the solar system. Journal of Geophysical Research, 79(32), 4829-4836.

Agee, C. B., Vaci, Z., Ziegler, K., & Spilde, M. N. (2019). Northwest Africa 12273: unique ungrouped metal-rich chondrite. In Lunar and Planetary Science Conference (No. 2132, p. 1176).

Asphaug, E. (2010). Similar-sized collisions and the diversity of planets. Geochemistry, 70(3), 199-219.

Becker, T. M., Cunningham, N., Molyneux, P., Roth, L., Feaga, L. M., Retherford, K. D., et al. (2020). HST UV Observations of Asteroid (16) Psyche. The Planetary Science Journal, 1(3), 53.

Bell, III, J. F., Elkins-Tanton, L. T., Polanskey, C. A., Ravine, M. A., Caplinger, M. A., Asphaug, E., et al. (2016). The Psyche multispectral imager investigation: Characterizing the geology, topography, and compositional properties of a metallic world.

Bell, III, J. F., Maki, J. N., Mehall, G. L., Ravine, M. A., Caplinger, M. A., Bailey, Z. J., et al. (2021). The Mars 2020 perseverance rover mast camera zoom (Mastcam-Z) multispectral, stereoscopic imaging investigation. Space Science Reviews, 217(1), 1-40.

Bercovici, H. L. (2020). The Effect of Bulk Composition on the Sulfur Content of Cores (Master's thesis). Retrieved from ProQuest. Location:Arizona State University.

Berger, E. L., Zega, T. J., Keller, L. P., & Lauretta, D. S. (2011). Evidence for aqueous activity on comet 81P/Wild 2 from sulfide mineral assemblages in Stardust samples and CI chondrites. Geochimica et Cosmochimica Acta, 75(12), 3501-3513.

Berger, E. L., Keller, L. P., & Lauretta, D. S. (2015). An experimental study of the formation of cubanite (CuFe2S3) in primitive meteorites. Meteoritics & Planetary Science, 50(1), 1-14.

Bild, R. W., & Wasson, J. T. (1976). The Lodran meteorite and its relationship to the ureilites. Mineralogical Magazine, 40(315), 721-735.

Binzel, R. P., Bus, S. J., Xu, S., Sunshine, J., Burbine, T. H., Neely, A. W., & Brown, R. W. (1995). Rotationally resolved spectra of asteroid 16 Psyche. Icarus, 117(2), 443-445.

Bouvier, A., Gattacceca, J., Agee, C., Grossman, J., & Metzler, K. (2017). The meteoritical bulletin, no. 104. Meteoritics & Planetary Science, 52(10), 2284-2284.

Bowman, L. E., Papike, J. J., & Spilde, M. N. (1996). Modal abundances in diogenites: Insights into phase percentages using electron microprobe techniques. In Lunar and Planetary Science Conference (Vol. 27).

Britt, D. T., & Pieters, C. M. (1988). Bidirectional reflectance properties of iron-nickel meteorites. In Lunar and Planetary Science Conference Proceedings (Vol. 18, pp. 503-512).

Brownlee, D. (2014). The Stardust mission: analyzing samples from the edge of the solar system. Annual Review of Earth and Planetary Sciences, 42, 179-205.

Bunch, T. E., Keil, K., & Huss, G. I. (1972). The Landes meteorite. Meteoritics, 7(1), 31-38.

Burbine, T. H., McCoy, T. J., Nittler, L. R., Benedix, G. K., Cloutis, E. A., & Dickinson, T. L. (2002). Spectra of extremely reduced assemblages: Implications for Mercury. Meteoritics & Planetary Science, 37(9), 1233-1244.

Burbine, T. H., Greenwood, R. C., Buchanan, P. C., Franchi, I. A., & Smith, C. L. (2007a). Reflectance spectra of Mesosiderites: Implications for asteroid 4 Vesta. In Lunar and Planetary Science Conference (Vol. 38).

Burbine, T. H., Buchanan, P. C., & Binzel, R. P. (2007b). Deriving formulas from HED spectra for determining the pyroxene mineralogy of Vesta and Vestoids. In Lunar and Planetary Science Conference (Vol.38).

Burgess, K. D., & Stroud, R. M. (2021). Exogenous copper sulfide in returned asteroid Itokawa regolith grains are likely relicts of prior impacting body. Communications Earth & Environment, 2(1), 1-6.

Bus, S. J., & Binzel, R. P. (2002). Phase II of the small main-belt asteroid spectroscopic survey: The observations. Icarus, 158(1), 106-145.

Buseck, P. R. (1977). Pallasite meteorites—mineralogy, petrology and geochemistry. Geochimica et Cosmochimica Acta, 41(6), 711-740.

Cantillo, D. C., Reddy, V., Sharkey, B. N., Pearson, N. A., Sanchez, J. A., Izawa, M. R., et al. (2021). Constraining the Regolith Composition of Asteroid (16) Psyche via Laboratory Visible Near-infrared Spectroscopy. The Planetary Science Journal, 2(3), 95.

Chabot, N. L. (2004). Sulfur contents of the parental metallic cores of magmatic iron meteorites. Geochimica et Cosmochimica Acta, 68(17), 3607-3618.

Clark, R. N., & Roush, T. L. (1984). Reflectance spectroscopy: Quantitative analysis techniques for remote sensing applications. Journal of Geophysical Research: Solid Earth, 89(B7), 6329-6340.

Cloutis, E. A., & Gaffey, M. J. (1991). Pyroxene spectroscopy revisited: Spectral-compositional correlations and relationship to geothermometry. Journal of Geophysical Research: Planets, 96(E5), 22809-22826.

Cloutis, E. A., Gaffey, M. J., Smith, D. G., & Lambert, R. S. J. (1990). Reflectance spectra of “featureless” materials and the surface mineralogies of M-and E-class asteroids. Journal of Geophysical Research: Solid Earth, 95(B1), 281-293.

Cloutis, E. A., Hardersen, P. S., Reddy, V., Gaffey, M. J., Bailey, D. T., & Craig, M. A. (2009). Metal-Orthopyroxene and Metal-Olivine Mixtures: Spectral reflectance properties and implications for asteroid spectroscopy. In Lunar and Planetary Science Conference (p. 1332).

Cloutis, E. A., Hardersen, P. S., Bish, D. L., Bailey, D. T., Gaffey, M. J., & Craig, M. A. (2010). Reflectance spectra of iron meteorites: Implications for spectral identification of their parent bodies. Meteoritics & Planetary Science, 45(2), 304-332.

Cloutis, E. A., Hiroi, T., Gaffey, M. J., Alexander, C. O. D., & Mann, P. (2011a). Spectral reflectance properties of carbonaceous chondrites: 1. CI chondrites. Icarus, 212(1), 180-209.

Cloutis, E. A., Hudon, P., Hiroi, T., Gaffey, M. J., & Mann, P. (2011b). Spectral reflectance properties of carbonaceous chondrites: 2. CM chondrites. Icarus, 216(1), 309-346.

Cloutis, E. A., Hudon, P., Hiroi, T., & Gaffey, M. J. (2012a). Spectral reflectance properties of carbonaceous chondrites: 3. CR chondrites. Icarus, 217(1), 389-407.

Cloutis, E. A., Hudon, P., Hiroi, T., & Gaffey, M. J. (2012b). Spectral reflectance properties of carbonaceous chondrites 4: Aqueously altered and thermally metamorphosed meteorites. Icarus, 220(2), 586-617.

Cloutis, E. A., Hudon, P., Hiroi, T., Gaffey, M. J., & Mann, P. (2012c). Spectral reflectance properties of carbonaceous chondrites–5: CO chondrites. Icarus, 220(2), 466-486.

Cloutis, E. A., Hudon, P., Hiroi, T., Gaffey, M. J., Mann, P., & Bell III, J. F. (2012d). Spectral reflectance properties of carbonaceous chondrites: 6. CV chondrites. Icarus, 221(1), 328-358.

Cloutis, E. A., Hudon, P., Hiroi, T., & Gaffey, M. J. (2012e). Spectral reflectance properties of carbonaceous chondrites: 7. CK chondrites. Icarus, 221(2), 911-924.

Cloutis, E. A., Hudon, P., Hiroi, T., Gaffey, M. J., & Mann, P. (2012f). Spectral reflectance properties of carbonaceous chondrites: 8. “Other” carbonaceous chondrites: CH, ungrouped, polymict, xenolithic inclusions, and R chondrites. Icarus, 221(2), 984-1001.

Cloutis, E. A., Sanchez, J. A., Reddy, V., Gaffey, M. J., Binzel, R. P., Burbine, T. H., et al. (2015). Olivine–metal mixtures: Spectral reflectance properties and application to asteroid reflectance spectra. Icarus, 252, 39-82.

de Kleer, K., Cambioni, S., & Shepard, M. (2021). The Surface of (16) Psyche from Thermal Emission and Polarization Mapping. arXiv preprint arXiv:2105.11372.

DeMeo, F. E., Binzel, R. P., Slivan, S. M., & Bus, S. J. (2009). An extension of the Bus asteroid taxonomy into the near-infrared. Icarus, 202(1), 160-180.

Dibb, S., Bell, III, J. F., Elkins-Tanton, L. T., Williams, D. A., Binzel, R. P., and the Psyche Mission Team (2018). Optimized Narrowband Visible to Near-Infrared Filters for the Psyche Multispectral Imager. In Instrumentation for Planetary Missions 2018.

Dibb, S. D., Bell, III, J. F., & Garvie, L. A. J. (2021). Reflectance Spectra of Metal-Troilite Mixtures: Implications for M-/X-Type Asteroid Exploration. In Lunar and Planetary Science Conference (p. 1543).

Dyar, M. D., Sklute, E. C., Menzies, O. N., Bland, P. A., Lindsley, D., Glotch, T., et al. (2009). Spectroscopic characteristics of synthetic olivine: An integrated multi-wavelength and multi-technique approach. American Mineralogist, 94(7), 883-898.

Elkins-Tanton, L. T., Asphaug, E., Bell, J., Bercovici, D., Bills, B. G., Binzel, R. P., et al. (2016). Asteroid (16) Psyche: the science of visiting a metal world.

Elkins-Tanton, L. T., Asphaug, E., Bell III, J. F., Bercovici, H., Bills, B., Binzel, R., et al. (2020). Observations, meteorites, and models: a preflight assessment of the composition and formation of (16) Psyche. Journal of Geophysical Research: Planets, 125(3), e2019JE006296.

Fornasier, S., Clark, B. E., Dotto, E., Migliorini, A., Ockert-Bell, M., & Barucci, M. A. (2010). Spectroscopic survey of M-type asteroids. Icarus, 210(2), 655-673.

Gaffey, M. J., Cloutis, E. A., Kelley, M. S., & Reed, K. L. (2002). Mineralogy of Asteroids. In Bottke, W. F., Cellino, A., Paolicchi, P. & Binzel, R. P. (Eds.), Asteroids III. (p. 183-204). University of Arizona Press.

Garvie, L. A., Knauth, L. P., & Morris, M. A. (2017). Sedimentary laminations in the Isheyevo (CH/CBb) carbonaceous chondrite formed by gentle impact-plume sweep-up. Icarus, 292, 36-47.

Gattacceca, J., McCubbin, F. M., Bouvier, A., & Grossman, J. (2020). The Meteoritical Bulletin, No. 107. Meteoritics & Planetary Science, 55(2), 460-462.

Goldstein, J. I., Scott, E. R. D., & Chabot, N. L. (2009). Iron meteorites: Crystallization, thermal history, parent bodies, and origin. Geochemistry, 69(4), 293-325.

Goodrich, C. A., Fioretti, A., Zolensky, M., Shaddad, M., Hiroi, T., Young, E., et al. (2018, October). Compositional and Spectral Properties of Ureilitic Regolith from Samples of Almahata Sitta. In AAS/Division for Planetary Sciences Meeting Abstracts# 50 (pp. 100-08).

Hardersen, P. S., Gaffey, M. J., & Abell, P. A. (2005). Near-IR spectral evidence for the presence of iron-poor orthopyroxenes on the surfaces of six M-type asteroids. Icarus, 175(1), 141-158.

Hardersen, P. S., Cloutis, E. A., Reddy, V., Mothé-Diniz, T., & Emery, J. P. (2011). The M-/X-asteroid menagerie: Results of an NIR spectral survey of 45 main-belt asteroids. Meteoritics & Planetary Science, 46(12), 1910-1938.

Helbert, J., Maturilli, A., & D’Amore, M. (2013). Visible and near-infrared reflectance spectra of thermally processed synthetic sulfides as a potential analog for the hollow forming materials on Mercury. Earth and Planetary Science Letters, 369, 233-238.

Horgan, B. H., Cloutis, E. A., Mann, P., & Bell III, J. F. (2014). Near-infrared spectra of ferrous mineral mixtures and methods for their identification in planetary surface spectra. Icarus, 234, 132-154.

Hutchison, W. K., Bevan, A. W. R., Easton, A. J., & Agrell, S. O. (1981). Mineral chemistry and genetic relations among H-group chondrites. Proceedings of the Royal Society of London. A. Mathematical and Physical Sciences, 374(1757), 159-178.

Ivanova, M. A., Kononkova, N. N., Krot, A. N., Greenwood, R. C., Franchi, I. A., Verchovsky, A. B., et al. (2008). The Isheyevo meteorite: Mineralogy, petrology, bulk chemistry, oxygen, nitrogen, carbon isotopic compositions, and 40Ar-39Ar ages. Meteoritics & Planetary Science, 43(5), 915-940.

Izawa, M. R. M., King, P. L., Flemming, R. L., Peterson, R. C., & McCausland, P. J. A. (2010). Mineralogical and spectroscopic investigation of enstatite chondrites by X-ray diffraction and infrared reflectance spectroscopy. Journal of Geophysical Research: Planets, 115(E7).

Jarosewich, E. (1990). Chemical analyses of meteorites: A compilation of stony and iron meteorite analyses. Meteoritics, 25(4), 323-337.

Jenniskens, P., Betlem, H., Betlem, J., Barifaijo, E., Schlüter, T., Hampton, C., et al. (1994). The Mbale meteorite shower. Meteoritics, 29(2), 246-254.

Keil, K., & Fredriksson, K. (1963). Electron microprobe analysis of some rare minerals in the Norton County achondrite. Geochimica et Cosmochimica Acta, 27(9), 939-947.

Klima, R. L., Pieters, C. M., & Dyar, M. D. (2007). Spectroscopy of synthetic Mg-Fe pyroxenes I: Spin-allowed and spin-forbidden crystal field bands in the visible and near-infrared. Meteoritics & Planetary Science, 42(2), 235-253.

Koch, T. E., Brenker, F. E., Krot, A. N., & Bizzarro, M. (2016). Petrography of Quebrada Chimborazo 001—A New CBa Chondrite. In Lunar and Planetary Science Conference (No. 1903, p. 1968).

Krot, A. N., Ivanova, M. A., & Ulyanov, A. A. (2007). Chondrules in the CB/CH-like carbonaceous chondrite Isheyevo: Evidence for various chondrule-forming mechanisms and multiple chondrule generations. Geochemistry, 67(4), 283-300.

Landsman, Z. A., Emery, J. P., Campins, H., Hanuš, J., Lim, L. F., & Cruikshank, D. P. (2018). Asteroid (16) Psyche: Evidence for a silicate regolith from spitzer space telescope spectroscopy. Icarus, 304, 58-73.

Larson, W. J., & Wertz, J. R. (1992). Space mission analysis and design. Torrance, Calif: Microcosm.

Lauretta, D. S., Lodders, K., & Fegley, B. (1997). Experimental simulations of sulfide formation in the solar nebula. Science, 277(5324), 358-360.

Mason, B. (1963). Olivine composition in chondrites. Geochimica et Cosmochimica Acta, 27(10), 1011-1023.

Matter, A., Delbo, M., Carry, B., & Ligori, S. (2013). Evidence of a metal-rich surface for the Asteroid (16) Psyche from interferometric observations in the thermal infrared. Icarus, 226(1), 419-427.

McCoy, T. J., Keil, K., Bogard, D. D., Garrison, D. H., Casanova, I., Lindstrom, M. M., et al. (1995). Origin and history of impact-melt rocks of enstatite chondrite parentage. Geochimica et Cosmochimica Acta, 59(1), 161-175.

McSween Jr, H. Y., & Labotka, T. C. (1993). Oxidation during metamorphism of the ordinary chondrites. Geochimica et Cosmochimica Acta, 57(5), 1105-1114.

Mittlefehldt, D. W., McCoy, T. J., Goodrich, C. A., & Kracher, A. (2018). Non-chondritic meteorites from asteroidal bodies. Planetary materials, 523-718.

Moore, C. B., Lewis, C. F., & Clark, J. C. (1981). The Penwell Stony-Iron Meteorite. Meteoritics, 16, 361.

Moore, C. B., Lewis, C. F., & Clark, J. (1982). The Penwell Meteorite Revisited. Meteoritics, 17, 256.

Morris, M. A., Garvie, L. A., & Knauth, L. P. (2015). New insight into the solar system's transition disk phase provided by the metal-rich carbonaceous chondrite Isheyevo. The Astrophysical Journal Letters, 801(2), L22.

Nedelcu, D. A., Birlan, M., Vernazza, P., Descamps, P., Binzel, R. P., Colas, F., et al. (2007). Near infra-red spectroscopy of the asteroid 21 Lutetia-II. Rotationally resolved spectroscopy of the surface. Astronomy & Astrophysics, 470(3), 1157-1164.

Ockert-Bell, M. E., Clark, B. E., Shepard, M. K., Rivkin, A. S., Binzel, R. P., Thomas, C. A., et al. (2008). Observations of X/M asteroids across multiple wavelengths. Icarus, 195(1), 206-219.

Ockert-Bell, M. E., Clark, B. E., Shepard, M. K., Isaacs, R. A., Cloutis, E. A., Fornasier, S., & Bus, S. J. (2010). The composition of M-type asteroids: Synthesis of spectroscopic and radar observations. Icarus, 210(2), 674-692.

Olsen, E. J., Bunch, T. E., Jarosewich, E., Noonan, A. F., & Huss, G. I. (1977). Happy Canyon: A new type of enstatite achondrite. Meteoritics, 12(2), 109-124.

Pirard, E., Bernhardt, H. J., Catalina Hernández, J. C., Brea, C., Segundo, F., & Castroviejo Bolibar, R. (2008, December). From spectrophotometry to multispectral imaging of ore minerals in visible and near infrared (VNIR) microscopy. Australasian Institute of Mining and Metallurgy.

Powell, B. N. (1971). Petrology and chemistry of mesosiderites—II. Silicate textures and compositions and metal-silicate relationships. Geochimica et Cosmochimica Acta, 35(1), 5-34.

Reddy, V., Le Corre, L., O'Brien, D. P., Nathues, A., Cloutis, E. A., Durda, D. D., et al. (2012). Delivery of dark material to Vesta via carbonaceous chondritic impacts. Icarus, 221(2), 544-559.

Reid, A. M., Williams, R. J., & Takeda, H. (1974). Coexisting bronzite and clinobronzite and the thermal evolution of the Steinbach meteorite. Earth and Planetary Science Letters, 22(1), 67-74.

Rubin, A. E., & Scott, W. R. (1997). Abee and related EH chondrite impact-melt breccias. Geochimica et Cosmochimica Acta, 61(2), 425-435.

Rubin, A. E. (1997). Mineralogy of meteorite groups. Meteoritics & Planetary Science, 32(2), 231-247.

Rubin, A. E., & Ma, C. (2017). Meteoritic minerals and their origins. Geochemistry, 77(3), 325-385.

Russell, S. S., Zipfel, J., Folco, L., Jones, R., Grady, M. M., McCoy, T., & Grossman, J. N. (2003). The Meteoritical Bulletin, No. 87, 2003 July. Meteoritics & Planetary Science, 38(S7), A189-A248.

Ruzicka, A., Grossman, J., Bouvier, A., & Agee, C. B. (2017). The meteoritical bulletin, No. 103. Meteoritics & Planetary Science, 52(5), 1014.

Sanchez, J. A., Reddy, V., Shepard, M. K., Thomas, C., Cloutis, E. A., Takir, D., et al. (2016). Detection of rotational spectral variation on the M-type asteroid (16) Psyche. The Astronomical Journal, 153(1), 29.

Sarid, G., Stewart, S. T., & Leinhardt, Z. M. (2015). Erosive Hit-and-Run Impact Events: Debris Unbound. Proceedings of the International Astronomical Union, 10(S318), 9-15.

Schaudy, R., Watson, J. T., & Buchwald, V. F. (1972). The chemical classification of iron meteorites. VI. A reinvestigation of irons with Ge concentration lower than 1 ppm. Icarus, 17(1), 174-192.

Schrader, D. L., Davidson, J., & McCoy, T. J. (2016). Widespread evidence for high-temperature formation of pentlandite in chondrites. Geochimica et Cosmochimica Acta, 189, 359-376.

Scott, E. R. D., & Krot, A. N. (2003). Chondrites and their components. Treatise on geochemistry, 1, 711.

Scott, E. R., Haack, H., & McCoy, T. J. (1996). Core crystallization and silicate-metal mixing in the parent body of the IVA iron and stony-iron meteorites. Geochimica et Cosmochimica Acta, 60(9), 1615-1631.

Shepard, M. K., Clark, B. E., Ockert-Bell, M., Nolan, M. C., Howell, E. S., Magri, C., et al. (2010). A radar survey of M-and X-class asteroids II. Summary and synthesis. Icarus, 208(1), 221-237.

Shepard, M. K., de Kleer, K., Cambioni, S., Taylor, P. A., Virkki, A. K., Rívera-Valentin, E. G., et al. (2021). Asteroid 16 Psyche: Shape, Features, and Global Map. The Planetary Science Journal, 2(4), 125.

Siltala, L., & Granvik, M. (2021). Mass and Density of Asteroid (16) Psyche. The Astrophysical Journal Letters, 909(1), L14.

Takir, D., Reddy, V., Sanchez, J. A., Shepard, M. K., & Emery, J. P. (2016). Detection of water and/or hydroxyl on asteroid (16) Psyche. The Astronomical Journal, 153(1), 31.

Ulff-MØller, F. (1998). Effects of liquid immiscibility on trace element fractionation in magmatic iron meteorites: A case study of group IIIAB. Meteoritics & Planetary Science, 33(2), 207-220.

Ulff-Møller, F., Choi, B. G., Rubin, A. E., Tran, J., & Wasson, J. T. (1998). Paucity of sulfide in a large slab of Esquel: New perspectives on pallasite formation. Meteoritics & Planetary Science, 33(2), 221-227.

Urey, H. C., & Craig, H. (1953). The composition of the stone meteorites and the origin of the meteorites. Geochimica et Cosmochimica Acta, 4(1-2), 36-82.

Varatharajan, I., Maturilli, A., Helbert, J., Alemanno, G., & Hiesinger, H. (2019). Spectral behavior of sulfides in simulated daytime surface conditions of Mercury: Supporting past (MESSENGER) and future missions (BepiColombo). Earth and Planetary Science Letters, 520, 127-140.

Vernazza, P., Lamy, P., Groussin, O., Hiroi, T., Jorda, L., King, P. L., et al. (2011). Asteroid (21) Lutetia as a remnant of Earth's precursor planetesimals. Icarus, 216(2), 650-659.

Viikinkoski, M., Vernazza, P., Hanuš, J., Le Coroller, H., Tazhenova, K., Carry, B., et al. (2018). (16) Psyche: A mesosiderite-like asteroid?. Astronomy & Astrophysics, 619, L3.

Watters, T. R., & Prinz, M. (1979). Aubrites-Their origin and relationship to enstatite chondrites. In Proceedings of the 10th Lunar and Planetary Science Conference.

Weisberg, M. K., Bunch, T. E., Wittke, J. H., Rumble III, D., & Ebel, D. S. (2012). Petrology and oxygen isotopes of NWA 5492, a new metal-rich chondrite. Meteoritics & Planetary Science, 47(3), 363-373.

Wood, B. J., & Strens, R. G. J. (1979). Diffuse reflectance spectra and optical properties of some sulphides and related minerals. Mineralogical Magazine, 43(328), 509-518.

Zellner, B., Tholen, D. J., & Tedesco, E. F. (1985). The eight-color asteroid survey: Results for 589 minor planets. Icarus, 61(3), 355-416.

Zipfel, J., Wlotzka, F., & Spettel, B. (1998). Bulk chemistry and mineralogy of a new" unique" metal-rich chondritic breccia, Hammadah al Hamra 237. In Lunar and Planetary Science Conference (No. 1417, p. 1417).

CHAPTER 4

EVALUATION OF A BENCHTOP COMMERCIAL-OFF-THE-SHELF VERSION OF THE NASA PSYCHE MISSION'S MULTISPECTRAL IMAGER

Steven Dibb[a*], Andrew Winhold[a], James F. Bell III[a], and David A. Williams[a],

[a]Arizona State University, School of Earth and Space Exploration, 781 Terrace Road, Tempe, AZ, USA, 85281

Citation: Dibb, S., Winhold, A., Bell, III, J. F., and Williams, D. A. Evaluation of a Benchtop Commercial-Off-the-Shelf Version of the NASA Psyche Mission's Multispectral Imager. Submitted to *SPIE Journal of Electronic Imaging.*

Abstract

A comprehensive characterization of a commercial-off-the-shelf (COTS) version of the Psyche Multispectral Imager is presented. The 'COTS Imager' system was designed to mimic system-level properties of the flight Imager system and provide a testbed for developing procedures to be used in the eventual calibration and operation of the flight Imager. The COTS Imager system contains the same detector (a 1600x1200 monochrome KAI-2020 CCD), a commercial lens with a similar f-number, commercially available readout electronics, and can be equipped with flight-like filters. At both ambient and the expected in-flight temperature (~5°C), we measure the COTS Imager's read noise, gain, and full well, and demonstrate linearity with exposure time. Furthermore, we provide an assessment of the dark current and number of bad pixels of the detector at

5°C. We report the quantum efficiency and modulation transfer function of the COTS Imager at ambient conditions. Finally, we compare results of a radiometric model used to simulate COTS Imager performance to data measured with the system. This study demonstrates that low-cost, commercial hardware can be used to replicate some of the performance of higher-fidelity flight hardware and serve as an effective testbed for developing software and procedures intended for calibration of the flight Imagers.

4.1 Introduction

The NASA Psyche mission will explore the solar system's largest M-type asteroid, (16) Psyche, beginning in 2026[1]. The spacecraft will carry a set of instruments designed to make key measurements of the asteroid's composition and physical characteristics designed to test hypotheses of its origin. One of these instruments is a multispectral imaging system, the Psyche Multispectral Imager (henceforth called the "Imager")[2]. The Imager is composed of two identical camera heads and electronics boards and leverages high heritage from the Mars Science Laboratory Mastcam and Mars 2020 Mastcam-Z systems[3,4].

Early in the Imager's development, a benchtop version of the Imager was assembled from commercial-off-the-shelf (COTS) camera equipment to enable laboratory testing of expected Imager performance and develop software, documents, and procedures for the calibration of the flight Imagers. The "COTS Imager" is designed to have similar characteristics to the flight Imager design, including the same model of CCD and similar optical properties (Table 4.1). While the flight Psyche Multispectral Imager

Table 4.1 Properties of Psyche Multispectral Imager and COTS Imager

Property	Psyche Multispectral Imager	COTS Imager
Sensor	Monochromatic ON-Semi KAI-2020 interline transfer CCD with microlenses	Monochromatic ON-Semi KAI-2020 interline transfer CCD with microlenses
Bandpass	1 broadband (540±140 nm) filter, 7 narrowband filters from 437 to 1041 nm	Unfiltered ~300-1100 nm, but can be equipped with single filters
F-number	2.9	2.8
Focal length	148 mm	150 mm
Field of view (FOV)	4.6° x 3.4°	4.52° x 3.39°
Instantaneous FOV	0.05 mrad	0.05 mrad
Active pixels	1600 x 1200, 7.4 μm pixels	1600 x 1200, 7.4 μm pixels
Bit depth	Commandable	8-bit, 12-bit
Focus	Fixed focused at infinity	Manual

makes use of a 9-position filter wheel to provide broadband, multispectral, and sun-blocking capability, the default COTS Imager configuration is unfiltered and sensitive to roughly the entire sensor quantum efficiency range (~300-1100 nm). To evaluate estimated signal-to-noise ratio through each filter from radiometric modeling, we used a 3D-printed filter holder to hold engineering test article filters from the same lot as the flight filters. All other testing with the COTS Imager was performed without filters in the optical path. Both the COTS Imager and the flight Imager use an OnSemi KAI-2020 monochrome CCD composed of a 1648x1200 array of microlensed 7.4 μm pixels.

We report results of several characteristics used to evaluate the COTS Imager in the context of instrument level requirements for the Psyche Multispectral Imager (Table 4.2). These characteristics are read noise, gain, full well, linearity, dark current, the number of bad pixels, quantum efficiency, and modulation transfer function (MTF). Finally, we report results of a radiometric model of Imager performance during nominal Psyche mission operations compared to results from the COTS Imager at similar conditions recreated in a laboratory setting. Our results demonstrate that low-cost commercial-off-the-shelf hardware can approach required mission-level performance and

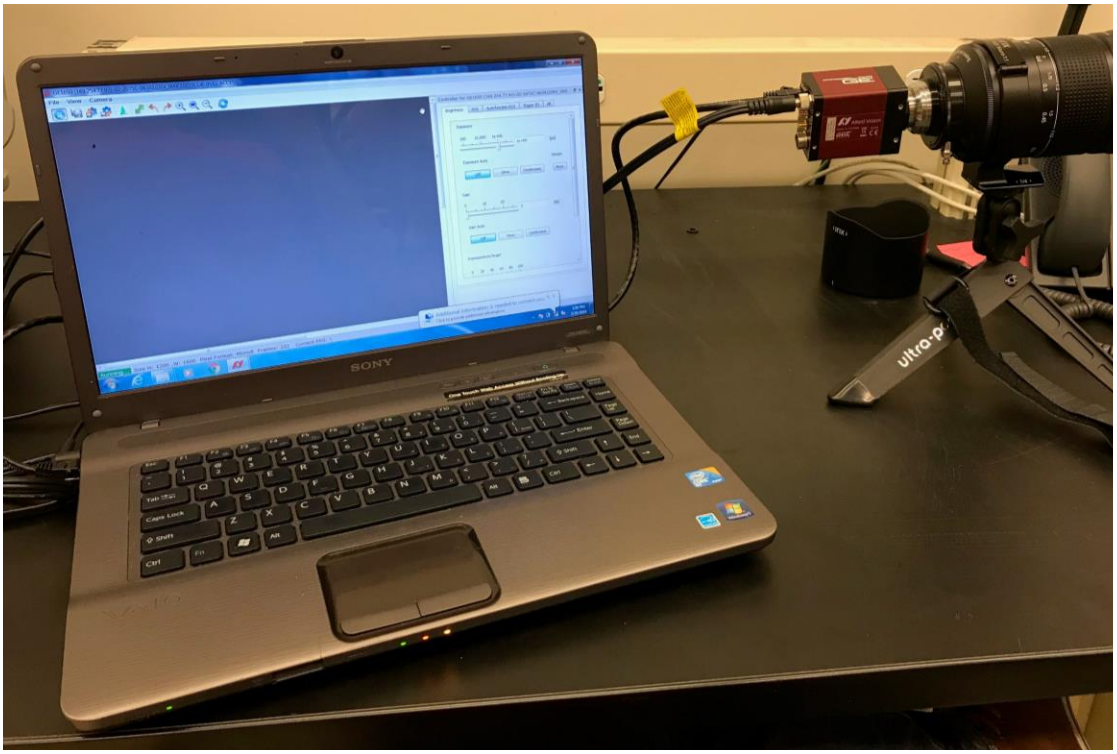

Fig. 4.1 The Psyche COTS Imager System.

therefore provides an effective low-cost testbed for developing calibration procedures for the flight system.

4.1.1 Acquisition and operation of the COTS Imager system

The COTS Imager system consists of three main components: an Allied Vision ProSilica GE-1650 camera body (in which the KAI-2020 sensor and commercial readout electronics are housed), an Irix 150 mm f/2.8 macro lens, and a Sony VAIO laptop for commanding the system (Figure 4.1). The camera body and lens are mated with a Nikon F to C mount adapter. The camera body is connected to the laptop via a standard Cat5 ethernet cable. The COTS Imager is commanded through Allied Vision's Vimba Viewer software and by modified C scripts for automated image capture. The entire system

Table 4.2 Requirements of the flight Psyche Multispectral Imager and performance by COTS Imager

Property	Flight Imager Requirement	COTS Imager Performance
Read noise (e-)	≤20	22 (ambient), 24 (5 °C)
Dark current (e-/s)	≤2500	301.6 (5 °C)
Gain (e-/DN)	N/A	77.39 (ambient), 74.47 (5 °C)
Full well (e-)	N/A	19401.7 (ambient), 18803.7 (5 °C)
Linearity	Linear up to 80% full well	Linear up to 95% full well
# of 'bad' pixels	N/A	16
MTF	≥0.2 at Nyquist frequency (67.6 lp/mm) through broadband filter (540±140 nm)	0.2 at 32.9 lp/mm over full CCD QE range (~300-1100 nm)
Signal-to-noise ratio	≥50:1	>30:1 (from Photon Transfer)

requires two standard 120V electrical outlets to operate. For filter-specific tests (i.e., validating the radiometric model), we used a series of thread adaptors and a custom 3D-printed filter holder manufactured at Arizona State University.

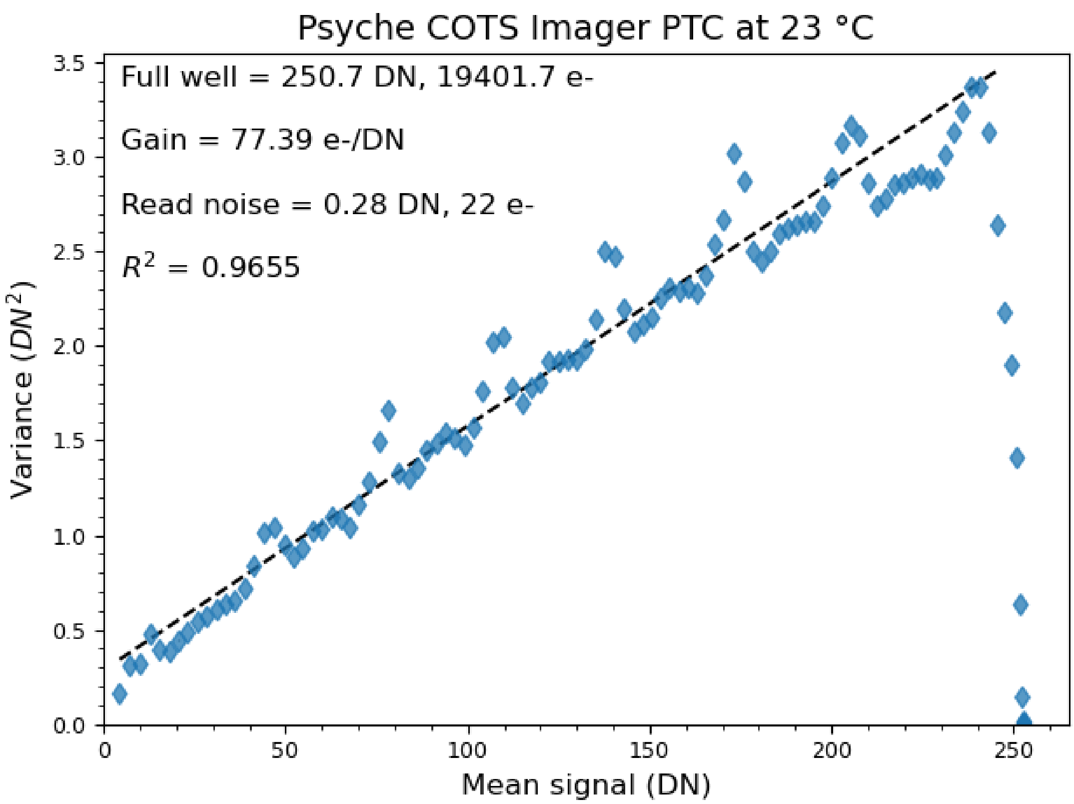

Fig. 4.2 Photon Transfer Curve for the Psyche COTS Imager at ambient (~23°C). Uncertainty on both mean signal and variance is smaller than the size of plot markers.

4.2 Photon Transfer Testing

Photon transfer (PT) is a widespread testing methodology for quantifying the signal-to-noise performance and responsivity characteristics of a camera system and its detector[5,6]. The primary purpose of PT testing is to translate the signal measured by a camera system from relative units (i.e., DN values) to absolute units (i.e., electrons, e-) such that requirements can be physically validated. One of the primary products of PT testing is the conversion between these units, often referred to as the gain, sensitivity, or scale factor (in e-/DN) of the detector[5,6].

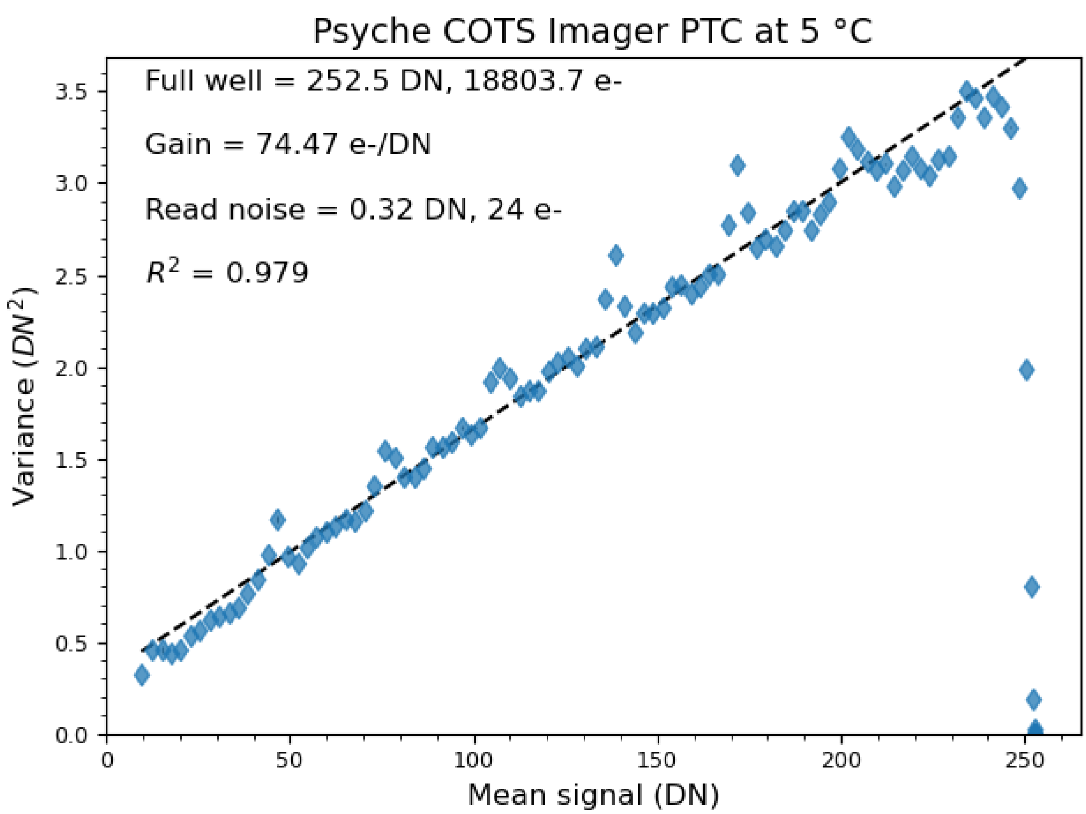

Fig. 4.3 Photon Transfer Curve for the Psyche COTS Imager at ambient (~5°C). Uncertainty on both mean signal and variance is smaller than the size of plot markers.

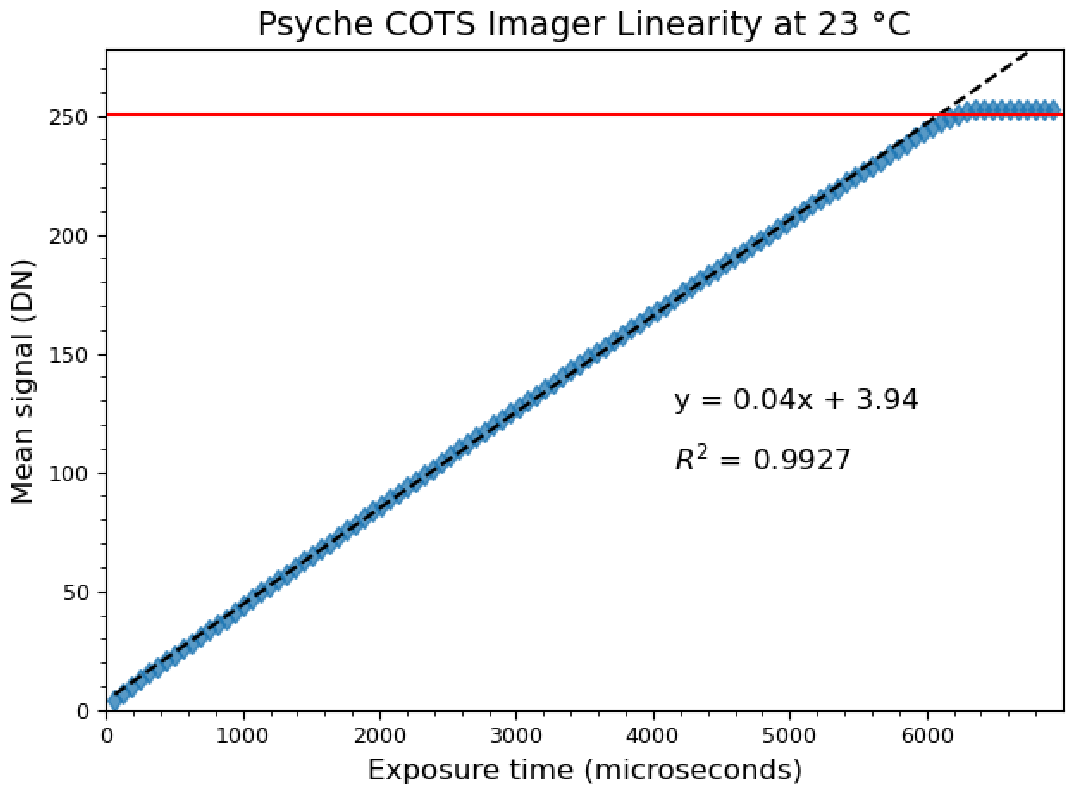

Fig. 4.4 Linearity of the Psyche COTS Imager at ambient (~23°C). A solid red line indicates the full well value from PT testing. Uncertainty on mean signal is smaller than the size of plot markers.

To perform PT testing at a single temperature, two datasets are required: a series of uniformly illuminated images at a known set of exposure times of a calibrated light source, and a series of images at the same exposure times but not exposed to light[5,6]. Our light source for PT testing is a LabSphere CSTM-USS-1200C 12-inch diameter integrating sphere equipped with a QTH lamp, NIST-calibrated Si and InGaAs radiometers, and an adjustable shutter. For all PT testing, we set the radiance of the integrating sphere to 0.167 mW/cm2-sr over the 300-1100 nm wavelength range. This radiance is an estimate of the radiance of asteroid (16) Psyche viewed at a 70° incidence angle during the spacecraft's Orbit B operations (approximately 290 km altitude and 2.81 AU solar distance)[1]. We acquired PT datasets at two temperatures: ambient (~23°C) and

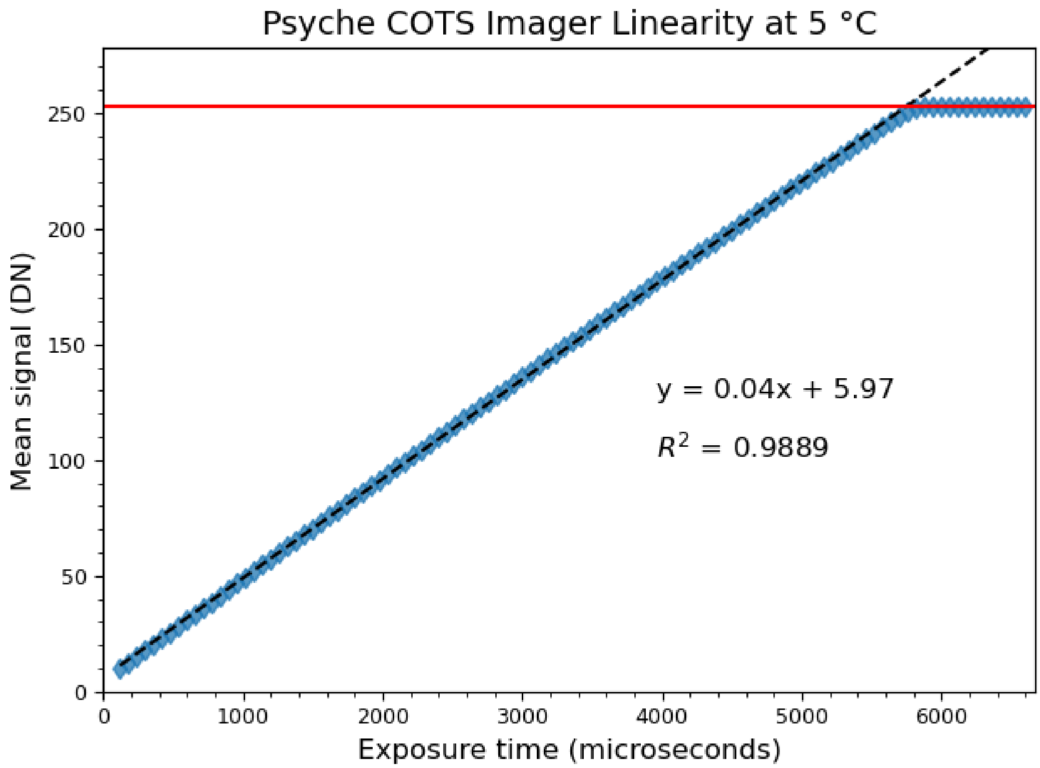

Fig. 4.5 Linearity of the Psyche COTS Imager at ambient (~23 °C). A solid red line indicates the full well value from PT testing. Uncertainty on mean signal is smaller than the size of plot markers.

5°C, which is the predicted nominal in-flight temperature of the Psyche Imager. Temperature control for the COTS Imager was provided using a Peltier thermoelectric cooler sandwiched between the camera body and a dry ice heat sink. The internal temperature of the camera was monitored using a platinum-resistance thermometer adhered to the internal camera board holding the KAI-2020 CCD. To determine the exposure times of our PT datasets, we visually-estimated the exposure time that saturated images in the Vimba Viewer software (~6.5 ms). We then captured 20 images at every 1% interval in exposure time from 1% up to 110% of the visually estimated saturation time with the COTS Imager pointed into the output port of the integrating sphere. Fig. 4.2 shows the PT curve for the COTS Imager at ambient temperature (~23°C). The full well is assumed to be the mean of the mean signal values from 95-105% of visually estimated full well (250.7 DN, 19401.7 e-). We then fit a line to the first 85% of the mean signal values and used the inverse of the slope as the gain (77.39 e-/DN) and the y-intercept as the read noise (0.28 DN, 22 e-). These values are consistent with manufacturer specifications for the KAI-2020 CCD (full well = 20,000 e-, readnoise = 20 e-)[7]. Fig. 4.3 shows the PT curve for the COTS Imager at expected in-flight temperature of the flight Imager (~5°C). The same procedure was used to generate estimates for the full well, gain, and read noise as at ambient temperatures. At 5°C, we measured the full well as 252.5 DN (18803.7 e-), the gain as 74.47 e-/DN, and the read noise as 0.32 DN (24 e-). The minimum signal-to-noise ratio (taken as the ratio between the variance and signal) from our PT testing is ~30.

In both PT curves, a periodic feature is present. In the ~23°C data, the peaks are at roughly 12.5, 45.5, 78.5, 108.4, 138.8, 173.2, 205.1, and 238.4. In the 5°C data, the peaks are at roughly 12.5, 46.7, 75.6, 107.1, 138.4, 171.8, 202.0, and 234.0. The separation of the peaks by ~32 DN indicates that the source of the noise may be an ADC bit quantization error[5]. This feature is likely unique to the electronics of the COTS Imager and is not expected in the flight Imager as past instruments using the KAI-2020 CCD have not measured this phenomenon[3,8]. Figs. 4.4 and 4.5 show the mean signal from the 20 images captured at each exposure time as a function of exposure time. A line fit to the mean signal values up to 95% of the full well signal value (as derived from PT testing) demonstrates the linear response of the COTS Imager at ambient (R2 = 0.9927) and 5°C (R2 = 0.9889).

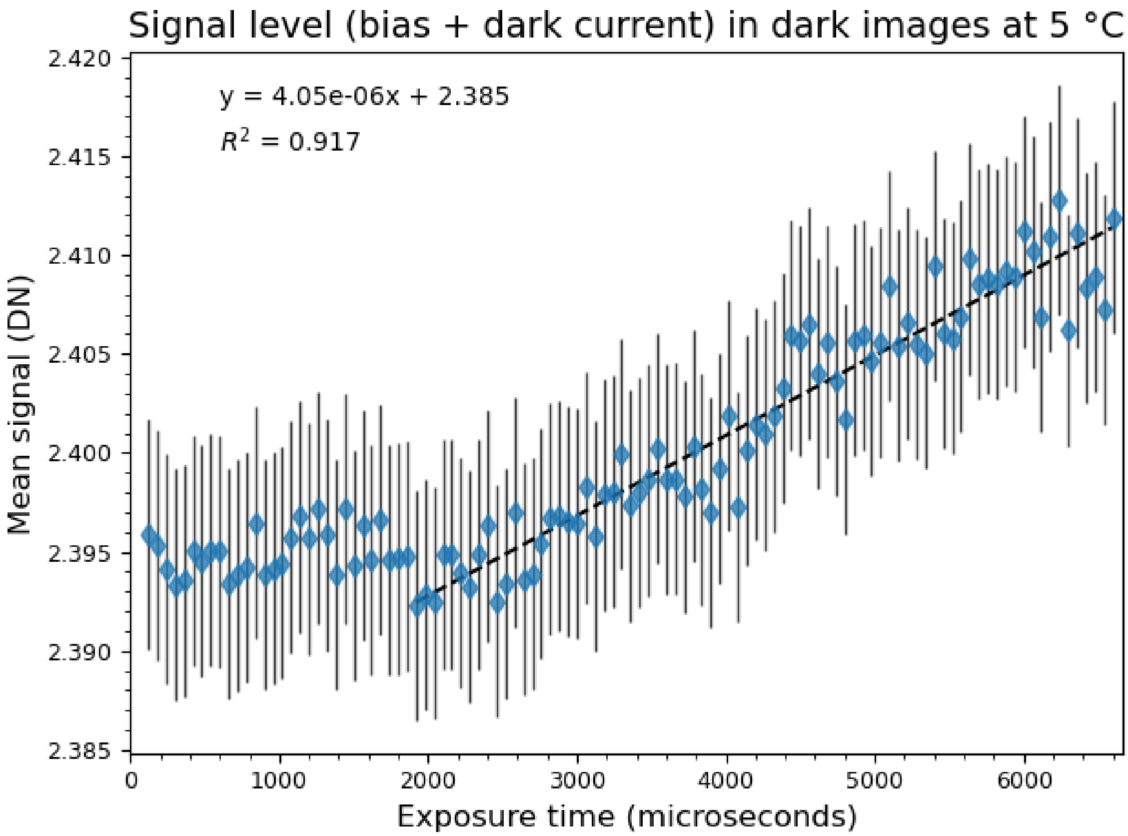

Fig. 4.6 Dark images at 5°C exhibit increasing linearly increasing mean signal at exposure times >2000 microseconds.

4.3 Dark Current and 'Bad' Pixel Assessment

Two sources of noise are present in images from the COTS Imager but are not actually related to scene illumination. The first is 'dark current', which refers to signal generated from electron-hole pairs induced by random thermal motion of atoms in the silicon lattice[9]. The rate of dark current generated is strongly dependent on the temperature of the detector and is generated even when the detector is not illuminated. Fig. 4.6 shows the mean signal from dark images acquired at ~5°C as a function of exposure time. An increase in the mean signal is evident beginning at around 2000 microseconds. The slope of the best fit line to the data at >2000 microseconds is 4.05 x

10^{-6} DN/microsecond, or 301.6 e-/s. This value for dark current rate is ~10x higher than manufacturer specifications for the KAI-2020 CCD alone and previous flight instruments using this detector at this temperature, which may be due to electronic noise in the COTS Imager system[3,7,8]. However, this value is still well below the flight Imager requirement (<2500 e-/s). No clear increase in signal with exposure time for dark images at ambient temperatures was observed.

Table 4.3 Bad pixels on the Psyche COTS Imager CCD

Pixel location (row, col)[a]	**Type**[b]
(160, 1125)	Gray
(370, 1590)	Gray
(413, 251)	Gray
(618, 1111)	Gray
(619, 469)	Gray
(1104, 929)	Gray, likely dust
(1153, 1205)	Gray, likely dust
(1195, 1378)	Gray, likely dust
(29, 906)	Hot
(148, 1301)	Hot
(205, 1428)	Hot
(312, 691)	Hot
(350, 926)	Hot
(613, 1309)	Hot
(970, 246)	Hot
(1008, 826)	Hot

a – The upper left corner of the CCD is (0,0).

b – See text for disussion.

The second set of sources of apparent signal (or lack thereof) are ‘bad’ pixels. These pixels are defined by those that are ‘gray’ (unresponsive or less responsive relative to their neighbors) and those that are ‘hot’ (those that are more responsive or saturated relative to their neighbors). Hot pixels are typically caused by manufacturing defects and are usually limited to single pixels. Gray pixels can also be caused by manufacturing defects, but often are caused by dust or other particulate matter on the detector surface, which can prevent or decrease light incident on a single pixel or a cluster of pixels. We located bad pixels using images from the photon transfer dataset at ambient temperature. First, we generated a mean image from the 20 images taken of the light source at ~50% full well (corresponding to an exposure time of 3024 microseconds). We then located pixels in the mean image with DN values that were greater than 4x the standard deviation above the median DN value for the entire image (Table 4.3). We then repeated the analysis for a mean image generated from the dark images at the same exposure time.

4.4 Quantum Efficiency

Quantum efficiency (QE) refers to the number of electrons generated on the CCD per incident photon at a specific wavelength. A QE of 1.0 at a certain wavelength means all photons of that wavelength are converted to electrons and measured. To compare the spectral response of the COTS Imager to the manufacturer’s specifications and eventual data from the flight Imagers, we captured images of the output of an Oriel C260 monochromator from 300-1100 nm at 10 nm intervals. This instrument uses a quartz-tungsten-halogen lamp as a light source and is equipped with a C mount adapter to which

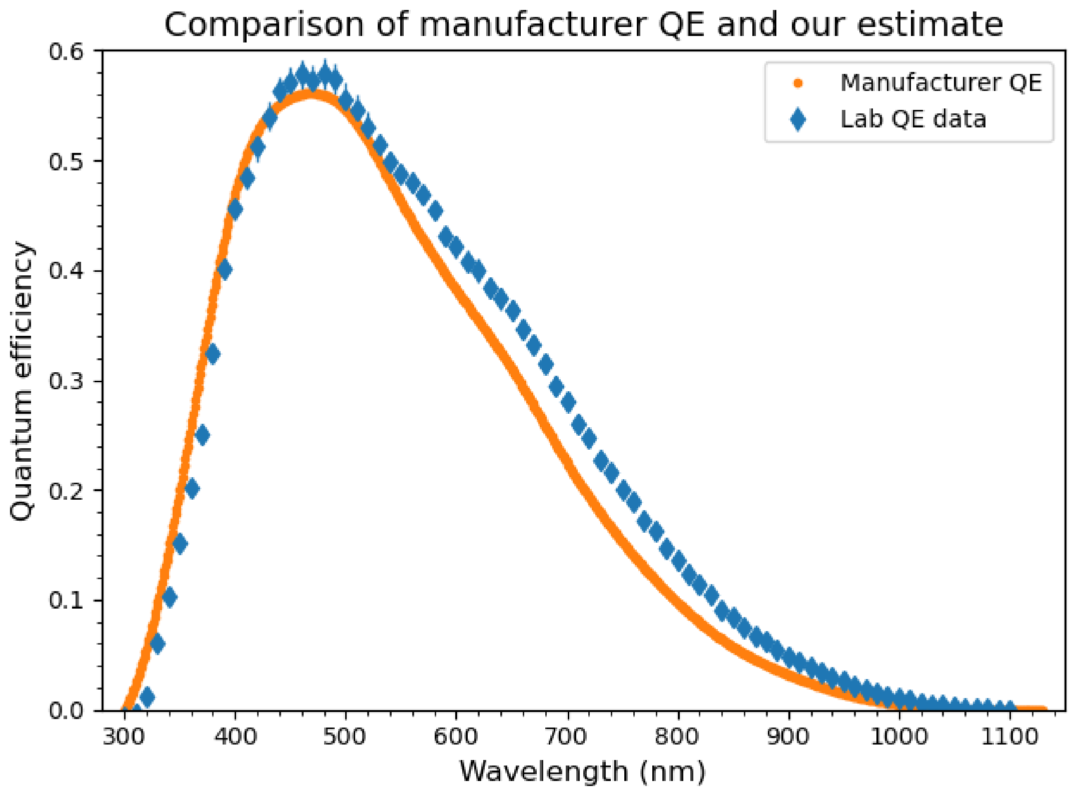

Fig. 4.7 Quantum efficiency of the COTS Imager with no lens attached. The uncertainty on the manufacturer data is +/- 0.1. For most values, uncertainty is smaller than the size of plot markers.

the COTS Imager mounts directly, without the Irix lens. We computed quantum efficiency using Equation 2.4 from Ref. 5:

$$QE(\lambda) = \frac{12{,}390 R_e(\lambda) A_D S(\lambda) K_{ADC}}{P_A S_D(\lambda) t_i \lambda} \quad (1)$$

where $R_e(\lambda)$ is the responsivity (in A/W) of a calibrated photodiode at wavelength λ, A_D is the active area of the photodiode, K_{ADC} is the gain of the CCD (in e-/DN), P_A is the active area of a pixel, $S_D(\lambda)$ is the signal from the photodiode at wavelength λ, t_i is the exposure time (2 ms), and $S(\lambda)$ is the mean of the central 200x200 pixels from 5 images captured at wavelength λ. The photodiode we used was a Newport 818-UV/DB silicon photodetector. Fig. 4.7 shows the quantum efficiency of the COTS Imager compared to the manufacturer specification[7]. In general, there is good agreement between our measured

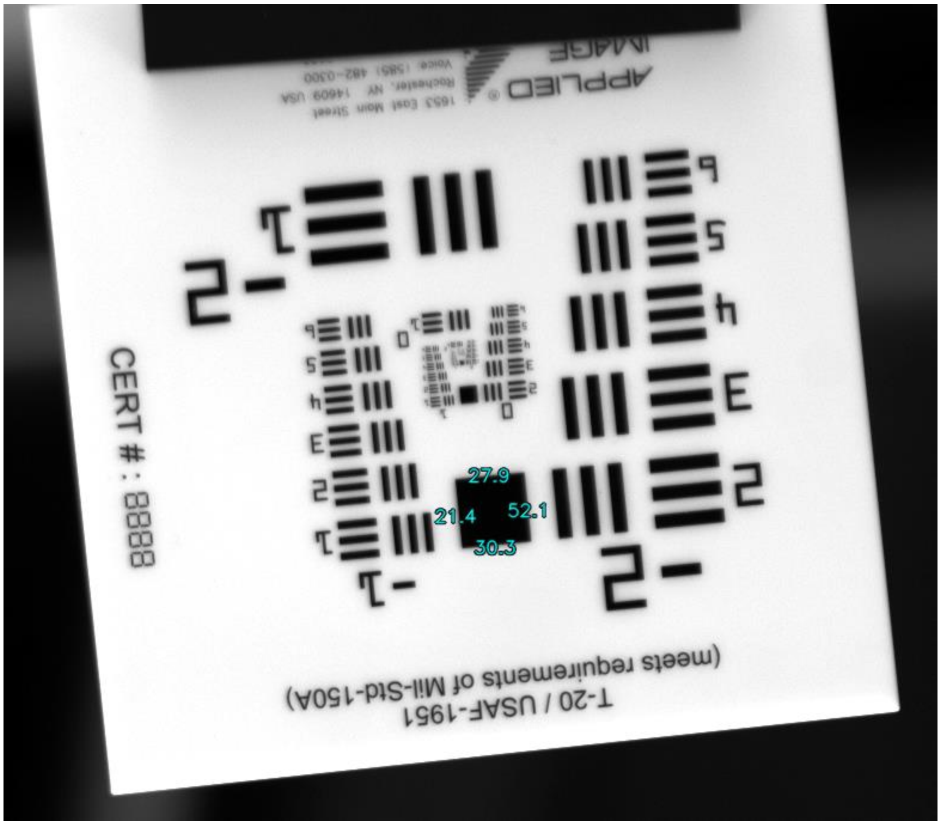

Fig. 4.8 Image of USAF-1951 target used to measure MTF with the COTS Imager. Cyan numbers on the edges of the largest target square indicate the spatial frequency at which MTF20 is reached.

QE and the manufacturer specification. A difference of ~0.05 at wavelengths greater than ~550 nm is within the +/- 0.1 variation expected[7].

4.5 Modulation Transfer Function

The modulation transfer function (MTF) of an imaging system quantifies the ability of the system to measure spatial variation in contrast and is one component of the system's spatial resolution[10,11]. We measure the system-level MTF by capturing 10 ms images of a USAF-1951 Resolution Target tilted at ~12° and under ambient environmental conditions (Fig. 4.8). We use the open-source software MTF Mapper to generate estimates of the system-level MTF, which has been used to evaluate MTF for

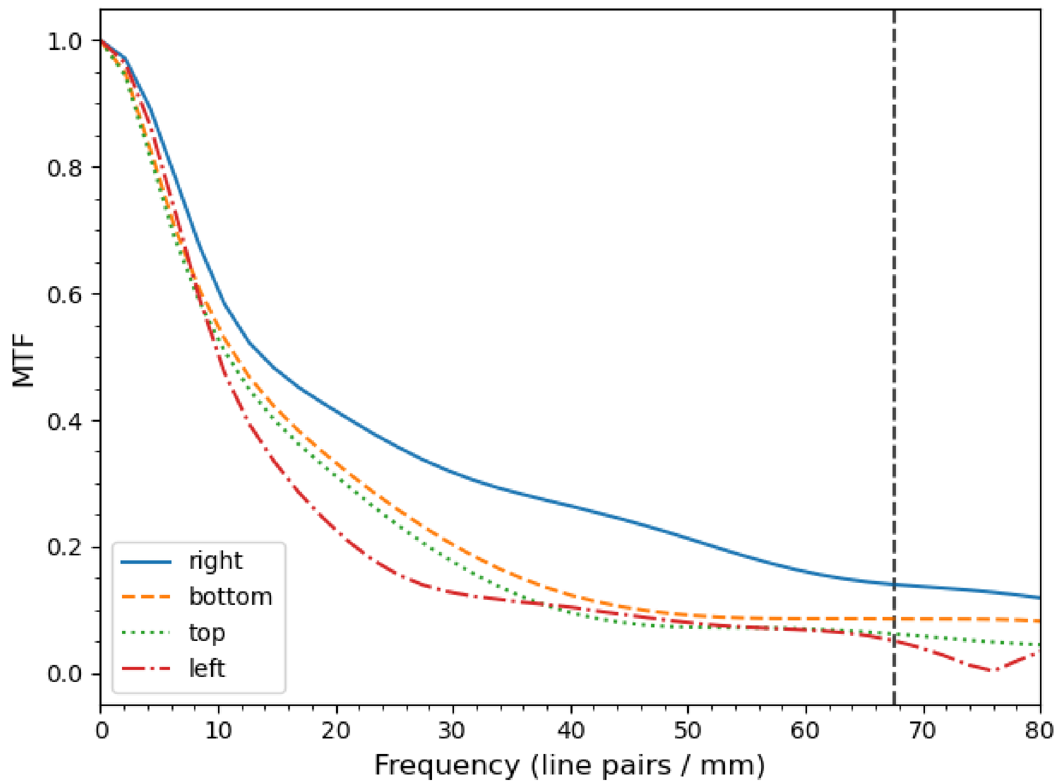

Fig. 4.9 MTF curves from the 4 edges identified in our test image and shown in Fig. 8. The vertical black dashed line indicates the Nyquist frequency (67.6 lp/mm)

flight instruments like the Psyche Imager[8]. MTF Mapper identifies the slant edges present in an image, the number of pixels present across the slant, and calculates the MTF curve for each edge with sufficient pixels using the edge step function method similar to ISO 12233. To recreate the focal distance of the flight Imager, we acquired the images of the target with the Irix lens focused to approximately infinity, which required the target to be >3.4 m away from the COTS Imager. Because the COTS Imager is manually focused, we took 10 images of the target while incrementally adjusting the focus ring and then used the best-focused image with MTF Mapper. Cyan numbers on certain edges of the target present in Fig. 4.8 indicate the spatial frequency (in lp/mm) at which an MTF of 0.2 is achieved (called MTF20). Because of the distance to the target, only 4 edges are detected by MTF Mapper as having sufficient pixels to reliably measure MTF. The average MTF20 frequency is 32.9 lp/mm. Fig. 4.9 shows the MTF curve for the four sides of the square identified in Fig. 4.8. The closest MTF value to the requirement is ~0.13 at the Nyquist frequency.

There are several properties of the COTS Imager system that could result in MTF values at the Nyquist frequency lower than the flight Imager requirement. The first, and perhaps most obvious, is that a commercial lens is likely of lower material and alignment quality than custom spaceflight hardware. Second, because the COTS Imager system uses a manual focus ring, it is possible that the images collected for MTF assessment were near the best focus but not truly at the best possible setting. Thirdly because the COTS Imager system and USAF-1951 target were deployed on separate optical air tables due to the required infinity focus, it is possible that ambient vibration in our laboratory resulted in slight blurring of the images.

4.6 Radiometric Modeling of Imager Performance

We developed a radiometric model using equations from Table 9-15 in Ref. 12 to simulate Imager performance under different lighting and orbital conditions that will be experienced in-flight. This model ingests user-defined camera properties and mission parameters to estimate the signal (in number of electrons) generated by the Imager CCDs through each filter using the following equation:

$$S(e^-) = \frac{T_o L_{px}^2 t_i \pi}{4 t_\#^2} * \int_{\lambda_1}^{\lambda_2} \frac{R(\lambda) QE(\lambda) T_f(\lambda)}{E(\lambda)} d\lambda \tag{2}$$

where T_o is the transmission of the optics (assumed 0.9 across the entire 300-1100 nm range), L_{px} is the dimension of one of the KAI-2020 pixels, t_i is the integration time (in seconds), $t_{\#}$ is the t-number of the system, $R(\lambda)$ is the radiance of the target (e.g., asteroid (16) Psyche or our integrating sphere) at wavelength λ, $QE(\lambda)$ is the quantum efficiency of the CCD at wavelength λ, $T_f(\lambda)$ is the wavelength-dependent transmission of the filter, and $E(\lambda)$ is the energy of a photon at wavelength λ.

Table 4.4 Predicted and measured exposure times to reach full well.

Filter	Center (nm)	FWHM (nm)	Predicted (ms)	Measured (ms)
1	540	280	12	13.2
2	437	50	195	275
3	495	25	205	212
4	550	25	110	135
5	725	40	76	73.5
6	850	50	160	178
7	948	50	550	940
8	1041	90	2500	2820
no filter	--	--	7	6.3

We use our measurements of full well from PT testing to validate the radiometric model and demonstrate confidence in the model's results for flight-like scenarios. In addition to validating the radiometric model for the unfiltered COTS Imager, we used Newport LT10-CMT-X, LT10-CMT-N, and LT10-05 thread adapters and a 3D-printed filter holder to collect images through engineering spare filters for the flight Imagers. We collected the images with the COTS Imager pointed towards our integrating sphere set to a radiance of 0.167 mW/cm2-sr. The Allied Vision Vimba Viewer software can display a histogram of image DN values in real time as the exposure time is varied. We collected a series of images using each filter such that the mean DN value in the image was approximately equal to the full well value measured in our PT testing (~251 DN). Table 4.4 shows the exposure time predicted by the radiometric model required to produce an image with a mean signal approximately equal to the full well value for each of the filters versus the measured time from actual images using the COTS Imager. The differences for the shortest and longest wavelength filters (Filters 2, 7, and 8) are likely caused by differences in the assumed and actual transmission of the COTS lens (i.e., the COTS lens is likely less transmissive at UV and near-IR wavelengths than the model assumes). Unfortunately, no transmission data is available from the manufacturer.

4.7 Conclusions

A commercial-off-the-shelf version of the Psyche Multispectral Imager has been developed to validate instrument requirement and develop procedures for the calibration of the flight instrument. The COTS Imager shares the same model CCD detector as the flight Imager and uses an Irix lens with a similar f-number. Photon transfer testing was performed to characterize the COTS Imager’s read noise, gain, full well, linearity, dark current, and assess the number of bad pixels. The quantum efficiency of the KAI-2020 sensor in the COTS Imager was measured and the system-level MTF of the COTS Imager was measured. Aside from MTF, the characteristics of the COTS Imager are consistent with manufacturer specifications, similar flight instruments on past missions, and/or meet the requirements for the flight Imager. Finally, a radiometric model useful for predicting the performance of the Imager in flight was validated using the COTS Imager. Our results indicate that the COTS Imager serves as an effective testbed for procedures and software intended for use with the Psyche Multispectral Imager.

Acknowledgements and Funding Sources

This study was funded by National Aeronautics and Space Administration Grant NNM16AA09C.

Code, Data, and Materials Availability

Data used in this study are available at the Open Science Framework repository DOI 10.17605/OSF.IO/VBPY5.

References

1. Elkins-Tanton, L. T., et al. "Observations, meteorites, and models: a preflight assessment of the composition and formation of (16) Psyche." Journal of Geophysical Research: Planets 125.3 (2020): e2019JE006296.

2. Bell III, J. F., et al. "The Psyche multispectral imager investigation: Characterizing the geology, topography, and compositional properties of a metallic world." Lunar and Planetary Science Conference p. 1366 (2016).

3. Bell III, J. F., et al. "The Mars Science Laboratory Curiosity rover Mastcam instruments: Preflight and in-flight calibration, validation, and data archiving." Earth and Space Science 4.7 (2017): 396-452.

4. Bell III, J. F., et al. "The Mars 2020 perseverance rover mast camera zoom (Mastcam-Z) multispectral, stereoscopic imaging investigation." Space Science Reviews 217.1 (2021): 1-40.

5. Janesick, J. R. "Photon Transfer - DN -> λ". 1st ed., SPIE (2007), doi:10.1117/3.725073.

6. Janesick, James, Kenneth Klaasen, and Tom Elliott. "CCD Charge Collection Efficiency and the photon transfer technique." Society of Photo-Optical Instrumentation Engineers (SPIE) Conference Series. Vol. 726 (1987).

7. ON Semiconductor, "KAI-2020 1600 (H) x 1200 (V) Interline CCD Image Sensor". Dec. 2015, www.onsemi.com/pdf/datasheet/kai-2020-d.pdf.

8. Hayes, A. G., et al. "Pre-flight calibration of the Mars 2020 Rover Mastcam Zoom (Mastcam-Z) multispectral, stereoscopic imager." Space Science Reviews 217.2 (2021): 1-95.

9. McLean, I. S. "Electronic Imaging in Astronomy: Detectors and Instrumentation". 2nd ed., Springer Berlin Heidelberg, (2008) doi:10.1007/978-3-540-76583-7.

10. Smith, W. J. "Modern Optical Engineering: The Design of Optical Systems". 3rd ed., McGraw Hill, (2000).

11. Boreman, G. D. "Modulation transfer function in optical and electro-optical systems". Vol. 4. Bellingham, WA: SPIE press (2001).

12. Wertz, J. R., and W. J. Larson. "Space mission analysis and design", Microcosm. Inc., (1999).

CHAPTER 5

CONCLUSIONS AND FUTURE WORK

The work presented in this dissertation has made a small contribution to our understanding of the surface compositions of some types of asteroids. These types of asteroids, which I have label "spectrally featureless" due to their lack of obvious absorption features, are the subject of much study as they may be remnant core materials. They are the subject of multiple space missions either currently in flight or in development.

In Chapter 1, I provided an overview of the Psyche Mission and gave a short discussion on the causes of absorption features in minerals. In Chapter 2, I presented visible-to-near infrared reflectance spectra of some meteorites and minerals with "featureless" spectra and compared them to asteroids with similarly "featureless" spectra. Some of the meteorite spectra are consistent with some types of asteroids (e.g., the aubrites and the Xe-type asteroids, the metal-rich chondrites and the X-complex asteroids) while other minerals do not strongly match a single asteroid type (e.g., the sulfides).

In Chapter 3, I presented a large spectral library that I used to provide a pre-flight assessment of the surface composition of asteroid (16) Psyche, the target of the NASA Psyche Mission. This assessment is consistent with recent studies suggesting that the surface of Psyche may not be as metal-rich as previously thought. Spectra of Psyche are consistent with iron meteorites, sulfide minerals, and the metal-rich CH/CBb carbonaceous chondrite Isheyevo. Furthermore, I demonstrated that absorption band parameters can be recovered from spectra convolved to the Imager's spectral throughput. Last, I provided some preliminary strategies for mapping the surface of the asteroid.

Finally, in Chapter 4, I presented work characterizing a commercial-off-the-shelf (COTS) version of the Psyche Multispectral Imager. I showed that the COTS Imager can approach or exceed requirements of the flight Imager. I also demonstrated some work validating a radiometric model developed for the flight Imager using data collected by the COTS Imager.

There are many further questions that have arisen from the work presented in this dissertation. Some questions focus specifically on interpretation of future Imager data and work that could be done to further prepare for characterizing the surface composition of (16) Psyche, while others are more about asteroid spectroscopy in general.

There is much work to be done characterizing the spectral properties of sulfide minerals. Spectra of synthetic sulfide minerals can be significantly different than their natural counterparts (e.g., Helbert et al. 2013, Varatharajan et al. 2019). What are the physical and chemical differences between natural and synthetic sulfides that cause differences in their spectral properties? Cloutis and Gaffey (1994) showed that synthetic troilite develops a pair of subtle absorption features at ~930 and 2490 nm and claimed the cause was Fe^{2+} crystal field transitions. Such features were not observed in spectra of synthetic sulfides by Varatharajan et al. (2019). If these features can be confirmed in modern studies of synthetic troilite, might the ~1000 nm feature seen in spectra of Psyche instead be caused by abundant troilite? Such a study may require manufacturing of synthetic sulfide minerals or collecting microscopic spectral data of single crystals.

Next, what are the ultraviolet reflectance properties of sulfide minerals, and how do they compare with UV observations of Psyche (e.g., Becker et al. 2018)? Can such observations further constrain the surface composition? Next, what do hypervelocity impacts into sulfide-rich targets look like? Is there substantial deposition of sulfur vapor after the impact, or is much of the volatile sulfur lost to space? Do the collective processes called “space weathering” affect sulfide-rich surfaces like rocky surfaces? As noted in Chapter 3, one constraint that may be placed on the formation history of Psyche is the maximum temperature reached. This may be inferred by the presence of cubanite ($CuFe_2S_3$) on the surface, which is not stable above ~200 °C.

Furthermore, additional spectral data of oldhamite (CaS) will be critical to addressing the Psyche Mission science questions regarding redox state. Currently, the features identified in spectra of oldhamite come from spectra of just one sample from the Norton County aubrite, which may not be a truly representative sample. Spectra of synthetic oldhamite do not exhibit any of the strong features present in the spectrum of oldhamite from Norton County and resolving this discrepancy will be critical for using oldhamite as a mineral indicator of redox conditions.

Finally, it must be noted that sulfide minerals on Earth are the dominant source of ores for non-ferrous metals (e.g., Cu, Mo, Ag, and the platinum group elements; Vaughan and Craig 1978). It is unlikely that the demand for these metals will shrink considerably in the near future, but their accessibility on Earth may become increasingly restricted or costly. Locating such elements on asteroids and exploiting them for industrial applications both on and off Earth may be a key to a future commercial space economy.

Thus, the identification of sulfide minerals on near-Earth asteroids will be an important first step towards establishing a permanent commercial presence in space. A further use of the spectral data in this dissertation would be to infer the presence of sulfide minerals on large near-Earth asteroids.

Additionally, in writing this dissertation, I have come up with what I think are PhD-level projects related to the Psyche Imager and asteroid spectral-compositional studies in general. The first is an update to commonly used radiative transfer models (e.g., the Hapke and Shkuratov models) for use with metal or sulfide dominated surfaces. Currently these models have been validated for S-type asteroids from data from the NEAR/Shoemaker mission, but a future graduate student could work on updating such models to be useful for X/M-type asteroid spectral analysis as well using data returned by the Imager. Furthermore, it is currently unclear how successful such radiative transfer models are at simulating the spectral changes induced by space weathering, which likely be a large part of the updated modeling.

The second PhD-level project I can think of is a greatly expanded visible-to-near-infrared spectral library of metal-sulfide-silicate-carbonaceous chondrite mixtures. This would be useful for interpretation of spectral data from essentially all asteroids, but particularly for space missions that collect spatially resolved spectral data of asteroid surfaces (like the Psyche Mission). Such a mixing study would likely involve hundreds of spectral measurements because the number of possible combinations grows very quickly with the number of components and the mixing ratio. Including multiple silicate compositions (e.g., a range of Fe-content pyroxenes) would be required.

The final PhD-level project would be to develop more equations for relating pyroxene and olivine spectral features to their mineralogy. This has been done for some groups of meteorites (e.g., Burbine et al. 2007) useful for specific types of asteroids but seeing a more global set of equations would be useful for more generic interpretation of asteroid surface mineralogy. One part of this study would be to explore any relationships that can be established between the redox state of an asteroid's formation and the pyroxene/olivine ratio measured from remote sensing (e.g., McSween 1992).

Finally, with the spectral library developed in this dissertation, I would like to apply the same methods of analysis for assessing the surface compositions of asteroids that are targets of future or current space missions. In particular, there are at least two missions currently targeting X-complex asteroids (the same larger spectral class as (16) Psyche). These are the DART/Hera Missions to the X-complex binary system 65803 Didymos and Lucy Mission to the Jupiter Trojan asteroids, several of which are Tholen X-type asteroids. Spectral data of the surface of Didymos will be provided by the LICIACube spacecraft as part of the DART Mission, and thus the spectral data in this dissertation may be useful for constraining the surface composition of Didymos. The data in this dissertation may have implications for the results of the kinetic impactor test of DART. While estimates of density suggest that it is unlikely that any of the Lucy Mission targets are dominated by metal and or sulfides, these materials may be components of their surface compositions. Spectral mixing analysis of the spectra in this library may support interpretations of data from the L'Ralph instrument on the Lucy spacecraft.

REFERENCES

Adams, J. B. (1974). Visible and near-infrared diffuse reflectance spectra of pyroxenes as applied to remote sensing of solid objects in the solar system. Journal of Geophysical Research, 79(32), 4829-4836.

Adams, J. B. (1975). Interpretation of visible and near-infrared diffuse reflectance spectra of pyroxenes and other rock-forming minerals. In Infrared and Raman spectroscopy of lunar and terrestrial minerals, 1st ed., edited by Karr C. Elsevier. pp.91-116.

Agee, C. B., Vaci, Z., Ziegler, K., & Spilde, M. N. (2019). Northwest Africa 12273: unique ungrouped metal-rich chondrite. In Lunar and Planetary Science Conference (No. 2132, p. 1176).

Asphaug, E. (2010). Similar-sized collisions and the diversity of planets. Geochemistry, 70(3), 199-219.

Baer, J., & Chesley, S. R. (2017). Simultaneous mass determination for gravitationally coupled asteroids. The Astronomical Journal, 154(2), 76.

Becker, T. M., Cunningham, N., Molyneux, P., Roth, L., Feaga, L. M., Retherford, K. D., et al. (2020). HST UV Observations of Asteroid (16) Psyche. The Planetary Science Journal, 1(3), 53.

Bell, III J., Elkins-Tanton L.T., Polanskey C.A., Ravine M.A., Caplinger M.A., Asphaug E., et al. (2016). The Psyche multispectral imager investigation: Characterizing the geology, topography, and compositional properties of a metallic world (abstract #1366). 47th Lunar and Planetary Science Conference.

Bell, III, J. F., Godber, A., McNair, S., Caplinger, M. A., Maki, J. N., Lemmon, M. T., et al. (2017). The Mars Science Laboratory Curiosity rover Mastcam instruments: Preflight and in-flight calibration, validation, and data archiving. Earth and Space Science, 4(7), 396-452.

Bell, III, J. F., Maki, J. N., Mehall, G. L., Ravine, M. A., Caplinger, M. A., Bailey, Z. J., et al. (2021). The Mars 2020 perseverance rover mast camera zoom (Mastcam-Z) multispectral, stereoscopic imaging investigation. Space Science Reviews, 217(1), 1-40.

Bercovici, H. L. (2020). The Effect of Bulk Composition on the Sulfur Content of Cores (Master's thesis). Retrieved from ProQuest. Location:Arizona State University.

Berger, E. L., Zega, T. J., Keller, L. P., & Lauretta, D. S. (2011). Evidence for aqueous activity on comet 81P/Wild 2 from sulfide mineral assemblages in Stardust samples and CI chondrites. Geochimica et Cosmochimica Acta, 75(12), 3501-3513.

Berger, E. L., Keller, L. P., & Lauretta, D. S. (2015). An experimental study of the formation of cubanite (CuFe2S3) in primitive meteorites. Meteoritics & Planetary Science, 50(1), 1-14.

Bild, R. W., & Wasson, J. T. (1976). The Lodran meteorite and its relationship to the ureilites. Mineralogical Magazine, 40(315), 721-735.

Binzel R.P. and Xu S. (1993). Chips off of asteroid 4 Vesta: Evidence for the parent body of basaltic achondrite meteorites. Science 260(5105):186-191.

Binzel, R. P., Bus, S. J., Xu, S., Sunshine, J., Burbine, T. H., Neely, A. W., & Brown, R. W. (1995). Rotationally resolved spectra of asteroid 16 Psyche. Icarus, 117(2), 443-445.

Bonal L., Huss G.R., Krot A.N., Nagashima K., Ishii H.A., and Bradley J.P. (2010). Highly 15N-enriched chondritic clasts in the CB/CH-like meteorite Isheyevo. Geochimica et Cosmochimica Acta 74(22):6590-6609.

Boreman, G. D. (2001). Modulation transfer function in optical and electro-optical systems. Vol. 4. Bellingham, WA: SPIE press.

Bouvier, A., Gattacceca, J., Agee, C., Grossman, J., & Metzler, K. (2017). The meteoritical bulletin, no. 104. Meteoritics & Planetary Science, 52(10), 2284-2284.

Bowman, L. E., Papike, J. J., & Spilde, M. N. (1996). Modal abundances in diogenites: Insights into phase percentages using electron microprobe techniques. In Lunar and Planetary Science Conference (Vol. 27).

Bradley J.P., Keller L.P., Brownlee D.E., and Thomas K.L. (1996). Reflectance spectroscopy of interplanetary dust particles. Meteoritics & Planetary Science 31(3):394-402.

Bradley J.P. (2003). Interplanetary dust particles. In Treatise on Geochemistry, 1st ed., edited by Holland H.D. and Turekian K.K. Elsevier Science. pp.711-735.

Britt, D. T., & Pieters, C. M. (1988). Bidirectional reflectance properties of iron-nickel meteorites. In Lunar and Planetary Science Conference Proceedings (Vol. 18, pp. 503-512).

Britt, D. T., Bell J.F., Haack H., and Scott E.R.D. (1992). The reflectance spectrum of troilite (abstract #1083). 23rd Lunar and Planetary Science Conference.

Brownlee, D. (2014). The Stardust mission: analyzing samples from the edge of the solar system. Annual Review of Earth and Planetary Sciences, 42, 179-205.

Bunch, T. E., Keil, K., & Huss, G. I. (1972). The Landes meteorite. Meteoritics, 7(1), 31-38.

Burbine T.H., Gaffey M.J., and Bell J.F. (1992). S-asteroids 387 Aquitania and 980 Anacostia: Possible fragments of the breakup of a spinel-bearing parent body with C03/CV3 affinities. Meteoritics 27(4):424-434.

Burbine T.H., McCoy T.J., Nittler L.R., Benedix G.K., Cloutis E.A., and Dickinson T.L. (2002). Spectra of extremely reduced assemblages: Implications for Mercury. Meteoritics & Planetary Science 37(9):1233-1244.

Burbine, T. H., Greenwood, R. C., Buchanan, P. C., Franchi, I. A., & Smith, C. L. (2007a). Reflectance spectra of Mesosiderites: Implications for asteroid 4 Vesta. In Lunar and Planetary Science Conference (Vol. 38).

Burbine, T. H., Buchanan, P. C., & Binzel, R. P. (2007b). Deriving formulas from HED spectra for determining the pyroxene mineralogy of Vesta and Vestoids. In Lunar and Planetary Science Conference (Vol.38).

Burgess, K. D., & Stroud, R. M. (2021). Exogenous copper sulfide in returned asteroid Itokawa regolith grains are likely relicts of prior impacting body. Communications Earth & Environment, 2(1), 1-6.

Burns, R. G., & Burns, R. G. (1993). Mineralogical applications of crystal field theory (No. 5). Cambridge University Press.

Bus, S. J., & Binzel, R. P. (2002). Phase II of the small main-belt asteroid spectroscopic survey: The observations. Icarus, 158(1), 106-145.

Bus S.J. and Binzel R.P. (2002). Phase II of the small main-belt asteroid spectroscopic survey: A feature-based taxonomy. Icarus 158(1):146-177.

Buseck, P. R. (1977). Pallasite meteorites—mineralogy, petrology and geochemistry. Geochimica et Cosmochimica Acta, 41(6), 711-740.

Cahill, J. T., Blewett, D. T., Nguyen, N. V., Boosalis, A., Lawrence, S. J., & Denevi, B. W. (2019). Optical constants of iron and nickel metal and an assessment of their relative influences on silicate mixture spectra from the FUV to the NIR. Icarus, 317, 229-241.

Cantillo, D. C., Reddy, V., Sharkey, B. N., Pearson, N. A., Sanchez, J. A., Izawa, M. R., et al. (2021). Constraining the Regolith Composition of Asteroid (16) Psyche via Laboratory Visible Near-infrared Spectroscopy. The Planetary Science Journal, 2(3), 95.

Carry B. (2012). Density of asteroids. Planetary and Space Science 73(1):98-118.

Chabot, N. L. (2004). Sulfur contents of the parental metallic cores of magmatic iron meteorites. Geochimica et Cosmochimica Acta, 68(17), 3607-3618.

Clark B. E., Veverka J., Helfenstein P., Thomas P.C., Bell III J.F., Harch A., et al. (1999). NEAR photometry of Asteroid 253 Mathilde. Icarus 140(1):53-65.

Clark B.E., Bus S.J., Rivkin A.S., McConnochie T., Sanders J., Shah S., Hiroi T., and Shepard M. (2004a). E-type asteroid spectroscopy and compositional modeling. Journal of Geophysical Research: Planets 109(E2).

Clark B.E., Bus S.J., Rivkin A.S., Shepard M.K., and Shah S. (2004b). Spectroscopy of X-type asteroids. The Astronomical Journal 128(6):3070-3081.

Clark, R. N., & Roush, T. L. (1984). Reflectance spectroscopy: Quantitative analysis techniques for remote sensing applications. Journal of Geophysical Research: Solid Earth, 89(B7), 6329-6340.

Clark R.N. (1999). Spectroscopy of rocks and minerals, and principles of spectroscopy. In Manual of Remote Sensing, 3rd ed., edited by Rencz A. N. John Wiley & Sons. pp.3-58.

Cloutis E.A., Gaffey M.J., Smith D.G., and Lambert R.S.J. (1990). Reflectance spectra of “featureless” materials and the surface mineralogies of M-and E-class asteroids. Journal of Geophysical Research: Solid Earth 95(B1):281-293.

Cloutis E.A. and Gaffey M.J. (1991). Pyroxene spectroscopy revisited: Spectral-compositional correlations and relationship to geothermometry. Journal of Geophysical Research: Planets 96(E5):22809-22826.

Cloutis E.A. and Gaffey M.J. (1994). An X-ray diffraction and reflectance spectroscopy study of iron sulphides (abstract #273). 25th Lunar and Planetary Science Conference.

Cloutis E.A. and Burbine T.H. (1999). The spectral properties of troilite/pyrrhotite and implications for the E-asteroids (abstract #1875). 30th Lunar and Planetary Science Conference.

Cloutis, E. A., Hardersen, P. S., Reddy, V., Gaffey, M. J., Bailey, D. T., & Craig, M. A. (2009). Metal-Orthopyroxene and Metal-Olivine Mixtures: Spectral reflectance properties and implications for asteroid spectroscopy. In Lunar and Planetary Science Conference (p. 1332).

Cloutis, E. A., Hardersen, P. S., Bish, D. L., Bailey, D. T., Gaffey, M. J., & Craig, M. A. (2010). Reflectance spectra of iron meteorites: Implications for spectral identification of their parent bodies. Meteoritics & Planetary Science, 45(2), 304-332.

Cloutis, E. A., Hiroi, T., Gaffey, M. J., Alexander, C. O. D., & Mann, P. (2011a). Spectral reflectance properties of carbonaceous chondrites: 1. CI chondrites. Icarus, 212(1), 180-209.

Cloutis, E. A., Hudon, P., Hiroi, T., Gaffey, M. J., & Mann, P. (2011b). Spectral reflectance properties of carbonaceous chondrites: 2. CM chondrites. Icarus, 216(1), 309-346.

Cloutis, E. A., Hudon, P., Hiroi, T., & Gaffey, M. J. (2012a). Spectral reflectance properties of carbonaceous chondrites: 3. CR chondrites. Icarus, 217(1), 389-407.

Cloutis, E. A., Hudon, P., Hiroi, T., & Gaffey, M. J. (2012b). Spectral reflectance properties of carbonaceous chondrites 4: Aqueously altered and thermally metamorphosed meteorites. Icarus, 220(2), 586-617.

Cloutis, E. A., Hudon, P., Hiroi, T., Gaffey, M. J., & Mann, P. (2012c). Spectral reflectance properties of carbonaceous chondrites–5: CO chondrites. Icarus, 220(2), 466-486.

Cloutis, E. A., Hudon, P., Hiroi, T., Gaffey, M. J., Mann, P., & Bell III, J. F. (2012d). Spectral reflectance properties of carbonaceous chondrites: 6. CV chondrites. Icarus, 221(1), 328-358.

Cloutis, E. A., Hudon, P., Hiroi, T., & Gaffey, M. J. (2012e). Spectral reflectance properties of carbonaceous chondrites: 7. CK chondrites. Icarus, 221(2), 911-924.

Cloutis, E. A., Hudon, P., Hiroi, T., Gaffey, M. J., & Mann, P. (2012f). Spectral reflectance properties of carbonaceous chondrites: 8. “Other” carbonaceous chondrites: CH, ungrouped, polymict, xenolithic inclusions, and R chondrites. Icarus, 221(2), 984-1001.

Cloutis E.A., Sanchez J.A., Reddy V., Gaffey M.J., Binzel R.P., Burbine T.H., et al. (2015). Olivine–metal mixtures: Spectral reflectance properties and application to asteroid reflectance spectra. Icarus 252:39-82.

Cloutis E.A., Gaffey M.J., and Applin D.M. (2016). Spectral reflectance properties of aubrites (abstract #1709). 47th Lunar and Planetary Science Conference.

Coradini A., Capaccioni F., Erard S., Arnold G., De Sanctis M.C., Filacchione G., et al. (2011). The surface composition and temperature of asteroid 21 Lutetia as observed by Rosetta/VIRTIS. Science 334(6055):492-494.

Crane, K. T., Minton, D. A., & Emery, J. P. (2013). Thermal Inertia of a Metallic Regolith: A Simulant Sample Experiment. In Lunar and Planetary Science Conference (No. 1719, p. 1018).

de Kleer, K., Cambioni, S., & Shepard, M. (2021). The Surface of (16) Psyche from Thermal Emission and Polarization Mapping. arXiv preprint arXiv:2105.11372.

DeMeo, F. E., Binzel, R. P., Slivan, S. M., & Bus, S. J. (2009). An extension of the Bus asteroid taxonomy into the near-infrared. Icarus, 202(1), 160-180.

Devogèle M., Tanga P., Cellino A., Bendjoya P., Rivet J.P., Surdej J., et al. (2018). New polarimetric and spectroscopic evidence of anomalous enrichment in spinel-bearing calcium-aluminium-rich inclusions among L-type asteroids. Icarus 304:31-57.

Dibb, S., Bell, III, J. F., Elkins-Tanton, L. T., Williams, D. A., Binzel, R. P., and the Psyche Mission Team (2018). Optimized Narrowband Visible to Near-Infrared Filters for the Psyche Multispectral Imager. In Instrumentation for Planetary Missions 2018.

Dibb, S. D., Bell, III, J. F., & Garvie, L. A. J. (2021). Reflectance Spectra of Metal-Troilite Mixtures: Implications for M-/X-Type Asteroid Exploration. In Lunar and Planetary Science Conference (p. 1543).

Dollfus A., Mandeville J.C., and Duseaux M. (1979). The nature of the M-type asteroids from optical polarimetry. Icarus 37(1):124-132.

Dresselhaus, M. S. (2001). Solid state physics part ii optical properties of solids. Lecture Notes (Massachusetts Institute of Technology, Cambridge, MA), 17, 15-16.

Dyar, M. D., Sklute, E. C., Menzies, O. N., Bland, P. A., Lindsley, D., Glotch, T., et al. (2009). Spectroscopic characteristics of synthetic olivine: An integrated multi-wavelength and multi-technique approach. American Mineralogist, 94(7), 883-898.

Elkins-Tanton, L. T., Asphaug, E., Bell, J., Bercovici, D., Bills, B. G., Binzel, R. P., et al. (2016). Asteroid (16) Psyche: the science of visiting a metal world.

Elkins-Tanton L.T., Asphaug E., Bell III J.F., Bercovici H., Bills B., Binzel R., et al. (2020). Observations, meteorites, and models: a preflight assessment of the composition and formation of (16) Psyche. Journal of Geophysical Research: Planets 125(3):e2019JE006296.

Emery J.P. and Brown R.H. (2003). Constraints on the surface composition of Trojan asteroids from near-infrared (0.8–4.0 μm) spectroscopy. Icarus 164(1):104-121.

Emery J.P., Burr D.M. and Cruikshank D.P. (2010). Near-infrared spectroscopy of Trojan asteroids: Evidence for two compositional groups. The Astronomical Journal 141(1):25.

Emery J.P., Marzari F., Morbidelli A., French L.M. and Grav T. (2015). The complex history of Trojan asteroids. Asteroids IV 203.

Ferrais, M., Vernazza, P., Jorda, L., Rambaux, N., Hanuš, J., Carry, B., et al. (2020). Asteroid (16) Psyche's primordial shape: A possible Jacobi ellipsoid. Astronomy & Astrophysics, 638, L15.

Ferrari F., Franzese V., Pugliatti M., Giordano C. and Topputo F. (2021). Preliminary mission profile of Hera's Milani CubeSat. Advances in Space Research 67(6):2010-2029.

Fornasier S., Migliorini A., Dotto E., and Barucci M.A. (2008). Visible and near infrared spectroscopic investigation of E-type asteroids, including 2867 Steins, a target of the Rosetta mission. Icarus 196(1):119-134.

Fornasier, S., Clark, B. E., Dotto, E., Migliorini, A., Ockert-Bell, M., & Barucci, M. A. (2010). Spectroscopic survey of M-type asteroids. Icarus, 210(2), 655-673.

Fornasier S., Lantz C., Barucci M.A., and Lazzarin M. (2014). Aqueous alteration on main belt primitive asteroids: Results from visible spectroscopy. Icarus 233:163-178.

Friend P., Zipfel J., Gellissen M., Kleinschrodt R., Muenker C., Pack A., et al. (2011). Northwest Africa 5492: An extremely reduced chondritic meteorite with low volatile element contents (abstract #1095). 42nd Lunar and Planetary Science Conference.

Füri E. and Marty B. (2015). Nitrogen isotope variations in the Solar System. Nature Geoscience 8(7):515-522.

Gaffey M.J. (1976). Spectral reflectance characteristics of the meteorite classes. Journal of Geophysical Research 81(5):905-920.

Gaffey, M. J., Cloutis, E. A., Kelley, M. S., & Reed, K. L. (2002). Mineralogy of Asteroids. In Bottke, W. F., Cellino, A., Paolicchi, P. & Binzel, R. P. (Eds.), Asteroids III. (p. 183-204). University of Arizona Press.

Gaffey M.J. and Kelley M.S. (2004). Mineralogical variations among high albedo E-type asteroids: Implications for asteroid igneous processes (abstract #1812). 35th Lunar and Planetary Science Conference.

Garvie, L. A., Knauth, L. P., & Morris, M. A. (2017). Sedimentary laminations in the Isheyevo (CH/CBb) carbonaceous chondrite formed by gentle impact-plume sweep-up. Icarus, 292, 36-47.

Gattacceca, J., McCubbin, F. M., Bouvier, A., & Grossman, J. (2020). The Meteoritical Bulletin, No. 107. Meteoritics & Planetary Science, 55(2), 460-462.

Goldstein, J. I., Scott, E. R. D., & Chabot, N. L. (2009). Iron meteorites: Crystallization, thermal history, parent bodies, and origin. Geochemistry, 69(4), 293-325.

Goodrich, C. A., Fioretti, A., Zolensky, M., Shaddad, M., Hiroi, T., Young, E., et al. (2018, October). Compositional and Spectral Properties of Ureilitic Regolith from Samples of Almahata Sitta. In AAS/Division for Planetary Sciences Meeting Abstracts# 50 (pp. 100-08).

Gulkis S., Keihm S., Kamp L., Backus C., Janssen M., Lee S., et al. (2010). Millimeter and submillimeter measurements of asteroid (2867) Steins during the Rosetta fly-by. Planetary and Space Science 58(9):1077-1087.

Hanuš, J., Viikinkoski, M., Marchis, F., Ďurech, J., Kaasalainen, M., Delbo, M., et al. (2017). Volumes and bulk densities of forty asteroids from ADAM shape modeling. Astronomy & Astrophysics, 601, A114.

Hardersen, P. S., Gaffey, M. J., & Abell, P. A. (2005). Near-IR spectral evidence for the presence of iron-poor orthopyroxenes on the surfaces of six M-type asteroids. Icarus, 175(1), 141-158.

Hardersen, P. S., Cloutis, E. A., Reddy, V., Mothé-Diniz, T., & Emery, J. P. (2011). The M-/X-asteroid menagerie: Results of an NIR spectral survey of 45 main-belt asteroids. Meteoritics & Planetary Science, 46(12), 1910-1938.

Hayes, A. G., Corlies, P., Tate, C., Barrington, M., Bell, J. F., Maki, J. N., et al. (2021). Pre-flight calibration of the Mars 2020 Rover Mastcam Zoom (Mastcam-Z) multispectral, stereoscopic imager. Space science reviews, 217(2), 1-95.

Helbert, J., Maturilli, A., & D'Amore, M. (2013). Visible and near-infrared reflectance spectra of thermally processed synthetic sulfides as a potential analog for the hollow forming materials on Mercury. Earth and Planetary Science Letters, 369, 233-238.

Hiroi T., Zolensky M.E., and Pieters C.M. (2001). The Tagish Lake meteorite: A possible sample from a D-type asteroid. Science 293(5538):2234-2236.

Hiroi T., Pieters C.M., Rutherford M.J., Zolensky M.E., Sasaki S., Ueda Y., and Miyamoto M. (2004). What are the P-type asteroids made of? (abstract #1616). 35th Lunar and Planetary Science Conference.

Horgan, B. H., Cloutis, E. A., Mann, P., & Bell III, J. F. (2014). Near-infrared spectra of ferrous mineral mixtures and methods for their identification in planetary surface spectra. Icarus, 234, 132-154.

Hunt, G. R., Salisbury, J. W., Lenhoff, C. J. (1971). Visible and near-infrared spectra of minerals and rocks: IV sulphides and sulphates. Modern Geology, 3, 1-14.

Hutchison, W. K., Bevan, A. W. R., Easton, A. J., & Agrell, S. O. (1981). Mineral chemistry and genetic relations among H-group chondrites. Proceedings of the Royal Society of London. A. Mathematical and Physical Sciences, 374(1757), 159-178.

International tables for crystallography. Vol. C. Mathematical, physical, and chemical tables. (1993). Edited by A. J. C. Wilson. Dordrecht:Kluwer Academic Publishers.

Ivanova M.A., Kononkova N.N., Franchi I.A., Verchovsky A.B., Korochantseva E.V., Trieloff M., Krot A.N., and Brandstätter F. (2006). Isheyevo Meteorite: Genetic link between CH and CB chondrites? (abstract #1100). 37th Lunar and Planetary Science Conference.

Ivanova, M. A., Kononkova, N. N., Krot, A. N., Greenwood, R. C., Franchi, I. A., Verchovsky, A. B., et al. (2008). The Isheyevo meteorite: Mineralogy, petrology, bulk chemistry, oxygen, nitrogen, carbon isotopic compositions, and 40Ar-39Ar ages. Meteoritics & Planetary Science, 43(5), 915-940.

Izawa, M. R. M., King, P. L., Flemming, R. L., Peterson, R. C., & McCausland, P. J. A. (2010). Mineralogical and spectroscopic investigation of enstatite chondrites by X-ray diffraction and infrared reflectance spectroscopy. Journal of Geophysical Research: Planets, 115(E7).

Izawa M.R., Flemming R.L., King P.L., Peterson R.C., and McCausland P.J. (2010). Mineralogical and spectroscopic investigation of the Tagish Lake carbonaceous chondrite by X-ray diffraction and infrared reflectance spectroscopy. Meteoritics & Planetary Science 45(4):675-698.

Izawa M.R.M., Applin D.M., Mann P., Craig M.A., Cloutis E.A., Helbert J., and Maturilli A. (2013). Reflectance spectroscopy (200–2500 nm) of highly-reduced phases under oxygen-and water-free conditions. Icarus 226(2):1612-1617.

Janesick, J., Klaasen, K., and Elliott, T. (1987). CCD Charge Collection Efficiency and the photon transfer technique. Society of Photo-Optical Instrumentation Engineers (SPIE) Conference Series. Vol. 726.

Janesick, J. R. (2007). Photon Transfer - DN -> λ. 1st ed., SPIE, doi:10.1117/3.725073.

Jarosewich, E. (1990). Chemical analyses of meteorites: A compilation of stony and iron meteorite analyses. Meteoritics, 25(4), 323-337.

Jenniskens, P., Betlem, H., Betlem, J., Barifaijo, E., Schlüter, T., Hampton, C., et al. (1994). The Mbale meteorite shower. Meteoritics, 29(2), 246-254.

Jones T.D., Lebofsky L.A., Lewis J.S., and Marley M.S. (1990). The composition and origin of the C, P, and D asteroids: Water as a tracer of thermal evolution in the outer belt. Icarus 88(1):172-192.

Keil K. (2010). Enstatite achondrite meteorites (aubrites) and the histories of their asteroidal parent bodies. Geochemistry 70(4):295-317.

Keil, K., & Fredriksson, K. (1963). Electron microprobe analysis of some rare minerals in the Norton County achondrite. Geochimica et Cosmochimica Acta, 27(9), 939-947.

Keller H.U., Barbieri C., Koschny D., Lamy P., Rickman H., Rodrigo R., et al. (2010). E-type asteroid (2867) Steins as imaged by OSIRIS on board Rosetta. Science 327(5962):190-193.

Kiddell C.B., Cloutis E.A., Dagdick B.R., Stromberg J.M., Applin D.M., and Mann J.P. (2018). Spectral reflectance of powder coatings on carbonaceous chondrite slabs:

Implications for asteroid regolith observations. Journal of Geophysical Research: Planets 123(10):2803-2840.

Klima, R. L., Pieters, C. M., & Dyar, M. D. (2007). Spectroscopy of synthetic Mg-Fe pyroxenes I: Spin-allowed and spin-forbidden crystal field bands in the visible and near-infrared. Meteoritics & Planetary Science, 42(2), 235-253.

Koch, T. E., Brenker, F. E., Krot, A. N., & Bizzarro, M. (2016). Petrography of Quebrada Chimborazo 001—A New CBa Chondrite. In Lunar and Planetary Science Conference (No. 1903, p. 1968).

Krot A.N., Ulyanov A.A., and Ivanova M.A. (2008). Refractory inclusions in the CH/CB-like carbonaceous chondrite Isheyevo: I. Mineralogy and petrography. Meteoritics & Planetary Science 43(9):1531-1550.

Krot, A. N., Ivanova, M. A., & Ulyanov, A. A. (2007). Chondrules in the CB/CH-like carbonaceous chondrite Isheyevo: Evidence for various chondrule-forming mechanisms and multiple chondrule generations. Geochemistry, 67(4), 283-300.

Landsman, Z. A., Emery, J. P., Campins, H., Hanuš, J., Lim, L. F., & Cruikshank, D. P. (2018). Asteroid (16) Psyche: Evidence for a silicate regolith from spitzer space telescope spectroscopy. Icarus, 304, 58-73.

Larson, W. J., & Wertz, J. R. (1992). Space mission analysis and design. Torrance, Calif: Microcosm.

Lauretta, D. S., Lodders, K., & Fegley, B. (1997). Experimental simulations of sulfide formation in the solar nebula. Science, 277(5324), 358-360.

Lebofsky L.A., Jones T.D., Owensby P.D., Feierberg M.A., and Consolmagno G.J. (1990). The nature of low-albedo asteroids from 3-μm multi-color photometry. Icarus 83(1):16-26.

Levison H.F. and the Lucy Science Team. (2016). Lucy: surveying the diversity of the Trojan asteroids, the fossils of planet formation (abstract #2061). 47th Lunar and Planetary Science Conference.

Leyrat C., Coradini A., Erard S., Capaccioni F., Capria M.T., Drossart P., De Sanctis M.C., Tosi F., and VIRTIS Team. (2011). Thermal properties of the asteroid (2867) Steins as observed by VIRTIS/Rosetta. Astronomy & Astrophysics 531:A168.

Macke R.J., Britt D.T., and Consolmagno G.J. (2011). Density, porosity, and magnetic susceptibility of achondritic meteorites. Meteoritics & Planetary Science 46(2):311-326.

Mason, B. (1963). Olivine composition in chondrites. Geochimica et Cosmochimica Acta, 27(10), 1011-1023.

Matter, A., Delbo, M., Carry, B., & Ligori, S. (2013). Evidence of a metal-rich surface for the Asteroid (16) Psyche from interferometric observations in the thermal infrared. Icarus, 226(1), 419-427.

McCoy, T. J., Keil, K., Bogard, D. D., Garrison, D. H., Casanova, I., Lindstrom, M. M., et al. (1995). Origin and history of impact-melt rocks of enstatite chondrite parentage. Geochimica et Cosmochimica Acta, 59(1), 161-175.

McLean, I. S. "Electronic Imaging in Astronomy: Detectors and Instrumentation". 2nd ed., Springer Berlin Heidelberg, (2008) doi:10.1007/978-3-540-76583-7.

McSween Jr, H. Y., & Labotka, T. C. (1993). Oxidation during metamorphism of the ordinary chondrites. Geochimica et Cosmochimica Acta, 57(5), 1105-1114.

Meibom A., Righter K., Chabot N., Dehn G., Antignano A., McCoy T.J., et al. (2005). Shock melts in QUE 94411, Hammadah al Hamra 237, and Bencubbin: Remains of the missing matrix?. Meteoritics & Planetary Science 40(9-10):1377-1391.

Mittlefehldt D.W., McCoy T.J., Goodrich C.A., and Kracher A. (1998). Non-chondritic meteorites from asteroidal bodies. In Planetary Materials, edited by Papike J.J. Albuquerque:De Gruyter. pp.523-718.

Mittlefehldt, D. W., McCoy, T. J., Goodrich, C. A., & Kracher, A. (2018). Non-chondritic meteorites from asteroidal bodies. Planetary materials, 523-718.

Moore, C. B., Lewis, C. F., & Clark, J. C. (1981). The Penwell Stony-Iron Meteorite. Meteoritics, 16, 361.

Moore, C. B., Lewis, C. F., & Clark, J. (1982). The Penwell Meteorite Revisited. Meteoritics, 17, 256.

Morris, M. A., Garvie, L. A., & Knauth, L. P. (2015). New insight into the solar system’s transition disk phase provided by the metal-rich carbonaceous chondrite Isheyevo. The Astrophysical Journal Letters, 801(2), L22.

Moyano-Cambero C.E., Trigo-Rodríguez J.M., Llorca J., Fornasier S., Barucci M.A., and Rimola A. 2016. A plausible link between the asteroid 21 Lutetia and CH carbonaceous chondrites. Meteoritics & Planetary Science 51(10):1795-1812.

Nedelcu, D. A., Birlan, M., Vernazza, P., Descamps, P., Binzel, R. P., Colas, F., et al. (2007). Near infra-red spectroscopy of the asteroid 21 Lutetia-II. Rotationally resolved spectroscopy of the surface. Astronomy & Astrophysics, 470(3), 1157-1164.

Ockert-Bell, M. E., Clark, B. E., Shepard, M. K., Rivkin, A. S., Binzel, R. P., Thomas, C. A., et al. (2008). Observations of X/M asteroids across multiple wavelengths. Icarus, 195(1), 206-219.

Ockert-Bell, M. E., Clark, B. E., Shepard, M. K., Isaacs, R. A., Cloutis, E. A., Fornasier, S., & Bus, S. J. (2010). The composition of M-type asteroids: Synthesis of spectroscopic and radar observations. Icarus, 210(2), 674-692.

Olsen, E. J., Bunch, T. E., Jarosewich, E., Noonan, A. F., & Huss, G. I. (1977). Happy Canyon: A new type of enstatite achondrite. Meteoritics, 12(2), 109-124.

ON Semiconductor, "KAI-2020 1600 (H) x 1200 (V) Interline CCD Image Sensor". Dec. 2015, www.onsemi.com/pdf/datasheet/kai-2020-d.pdf.

Ostro, S. J. (1993). Planetary radar astronomy. Reviews of Modern Physics, 65(4), 1235.

Ostro, S. J., Hudson, R. S., Benner, L. A., Giorgini, J. D., Magri, C., Margot, J. L., & Nolan, M. C. (2002). Asteroid radar astronomy. Asteroids III, 151-168.

Pirard, E., Bernhardt, H. J., Catalina Hernández, J. C., Brea, C., Segundo, F., & Castroviejo Bolibar, R. (2008, December). From spectrophotometry to multispectral imaging of ore minerals in visible and near infrared (VNIR) microscopy. Australasian Institute of Mining and Metallurgy.

Powell, B. N. (1971). Petrology and chemistry of mesosiderites—II. Silicate textures and compositions and metal-silicate relationships. Geochimica et Cosmochimica Acta, 35(1), 5-34.

Reddy, V., Le Corre, L., O'Brien, D. P., Nathues, A., Cloutis, E. A., Durda, D. D., et al. (2012). Delivery of dark material to Vesta via carbonaceous chondritic impacts. Icarus, 221(2), 544-559.

Reddy V., Pearson N., Agee C.B., Cantillo D.C., Le Corre L., Campbell T., and Chabra O. (2019). Spectral Investigation of Anomalous Metal-Rich Chondrite Northwest Africa (NWA) 12273: Implications for Asteroid (16) Psyche (abstract #2212). 50th Lunar and Planetary Science Conference.

Reid, A. M., Williams, R. J., & Takeda, H. (1974). Coexisting bronzite and clinobronzite and the thermal evolution of the Steinbach meteorite. Earth and Planetary Science Letters, 22(1), 67-74.

Rivkin A.S., Howell E.S., Britt D.T., Lebofsky L.A., Nolan M.C., and Branston D.D. (1995). 3-µm spectrophotometric survey of M-and E-class asteroids. Icarus 117(1):90-100.

Rivkin A.S., Howell E.S., Lebofsky L.A., Clark B.E., and Britt D.T. (2000). The nature of M-class asteroids from 3-µm observations. Icarus 145(2):351-368.

Rivkin A.S., Howell E.S., Vilas F., and Lebofsky L.A. (2002). Hydrated minerals on asteroids: The astronomical record. In Asteroids III, edited by Bottke W.F., Cellino A., Paolicchi P., Binzel R.P. Tucson:University of Arizona Press. pp.235-253.

Rossman, G. R., & Ehlmann, B. L. (2019). Electronic Spectra of Minerals in the Visible and Near-Infrared Regions. Remote Compositional Analysis: Techniques for Understanding Spectroscopy, 3-20.

Rubin, A. E. (1997). Mineralogy of meteorite groups. Meteoritics & Planetary Science, 32(2), 231-247.

Rubin, A. E., & Scott, W. R. (1997). Abee and related EH chondrite impact-melt breccias. Geochimica et Cosmochimica Acta, 61(2), 425-435.

Rubin, A. E., & Ma, C. (2017). Meteoritic minerals and their origins. Geochemistry, 77(3), 325-385.

Russell, S. S., Zipfel, J., Folco, L., Jones, R., Grady, M. M., McCoy, T., & Grossman, J. N. (2003). The Meteoritical Bulletin, No. 87, 2003 July. Meteoritics & Planetary Science, 38(S7), A189-A248.

Ruzicka, A., Grossman, J., Bouvier, A., & Agee, C. B. (2017). The meteoritical bulletin, No. 103. Meteoritics & Planetary Science, 52(5), 1014.

Sanchez J. A., Reddy V., Shepard M. K., Thomas C., Cloutis E. A., Takir D., et al. (2017). Detection of rotational spectral variation on the M-type asteroid (16) Psyche. The Astronomical Journal 153(1):29-37.

Sarid, G., Stewart, S. T., & Leinhardt, Z. M. (2015). Erosive Hit-and-Run Impact Events: Debris Unbound. Proceedings of the International Astronomical Union, 10(S318), 9-15.

Schaudy, R., Watson, J. T., & Buchwald, V. F. (1972). The chemical classification of iron meteorites. VI. A reinvestigation of irons with Ge concentration lower than 1 ppm. Icarus, 17(1), 174-192.

Schrader, D. L., Davidson, J., & McCoy, T. J. (2016). Widespread evidence for high-temperature formation of pentlandite in chondrites. Geochimica et Cosmochimica Acta, 189, 359-376.

Scott, E. R. D., & Krot, A. N. (2003). Chondrites and their components. Treatise on geochemistry, 1, 711.

Scott, E. R., Haack, H., & McCoy, T. J. (1996). Core crystallization and silicate-metal mixing in the parent body of the IVA iron and stony-iron meteorites. Geochimica et Cosmochimica Acta, 60(9), 1615-1631.

Shepard, M. K., Clark, B. E., Nolan, M. C., Howell, E. S., Magri, C., Giorgini, J. D., et al. (2008). A radar survey of M-and X-class asteroids. Icarus, 195(1), 184-205.

Shepard, M. K., Clark, B. E., Ockert-Bell, M., Nolan, M. C., Howell, E. S., Magri, C., et al. (2010). A radar survey of M-and X-class asteroids II. Summary and synthesis. Icarus, 208(1), 221-237.

Shepard M.K., Taylor P.A., Nolan M.C., Howell E.S., Springmann A., Giorgini J.D., et al. (2015). A radar survey of M-and X-class asteroids. III. Insights into their composition, hydration state, & structure. Icarus 245:38-55.

Shepard M.K., Richardson J., Taylor P.A., Rodriguez-Ford L.A., Conrad A., de Pater I., et al. (2017). Radar observations and shape model of asteroid 16 Psyche. Icarus 281:388-403.

Shepard, M. K., de Kleer, K., Cambioni, S., Taylor, P. A., Virkki, A. K., Rívera-Valentin, E. G., et al. (2021). Asteroid 16 Psyche: Shape, Features, and Global Map. The Planetary Science Journal, 2(4), 125.

Siltala, L., & Granvik, M. (2021). Mass and Density of Asteroid (16) Psyche. The Astrophysical Journal Letters, 909(1), L14.

Smith, W. J. (2000) Modern Optical Engineering: The Design of Optical Systems. 3rd ed., McGraw Hill.

Sunshine J.M., Connolly H.C., McCoy T.J., Bus S.J., and La Croix L.M. 2008. Ancient asteroids enriched in refractory inclusions. Science 320(5875):514-517.

Takir D. and Emery J.P. (2012). Outer main belt asteroids: Identification and distribution of four 3-μm spectral groups. Icarus 219(2):641-654.

Takir, D., Reddy, V., Sanchez, J. A., Shepard, M. K., & Emery, J. P. (2016). Detection of water and/or hydroxyl on asteroid (16) Psyche. The Astronomical Journal, 153(1), 31.

Takir D., Stockstill-Cahill K.R., Hibbitts C.A., and Nakauchi Y. (2019). 3-μm reflectance spectroscopy of carbonaceous chondrites under asteroid-like conditions. Icarus 333:243-251.

Tedesco E.F., Noah P.V., Noah M., and Price S.D. (2002). The supplemental IRAS minor planet survey. The Astronomical Journal, 123(2):1056-1085.

Tholen D. J. (1984). Asteroid taxonomy from cluster analysis of photometry. Ph.D. thesis, University of Arizona, Tucson, Arizona, United States.

Trigo-Rodriguez J.M., Moyano-Cambero C.E., Llorca J., Fornasier S., Barucci M.A., Belskaya I., et al. (2013). UV to far-IR reflectance spectra of carbonaceous chondrites–I. Implications for remote characterization of dark primitive asteroids targeted by sample-return missions. Monthly Notices of the Royal Astronomical Society 437(1):227-240.

Ulff-Møller, F. (1998). Effects of liquid immiscibility on trace element fractionation in magmatic iron meteorites: A case study of group IIIAB. Meteoritics & Planetary Science, 33(2), 207-220.

Ulff-Møller, F., Choi, B. G., Rubin, A. E., Tran, J., & Wasson, J. T. (1998). Paucity of sulfide in a large slab of Esquel: New perspectives on pallasite formation. Meteoritics & Planetary Science, 33(2), 221-227.

Urey, H. C., & Craig, H. (1953). The composition of the stone meteorites and the origin of the meteorites. Geochimica et Cosmochimica Acta, 4(1-2), 36-82.

Varatharajan, I., Maturilli, A., Helbert, J., Alemanno, G., & Hiesinger, H. (2019). Spectral behavior of sulfides in simulated daytime surface conditions of Mercury: Supporting past (MESSENGER) and future missions (BepiColombo). Earth and Planetary Science Letters, 520, 127-140.

Vaughan D.J. and Craig J. R. (1978). Mineral chemistry of metal sulfides, 1st ed., Cambridge: Cambridge University Press.

Vernazza, P., Lamy, P., Groussin, O., Hiroi, T., Jorda, L., King, P. L., et al. (2011). Asteroid (21) Lutetia as a remnant of Earth's precursor planetesimals. Icarus, 216(2), 650-659.

Vernazza P., Marsset M., Beck P., Binzel R.P., Birlan M., Brunetto R., et al. (2015). Interplanetary dust particles as samples of icy asteroids. The Astrophysical Journal 806(2):204-214.

Viikinkoski, M., Vernazza, P., Hanuš, J., Le Coroller, H., Tazhenova, K., Carry, B., et al. (2018). (16) Psyche: A mesosiderite-like asteroid?. Astronomy & Astrophysics, 619, L3.

Watters, T. R., & Prinz, M. (1979). Aubrites-Their origin and relationship to enstatite chondrites. In Proceedings of the 10th Lunar and Planetary Science Conference.

Weisberg M.K., Prinz M., Clayton R.N., Mayeda T.K., Sugiura N., and Zashu S. (1998). The Bencubbinite (B) group of the CR clan. Meteoritics and Planetary Science Supplement 33:A166.

Weisberg, M. K., Bunch, T. E., Wittke, J. H., Rumble III, D., & Ebel, D. S. (2012). Petrology and oxygen isotopes of NWA 5492, a new metal-rich chondrite. Meteoritics & Planetary Science, 47(3), 363-373.

Wertz, J. R., and W. J. Larson. "Space mission analysis and design", Microcosm. Inc., (1999).

Wheelock M.M., Keil K., Floss C., Taylor G.J., and Crozaz G. 1994. REE geochemistry of oldhamite-dominated clasts from the Norton County aubrite: Igneous origin of oldhamite. Geochimica et Cosmochimica Acta 58(1):449-458.

Wood, B. J., & Strens, R. G. J. (1979). Diffuse reflectance spectra and optical properties of some sulphides and related minerals. Mineralogical Magazine, 43(328), 509-518.

Zellner B. (1975). 44 NYSA-an iron-depleted asteroid. The Astrophysical Journal 198:L45-L47.

Zellner B., Leake M., Morrison D., and Williams J.G. (1977). The E asteroids and the origin of the enstatite achondrites. Geochimica et Cosmochimica Acta 41(12):1759-1767.

Zellner, B., Tholen, D. J., & Tedesco, E. F. (1985). The eight-color asteroid survey: Results for 589 minor planets. Icarus, 61(3), 355-416.

Zipfel, J., Wlotzka, F., & Spettel, B. (1998). Bulk chemistry and mineralogy of a new" unique" metal-rich chondritic breccia, Hammadah al Hamra 237. In Lunar and Planetary Science Conference (No. 1417, p. 1417).

APPENDIX A

SUPPLEMENTAL FIGURES AND TABLES FOR CHAPTER 2

Supporting Information for **Spectral Reflectance Variations of Aubrites, Metal-rich Meteorites, and Sulfides: Implications for Exploration of (16) Psyche and other 'Spectrally Featureless' Asteroids**

Authors: Steven D. Dibb[1]*, James F. Bell III[1], and Laurence A.J. Garvie[1,2]

1 – School of Earth and Space Exploration, Arizona State University, Tempe, AZ

2 – Center for Meteorite Studies, Arizona State University, Tempe, AZ

*Corresponding author. E-mail: sd.dibb@gmail.com

Contents:

1.0 Sample Descriptions and Mineralogy

Aubrites: Aubrites are highly reduced achondrites widely regarded to be igneous products of fractional crystallization (Watterz and Prinz 1979; Keil 2010). Most are either regolith or fragmental breccias with a few notable exceptions (e.g., Shallowater)(Keil 2010). They are dominated by very low-Fe pyroxene (e.g., enstatite) with accessory plagioclase, forsterite, and diopside with minor sulfides and metal (Watters and Prinz 1979; Mittlefehldt et al. 1998). The samples in our study sample the range of aubrite compositions outlined by Watterz and Prinz (1979), Mittlefehldt et al. (1998), and Keil (2010). Enstatite abundance of the aubrites in our study ranges from 81.6 vol. % (Shallowater) to 97.5 vol. % (Mayo Belwa) and the pyroxene is >En_{98} in all the aubrites in our study (Watters and Prinz 1979; Mittlefehldt et al. 1998). Plagioclase in our samples ranges from 0.3 vol. % (Mayo Belwa) to 6.6 vol. % (Khor Temiki) and is mostly albite (Watterz and Prinz 1979). Forsterite in our samples ranges from 0.8 vol. % (Aubres) to 10 vol. % (Norton County) and is nearly Fe-free (>Fo99.7) in all samples (Watterz and Prinz 1979). Finally, diopside in our samples ranges from 0.2 vol. % (Aubres) to 2.7 vol. % (Norton County) (Watterz and Prinz, 1979). The diopside is essentially Fs free and ranges from $Wo_{42.4}$ (Mayo Belwa) to $Wo_{44.5}$ (Aubres, Khor Temiki) (Watterz and Prinz 1979). Shallowater has no measured diopside (Watterz and Prinz, 1979).

Metal-rich chondrites: We studied NWA 5492 (chond-ung), Hammadah al Hamra 237 (CBb), Quebrada Chimborazo 001 (CBa), Isheyevo (CH/CBb), and NWA 12273 (chond-ung). These samples were chosen because of their high metal content (~20-80 vol.%) and abundant chondrules rich in low-Fe mafic silicates (e.g., olivine, pyroxene). Generally, pyroxene in these meteorites has low to intermediate Fs values (~$Fs_{0.5-16}$). Troilite and glass are also variably abundant in these meteorites. Because each of these meteorites is rare and relatively unique, a brief description of each is offered here.

NWA 5492: NWA 5492 is an ungrouped chondrite breccia with ~20 vol.% metal (Friend et al. 2011; Weisberg et al. 2012). The remainder of the meteorite is made up of chondrules and lithic fragments. Silicates in these components are very Mg-rich, with olivine (5.6 vol.%) averaging $Fa_{0.3}$ and low-Ca pyroxene (39.9 vol.%) averaging $Fs_{0.8}$, $Wo_{0.5}$. High-Ca pyroxene is present (3.7 vol. %) and is $Fs_{0.4}$, Wo_{51}. Feldspathic glass and silica occupy another 16.0 vol.%. Sulfides are 2.2 vol.% of the meteorite and mostly consist of troilite. Oxygen isotopes values of NWA 5492 differ from the CB chondrites and are between E and O chondrites, while the trends in the siderophile elements in metal show some affinity for H-chondrites (Friend et al. 2011; Weisberg et al. 2015).

Hammadah al Hamra 237: HaH 237 is a metal-rich CBb chondrite (~70 vol.% metal). The metal is fine-grained and has irregular shapes (Zipfel et al. 1998). These irregular shapes include angular fragments and intact spherules, the origins of which are still debated (Zipfel et al., 1998; Weisberg et al. 1998; Meibom et al. 2005). Olivine (14.3 vol.%) and pyroxene (14.2 vol.%) are mostly Fe-poor (Fa_{2-10} and $Fs_{0.5-14}$). Troilite is a minor component of this meteorite (0.3 vol.%). Feldspar and other silicates occupy another 10 vol.% of this meteorite. Oxygen isotopes and shock features in this meteorite suggest a common asteroidal parent body for this meteorite and other CB chondrites (Weisberg et al., 1998, Meibom et al., 2005).

Quebrada Chimborazo 001: The mineralogy and texture of QC 001 is similar to other metal-rich CBa chondrites. It contains 60-80 vol.% metal with magnesian, non-porphyritic, <~1 cm sized chondrules (Koch et al. 2016). Like other CBs, the silicates in the chondrules are Fe-poor and consist mostly of olivine (Fa_{2-5}), low-Ca pyroxene (Fs_{2-5} $Wo_{0.5-1}$), and high-Ca pyroxene (Fs_{2-4} Wo_{40-50}) which can be Al-rich (7.6-18.9 wt.% Al_2O_3). These chondrules are occasionally crosscut by metal droplets interpreted to be shock melts (Koch et al., 2016). Some of the metal in QC 001 contains a high abundance of sulfide droplets. These sulfides are mostly troilite with minor daubréelite ($Fe^{2+}Cr^{3+}{}_2S_4$). Impact melts, composed mostly of ferroan silicates, metal, and sulfides are common in QC 001 and exhibit a flowing texture (Koch et al. 2016).

Isheyevo: Multiple lithologies present in this meteorite show affinity for either CH or CBb chondrites (Ivanova et al. 2006; Krot et al. 2007; Ivanova et al. 2008; Krot et al. 2008). The metal abundances of these lithologies vary from <20 vol. % (the CH-like lithology) to ~90 vol.% (the CBb-like lithology). Chondrules in Isheyevo are divided into two compositional subgroups: ferromagnesian and Al-rich. Two other features of Isheyevo stand out: the first is the presence of sedimentary laminations consistent with the Isheyevo meteorite being the end result of a gently-accreted impact plume (Morris et al. 2015; Garvie et al. 2017). The second is the extreme whole-rock enrichment in ^{15}N ($\delta^{15}N$ up to 1500 ‰), the highest ever measured for any planetary material (Ivanova et al., 2008; Bonal et al. 2010). These two features suggest Isheyevo is the product of a collision between two planetesimals that may have involved outer solar system material (Füri and Marty 2015; Garvie et al. 2017).

NWA 12273: The other ungrouped chondrite in our study, NWA 12273, consists of mostly metal (~64 vol.%) and small ferromagnesian chondrules (~30 vol.%) (Agee et al. 2019). It is unlike other CB chondrites in that its chondrules are almost exclusively ferroan as opposed to Al-rich like those in Isheyevo. The silicates in the chondrules of

NWA 12273 are significantly more Fe-rich than other CBs ($Fa_{26.3}$ and $Fs_{15.4}$, $Wo_{1.0}$). Minor troilite and glass are also present. Oxygen isotope values of NWA 12273 also separate it from other CBs in that it plots above the terrestrial fractionation line, near the values for NWA 5492 and in the region of ordinary (specifically LL) chondrites (Agee et al. 2019).

Sulfides: We studied troilite (FeS), pyrrhotite ($Fe_{1-x}S$), pentlandite ($(Fe,Ni)_9S_8$), oldhamite (CaS), and chalcopyrite ($CuFeS_2$). We collected spectra of troilite inclusions from the Nantan (IAB) and Auburn (IIG) iron meteorites and a terrestrial sample from a mine in Del Norte County, California. The meteoritic troilite contains minor daubréelite ($Fe^{2+}Cr^{3+}{}_2S_4$), schreibersite ($(Fe,Ni)_3P$), cohenite ($(Fe,Ni,Co)_3C$), and graphite. Our pyrrhotite sample was from a mine in Minas Gerais, Brazil. Thirdly, we collected spectra of two terrestrial pentlandite samples: the first is almost pure pentlandite with minor chalcopyrite from a mine near the Bushveld complex in South Africa and the other is a mixture of pentlandite and chalcopyrite from a mine in Norilsk, Russia. While chalcopyrite is not a significant mineral in meteorites, it is difficult to find large terrestrial samples of pentlandite without some additional sulfide minerals. Finally, we collected spectra of oldhamite separated from the Norton County aubrite.

Supplemental Table S2.1. Samples used in this study.

Sample name	Metal (vol.%)	Major non-metal minerals	Mineralogy references
Aubrites			
Mayo Belwa	trace	Low-Ca Pyx (97.5 vol.%, En98.97), Olv (1.6 vol.%, Fo99.79), High-Ca Pyx (0.6 vol.%, En57.47, Wo44.43), Plag (0.3 vol.%, Ab92.13, An3.26), Tro (0.1 vol.%)	
Aubres	0.1	Low-Ca Pyx (96.7 vol.%, En99.2), Plag (1.3 vol.%, Ab 91.69, An 5.54), Tro (0.9 vol.%), Olv (0.8 vol.%, Fo99.99), High-Ca Pyx (0.2 vol.%, En55.32, Wo44.53)	
Khor Temiki	0.1	Low-Ca Pyx (88.5 vol.%, En99.15), Plag (6.6 vol.%, Ab 74.98, An 23.76), Olv (3.6 vol.%, Fo99.99), High-Ca Pyx (1.5 vol.%, En 55.43, Wo 44.52), Tro (0.1 vol.%)	Watters and Prinz 1979, Mittlefehldt et al., 1998, Keil et al., 2010
Norton County	0.3	Low-Ca Pyx (84.5 vol.%, En 98.76), Olv (10.0 vol.%, Fo99.99), High-Ca Pyx (2.7 vol.%, En 57.38, Wo 42.58), Plag (1.0 vol.%, Ab 88.64, An 8.24), Tro (1.0 vol.%)	
Shallowater	3.7	Low-Ca Pyx (81.6 vol.%, En99.54), Tro (7.1 vol.%), Olv (4.7 vol.%, Fo99.86), Plag (2.9 vol.%, Ab 88.5, An 7.70)	
Chondrites			
NWA 5492	20.1	Low-Ca Pyx (44.7 vol.%, Fs 0.6, Wo 0.5), High-Ca Pyx (4.1 vol.%), Olv (6.3 vol.%, Fa 0.3), Gla (14.9 vol.%), Tro (2.5 vol.%)	Weisberg et al., 2012
Hammadah al Hamra 237	61-65	Low-Ca Pyx (14.2 vol.%, Fs 0.5-14), Olv (14,3 vol.%, Fa 2-10), Tro (0.3 vol.%), other silicates (10 vol.%)	Zipfel et al., 1998, Weisberg et al., 1998
Quebrada Chimborazo 001	60-80	Low-Ca Pyx (Fs 2-5, Wo0.5-1), Olv (Fa ~3.5), High-Ca Pyx (Fs2-4, Wo40-50), Tro	Koch et al., 2016
Isheyevo	~60	Olv (Fa 0.3-45.2), Pyx (Fs 1.8-4.6, Wo 1.7-40.8), Tro	Krot et al., 2007, Ivanova et al., 2008
NWA 12273	~64	Olv (Fa 17-28), Pyx (Fs 10-16, Wo 1.0), Tro (2.5 vol.%)	Agee et al., 2019
Sulfides			
Bushveld Pentlandite	~0	Pent, Pyr	--
Norton County CaS	~0	Old	Wheelock et al., 2004
Nantan FeS	~0	Tro, Pyr, Daub, Schr, Coh, Grap	--
Auburn FeS	~0	Tro, Pyr, Daub, Schr, Coh, Grap	--
Del Norte County FeS	~0	Tro, Pyr, Pent	--
Minas Gerais Pyrrhotite	~0	Pyr, Pent	--
Norilsk Pentlandite/ Chalcopyrite	~0	Pent, Chal	--

2.0 Powder X-ray Diffraction Analysis

Supplemental Fig. 1 shows the diffractogram of the Isheyevo powder with synthetic diffractograms of the three major components expected from previous compositional studies of this meteorite (e.g., Ivanova et al. 2008). These are α-iron (i.e., kamacite), ferromagnesian orthopyroxene, and forsterite. The majority of reflections in the diffractogram of Isheyevo are consistent with these three minerals, with the strongest peaks (at 44.75° and 65° 2θ) from the metal fraction. Visual inspection of the Isheyevo piece prior to milling suggests it belonged to the metal-rich lithology. However, this is difficult to confirm because it is unknown exactly how the smaller sections of Isheyevo in the CMS collection relate to larger samples (Garvie et al. 2017). Our XRD data suggest that the piece of Isheyevo used for powdering in this study was indeed dominated by metal with a large component of Mg-rich forsterite and some Fe-bearing orthopyroxene.

Diffractograms of the three troilite samples used in our study are shown in Supp. Fig. 2. Synthetic diffractograms of troilite and minerals commonly associated with troilite in meteorites are also shown. These minerals are pyrrhotite, pentlandite, daubréelite ($FeCr_2S_4$), and graphite. Strong peaks at 2θ angles of 30°, 33.7°, 43.2°, 47.2°, and 53.2° in the diffractograms of our samples suggest these samples are dominated by troilite. Most of these peaks have weaker reflections on either shoulder indicative of pyrrhotite, pentlandite, or daubréelite. Peaks from schreibersite and cohenite, common accessory phases of troilite in iron meteorites, are absent. Additional peaks at 44.0°, 48.8°, and 71.6° in the diffractogram of the Del Norte County terrestrial troilite suggest this sample has a relatively larger fraction of pyrrhotite than the meteoritic troilite samples. Peaks at 29.2° and 51.3° in the diffractogram of the Auburn troilite suggest this sample is more enriched in pentlandite than the other two troilite samples. Minor daubréelite is present in our three troilite samples as evidenced by peaks at 25.6° and 35.9°. A peak at 26.6° in the diffractogram of the Nantan troilite is consistent with graphite.

X-ray diffraction data from three of the other sulfides in our study are shown in Supp. Fig. 3. Synthetic diffractograms generated in CrystalDiffract of chalcopyrite, pentlandite, and pyrrhotite are shown as well. Strong reflection peaks at 15.2°, 30.8°, 39.0°, 47.0°, 51.4°, 60.5°, and 61.1° in the diffractogram of the Bushveld sample suggest it is dominated (>90 vol. %) by pentlandite. There is a minor component of pyrrhotite in this sample as evidenced by reflection peaks at 30.0°, 34.2°, 44.1°, and 53.2° 2θ. Similar reflection peaks in the diffractogram of the Minas Gerais sample suggest this sample is dominated by pyrrhotite. Finally, the sample from Norilsk has strong reflection peaks at 29.7°, 41.9°, 49.5°, 58.4°, and 59.2° 2θ consistent with the synthetic diffractogram of chalcopyrite. Weak reflections at 15.3°, 30.8°, 47.1°, and 51.6° 2θ and a broadening of the 29.7° peak are consistent with the presence of pentlandite in this sample.

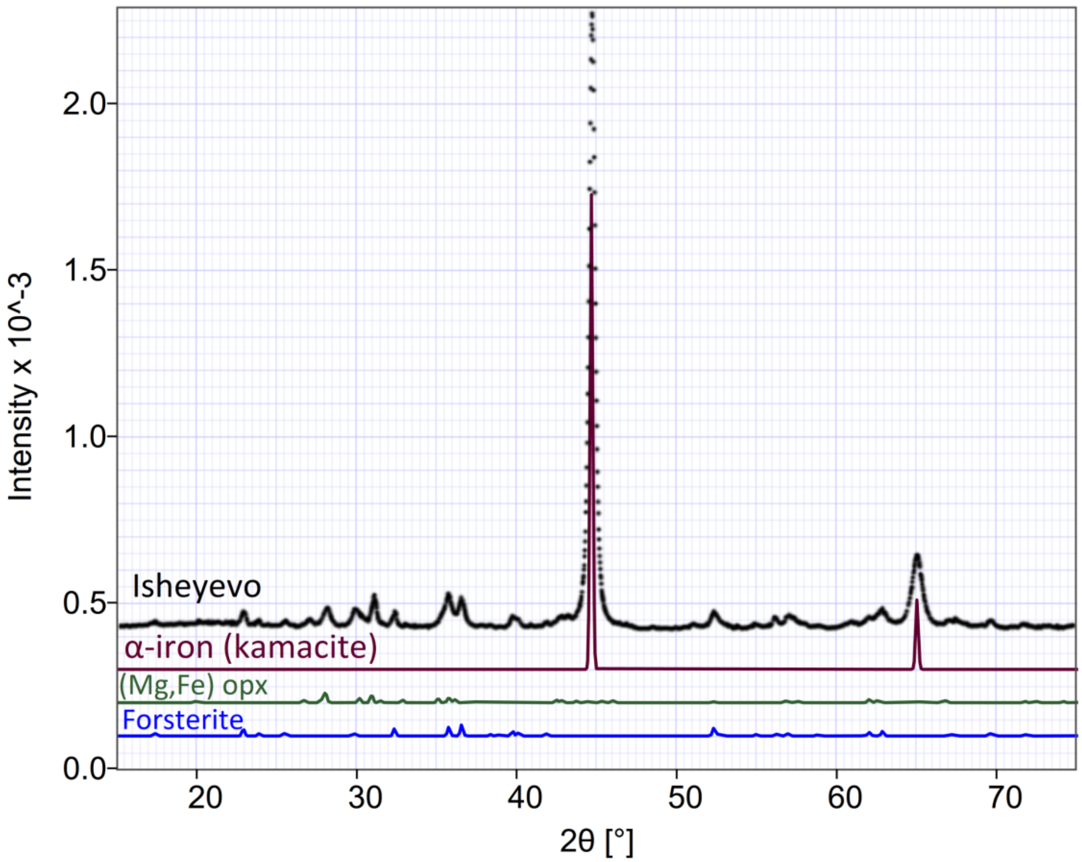

Supp. Fig. S2.1. Reflection peaks in the diffractogram of Isheyevo are consistent with a mineralogy dominated by α-iron (kamacite) with minor Fe-bearing orthopyroxene and forsterite. This composition is consistent with more detailed mineralogical studies of this meteorite (e.g., Ivanova et al. 2008). Data are scaled and offset for clarity.

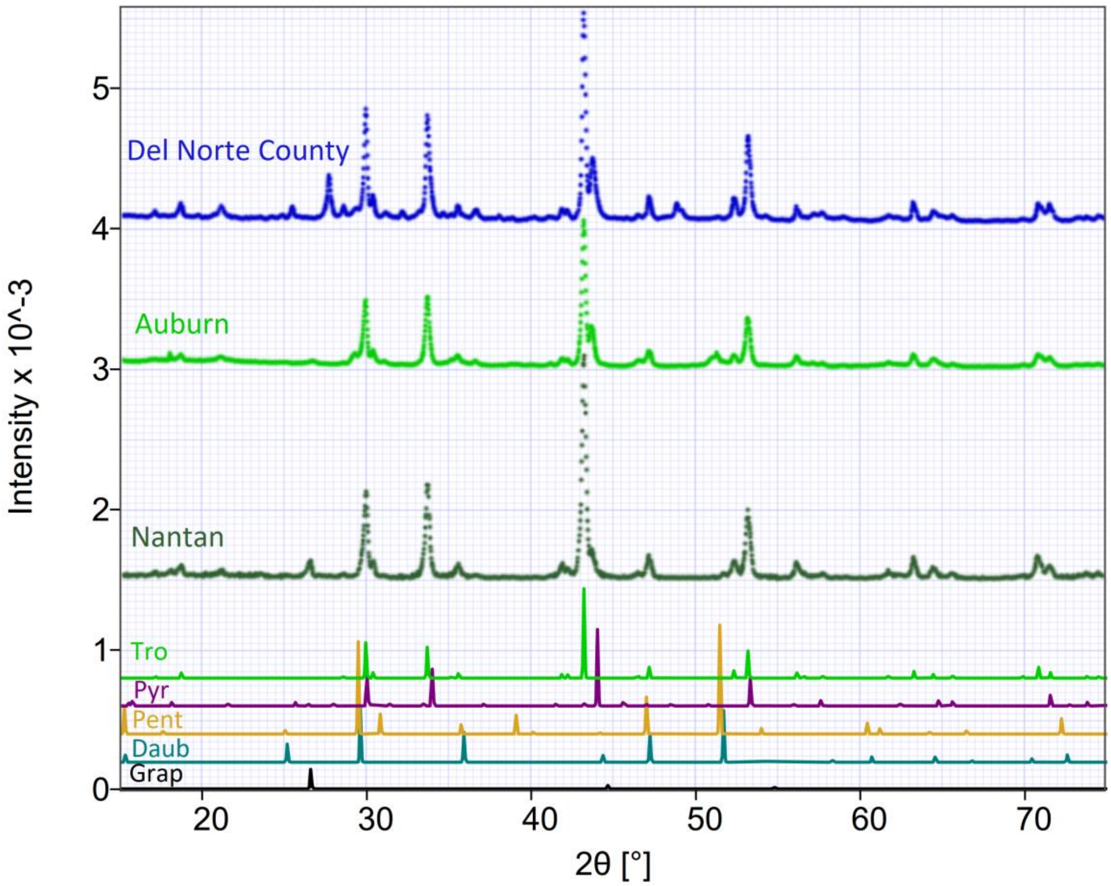

Supp. Fig. S2.2. XRD patterns for the troilites. The reflections show that troilite dominates with minor pyrrhotite, pentlandite, daubréelite, and graphite. Data are scaled and offset for clarity.

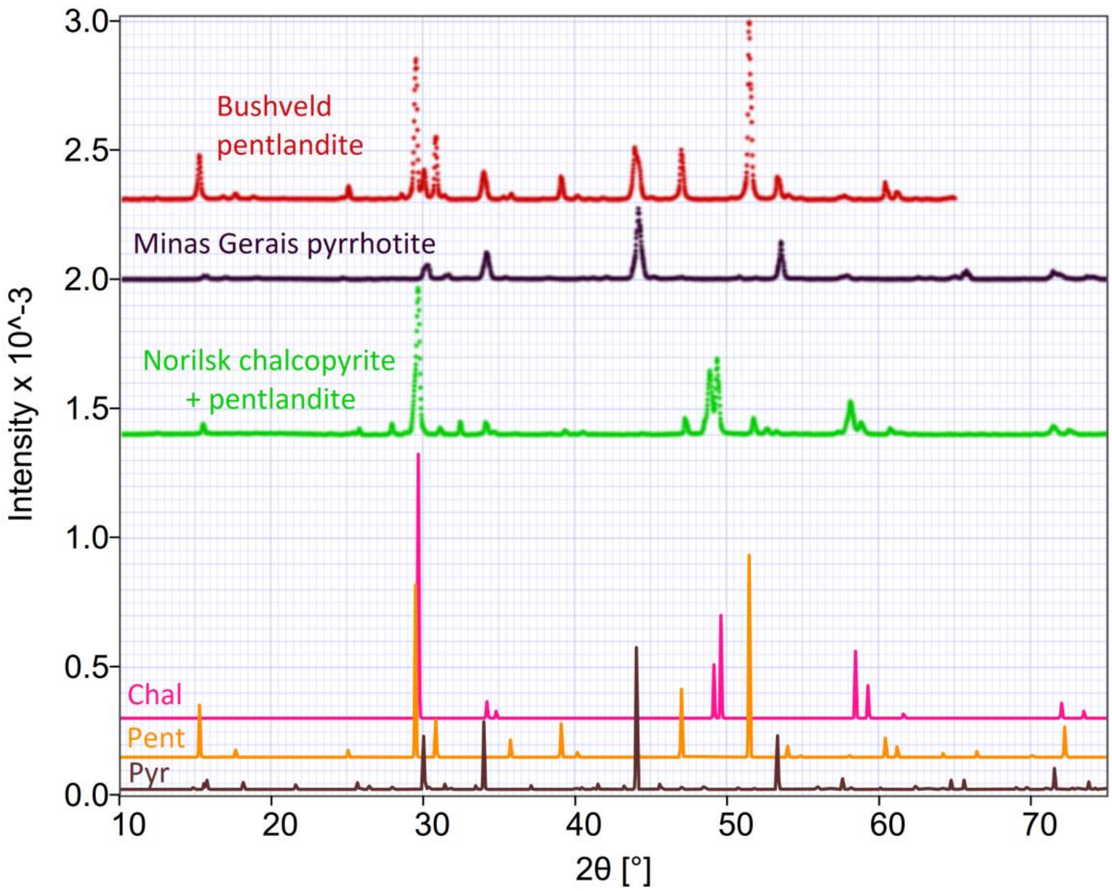

Supp. Fig. S2.3. Reflection peaks in the diffractograms of other sulfides are consistent with compositions of varying amounts of chalcopyrite, pentlandite, and pyrrhotite. Data are scaled and offset for clarity.

APPENDIX B

SUPPLEMENTAL TABLES FOR CHAPTER 3

Table S3.1. Samples used in this study.											**Pyroxene chemistry (if applicable)**			**1000 nm band parameters**			
Source	**Type**	**ID_Spectrum_name**	**Sample name**	**Physical Form**	**Class/Description/Details**	**Metal**	**Major non-metal minerals**	Grain size (microns) or ***Roughness****	**Phase angle (i/e)**	**Mineralogical or *Spectral* References**	**Fs**	**En**	**Wo**	**Band center (nm)**	**Band center err. (nm)**	**Band depth (%)**	**Band depth err. (%)**
ASU/Center for Meteorite Studies	Meteorite	01_01	Mayo Belwa	hand sample	Aubrite	trace	Pyx (En>99), Olv (Fo>99)	***1, no rust***	30/0	Watters and Prinz 1979	0.5	99	0.5	940.4	0.95	0.14	0.03
	Meteorite	01_02	Mayo Belwa	gravel				unsorted, subcentimeter	30/0					875.0	0.20	0.86	0.01
	Meteorite	02_01	Shalka	hand sample	Diogenite	0.02 vol.%	Pyx (Fs 24, En74)	***1, no rust***	30/0	Urey and Craig 1953, Bowman et al., 1996	24	74	2	919.0	<0.1	45.05	0.02
	Meteorite	02_02	Shalka	gravel				unsorted, subcentimeter	30/0					920.0	<0.1	57.13	0.02
	Meteorite	02_03	Shalka	powder				100 - 1000	30/0					920.0	<0.1	60.20	0.03
	Meteorite	02_04	Shalka	powder				<300	30/0					920.0	<0.1	59.95	0.00
	Meteorite	03_01	Aubres	slab	Aubrite	0.1 vol.%	Pyx (En>99), Plag (Ab 91.69, An 5.54), Tro	***4***	30/0	Watters and Prinz 1979	0.5	99	0.5	--	--	--	--
	Meteorite	04_01	Khor Temiki	powder	Aubrite	0.1 vol.%	Pyx (En>99), Plag (Ab 74.98, An	unsorted, submillimeter	30/0	Watters and Prinz 1979	0.5	99	0.5	--	--	--	--

							23.76), Olv (Fo~100), Diop (En 55.43, Wo 44.52)										
	Meteorite	05_01	Norton County	hand sample	Aubrite	0.16 wt.%	Pyx (En 98.8), Olv (Fo~100), Diop (En 57.38, Wo 42.58), Plag (Ab 88.64, An 8.24)	***1, no rust***	30/0	Urey and Craig 1953, Keil and Fredriksson 1963	0.6	98.8	0.6	888.8	0.62	0.54	0.01
	Meteorite	05_02	Norton County	powder				unsorted, submillimeter	30/0					867.0	0.10	1.65	0.01
	Meteorite	06_01	Shallowater	slab	Aubrite	3.7 vol.%	Pyx (En>99), Tro, Olv (Fo>99), Plag (Ab 88.5, An 7.70)	***6***	30/0	Watters and Prinz 1979	0.5	99	0.5	966.2	0.42	7.51	0.06
	Meteorite	07_01	Creston	slab	L6 Ordinary Chondrite	4-10 vol.%	Olv (Fa 24.8), Pyx (Fs 21.1,	***4***	30/0	Bouvier et al., 2017	21.1	77.6	1.3	946.0	<0.1	39.69	0.03

							Wo 1.3)										
	Meteorite	07_02	Creston	fragments				***1, no rust***	30/0					960.0	<0.1	33.82	0.03
	Meteorite	08_01	St Michel	slab	L6 Ordinary Chondrite	4.10 vol.%	Olv (Fa 24)	***4***	30/0	Mason 1963				944.0	<0.1	20.27	0.01
	Meteorite	09_01	Mbale	slab	L5/6 Ordinary Chondrite	15-20 wt.%	Olv (Fa 25.4), Pyx (Fs 21.8), Tro	***3***	30/0	Jenniskens et al., 1994	21.8	78.2	0	918.2	0.36	19.39	0.03
	Meteorite	09_02	Mbale	powder				unsorted, subcentimeter	30/0					940.0	<0.1	25.81	0.01
	Meteorite	10_01	Allegan	hand sample	H5 Ordinary Chondrite	17.95 wt.%	Olv (Fo 82), Pyx (En 83.8, Wo 0.65), Tro	***1, no rust***	30/0	Jarosewich 1990, Hutchison et al., 1981	15.55	83.8	0.65	922.0	<0.1	23.77	0.01
	Meteorite	10_02	Allegan	gravel				unsorted, subcentimeter	30/0					925.0	<0.1	25.72	0.01
	Meteorite	11_01	Eagle Station	slab	Pallasite	21.4 vol.%	Olv (Fa 20.5), Tro	***4***	30/0	Buseck 1977				1050.3	29.96	25.50	0.04
	Meteorite	12_01	Milton	slab	Pallasite	27 vol.%	Olv (Fa 17.2)	***6***	30/0	Russell et al., 2003				1054.0	<0.1	28.02	0.03
	Meteorite	12_02	Milton	slab				***6***	30/0					1047.1	0.29	11.54	0.02
	Meteorite	12_03	Milton	slab				***3***	30/0					1087.0	0.10	9.89	0.02
	Meteorite	12_04	Milton	silicate powder				unsorted, subcentimeter	30/0					1065.0	<0.1	42.42	0.02

	Meteorite	13_01	Abee	slab	EH4	27 wt. %	Pyx (En>98), Tro	***4***	30/0	Rubin and Scott 1997	1	98	1	--	--	--	--
	Meteorite	13_02	Abee	powder				<300	30/0					--	--	--	--
	Meteorite	14_01	Springwater	slab	Pallasite	27.9 vol. %	Olv (Fa 19.0)	***2***	38/8	Buseck 1977				1017.0	<0.1	23.19	0.06
	Meteorite	14_02	Springwater	Silicate powder				unsorted, subcentimeter	30/0					1065.0	<0.1	72.99	0.02
	Meteorite	15_01	Lodran	hand sample	Lodranite	28 vol. %	Pyx (Fs 13.8, Wo 2.6), Olv (Fa 12.6), Diop (Fs 6.4, Wo 43), Tro	***3***	30/0	Bild and Wasson 1976	13.8	83.6	2.6	945.0	0.20	41.79	0.01
	Meteorite	16_01	Esquel	slab	Pallasite	32 vol. %	Olv (Fa 12), Tro, Chr, Sch	***4***	30/0	Ulff-Moeller et al., 1998, Buseck 1977				--	--	--	--
	Meteorite	17_01	Steinbach	smooth slab	IVA Iron	32.2 vol. %	Pyx (En 84.82, Fs 14.80), Tro, Tri	***7***	38/8	Reid et al., 1974, Scott et al., 1996	14.8	84.82	0.38	930.1	0.32	44.38	0.05
	Meteorite	17_02	Steinbach	rough slab				***4***	38/8					910.7	0.46	15.26	0.03
	Meteorite	17_03	Steinbach	gravel				***2***	38/8					962.3	0.80	18.91	0.02
	Meteorite	18_01	NWA 8234	slab, fissured side	C2 Mesosiderite	35 wt. %	Pyx (Fs 25.5,	***5***	38/8	Ruzicka et al., 2017	25.5	72.3	2.2	903.8	0.42	24.84	0.05

	Meteorite	18_02	NWA 8234	slab, nonfissured side			Wo 2.2), Tro, Plag (An 93.1, Ab 6.6), Olv (Fa 28.4)	***5***	38/8					909.0	0.10	26.48	0.07
	Meteorite	19_01	Odessa 'Penwell'	slab	IAB Iron	50 wt.%	Gra, Olv (Fa 4.9), Pyx (Fs 6.6), Plag (An 11.8)	***4***	38/8	Moore et al., 1981, Moore et al., 1982	6.6	93.4	0	946.8	0.36	6.12	0.06
	Meteorite	20_01	Clover Springs	slab	A3/4 Mesosiderite	37 wt.%	Pyx (Fs 34, Wo 3.6), Tro	***4***	38/8	Wasson 1970, Mittlefehldt 1998	34	62.4	3.6	919.0	<0.1	16.47	0.03
	Meteorite	20_02	Clover Springs	slab				***3***	38/8					907.0	<0.1	11.81	0.03
	Meteorite	20_03	Clover Springs	powder				unsorted, submillimeter	30/0					929.1	0.32	21.53	0.05
	Meteorite	20_04	Clover Springs	gravel				unsorted, subcentimeter	30/0					934.0	<0.1	15.39	0.03
	Meteorite	21_01	Estherville	slab	A3/4 Mesosiderite	56.4 wt.%	Pyx (Fs 21.7, En 35.3), Plag (An 20.3, Ab 5.2), Tro	***3***	30/0	Powell 1971	21.7	35.3	43	918.0	<0.1	20.36	0.01

	Meteorite	22_01	Landes	slab	IAB Iron	81 wt.%	Olv (Fa 4), Pyx (Fs 6.2, Wo 1.7), Gra, Diop (Fs 3.2, En 51.4), Tro	***3***	38/8	Bunch et al., 1972, Mittlefehldt 1998	6.2	92.1	1.7	887.0	0.22	6.33	0.03
	Meteorite	22_02	Landes	slab				***4***	38/8		3.2	51.4	45.4	889.0	<0.1	8.95	0.08
	Meteorite	23_01	Canyon Diablo, troilite	slab	Troilite from IAB Iron	0 wt.%	Tro	***7***	30/0					--	--	--	--
	Meteorite	24_01	Santiago Papasquiero	rough slab	Ungrouped Iron	>99 wt.%	Tro	***2***	38/8					--	--	--	--
	Meteorite	24_02	Santiago Papasquiero	smooth slab				***4***	38/8					--	--	--	--
	Meteorite	24_03	Santiago Papasquiero	powder				unsorted, submillimeter	30/0					--	--	--	--
	Meteorite	25_01	Gibeon	slab	IVA Iron	>99 wt.%		***3***	38/8	Schaudy et al., 1972				--	--	--	--
	Meteorite	25_02	Gibeon	powder				unsorted, submillimeter	30/0					--	--	--	--
	Meteorite	25_03	Gibeon	powder				unsorted, submillimeter	38/8					--	--	--	--
	Meteorite	25_04	Gibeon	powder				<75	38/8					--	--	--	--
	Meteorite	25_05	Gibeon	powder				>75	38/8					--	--	--	--
	Meteorite	25_06	Gibeon	powder				<75	23/8					--	--	--	--
	Meteorite	25_07	Gibeon	powder				>75	23/8					--	--	--	--
	Meteorite	25_08	Gibeon	powder				<75	53/8					--	--	--	--

	Meteorite	25_09	Gibeon	powder				>75	53/8					--	--	--	--
	Meteorite	26_01	Odessa	metal	IAB Iron	>99 wt. %	Gra, Tro	***7***	30/0					--	--	--	--
	Meteorite	26_02	Odessa	FeS		0 wt. %	Tro	***7***	30/0					--	--	--	--
	Meteorite	27_01	NWA 5492	rough slab	Ungrouped Chondrite	20.1 vol. %	Pyx (Fs 0.8, Wo 0.5), Olv (Fa 2.0), Gla, Tro	***3***	38/8	Weisberg et al., 2012	0.8	98.7	0.5	934.0	<0.1	5.00	0.02
	Meteorite	27_02	NWA 5492	smooth slab				***6***	38/8					925.0	<0.1	5.42	0.01
	Meteorite	28_01	Hammadah al Hamra 237	rough slab	CBb Chondrite	57 vol. %	Pyx (Fs ~7), Olv (Fa<5), Tro	***3***	38/8	Zipfel et al., 1998	7	92	1	896.0	0.10	6.84	0.02
	Meteorite	28_02	Hammadah al Hamra 237	smooth slab				***4***	38/8					932.2	0.36	10.78	0.06
	Meteorite	29_01	Quebrada Chimborazo 001	roughened slab	CBa Chondrite	60-80 vol. %	Pyx (Fs ~3.5), Olv (Fa ~3.5)	***4***	38/8	Koch et al., 2016	3.5	95.5	1	930.0	<0.1	10.74	0.04
	Meteorite	29_02	Quebrada Chimborazo 001	smooth slab				***6***	38/8		3	52	45	921.0	<0.1	18.86	0.04
	Meteorite	30_01	Isheyevo	slab	CH/CBb Chondrite	50-70 vol. %	Fo (Fa 2 and Fa 10-38), Pyx (Fs 2 and Fs	***6***	38/8	Ivanova et al., 2008	2	96.5	1.5	934.4	0.49	1.53	0.10
	Meteorite	30_02	Isheyevo	powder				unsorted, submillimeter	38/8		11	87.5	1.5	872.2	0.38	1.89	0.03

							10-12, Wo 1-2), Tro										
	Meteorite	30_03	Isheyevo	powder				<75	38/8					947.4	0.49	0.39	0.01
	Meteorite	30_04	Isheyevo	powder				>75	38/8					927.0	0.10	1.50	0.01
	Meteorite	30_05	Isheyevo	powder				<75	23/8					901.1	0.27	0.92	0.01
	Meteorite	30_06	Isheyevo	powder				>75	23/8					941.1	0.34	1.68	0.02
	Meteorite	30_07	Isheyevo	powder				<75	53/8					857.0	<0.1	3.52	0.03
	Meteorite	30_08	Isheyevo	powder				>75	53/8					879.4	0.48	3.10	0.02
	Meteorite	31_01	NWA 12273	smooth	Ungrouped Chondrite	75 vol. %	Olv (Fa 26.3), Pyx (Fs 15.4, Wo 1.0)	***6***	38/8	Agee et al., 2019, Gattacceca et al., 2020	15.4	83.6	1	929.3	0.47	16.91	0.05
	Meteorite	31_02	NWA 12273	rough				***4***	38/8					919.0	<0.1	9.57	0.04
	Mineral	32_01	Nickel sulfide	hand sample	Pentlandite hand sample	0 wt. %	Pent, pyr	***1, no rust***	30/0	*Dibb et al. 2021a*				--	--	--	--
	Mineral	32_02	Nickel Sulfide	powder				unsorted, submillimeter	30/0					--	--	--	--
	Meteorite	33_01	Norton County CaS	powder	Oldhamite extracted from Norton County aubrite	0 wt. %	Old	unsorted, submillimeter	30/0	*Dibb et al. 2021a*				951.0	<0.1	22.33	0.08
	Meteorite	34_01	Nantan FeS	slab	Troilite from IAB Iron	0 wt. %	Tro	***5***	38/8	*Dibb et al. 2021a*				--	--	--	--
	Meteorite	34_02	Nantan FeS	slab				***3***	38/8					--	--	--	--
	Meteorite	34_03	Nantan FeS	powder				<500	38/8					--	--	--	--
	Meteorite	34_04	Nantan FeS	powder				<75	38/8					--	--	--	--
	Meteorite	34_05	Nantan FeS	powder				>75	38/8					--	--	--	--

	Meteorite	34_06	Nantan FeS	powder				<75	23/8						--	--	--	--
	Meteorite	34_07	Nantan FeS	powder				>75	23/8						--	--	--	--
	Meteorite	34_08	Nantan FeS	powder				<75	53/8						--	--	--	--
	Meteorite	34_09	Nantan FeS	powder				>75	53/8						--	--	--	--
	Meteorite	35_01	Auburn FeS	slab	Troilite from IIG Iron	0 wt. %	Tro	***5***	38/8						--	--	--	--
	Meteorite	35_02	Auburn FeS	powder				unsorted, submillimeter	38/8	*Dibb et al. 2021a*					--	--	--	--
	Meteorite	35_03	Auburn FeS	powder				<75	38/8						--	--	--	--
	Meteorite	35_04	Auburn FeS	powder				>75	38/8						--	--	--	--
	Mineral	36_01	Del Norte County FeS	slab	Troilite from terrestrial mine in USA	0 wt. %	Tro	***5***	38/8						--	--	--	--
	Mineral	36_02	Del Norte County FeS	powder				unsorted, submillimeter	38/8	*Dibb et al. 2021a*					--	--	--	--
	Mineral	36_03	Del Norte County FeS	powder				<75	38/8						--	--	--	--
	Mineral	36_04	Del Norte County FeS	powder				>75	38/8						--	--	--	--
	Mineral	37_01	Bushveld Pyrrhotite	hand sample	Pyrrhotite sample from Bushveld Complex, SA	0 wt. %	Pyr	***1, no rust***	38/8	*Dibb et al. 2021a*					--	--	--	--
	Mineral	38_01	Minas Gerais Pyrrhotite	powder	Pyrrhotite sample from Minas Gerais mine, Brazil	0 wt. %	Pyr	unsorted, subcentimeter	38/8						--	--	--	--
	Mineral	38_02	Minas Gerais Pyrrhotite	powder				<75	38/8	*Dibb et al. 2021a*					--	--	--	--
	Mineral	38_03	Minas Gerais Pyrrhotite	powder				>75	38/8						--	--	--	--
	Mineral	38_04	Minas Gerais Pyrrhotite	powder				<75	23/8						--	--	--	--

	Mineral	38_05	Minas Gerais Pyrrhotite	powder				>75	23/8					--	--	--	--
	Mineral	38_06	Minas Gerais Pyrrhotite	powder				<75	53/8					--	--	--	--
	Mineral	38_07	Minas Gerais Pyrrhotite	powder				>75	53/8					--	--	--	--
	Meteorite	39_01	Sikhote-Alin	powder	IIAB Iron	>99 wt. %		unsorted, submillimeter	38/8					--	--	--	--
	Meteorite	39_02	Sikhote-Alin	powder				<75	38/8					--	--	--	--
	Meteorite	39_03	Sikhote-Alin	powder				>75	38/8					--	--	--	--
	Meteorite	39_04	Sikhote-Alin	powder				<75	23/8					--	--	--	--
	Meteorite	39_05	Sikhote-Alin	powder				>75	23/8					--	--	--	--
	Meteorite	39_06	Sikhote-Alin	powder				<75	53/8					--	--	--	--
	Meteorite	39_07	Sikhote-Alin	powder				>75	53/8					--	--	--	--
	Mineral	40_01	Norilsk Pentlandite	powder	Pentlandite from Norilsk mine, Russia	0 wt. %	Pent, chal	***1, no rust***	38/8					--	--	--	--
	Mineral	40_02	Norilsk Pentlandite	powder				unsorted, submillimeter	38/8					897.8	0.36	6.09	0.02
	Mineral	40_03	Norilsk Pentlandite	powder				<75	38/8					906.0	<0.1	5.49	<0.01
	Mineral	40_04	Norilsk Pentlandite	powder				>75	38/8	*Dibb et al. 2021a*				890.0	<0.1	5.66	0.01
	Mineral	40_05	Norilsk Pentlandite	powder				<75	23/8					904.0	<0.1	5.06	0.01
	Mineral	40_06	Norilsk Pentlandite	powder				>75	23/8					906.2	0.39	5.97	0.01
	Mineral	40_07	Norilsk Pentlandite	powder				<75	53/8					910.0	<0.1	5.06	0.01

	Mineral	40_08	Norilsk Pentlandite	powder				>75	53/8					887.0	0.17	5.35	0.02
	Mixtures	41_01	MTMIX1	powder	100 wt.% Gibeon + 0 wt. % Nantan FeS	100 wt. %	Tro	<75	38/8					--	--	--	--
	Mixtures	41_02	MTMIX2	powder	80 wt.% Gibeon + 20 wt.% Nantan FeS	80 wt. %	Tro	<76	38/8					--	--	--	--
	Mixtures	41_03	MTMIX3	powder	60 wt.% Gibeon + 40 wt.% Nantan FeS	60 wt. %	Tro	<77	38/8	*Dibb et al. 2021b*				--	--	--	--
	Mixtures	41_04	MTMIX4	powder	40 wt.% Gibeon + 60 wt.% Nantan FeS	40 wt. %	Tro	<78	38/8					--	--	--	--
	Mixtures	41_05	MTMIX5	powder	20 wt.% Gibeon + 80 wt.% Nantan FeS	20 wt. %	Tro	<79	38/8					--	--	--	--
	Mixtures	41_06	MTMIX6	powder	0 wt.% Gibeon + 100 wt.% Nantan FeS	0 wt. %	Tro	<80	38/8					--	--	--	--
														--	--	--	--
	Mixtures	MPMIX 1001	Orthopyroxene (PYX042) + metal (MET101A)	powder	100 wt.% En50.8 Fs45.6 OPX + 0 wt.% Odessa	0 wt. %	Pyx (En 50.8, Fs 45.6)	<45 microns	35/0		45.6	50.8	3.6	916.0	<0.1	50.24	0.01
UWinnipeg/ Planetary Spectrophotometer Facility		MPMIX 1002	Orthopyroxene (PYX042) + metal (MET101A)	powder	90 wt.% En50.8 Fs45.6 OPX + 10 wt.% Odessa	10 wt. %		<45 microns	35/0	*Cloutis et al., 1990*				916.0	<0.1	40.04	<0.01
		MPMIX 1003	Orthopyroxene (PYX042) + metal (MET101A)	powder	80 wt.% En50.8 Fs45.6 OPX + 20wt.% Odessa	20 wt. %		<45 microns	35/0					915.0	<0.1	32.93	0.01
		MPMIX 1004	Orthopyroxene (PYX042) + metal	powder	70 wt.% En50.8 Fs45.6 OPX + 30 wt.% Odessa	30 wt. %		<45 microns	35/0					915.0	<0.1	27.76	0.01

			(MET101 A)														
		MPMIX 1005	Orthopyroxene (PYX042) + metal (MET101 A)	powder	60 wt.% En50.8 Fs45.6 OPX + 40 wt.% Odessa	40 wt.%		<45 microns	35/0					915.0	<0.1	20.82	0.01
		MPMIX 1006	Orthopyroxene (PYX042) + metal (MET101 A)	powder	50 wt.% En50.8 Fs45.6 OPX +50 wt.% Odessa	50 wt.%		<45 microns	35/0					914.1	0.26	17.02	0.01
		MPMIX 1007	Orthopyroxene (PYX042) + metal (MET101 A)	powder	40 wt.% En50.8 Fs45.6 OPX + 60 wt.% Odessa	60 wt.%		<45 microns	35/0					915.0	<0.1	17.38	0.01
		MPMIX 1008	Orthopyroxene (PYX042) + metal (MET101 A)	powder	30 wt.% En50.8 Fs45.6 OPX + 70 wt.% Odessa	70 wt.%		<45 microns	35/0					917.0	<0.1	9.94	0.02
		MPMIX 1009	Orthopyroxene (PYX042) + metal (MET101 A)	powder	20 wt.% En50.8 Fs45.6 OPX + 80 wt.% Odessa	80 wt.%		<45 microns	35/0					918.0	<0.1	5.88	0.02
		MPMIX 1010	Orthopyroxene (PYX042) + metal (MET101 A)	powder	10 wt.% En50.8 Fs45.6 OPX + 90 wt.% Odessa	90 wt.%		<45 microns	35/0					922.0	<0.1	2.63	0.02
		MPMIX 1011	Orthopyroxene (PYX042) + metal (MET101 A)	powder	0 wt.% En50.8 Fs45.6 OPX + 100 wt.% Odessa	100 wt.%		<45 microns	35/0					1130.8	4.64	0.22	0.01

		MOMIX 2001	Olivine (OLV003) + metal (MET101A)	powder	100 wt.% Fo90.4 OLV + 0 wt. % Odessa	0 wt. %	Olv (Fo 90.4)	<45 microns	35/0					1053.0	<0.1	33.81	0.04
		MOMIX 2002	Olivine (OLV003) + metal (MET101A)	powder	90 wt.% Fo90.4 OLV + 10 wt. % Odessa	10 wt. %		<45 microns	35/0					1053.0	0.10	19.98	0.01
		MOMIX 2003	Olivine (OLV003) + metal (MET101A)	powder	80 wt.% Fo90.4 OLV + 20 wt. % Odessa	20 wt. %		<45 microns	35/0					1052.0	<0.1	13.29	0.02
		MOMIX 2004	Olivine (OLV003) + metal (MET101A)	powder	70 wt.% Fo90.4 OLV + 30 wt. % Odessa	30 wt. %		<45 microns	35/0					1050.0	<0.1	10.40	0.00
		MOMIX 2005	Olivine (OLV003) + metal (MET101A)	powder	60 wt.% Fo90.4 OLV + 40 wt. % Odessa	40 wt. %		<45 microns	35/0	*Cloutis et al., 1990*				1051.0	<0.1	7.88	0.01
		MOMIX 2006	Olivine (OLV003) + metal (MET101A)	powder	50 wt.% Fo90.4 OLV + 50 wt. % Odessa	50 wt. %		<45 microns	35/0					1054.0	<0.1	5.80	0.01
		MOMIX 2007	Olivine (OLV003) + metal (MET101A)	powder	40 wt.% Fo90.4 OLV + 60 wt. % Odessa	60 wt. %		<45 microns	35/0					1053.2	0.38	4.25	0.02
		MOMIX 2008	Olivine (OLV003) + metal (MET101A)	powder	30 wt.% Fo90.4 OLV + 70 wt. % Odessa	70 wt. %		<45 microns	35/0					1045.0	<0.1	2.29	0.01
		MOMIX 2009	Olivine (OLV003) + metal (MET101A)	powder	20 wt.% Fo90.4 OLV + 80 wt. % Odessa	80 wt. %		<45 microns	35/0					1050.6	0.73	1.50	0.01

		MOMIX 2010	Olivine (OLV003) + metal (MET101A)	powder	10 wt.% Fo90.4 OLV + 90 wt. % Odessa	90 wt. %		<45 microns	35/0					1044.0	<0.1	0.86	0.01
		MOMIX 2011	Olivine (OLV003) + metal (MET101A)	powder	0 wt.% Fo90.4 OLV + 100 wt. % Odessa	100 wt. %		<45 microns	35/0					1153.0	0.10	0.52	0.02
		MET101	MET101	powder	Odessa IAB iron meteorite powder	100 wt. %		45-90 microns	0/15					--	--	--	--
		OLV003	Olivine (OLV003)	powder	Fo90.4 olivine	0 wt. %	Olv (Fo 90.4)	45-90 microns	0/15					1056.0	<0.1	69.53	0.03
		PYX117	Orthopyroxene (PYX117)	powder	En73.67 Fs25.65 orthopyroxene	0 wt. %	Pyx (En 73.67, Fs 25.65)	45-90 microns	0/15		25.65	73.67	0.68	922.9	0.29	80.44	0.04
		MIX266	Olivine (OLV003) + orthopyroxene (PYX117) + metal (MET101)	powder	30 wt.% OLV003 + 40 wt.% PYX117 + 30 wt.% MET101	30 wt. %		45-90 microns	0/15	*Cloutis et al., 1990*				922.0	<0.1	40.63	0.03
		MIX271	Olivine (OLV003) + orthopyroxene (PYX117) + metal (MET101)	powder	42.9 wt.% OLV003 + 57.1 wt.% PYX117 + 0 wt.% MET101	0 wt. %		45-90 microns	0/15					927.0	0.14	69.65	0.02
		MIX275	Troilite + metal (MET101A)	powder	90 wt.% metal + 10 wt.% troilite	90 wt. %	Tro	<45 microns						--	--	--	--
		MET101	MET101A	powder	100 wt.% metal	100 wt. %		<45 microns						--	--	--	--

		TRO201	Troilite	powder	100 wt.% troilite	0 wt.%	Tro	<45 microns						--	--	--	--
		PMIX1101	Clinopyroxene (PYX005) + Orthopyroxene (PYX023)	powder	100 wt.% Fs 29.66 En 67.08 CPX + 0 wt.% Fs 10.36 En 88.43 OPX	0 wt.%	Pyx (Fs 29.66, En 67.08), Pyx (Fs 10.36, En 88.43)	<45 microns	30/0	*Horgan et al., 2014*	29.66	67.08	3.26	1035.0	<0.1	11.69	0.03
		PMIX1102	Clinopyroxene (PYX005) + Orthopyroxene (PYX023)	powder	90 wt.% Fs 29.66 En 67.08 CPX + 10 wt.% Fs 10.36 En 88.43 OPX	0 wt.%		<45 microns	30/0					1028.0	<0.1	11.33	0.03
		PMIX1103	Clinopyroxene (PYX005) + Orthopyroxene (PYX023)	powder	80 wt.% Fs 29.66 En 67.08 CPX + 20 wt.% Fs 10.36 En 88.43 OPX	0 wt.%		<45 microns	30/0					1010.0	0.14	11.01	0.01
		PMIX1104	Clinopyroxene (PYX005) + Orthopyroxene (PYX023)	powder	70 wt.% Fs 29.66 En 67.08 CPX + 30 wt.% Fs 10.36 En 88.43 OPX	0 wt.%		<45 microns	30/0					948.0	<0.1	12.84	0.01
		PMIX1105	Clinopyroxene (PYX005) + Orthopyroxene (PYX023)	powder	60 wt.% Fs 29.66 En 67.08 CPX + 40 wt.% Fs 10.36 En 88.43 OPX	0 wt.%		<45 microns	30/0					933.0	<0.1	16.34	0.02
		PMIX1106	Clinopyroxene (PYX005) + Orthopyroxene (PYX023)	powder	50 wt.% Fs 29.66 En 67.08 CPX + 50 wt.% Fs 10.36 En 88.43 OPX	0 wt.%		<45 microns	30/0					925.6	0.49	19.87	0.03

		PMIX1107	Clinopyroxene (PYX005) + Orthopyroxene (PYX023)	powder	40 wt.% Fs 29.66 En 67.08 CPX + 60 wt.% Fs 10.36 En 88.43 OPX	0 wt.%		<45 microns	30/0					922.0	<0.1	24.34	0.03
		PMIX1108	Clinopyroxene (PYX005) + Orthopyroxene (PYX023)	powder	30 wt.% Fs 29.66 En 67.08 CPX + 70 wt.% Fs 10.36 En 88.43 OPX	0 wt.%		<45 microns	30/0					919.0	<0.1	26.95	0.02
		PMIX1109	Clinopyroxene (PYX005) + Orthopyroxene (PYX023)	powder	20 wt.% Fs 29.66 En 67.08 CPX + 80 wt.% Fs 10.36 En 88.43 OPX	0 wt.%		<45 microns	30/0					917.0	<0.1	32.55	0.02
		PMIX1110	Clinopyroxene (PYX005) + Orthopyroxene (PYX023)	powder	10 wt.% Fs 29.66 En 67.08 CPX + 90 wt.% Fs 10.36 En 88.43 OPX	0 wt.%		<45 microns	30/0					916.0	<0.1	37.44	0.01
		PMIX1111	Clinopyroxene (PYX005) + Orthopyroxene (PYX023)	powder	0 wt.% Fs 29.66 En 67.08 CPX + 100 wt.% Fs 10.36 En 88.43 OPX	0 wt.%		<45 microns	30/0					915.0	<0.1	44.21	0.01
		PMIX2001	Clinopyroxene (PYX005) + Orthopyroxene (PYX023)	powder	100 wt.% Fs 9.79 En 46.64 CPX + 0 wt.% Fs 45.85 En 50.84 OPX	0 wt.%	Pyx (Fs 9.79, En 46.64), Pyx (Fs 45.85, En 50.84)	90-180 microns	35/0		9.79	46.64	43.57	1039.0	<0.1	59.16	0.15
		PMIX2002	Clinopyroxene (PYX005) +	powder	80 wt.% Fs 9.79 En 46.64 CPX + 20 wt.% Fs 45.85 En 50.84 OPX	0 wt.%		90-180 microns	35/0					1018.0	<0.1	54.70	0.05

			Orthopyroxene (PYX023)														
		PMIX2003	Clinopyroxene (PYX005) + Orthopyroxene (PYX023)	powder	60 wt.% Fs 9.79 En 46.64 CPX + 40 wt.% Fs 45.85 En 50.84 OPX	0 wt.%		90-180 microns	35/0					997.0	0.17	53.30	0.06
		PMIX2004	Clinopyroxene (PYX005) + Orthopyroxene (PYX023)	powder	40 wt.% Fs 9.79 En 46.64 CPX + 60 wt.% Fs 45.85 En 50.84 OPX	0 wt.%		90-180 microns	35/0					992.0	0.17	54.44	0.05
		PMIX2005	Clinopyroxene (PYX005) + Orthopyroxene (PYX023)	powder	20 wt.% Fs 9.79 En 46.64 CPX + 80 wt.% Fs 45.85 En 50.84 OPX	0 wt.%		90-180 microns	35/0					968.0	0.17	54.52	0.03
		PMIX2006	Clinopyroxene (PYX005) + Orthopyroxene (PYX023)	powder	0 wt.% Fs 9.79 En 46.64 CPX + 100 wt.% Fs 45.85 En 50.84 OPX	0 wt.%		90-180 microns	35/0					948.0	<0.1	54.07	0.05
		POMIX1001	Orthopyroxene (PYX042) + Olivine (OLV003)	powder	0 wt.% En50.8 Fs45.6 OPX + 100 wt.% Fo90.4 OLV	0 wt.%	Pyx (En 50.8, Fs 45.6), Olv (Fo 90.4)	<38 microns	30/0	*Horgan et al., 2014*	45.6	50.8	3.6	1055.0	<0.1	30.96	0.01
		POMIX1002	Orthopyroxene (PYX042) + Olivine (OLV003)	powder	10 wt.% En50.8 Fs45.6 OPX + 90 wt.% Fo90.4 OLV	0 wt.%		<38 microns	30/0					1042.0	<0.1	29.03	0.04
		POMIX1003	Orthopyroxene (PYX042)	powder	20 wt.% En50.8 Fs45.6 OPX + 80	0 wt.%		<38 microns	30/0					969.1	0.32	29.49	0.02

			+ Olivine (OLV003)		wt.% Fo90.4 OLV												
		POMIX1004	Orthopyroxene (PYX042) + Olivine (OLV003)	powder	30 wt.% En50.8 Fs45.6 OPX + 70 wt.% Fo90.4 OLV	0 wt. %		<38 microns	30/ 0					932. 0	<0.1	35. 29	0.0 3
		POMIX1005	Orthopyroxene (PYX042) + Olivine (OLV003)	powder	40 wt.% En50.8 Fs45.6 OPX + 60 wt.% Fo90.4 OLV	0 wt. %		<38 microns	30/ 0					923. 0	<0.1	41. 32	0.0 2
		POMIX1006	Orthopyroxene (PYX042) + Olivine (OLV003)	powder	50 wt.% En50.8 Fs45.6 OPX + 50 wt.% Fo90.4 OLV	0 wt. %		<38 microns	30/ 0					919. 0	<0.1	45. 55	0.0 2
		POMIX1007	Orthopyroxene (PYX042) + Olivine (OLV003)	powder	60 wt.% En50.8 Fs45.6 OPX + 40 wt.% Fo90.4 OLV	0 wt. %		<38 microns	30/ 0					917. 0	<0.1	50. 11	0.0 2
		POMIX1008	Orthopyroxene (PYX042) + Olivine (OLV003)	powder	70 wt.% En50.8 Fs45.6 OPX + 30 wt.% Fo90.4 OLV	0 wt. %		<38 microns	30/ 0					915. 0	<0.1	56. 45	0.0 2
		POMIX1009	Orthopyroxene (PYX042) + Olivine (OLV003)	powder	80 wt.% En50.8 Fs45.6 OPX + 20 wt.% Fo90.4 OLV	0 wt. %		<38 microns	30/ 0					913. 0	<0.1	61. 70	0.0 3
		POMIX1010	Orthopyroxene (PYX042) + Olivine (OLV003)	powder	90 wt.% En50.8 Fs45.6 OPX + 10 wt.% Fo90.4 OLV	0 wt. %		<38 microns	30/ 0					913. 0	<0.1	67. 54	0.0 1

		POMIX1011	Orthopyroxene (PYX042) + Olivine (OLV003)	powder	100 wt.% En50.8 Fs45.6 OPX + 0 wt.% Fo90.4 OLV	0 wt. %		<38 microns	30/0					913.0	<0.1	74.14	0.01
		PYX016	Clinopyroxene (PYX016)	powder	100 wt.% Fs 2.72 En 48.48 CPX + 0 wt.% Fo 90.4 OLV	0 wt. %	Pyx (En 48.48, Fs 2.72), Olv (Fo 90.4)	<45 microns	30/0	*Horgan et al., 2014*	2.72	48.48	48.8	1050.0	<0.1	24.45	0.01
		OLV003	Olivine (OLV003)	powder	0 wt.% Fs 2.72 En 48.48 CPX + 100 wt.% Fo 90.4 OLV	0 wt. %	Olv (Fo 90.4)	<45 microns	30/0					1056.0	<0.1	69.53	0.03
		MIX031	Clinopyroxene (PYX016) + Olivine (OLV003)	powder	20 wt.% Fs 2.72 En 48.48 CPX + 80 wt.% Fo90.4 OLV	0 wt. %		<45 microns	30/0					1054.0	<0.1	30.79	0.02
		MIX032	Clinopyroxene (PYX016) + Olivine (OLV003)	powder	40 wt.% Fs 2.72 En 48.48 CPX + 60 wt.% Fo90.4 OLV	0 wt. %		<45 microns	30/0					1052.0	<0.1	28.91	0.02
		MIX033	Clinopyroxene (PYX016) + Olivine (OLV003)	powder	60 wt.% Fs 2.72 En 48.48 CPX + 40 wt.% Fo90.4 OLV	0 wt. %		<45 microns	30/0					1052.0	<0.1	28.25	0.01
		MIX034	Clinopyroxene (PYX016) + Olivine (OLV003)	powder	80 wt.% Fs 2.72 En 48.48 CPX + 20 wt.% Fo90.4 OLV	0 wt. %		<45 microns	30/0					1050.0	<0.1	25.07	0.01
	Meteorites	feb2107.022	MET01 400 grit	slab	Odessa IAB Iron	>99 wt. %		400 grit	35/0	*Cloutis et al., 2010*				--	--	--	--

		feb2107.023	MET02 400 grit	slab	Hoba IVB Iron	>99 wt. %		400 grit	35/0					--	--	--	--
		feb2107.024	MET03 400 grit	slab	North Chile IIAB Iron	>99 wt. %		400 grit	35/0					--	--	--	--
		feb2107.025	MET01 220 grit	slab	Odessa IAB Iron	>99 wt. %		220 grit	35/0					--	--	--	--
		feb2107.026	MET02 220 grit	slab	Hoba IVB Iron	>99 wt. %		220 grit	35/0					--	--	--	--
		feb2107.027	MET03 220 grit	slab	North Chile IIAB Iron	>99 wt. %		220 grit	35/0					--	--	--	--
		feb2107.028	MET01 120 grit	slab	Odessa IAB Iron	>99 wt. %		120 grit	35/0					--	--	--	--
		feb2107.029	MET02 120 grit	slab	Hoba IVB Iron	>99 wt. %		120 grit	35/0					--	--	--	--
		feb2107.030	MET03 120 grit	slab	North Chile IIAB Iron	>99 wt. %		120 grit	35/0					--	--	--	--
		feb2107.031	MET01 60 grit	slab	Odessa IAB Iron	>99 wt. %		60 grit	35/0					--	--	--	--
		feb2107.032	MET02 60 grit	slab	Hoba IVB Iron	>99 wt. %		60 grit	35/0					--	--	--	--
		feb2107.033	MET03 60 grit	slab	North Chile IIAB Iron	>99 wt. %		60 grit	35/0					--	--	--	--
		feb1607.002	MET01A	powder	Odessa IAB Iron	>99 wt. %		<45 µm	30/0	*Cloutis et al., 2010*				--	--	--	--
		feb1607.004	MET01B	powder	Odessa IAB Iron	>99 wt. %		45-90 µm	30/0					--	--	--	--
		feb1607.005	MET01C	powder	Odessa IAB Iron	>99 wt. %		90-250 µm	30/0					--	--	--	--
		feb1607.006	MET02A	powder	Hoba IVB Iron	>99 wt. %		<45 µm	30/0					--	--	--	--

		feb1607.007	MET02B	powder	Hoba IVB Iron	>99 wt. %		45-90 µm	30/0					--	--	--	--
		feb1607.008	MET02C	powder	Hoba IVB Iron	>99 wt. %		90-250 µm	30/0					--	--	--	--
		feb1607.009	MET03A	powder	North Chile IIAB Iron	>99 wt. %		<45 µm	30/0					--	--	--	--
		feb1607.010	MET03B	powder	North Chile IIAB Iron	>99 wt. %		45-90 µm	30/0					--	--	--	--
		mar0107.004	MET01A	powder	Odessa IAB Iron	>99 wt. %		<45 µm	0/30					--	--	--	--
		mar0107.012	MET01A	powder	Odessa IAB Iron	>99 wt. %		<45 µm	0/45					--	--	--	--
		mar0107.020	MET01A	powder	Odessa IAB Iron	>99 wt. %		<45 µm	0/60					--	--	--	--
		mar0107.028	MET01A	powder	Odessa IAB Iron	>99 wt. %		<45 µm	0/75					--	--	--	--
		mar0707a.004	MET01A	powder	Odessa IAB Iron	>99 wt. %		<45 µm	30/60					--	--	--	--
		mar0207.012	MET01A	powder	Odessa IAB Iron	>99 wt. %		<45 µm	30/30	*Cloutis et al., 2010*				--	--	--	--
		mar0207.020	MET01A	powder	Odessa IAB Iron	>99 wt. %		<45 µm	30/0					--	--	--	--
		mar0207.028	MET01A	powder	Odessa IAB Iron	>99 wt. %		<45 µm	30/-60					--	--	--	--
		mar0207.036	MET01A	powder	Odessa IAB Iron	>99 wt. %		<45 µm	60/60					--	--	--	--
		mar0207.060	MET01A	powder	Odessa IAB Iron	>99 wt. %		<45 µm	60/-30					--	--	--	--
		mar0707.004	MET01A	powder	Odessa IAB Iron	>99 wt. %		<45 µm	0/0					--	--	--	--

		mar0707.012	MET01A	powder	Odessa IAB Iron	>99 wt. %		<45 µm	30/-30					--	--	--	--
		mar0707.020	MET01A	powder	Odessa IAB Iron	>99 wt. %		<45 µm	45/-45					--	--	--	--
		mar0707.028	MET01A	powder	Odessa IAB Iron	>99 wt. %		<45 µm	60/-60					--	--	--	--
		081222a.001	QUE 94204	powder	EH7	<3 wt. %	Pyx (En~100), Tro, Plag (An 22.5, Ab 77.5)	unsorted	30/0		0	100	0	952.3	0.45	6.68	0.01
		081222a.004	LAP 02225	powder	EH impact melt	7 wt. %	Pyx (En 99.7, Fs 0.3), Plag (Ab 97.5, Ol 2.5), Tro	unsorted	30/0	*Izawa et al., 2010*	0.3	99.7	0	--	--	--	--
		081222a.006	ALH 81021	powder	EL6	5 wt. %	Pyx (En 99, Wo 0.8), Plag (An 15, Ab 81, Ol 4)	unsorted	30/0		0.2	99	0.8	--	--	--	--
		081222a.007	TIL 91714	powder	EL5	< 3 wt. %	Pyx (En 98.9, Wo 0.7), Tro	unsorted	30/0		0.4	98.9	0.7	954.0	<0.1	6.16	0.01

		081222a.009	EET 87746	powder	EH4	12 wt. %	Tro, Pyx (En 99.7, Fs 0.3), Olv (Fo 98.5)	unsorted	30/0		0.3	99.7	0	--	--	--	--
		081222a.011	PCA 91020	powder	EL3	9 wt. %	Tro, Olv (Fo 98.4), Pyx (En 99, Fs 0.7)	unsorted	30/0		0.7	99	0.3	--	--	--	--
		081222a.013	LEW 88180	powder	EH5	13 wt. %	Pyx (En 99.7, Fs 0.3), Tro, Plag (Ab 98.4, An 0.5)	unsorted	30/0		0.3	99.7	0	--	--	--	--
		081222a.015	EET 96135.16	powder	EH4/5	12 wt. %	Pyx (En 99.5, Fs 0.5), Tro	unsorted	30/0		0.5	99.5	0	--	--	--	--
		081222a.016	MAC 02747	powder	EL4	4 wt. %	Pyx (En 97.5, Fs 2.5), Tro	unsorted	30/0		2.5	97.5	0	--	--	--	--
		081222a.017	MAC 02837	powder	EL3	< 3 wt. %	Tro, Olv (Fo~100), Pyx (En	unsorted	30/0		1.5	98.5	0	975.0	0.30	4.40	0.03

							98.5, Fs 1.5)										
		081222a.018	MET 00783	powder	EH4	6 wt. %	Pyx (En 99.5, Fs 0.5), Tro	unsorted	30/0		0.5	99.5	0	966.0	<0.1	2.87	0.01
		081222a.019	NWA 2212	powder	EL6	12 wt. %	Pyx (En 98.65, Fs 0.15), Tro	unsorted	30/0		0.15	98.65	1.2	--	--	--	--
		081222a.020	NWA 717	powder	EL6	7 wt. %	Pyx (En 99, Fs 0.15), Tro	unsorted	30/0		0.15	99	0.85	--	--	--	--
	Minerals	c1pp40.asc	PYX003	powder	En 68.5 Fs 28.2 Wo 3.3	0 wt. %	Pyx	<45	30/0	*Horgan et al., 2014*	28.2	68.5	3.3	924.0	<0.1	56.31	0.06
		c1pp46.asc	PYX015	powder	En 51 Fs 5.6 Wo 43.4	0 wt. %	Pyx	<45	30/0		5.6	51	43.4	918.0	<0.1	33.49	0.02
		c1pp13.asc	PYX023	powder	En 89.3 Fs 9.4 Wo 1.3	0 wt. %	Pyx	45-90	30/0		9.4	89.3	1.3	916.0	<0.1	66.43	0.02
		c1sc36.asc	PYX032	powder	En 54.9 Fs 41.5 Wo3.6	0 wt. %	Pyx	45-90	30/0		41.5	54.9	3.6	938.0	0.10	74.80	0.04
		c1pp87.asc	PYX042	powder	En 86.8 Fs 12.8 Wo 0.4	0 wt. %	Pyx	45-90	30/0		12.8	86.8	0.4	916.0	<0.1	77.24	0.01
		c1pp43.asc	PYX108	powder	En 91.1 Fs 7.8 Wo 1.1	0 wt. %	Pyx	45-90	30/0		7.8	91.1	1.1	915.0	<0.1	62.81	0.01
		c1pp47.asc	PYX110	powder	En 86.3 Fs 13.2 Wo 0.5	0 wt. %	Pyx	45-90	30/0		13.2	86.3	0.5	914.0	<0.1	78.61	0.01
		c1pp42.asc	PYX112	powder	En 64.8 Fs 26.9 Wo 8.3	0 wt. %	Pyx	<45	30/0		26.9	64.8	8.3	925.0	<0.1	47.23	0.04
		c1pp44.asc	PYX117	powder	En 74.7 Fs 24.6 Wo 0.7	0 wt. %	Pyx	<45	30/0		24.6	74.7	0.7	922.0	<0.1	66.08	0.04

		c1pp52.asc	PYX119	powder	En 85.1 Fs 14.6 Wo 0.3	0 wt. %	Pyx	45-90	30/0		14.6	85.1	0.3	918.0	<0.1	61.59	0.03
Brown University/ RELAB	Sulfide	C1TB38	TB-TJM-038	powder	Oldhamite (CaS) powder from Norton County aubrite	0 wt. %	Old	unsorted	30/0	None listed in RELAB database				956.0	<0.1	11.62	0.10
		C1TB52	TB-TJM-052	powder	Synthetic oldhamite (CaS) powder	0 wt. %	Old	<44 micron	30/0	None listed in RELAB database				--	--	--	--
		C2AG02	AG-BXR-002	powder	Pentlandite ((Fe,Ni)9S8) powder from Sudbury, Canada	0 wt. %	Pent	75-212 microns	0/-30	None listed in RELAB database				--	--	--	--
		C1AG03	AG-BXR-003	powder	Pentlandite ((Fe,Ni)9S8) powder from Sudbury, Canada	0 wt. %	Pent	212-600 microns	0/-30	None listed in RELAB database				--	--	--	--
		C1AG04	AG-BXR-004	slab	Pentlandite ((Fe,Ni)9S8) powder from Sudbury, Canada	0 wt. %	Pent	--	0/-30	None listed in RELAB database				--	--	--	--
		C1WV02	WV-JWH-002	powder	Synthetic FeS	0 wt. %	Tro	unsorted	30/0	None listed in RELAB database				--	--	--	--
		C1WV03	WV-JWH-003	powder	Synthetic (Fe 0.4 Mn 0.6) S	0 wt. %	Ala	unsorted	30/0	None listed in RELAB database				--	--	--	--
		C1WV04	WV-JWH-004	powder	Synthetic (Fe 0.25 Mn 0.75) S	0 wt. %	Ala	unsorted	30/0	None listed in RELAB database				--	--	--	--
		C1WV05	WV-JWH-005	powder	Synthetic MnS	0 wt. %	Ala	unsorted	30/0	None listed in RELAB database				--	--	--	--
		C1SC76	SC-EAC-076	powder	Synthetic Pyrrhotite	0 wt. %	Pyr	<45 micron	0/15	None listed in RELAB database				--	--	--	--

		C1SH49	SH-SJG-049	powder	Chalcopyrite	0 wt.%	Chal	<100 micron	30/0	None listed in RELAB database				895.0	<0.1	12.7	0.2
	Synthetic Olivine	C1DD85	DD-MDD-085	powder	Fa 0 Fo 100	0 wt.%	Olv (Fo 100)	<45 micron	30/0	*Dyar et al., 2009*				--	--	--	--
		C1DD98	DD-MDD-098	powder	Fa 100 Fo 0	0 wt.%	Olv (Fo 0)	<45 micron	30/0					1090.0	<0.1	51.32	0.06
		C1DD86	DD-MDD-086	powder	Fa 10.5 Fo 89.5	0 wt.%	Olv (Fo 89.5)	<45 micron	30/0					1058.0	<0.1	7.56	0.02
		C1DD87	DD-MDD-087	powder	Fa 20 Fo 80	0 wt.%	Olv (Fo 80)	<45 micron	30/0					1060.0	<0.1	22.15	0.02
		C1DD88	DD-MDD-088	powder	Fa 25 Fo 75	0 wt.%	Olv (Fo 75)	<45 micron	30/0					1061.0	<0.1	21.85	0.01
		C1DD89	DD-MDD-089	powder	Fa 30 Fo 70	0 wt.%	Olv (Fo 70)	<45 micron	30/0					1064.0	<0.1	25.94	0.01
		C1DD90	DD-MDD-090	powder	Fa 35 Fo 65	0 wt.%	Olv (Fo 65)	<45 micron	30/0					1067.0	<0.1	30.76	0.02
		C1DD91	DD-MDD-091	powder	Fa 40 Fo 60	0 wt.%	Olv (Fo 60)	<45 micron	30/0					1064.0	<0.1	54.06	0.02
		C1DD92	DD-MDD-092	powder	Fa 45 Fo 55	0 wt.%	Olv (Fo 55)	<45 micron	30/0					1069.0	<0.1	32.04	<0.01
		C1DD93	DD-MDD-093	powder	Fa 50 Fo 50	0 wt.%	Olv (Fo 50)	<45 micron	30/0					1071.0	<0.1	27.52	0.02
		C1DD94	DD-MDD-094	powder	Fa 60 Fo 40	0 wt.%	Olv (Fo 40)	<45 micron	30/0					1071.0	<0.1	38.81	0.07
		C1DD95	DD-MDD-095	powder	Fa 70 Fo 30	0 wt.%	Olv (Fo 30)	<45 micron	30/0					1073.0	<0.1	44.21	0.03
		C1DD96	DD-MDD-096	Powder	Fa 80 Fo 20	0 wt.%	Olv (Fo 20)	<45 micron	30/0					1082.0	<0.1	56.43	0.03
		C1DD97	DD-MDD-097	Powder	Fa 90 Fo 10	0 wt.%	Olv (Fo 10)	<45 micron	30/0					1085.0	<0.1	50.59	0.03

		C1DL01A	DL-CMP-001-A	powder	En 100	0 wt.%	Pyx (En 100)	<45 micron	30/0		0	100	0	934.0	0.22	1.37	0.02
	Synthetic Pyroxene	C1DL02A	DL-CMP-002-A	powder	En 80 Fs 20	0 wt.%	Pyx (En 80, Fs 20)	<45 micron	30/0		20	80	0	914.0	<0.1	72.94	0.01
		C1DL03A	DL-CMP-003-A	powder	En 75 Fs 25	0 wt.%	Pyx (En 75, Fs 25)	<45 micron	30/0		25	75	0	917.0	<0.1	62.15	0.01
		C1DL04A	DL-CMP-004-A	powder	En 50 Fs 50	0 wt.%	Pyx (En 50, Fs 50)	<45 micron	30/0		50	50	0	926.0	<0.1	79.52	<0.01
		C1DL05A	DL-CMP-005-A	powder	En 40 Fs 60 (97+% Cpx)	0 wt.%	Pyx (En 40, Fs 60)	<45 micron	30/0		60	40	0	925.0	<0.1	83.44	<0.01
		C1DL06A	DL-CMP-006-A	powder	En 25 Fs 75	0 wt.%	Pyx (En 25, Fs 75)	<45 micron	30/0	*Klima et al., 2007*	75	25	0	937.0	<0.1	86.02	0.01
		C1DL07A	DL-CMP-007-A	powder	Wo 16.7 En 83.3	0 wt.%	Pyx (En 83.3, Wo 16.7)	<45 micron	30/0		0	83.3	16.7	--	--	--	--
		C1DL08A	DL-CMP-008-A	powder	Wo 5 En 38 Fs 57 (E36-103, 100% opx)	0 wt.%	Pyx (En 38, Fs 57)	<45 micron	30/0		57	38	5	944.0	<0.1	85.10	<0.01
		C1DL09A	DL-CMP-009-A	powder	Wo 10 En 45 Fs 45 (EFW5-13)	0 wt.%	Pyx (En 45, Fs 27)	<45 micron	30/0		45	45	10	956.0	<0.1	70.87	0.01
		C1DL10A	DL-CMP-010-A	powder	Wo 10 En 63 Fs 27 (EFW13-4, 100% cpx)	0 wt.%	Pyx (En 63, Fs 27)	<45 micron	30/0		27	63	10	951.0	<0.1	68.88	<0.01
		C1DL11A	DL-CMP-011-A	powder	Wo 10 En 36 Fs 54 (E35-6, 100% cpx)	0 wt.%	Pyx (En 36, Fs 54)	<45 micron	30/0		54	36	10	958.0	<0.1	84.76	<0.01

		C1DL12A	DL-CMP-012-A	powder	Wo 5 En 47.5 Fs 47.5 (E14-11)	0 wt. %	Pyx (En 47.5, Fs 47.5)	<45 micron	30/0		47.5	47.5	5	940.0	<0.1	72.03	0.01
		C1DL13A	DL-CMP-013-A	powder	Wo 8 En 46 Fs 46 (E40-1: 99.5% cpx, 0.5% glass, Crist)	0 wt. %	Pyx (En 46, Fs 46)	<45 micron	30/0		46	46	8	944.0	<0.1	80.30	0.01
		C1DL14A	DL-CMP-014-A	powder	Wo 2.5 En 39 Fs 58.5 (E45-100, 95% hyp, 2-5% cpx)	0 wt. %	Pyx (En 39, Fs 58.5)	<45 micron	30/0		58.5	39	2.5	937.0	<0.1	76.87	0.01
		C1DL15A	DL-CMP-015-A	powder	Wo 5 En 66.5 Fs 28.5 (EFW29-5)	0 wt. %	Pyx (En 66.5, Fs 28.5)	<45 micron	30/0		28.5	66.5	5	929.0	<0.1	64.32	0.03
		C1DL16A	DL-CMP-016-A	powder	Wo 5 En 76 Fs 19 (EFW21-101)	0 wt. %	Pyx (En 76, Fs 19)	<45 micron	30/0		19	76	5	921.0	<0.1	70.08	0.01
		C1DL17A	DL-CMP-017-A	powder	Wo 20 En 64 Fs 16 (EFW8-3, 99.5% cpx)	0 wt. %	Pyx (En 64, Fs 16)	<45 micron	30/0		16	64	20	992.0	<0.1	64.18	<0.01
		C1DL18A	DL-CMP-018-A	powder	Wo 10 En 72 Fs 18 (EFW9-18, 100% cpx)	0 wt. %	Pyx (En 72, Fs 18)	<45 micron	30/0		18	72	10	942.0	<0.1	62.28	0.02
		C1DL19A	DL-CMP-019-A	powder	Wo 20 En 56 Fs 24 (EFW12-3, 99.5% cpx)	0 wt. %	Pyx (En 56, Fs 24)	<45 micron	30/0		24	56	20	999.0	<0.1	63.21	0.01
		C1DL20A	DL-CMP-020-A	powder	En 17 Fs 83	0 wt. %	Pyx (En 17, Fs 83)	<45 micron	30/0		83	17	0	944.0	<0.1	82.91	0.01
		C1DL21A	DL-CMP-021-A	powder	En 8 Fs 92	0 wt. %	Pyx (En 8, Fs 92)	<45 micron	30/0		92	8	0	946.0	<0.1	78.88	0.02
		C1DL22A	DL-CMP-022-A	powder	En 75 Fs 25	0 wt. %	Pyx (En 75, Fs 25)	<45 micron	30/0		25	75	0	915.0	<0.1	57.89	0.01

		C1DL23A	DL-CMP-023-A	powder	En 30 Fs 70	0 wt. %	Pyx (En 30, Fs 70)	<45 micron	30/0		70	30	0	938.0	<0.1	88.94	<0.01
		C1DL24A	DL-CMP-024-A	powder	En 17 Fs 83	0 wt. %	Pyx (En 17, Fs 83)	<45 micron	30/0		83	17	0	941.0	<0.1	83.81	0.01
		C1DL25A	DL-CMP-025-A	powder	En 35 Fs 65	0 wt. %	Pyx (En 35, Fs 65)	<45 micron	30/0		65	35	0	935.0	<0.1	76.86	0.01
		C1DL26A	DL-CMP-026-A	powder	En 70 Fs 30	0 wt. %	Pyx (En 70, Fs 30)	<45 micron	30/0		30	70	0	916.0	<0.1	70.01	0.01
		C1DL27A	DL-CMP-027-A	powder	En 80 Fs 20	0 wt. %	Pyx (En 80, Fs 20)	<45 micron	30/0		20	80	0	914.0	<0.1	70.08	0.01
		C1DL28A	DL-CMP-028-A	powder	En 25 Fs 75	0 wt. %	Pyx (En 25, Fs 75)	<45 micron	30/0		75	25	0	930.7	0.47	87.86	0.02
		C1DL29A	DL-CMP-029-A	powder	En 15 Fs 85 (Minor olivine)	0 wt. %	Pyx (En 15, Fs 85)	<45 micron	30/0		85	15	0	942.0	<0.1	59.04	0.01
		C1DL30A	DL-CMP-030-A	powder	F3-101	0 wt. %		<45 micron	30/0		--	--	--	917.0	<0.1	83.16	0.01
		C1DL31A	DL-CMP-031-A	powder	Fs 50 (F5-100)	0 wt. %	Pyx (Fs 50)	<45 micron	30/0		50	--	--	928.0	<0.1	84.99	<0.01
		C1DL32A	DL-CMP-032-A	powder	Wo 46.2 En 53.8	0 wt. %	Pyx (En 53.8, Wo 46.2)	<45 micron	30/0		0	53.8	46.2	1046.0	<0.1	2.87	0.01
		C1DL33A	DL-CMP-033-A	powder	Wo 50 En 40 Fs 10 (D2-11, 99% cpx, 1% crist)	0 wt. %	Pyx (En 40, Fs 10)	<45 micron	30/0		10	40	50	1049.0	<0.1	35.48	0.01
		C1DL34A	DL-CMP-034-A	powder	En 50 Fs 50 (Wo0 x=50 B)	0 wt. %	Pyx (En	<45 micron	30/0		50	50	0	927.0	<0.1	72.37	0.01

							50, Fs 50)										
		C1DL35A	DL-CMP-035-A	powder	Wo 50 En 10 Fs 40 (DH8-13B, 99.5% wo, 0.5% glass)	0 wt. %	Pyx (En 10, Fs 40)	<45 micron	30/0		40	10	50	1055.0	0.17	54.48	0.05
		C1DL36A	DL-CMP-036-A	powder	Wo 50 En 20 Fs 30 (D6-14, 95% aug, 5% bust)	0 wt. %	Pyx (En 20, Fs 30)	<45 micron	30/0		30	20	50	1053.0	<0.1	50.62	0.02
		C1DL37A	DL-CMP-037-A	powder	Wo 50 En 15 Fs 35 (D3H7-25, 100% pyx)	0 wt. %	Pyx (En 15, Fs 35)	<45 micron	30/0		35	15	50	1060.0	<0.1	47.00	0.01
		C1DL38A	DL-CMP-038-A	powder	Wo 9 En 91	0 wt. %	Pyx (En 91, Wo 9)	<45 micron	30/0		0	91	9	--	--	--	--
		C1DL39A	DL-CMP-039-A	powder	Wo 50 En 25 Fs 25 (D5-26, 99% aug)	0 wt. %	Pyx (En 25, Fs 25)	<45 micron	30/0		25	25	50	1056.0	<0.1	52.41	0.06
		C1DL40A	DL-CMP-040-A	powder	Wo 50 En 5 Fs 45 (D1H9-32, 100% wo)	0 wt. %	Pyx (En 5, Fs 45)	<45 micron	30/0		45	5	50	1052.0	<0.1	58.05	0.03
		C1DL41A	DL-CMP-041-A	powder	Wo 50 En 0 Fs 50 (D10-35, 100% pyx)	0 wt. %	Pyx (En 0, Fs 50)	<45 micron	30/0		50	0	50	1055.0	<0.1	33.99	0.03
		C1DL42A	DL-CMP-042-A	powder	Wo 60 En 20 Fs 20 (EFW22-2, 50% pyx, 45% wo, 5% glass)	0 wt. %	Pyx (En 20, Fs 20)	<45 micron	30/0		20	20	60	1063.1	0.31	44.59	0.04
		C1DL43A	DL-CMP-043-A	powder	Wo 50 En 40 Fs 10 (D8H2-4, 100% cpx)	0 wt. %	Pyx (En 40, Fs 10)	<45 micron	30/0		10	40	50	1056.0	0.14	46.30	0.02
		C1DL44A	DL-CMP-044-A	powder	Wo 50 En 35 Fs 15 (D7H3-18, 100% pyx)	0 wt. %	Pyx (En 35, Fs 15)	<45 micron	30/0		15	35	50	1052.0	<0.1	55.14	0.01
		C1DL45A	DL-CMP-045-A	powder	Wo 4 En 48 Fs 48 (E41-105)	0 wt. %	Pyx (En 48, Fs 15)	<45 micron	30/0		48	48	4	936.0	<0.1	82.16	0.02

		C1DL46A	DL-CMP-046-A	powder	Wo 15 En 34 Fs 51 (E43-100, 70% cpx)	0 wt.%	Pyx (En 34, Fs 51)	<45 micron	30/0		51	34	15	970.0	<0.1	74.78	0.02
		C1DL47A	DL-CMP-047-A	powder	Wo 25 En 30 Fs 45 (E44-101, 95-98% cpx)	0 wt.%	Pyx (En 30, Fs 45)	<45 micron	30/0		45	30	25	1018.0	<0.1	84.09	0.01
		C1DL48A	DL-CMP-048-A	powder	Wo 10 En 13.5 Fs 76.5 (Wo 10 X=85 B)	0 wt.%	Pyx (En 13.5, Fs 76.5)	<45 micron	30/0		76.5	13.5	10	951.1	0.30	43.83	0.01
		C1DL49A	DL-CMP-049-A	powder	Wo 10 En 13.5 Fs 76.5 (Wo 10 X=85)	0 wt.%	Pyx (En 13.5, Fs 76.5)	<45 micron	30/0		76.5	13.5	10	971.0	<0.1	84.08	0.01
		C1DL50A	DL-CMP-050-A	powder	Wo 15 En 21 Fs 64	0 wt.%	Pyx (En 21, Fs 64)	<45 micron	30/0		64	21	15	988.0	<0.1	87.55	<0.01
		C1DL51A	DL-CMP-051-A	powder	Wo 20 En 40 Fs 40 (EFW4-9, 100% pyx)	0 wt.%	Pyx (En 40, Fs 40)	<45 micron	30/0		40	40	20	1000.0	<0.1	79.71	0.01
		C1DL52A	DL-CMP-052-A	powder	Wo 10 En 90 Fs 0	0 wt.%	Pyx (En 90, Wo 10)	<45 micron	30/0		0	90	10	965.0	<0.1	0.55	0.01
		C1DL53A	DL-CMP-053-A	powder	Wo 10 En 22.5 Fs 67.5	0 wt.%	Pyx (En 22.5, Fs 67.5)	<45 micron	30/0		67.5	22.5	10	967.0	<0.1	84.22	<0.01
		C1DL54A	DL-CMP-054-A	powder	Wo 15.2 En 6.8 Fs 78 (Wo 15 X=92)	0 wt.%	Pyx (En 6.8, Fs 78)	<45 micron	30/0		78	6.8	15.2	999.1	0.35	87.67	0.01
		C1DL55A	DL-CMP-055-A	powder	Wo 20 En 20 Fs 60	0 wt.%	Pyx (En 20, Fs 60)	<45 micron	30/0		60	20	20	1005.0	<0.1	85.03	<0.01

		C1DL56A	DL-CMP-056-A	powder	Wo 20 En 20 Fs 60	0 wt. %	Pyx (En 20, Fs 60)	<45 micron	30/0		60	20	20	975.0	<0.1	69.95	0.01
		C1DL57A	DL-CMP-057-A	powder	Wo 20 En 32 Fs 48 (EFW34-2, 100% pyx)	0 wt. %	Pyx (En 32, Fs 48)	<45 micron	30/0		48	32	20	1002.0	<0.1	75.02	0.01
		C1DL58A	DL-CMP-058-A	powder	Wo 25 En 30 Fs 45	0 wt. %	Pyx (En 30, Fs 45)	<45 micron	30/0		45	30	25	1006.0	<0.1	74.96	<0.01
		C1DL59A	DL-CMP-059-A	powder	Wo 25 En 11 Fs 64	0 wt. %	Pyx (En 11, Fs 64)	<45 micron	30/0		64	11	25	1075.0	<0.1	43.15	0.02
		C1DL60A	DL-CMP-060-A	powder	Wo 30 En 70	0 wt. %	Pyx (En 70, Wo 30)	<45 micron	30/0		0	70	30	--	--	--	--
		C1DL61A	DL-CMP-061-A	powder	Fs 100 PP1	0 wt. %	Pyx (Fs 100)	<45 micron	30/0		100	0	0	948.0	<0.1	83.58	0.01
		C1DL62A	DL-CMP-062-A	powder	Fs 100 PP2	0 wt. %	Pyx (Fs 100)	<45 micron	30/0		100	0	0	946.0	<0.1	77.75	<0.01
		C1DL63A	DL-CMP-063-A	powder	Fs 100 PP3	0 wt. %	Pyx (Fs 100)	<45 micron	30/0		100	0	0	950.0	<0.1	79.52	0.01
		C1DL64A	DL-CMP-064-A	powder	En 97.5 Fs 2.5	0 wt. %	Pyx (En 97.5, Fs 2.5)	<45 micron	30/0		2.5	97.5	0	907.0	<0.1	36.65	0.02
		C1DL65A	DL-CMP-065-A	powder	En 90 Fs 10	0 wt. %	Pyx (En 90, Fs 10)	<45 micron	30/0		10	90	0	909.0	<0.1	44.02	0.01
		C1DL66A	DL-CMP-066-A	powder	Wo 30 En 17.5 Fs 52.5	0 wt. %	Pyx (En 17.5, Fs 52.5)	<45 micron	30/0		52.5	17.5	30	1019.0	<0.1	79.45	0.01
		C1DL67A	DL-CMP-067-A	powder	Wo 30 En 49 Fs 21 (EFW11-4, 95% cpx)	0 wt. %	Pyx (En	<45 micron	30/0		21	49	30	1018.0	<0.1	67.12	<0.01

							49, Fs 21)										
		C1DL68A	DL-CMP-068-A	powder	Wo 30 En 28 Fs 42 (E33-16, 100% cpx)	0 wt.%	Pyx (En 28, Fs 42)	<45 micron	30/0		42	28	30	1018.0	<0.1	82.93	0.00
		C1DL69A	DL-CMP-069-A	powder	Wo 34 En 20 Fs 46 (E46-7, 99.7% cpx)	0 wt.%	Pyx (En 20, Fs 46)	<45 micron	30/0		46	20	34	1029.0	<0.1	73.97	0.02
		C1DL70A	DL-CMP-070-A	powder	Wo 40 En 15 Fs 45	0 wt.%	Pyx (En 15, Fs 45)	<45 micron	30/0		45	15	40	1036.0	<0.1	75.02	0.01
		C1DL71A	DL-CMP-071-A	powder	Wo 40 En 24 Fs 36 (EFW1-2, 100% cpx)	0 wt.%	Pyx (En 24, Fs 36)	<45 micron	30/0		36	24	40	1031.0	<0.1	71.31	0.01
		C1DL72A	DL-CMP-072-A	powder	Wo 30 En 70	0 wt.%	Pyx (En 70, Wo 30)	<45 micron	30/0		0	70	30	--	--	--	--
		C1DL73A	DL-CMP-073-A	powder	Wo 30 En 35 Fs 35 (EFW3-9, 99% cpx)	0 wt.%	Pyx (En 35, Fs 35)	<45 micron	30/0		35	35	30	1017.0	<0.1	70.12	0.01
		C1DL74A	DL-CMP-074-A	powder	Wo 30 En 21 Fs 49 (E27-1, 97% cpx)	0 wt.%	Pyx (En 21, Fs 49)	<45 micron	30/0		49	21	30	1018.0	<0.1	75.48	0.01
		C1DL75A	DL-CMP-075-A	powder	Wo 40 En 48 Fs 12 (E6-7, 100% pyx)	0 wt.%	Pyx (En 48, Fs 12)	<45 micron	30/0		12	48	40	1029.0	<0.1	63.18	0.01
		C1DL76A	DL-CMP-076-A	powder	Wo 40 En 10 Fs 50 (EFW17-2, 95% pyx)	0 wt.%	Pyx (En 10, Fs 50)	<45 micron	30/0		50	10	40	1037.0	<0.1	43.99	0.02
		C1DL77A	DL-CMP-077-A	powder	Wo 40 En 55 Fs 5 (EFW19-3, 100% pyx)	0 wt.%	Pyx (En 55, Fs 5)	<45 micron	30/0		5	55	40	1027.0	<0.1	58.90	0.01
		C1DL78A	DL-CMP-078-A	powder	Wo 37.5 En 62.5	0 wt.%	Pyx (En 62.5,	<45 micron	30/0		0	62.5	37.5	--	--	--	--

							Wo 37.5)										
		C1DL79A	DL-CMP-079-A	powder	Wo 40 En 30 Fs 30 (EFW2-7, 100% pyx)	0 wt. %	Pyx (En 30, Fs 30)	<45 micron	30/0		30	30	40	1032.0	<0.1	69.78	0.01
		C1DL80A	DL-CMP-080-A	powder	Wo 40 En 20 Fs 40 (EFW15-10, 100% pyx)	0 wt. %	Pyx (En 20, Fs 40)	<45 micron	30/0		40	20	40	1042.0	<0.1	64.89	0.02
		C1DL81A	DL-CMP-081-A	powder	Wo 35 En 26 Fs 39 (E42-106, 100% cpx)	0 wt. %	Pyx (En 26, Fs 39)	<45 micron	30/0		39	26	35	1022.0	<0.1	80.98	0.01
		C1DL82A	DL-CMP-082-A	powder	Wo 50 Fs 50 (Ca Hd O)	0 wt. %	Pyx (Fs 50, Wo 50)	<45 micron	30/0		50	0	50	1061.0	<0.1	60.55	0.02
		C1DL83A	DL-CMP-083-A	powder	Wo 50 Fs 50 (Hd P)	0 wt. %	Pyx (Fs 50, Wo 50)	<45 micron	30/0		50	0	50	1084.0	<0.1	61.21	0.03
		C1DL84A	DL-CMP-084-A	powder	Wo 35 Fs 65	0 wt. %	Pyx (Fs 65, Wo 35)	<45 micron	30/0		65	0	35	1037.0	<0.1	82.60	0.01
		C1DL85A	DL-CMP-085-A	powder	Wo 30 Fs 70	0 wt. %	Pyx (Fs 70, Wo 30)	<45 micron	30/0		70	0	30	1027.0	<0.1	65.85	0.01
		C1DL86A	DL-CMP-086-A	powder	Wo 25 Fs 75	0 wt. %	Pyx (Fs 75, Wo 25)	<45 micron	30/0		75	0	25	1018.0	<0.1	80.34	0.01
		C1DL87A	DL-CMP-087-A	powder	Wo 20 Fs 80	0 wt. %	Pyx (Fs 80, Wo 20)	<45 micron	30/0		80	0	20	1014.0	<0.1	86.17	0.00
		C1DL88A	DL-CMP-088-A	powder	Wo 10 Fs 90	0 wt. %	Pyx (Fs 90, Wo 10)	<45 micron	30/0		90	0	10	990.0	<0.1	73.78	0.01
		C1DL89A	DL-CMP-089-A	powder	Wo 7 Fs 93	0 wt. %	Pyx (Fs 93, Wo 7)	<45 micron	30/0		93	0	7	972.0	<0.1	83.67	0.01

		C1DL90A	DL-CMP-090-A	powder	Wo 5 Fs 95	0 wt. %	Pyx (Fs 95, Wo 5)	<45 micron	30/0		95	0	5	965.0	<0.1	71.84	0.01
		C1DL91A	DL-CMP-091-A	powder	Wo 2 Fs 98	0 wt. %	Pyx (Fs 98, Wo 2)	<45 micron	30/0		98	0	2	970.0	<0.1	64.85	0.03

Mineralogy key: Pyx – pyroxene, Olv - olivine, Plag – plagioclase, Diop – diopside, Tro – troilite, Tri – tridymite, Ano – anorthite, Ab – albite, Gra – graphite, Sch – schreibersite, Gla – glass, Pent – pentlandite, Old – oldhamite, Pyr – pyrrhotite, Chal – chalcopyrite

Roughness key: 1) Rough, unprepared hand sample, 2) Rough surface with saw marks, 3) Finish with 180 grit paper, 4) Finished with 600 grit paper, 5) Finished with 1200 grit paper, 6) Polished with 1 micron diamond paste, 7) Polished and etched with nitric acid

Supplemental Table S3.2 can be found online at the Open Science Foundation repository DOI 10.17605/OSF.IO/Z6PHN.